2013-03-07

The Characterization of Military Aircraft Jet Noise Using Near-Field Acoustical Holography Methods

Alan Thomas Wall
Brigham Young University

The Characterization of Military Aircraft Jet Noise Using Near-Field Acoustical Holography Methods

Alan Thomas Wall

A dissertation submitted to the faculty of
Brigham Young University
in partial fulfillment of the requirements for the degree of

Doctor of Philosophy

Kent L. Gee, Chair
Scott D. Sommerfeldt
Jonathan D. Blotter
Timothy W. Leishman
Tracianne B. Neilsen

Department of Physics and Astronomy

Brigham Young University

March 2013

ABSTRACT

The Characterization of Military Aircraft Jet Noise Using
Near-Field Acoustical Holography Methods

Alan Thomas Wall
Department of Physics and Astronomy, BYU
Doctor of Philosophy

The noise emissions of jets from full-scale engines installed on military aircraft pose a significant hearing loss risk to military personnel. Noise reduction technologies and the development of operational procedures that minimize noise exposure to personnel are enhanced by the accurate characterization of noise sources within a jet. Hence, more than six decades of research have gone into jet noise measurement and prediction. In the past decade, the noise-source visualization tool near-field acoustical holography (NAH) has been applied to jets. NAH fits a weighted set of expansion wave functions, typically planar, cylindrical, or spherical, to measured sound pressures in the field. NAH measurements were made of a jet from an installed engine on a military aircraft. In the present study, the algorithm of statistically optimized NAH (SONAH) is modified to account for the presence of acoustic reflections from the concrete surface over which the jet was measured. The three dimensional field in the jet vicinity is reconstructed, and information about sources is inferred from reconstructions at the boundary of the turbulent jet flow. Then, a partial field decomposition (PFD) is performed, which represents the total field as the superposition of multiple, independent partial fields. This is the most direct attempt to equate partial fields with independent sources in a jet to date.

Keywords: jet, aeroacoustics, near-field acoustical holography, partial field decomposition

ACKNOWLEDGMENTS

To my wife, Kate, who has raised three children and carried a fourth, served as the ideal sounding board during late-night physics tutorials, and has borne with the constant forgetfulness of a physicist, I say, thank you. You are too beautiful, gentle, and kind for words, but I try anyway. (Let's do a bed-and-breakfast again, when this is over!)

To my advisor, Dr. Kent Gee—you helped me keep the big-picture perspective. Without your constant nudging me back to the road of sensibility, I'd have surely gone over the edge. I thank you for my passion for acoustics and my exposure to a world of professionalism. It was fun *and* beneficial! (Who'd have thought?)

To Dr. Tracianne Neilsen, my advisor who didn't have to be, thank you. You devoted gobs of your limited, precious time to edit, to listen, to edify and to befriend me.

A special thanks to my parents, for helping to watch the kids, granting me life, and teaching me to love what I do; to Evan, Rosemarie, and Peter, who simultaneously relieve my stress while they add to it; to my several office mates, who share my victories, my music, and my homework; to Dr. Gus Hart for recruiting me to BYU and teaching me handball; to Dr. J. Ward Moody for telling me I was the "best of the best of the best" and other words of encouragement; and to all the others not mentioned, but who will be listed in pencil below, once I have kicked myself for forgetting you. I won't say, "I couldn't have done it without you," but you made it all worthwhile.

This research was supported in part by the appointment of Alan Wall to the Student Research Participation Program at U.S. Air Force Research Laboratory, Human Effectiveness Directorate, Warfighter Interface Division, Battlespace Acoustics administered by the Oak Ridge Institute for Science and Education through an interagency agreement between the U.S. Department of Energy and USAFRL.

Contents

List of Figures

Chapter 1

Introduction

Tactical fighter aircraft have become essential for establishing air dominance in military operations. The primary noise source from a jet-propelled aircraft is the hot, turbulent, supersonic exhaust plume (i.e., the "jet").[1] As military aircraft become more technologically advanced and more powerful, their noise emissions also increase. Jet noise poses a significant hearing loss risk to military personnel. It also leads to community annoyance, school disruption, sleep disturbance and other health risks, and negatively impacts wildlife.[2] Noise reduction technologies and the development of operational procedures that minimize noise exposure are enhanced by the accurate characterization of noise sources within a jet. This chapter provides a historical summary of jet noise characterization methods, with an emphasis on reduced-order models and acoustical inverse methods, which pertain to the present work. It also presents the objectives and scope of the current work, which are to apply near-field acoustical holography (NAH) and partial field decomposition (PFD) to characterize the source and sound field of a full-scale jet, and to separate independent source mechanisms. Concerns regarding the application of NAH methods to an inherently nonlinear source are addressed. A brief overview of the general NAH process is also provided.

1.1 Jet Noise Research Overview

Jet noise investigations began in earnest with Sir James Lighthill, in response to the "public odium" directed toward the aircraft industry.[3,4] In 1952, Lighthill[3] developed what came to be known as the acoustic analogy for jet noise. In this model, the compressible equations of fluid motion were cast into a form that represented the propagation of acoustic waves (the wave equation), and the remaining terms were considered to be the sources. Many variants of Lighthill's basic theory have emerged, in an attempt to modify the source terms to account for known jet flow properties. Among the most popular variants include that of Lilley,[5,6] who sought to account for the refraction of acoustic waves through the nonuniform mean flow of the jet. He treated the problem as an inner flow problem that was matched to an outer radiation problem. Lilley's approach has been adopted by many researchers, and was the preferred treatment through the seventies and early eighties.[7] Jet noise models based on the acoustic analogy require detailed measurements of the turbulent flow field, which are generally difficult to obtain.

In addition to analytical source models based on fluid principles, numerical simulations of turbulent fluid flow have been utilized to predict acoustic radiation from jets. Challenges to computational aeroacoustics include the requirements that the method used must be designed to include quantities over length scales that differ by several orders of magnitude, and must be valid from the source region all the way out to measurement points many acoustic wavelengths away.[8] The computational expense required for high-velocity jets renders this approach impractical for engineering applications.[9] Hence, emphasis has been placed in recent years on direct measurements of flow and acoustic quantities, and on semi-empirical models based on such measurements.

Until the 1970s, jet noise was thought to consist entirely of a volumetric distribution of fine-scale turbulent eddies (FST).[10] In 1967, Mollo-Christensen[11] measured orderly structure in a jet near field, and suggested representing jet sources as a "wave packet." The presence of

large-scale, coherent turbulence structures was demonstrated by Crow and Champagne in 1971,[12] and by Brown and Roshko in 1974.[13] Then, Schlinker *et al*.[14] and Laufer *et al*.[15] observed that there are two distinct sources of jet noise: 1) large-scale turbulence (LST) structures, which radiate broadband acoustic energy in the aft, or downstream direction, and 2) FST, which has a weaker contribution and radiates omnidirectionally. Tam *et al*.[16] developed similarity spectra for these two components, which have been rigorously verified for subsonic and supersonic jets, particularly by Tam *et al*.[10] and by Viswanathan.[17] Since the radiation of LST is highly directional toward the downstream, FST radiation dominates the spectrum to a jet sideline. The LST structures are often associated with instability waves,[18-20] which are disturbances between the ambient fluid and the flow of the jet that grow rapidly and then decay away. Radiation from LST has also been compared to "Mach-wave radiation" from supersonically convecting structures, such as a traveling "wavy wall."[7,16] Since LST dominates the total energy radiated by all but the most modest flows,[21] it has become the focus of measurement and noise reduction studies. The following section explains why inverse methods are a useful tool to characterize the acoustic sources of LST structures.

1.2 Inverse Methods and Reduced-order Models

Advances in measurement technologies have paved the way for array-based acoustical inverse methods to characterize jet noise sources. In such methods, a sound field is represented by a linear combination of spatial basis functions. In other words, the field is expanded into a set of wave functions. This is often performed for complex acoustic pressures on a frequency-by-frequency basis. Hence, each wave function must obey the Helmholtz equation. This means that any superposition of these waves represents a total field that also obeys the Helmholtz equation. To obtain a weighted set of functions that accurately represents the field radiated by a given source, the coefficients of these functions are found to match the expansion to acoustic quantities

at a set of measurement locations in the field, often over a two dimensional surface. Then the field at another location is estimated from the sum of the weighted functions evaluated at the new position; this is referred to as the reconstruction. The accuracy of a sound field reconstruction from an inverse method relies heavily on (1) the ability of the wave functions to represent the field (completeness), and (2) the ability of the measurement to capture enough of the spatial variation in the acoustic field to represent each expansion function.

The reconstruction of an acoustic field is made simpler when the expansion functions are based on a reduced-order field model. The term reduced-order (or reduced-parameter) model refers to a method in which the basis set used to describe the total sound field consists of relatively few expansion terms. Equivalent source models (ESMs) and equivalent wave models (EWMs) are two approaches to designing basis sets. In jet noise literature there is currently little distinction between an ESM and EWM. Since both are methods of representing sound fields with simple functions, they might be considered equivalent. However, in the context of this work, an ESM represents a sound field with an expansion that relies on specific (known or inferred) information about a source. In this sense, Lighthill's acoustic analogy[3] could be considered an ESM (but probably not a reduced-order one, since it requires a detailed knowledge of the turbulence information in the flow field). In contrast, an EWM does not rely on information about the source beyond its geometry (shape and location). Rather, it represents a field with an expansion that is complete in the subspace of the homogeneous, source-free field. In other words, any arbitrary source-free sound field could be represented by the EWM. Traditional NAH based on a discrete Fourier transform of pressures measured over an array, which utilizes an expansion of planar, cylindrical, or spherical wave functions,[22] is a prime example of an EWM.

Simple sources of noise can usually be represented by a relatively small number of well-known expansion functions (e.g. planar, cylindrical, or spherical).[22,23] However, when the sources are large, of irregular shape, or otherwise complex (which most sources are), then the

large number of expansion functions required for such a representation can require an inordinate amount of measurement points, and is often computationally expensive. In these cases, some knowledge of the sound-field properties allows for a reduced-order approach. When the type of expansion functions are selected so as to reduce the number and order of expansion terms required, the requirement for the number of measurements can be reduced. Since LST is highly structured and characterized by partial spatial coherence its radiation can be represented by relatively few low-order basis functions, when properly selected.[24-26] FST, in contrast, is comprised of distributions of incoherent, compact radiators.[10] The extent and complexity of FST precludes any simple representation using reduced-order models.

The remainder of Section 1.2 provides examples of inverse methods that pertain to jet noise research, as well as examples of ESMs and EWMs that clarify the approach of the current work. Many of these methods rely on measurements in the near field of the jet, although what constitutes the near field of a jet is still in debate. (Hence, several of these studies were intended to elucidate the properties of the near field.) To put many of the investigations discussed here in context, it is important to understand that the hydrodynamic near field, acoustic near field, or linear hydrodynamic regime, is the ill-defined region immediately outside the jet shear layer, where pressure fluctuations obey the linear Helmholtz equation, but they decay exponentially with distance from the source. Many authors hesitate to call these pressure fluctuations "acoustic,"[26] but this region is equivalent to the acoustic near field insomuch that it can be considered "outside" the flow, or where pressure fluctuations obey the Helmholtz equation. In addition, this section discusses the critical role of partial field decomposition (PFD) in inverse methods applied to jet noise.

1.2.1 Inverse Methods

When a source generates acoustic waves, the propagation from the source to a point in the field is considered a "forward problem." The "inverse problem" seeks to use knowledge of

acoustic quantities in the field to reverse this process and predict quantities in the backward direction, toward the source. Most acoustical inverse methods share the following properties. (1) The sound field is represented as a linear combination of spatial basis functions. (2) The coefficients of the basis functions are optimized, such that their sum best matches the measured field at the microphone array. For example, traditional beamforming[23] assumes a sparse distribution of monopoles. Since beamforming measurements are made in the far field, radiation from monopole sources is assumed to be nearly planar when it reaches the array. Signals at the array are time-delayed based on a desired direction of arrival and summed. If a source is actually located in this desired "look direction," the signals add in a correlated fashion to return a large amplitude. This can be repeated for many look directions, and the locations and strengths of the sources can be estimated. Discrete-Fourier-transform based (DFT-based) NAH uses a set of elementary wave functions, usually planar, cylindrical, or spherical.[17,19] By far, beamforming and NAH methods are the most widely used in jet noise applications, but other methods that have been employed include the acoustic telescope,[27] polar correlation,[28] and the acoustic mirror.[29] There is a significant limitation of these three methods,[30] as well as traditional beamforming:[31] any inverse method that relies on measurements taken in the acoustic far field, where the amplitudes of exponentially-decaying evanescent waves are below the noise floor of the measurement system, cannot resolve two sources that are closer together than one wavelength. Hence, methods that can utilize near-field data are preferred.

Generally, beamforming algorithms do not perform well for extended, spatially coherent sources, because they are based on far-field measurements and assume sparse distributions of monopoles. They have often been employed to reconstruct jet noise at high frequencies[32,33] where FST (characterized by small, spatially incoherent sources) dominates. However, the LST, which dominates the field, requires alternative tactics. Although some beamforming methods have been developed to account for distributed, coherent sources and utilize measurements taken in the near field,[26,31,34] the focus of this study is on NAH methods, such as DFT-based NAH,[22,35]

the Helmholtz equation least-squares method HELS,[36] and statistically optimized near-field acoustical holography (SONAH).[37] Since the implementation of NAH was introduced to the jet noise community,[38] this and similar inverse methods have rapidly advanced in capability and usage.

1.2.2 Equivalent Source Models

ESMs are one type of model for inverse methods, in which an attempt is made to begin with assumptions about the source properties, such as size and distribution, shape, structure, and spatial coherence. Examples are given here of reduced-order ESMs used in past jet noise analyses. Suzuki and Colonius[26] employed an eigenfunction representation of acoustic waves in the jet near field, which eigenfunctions were derived from linear instability analysis (a model of the spatial development of magnitudes and phases of instability waves, or LST structures). They then applied beamforming to specify the near field in terms of these eigenfunctions (as opposed to monopoles). They showed that the hydrodynamic pressures dominated the near field over an extensive region, and that the interactions between LST and FST were negligible in the region of LST growth, before the end of the potential core.

Reba *et al*.[39,40] and Schlinker *et al*.[9] used a Gaussian wave-packet model to represent LST structures, and fitted their model to measurements made in the hydrodynamic regime. The model was based on pressure measurements in the near-field, without attempting to equate instability waves to measured flow quantities. It incorporated the effects of spatially varying amplitude, phase, and coherence. This model was then projected to the acoustic far field. The wave-packet model was shown to be a robust representation of the behavior of the LST structures in the linear hydrodynamic regime for many frequencies, with good agreement between measured and modeled pressures. It was a poor representation of FST behavior. An outward prediction (from the measurement surface to the far field) of jet noise was performed by Tam *et al*.[41], using an ESM defined on a measurement surface, which model is based on two-

point space-time pressure correlation measurements over the surface. With this model, it was demonstrated that FST pressures dominate the near field close to the nozzle, and LST dominates downstream.

Morgan *et al*.[42,43] applied a Rayleigh-distribution weighting to the amplitudes of a linear monopole array, and included both coherent and incoherent source components, to model radiation from a full-scale jet. The parameters of the model were optimized by Hart *et al*.[44] to match measured pressures. This provided an accurate prediction of levels in the near and mid-field regions. All the ESM approaches discussed here have improved modeling of jet sources by incorporating known properties of jets, such as decaying spatial coherence, the growth and decay of LST structures, and phase information.

Additional ESMs have been developed for use in arbitrary source distributions, which have not been applied specifically to jet noise problems, but are worth mentioning. For example, Ochmann[45] proposed the idea of using a multipoint multipole method to simulate acoustic radiation from arbitrary sources. Jeon and Ih[46] used a distribution of point sources inside a source surface to model the field in an inverse boundary-element method procedure. In both of these methods, the sound fields were modeled using some knowledge of the source distributions and radiation properties.

1.2.3 Equivalent Wave Models

Reduced-order EWMs seek to expand a sound field with a simplified set of wave functions. In theory, a complete basis, (i.e. one that spans the subspace of the homogeneous, source-free field), such as all possible plane waves, could describe an entire sound field exactly. Truncations (or subsets) of these bases that are based on some knowledge of the sound waves in a given field are often sufficient for an accurate reconstruction. This is why planar NAH (based on a sine/cosine expansion) works well for flat sources, cylindrical NAH (based on cylindrical functions) works for long sources, etc. More complicated source shapes and configurations

require modifications to these simple EWMs. For example, Wu[47,48] presented the HELS method (based on spherical wave functions) for reconstructing sound fields on and outside of a "minimum surface" that encloses a source of irregular shape. This method can also reconstruct pressures reasonably well inside the minimum surface, with errors increasing the farther inside the reconstruction point goes.[49,50] In HELS, a solution is found by matching the assumed-form solution (the expansion) to the measured hologram pressures in a least-squares sense. In general, an EWM representation works best (i.e. it provides an accurate reduced-order model) when its wave functions are suited to the geometry of the source.

One advantage of HELS is that the measurement grid need not completely cover the source, whereas a DFT-based NAH approach does require complete coverage. DFT-based NAH requires that a hologram be measured over an entire surface enclosing a source. The infinite coverage is performed implicitly in a planar or cylindrical DFT-based NAH approach, with an infinite measurement assumption incorporated into the wrap-around effect of a DFT. In contrast, the explicit measurement over an entire enclosing surface is required in a spherical approach.

SONAH[51-54] is one EWM inverse method that deserves special attention, as its algorithm is the starting point for the primary NAH method employed in this work. SONAH was developed to address some of the same problems that HELS does, in that it can reconstruct a total sound field from a truncated (patch) hologram measurement. This is because the SONAH algorithm does not employ a direct calculation of the wavenumbers using a DFT. Instead, it calculates a transfer function matrix between all hologram locations and reconstruction locations, then applies the transfer functions to the measured sound pressures. For example, a SONAH algorithm was applied to a laboratory-scale jet, in which cylindrical basis functions were used to represent the field.[55] For a second example, a planar SONAH formulation was applied to the current data set for full-scale jet measurements as a first attempt at holographic reconstruction.[56] To the author's knowledge, SONAH has never been applied to represent a distribution of spatially separated sources with multiple sets of wave functions. The closest example is the

work of Hald,[57] who developed a SONAH method that relied on measurements of two parallel planar arrays to separate incoming and outgoing waves by concatenating two matrices of wave functions, one for each direction.

The transfer-function approach of SONAH allows flexibility in the selection of the locations of hologram microphones (i.e. they are not restricted to a regular grid, and need not completely cover the source as in DFT-based NAH). In addition, it allows for a more convenient representation of the sound field than other NAH algorithms, because multiple sets of wave functions can be included in the generation of the transfer function matrix through a concatenation scheme similar to that of Hald.[57] The most comparable methods, to the author's knowledge, are the distributed point sources method (DPS)[58] and the distributed spherical waves method (DSW),[59] in that these both allow for a user-defined set of elementary wave functions, based on a rudimentary estimate of source location and shape. DPS was used by Shah *et al*.[60] to represent a jet as a distribution of point sources on a conical surface conformal to the shape of the shear layer boundary. DWS and DPS were compared by Semenova and Wu[49] (as well as a third method, the localized spherical wave method) to represent the sound field radiated by a loudspeaker. In each of these applications, a HELS approach was applied with the respective expansions of the field to reconstruct the source.

The flexibility of the SONAH (and HELS) methods in allowing for multiple sets of elementary wave functions is important in the context of the present work. The full-scale jet studied herein was, of necessity, measured over a concrete run-up pad.[61] This introduced an interference pattern from a rigid boundary into measured data, rendering a straightforward cylindrical representation of the jet inaccurate. Hence, a modified approach to SONAH, using a set of cylindrical functions for both the jet and its image source, has been found to be best suited to the geometry of the experiment.

1.2.4 Partial Field Decomposition Methods

Partial field decompositions (PFDs) are an integral part of many inverse methods and of the present work. PFD, based on the theory of principal component analysis,[62] serves to decompose a sound field into linearly independent components, referred to as eigenfunctions or "partial fields." This is critical for NAH to be successful, because the holograms (surface measurements) used must be spatially coherent. For a coherent source, the hologram can be captured by measuring complex pressures over an entire surface simultaneously. However, a single measured field cannot represent multiple incoherent processes (sources), so a PFD is required for jet noise fields, even with a simultaneous measurement.[63]

When a hologram aperture is too large to be measured by the available number of transducers a "patch-and-scan" approach may be taken, where a dense field array scans the aperture in a series of measurements. When a sound field is generated by a single source, the field array scans the hologram surface in conjunction with a fixed-location reference microphone. The transfer functions between the reference and field measurements may be used to generate a coherent, complex pressure measurement, which can then be projected to different locations using NAH. This process can be extended to multireference[63] procedures for multiple, independent sources. Multireference PFD methods can be utilized to provide (1) a set of coherent holograms (partial fields), (2) an estimate of the number of sources contributing to the field, and (3) an estimate of the measurement noise, as will be demonstrated in Section 3.2.

Care must be taken in the interpretation of partial fields. PFDs are not unique, and it is not always clear when the individual partial fields can be linked to independent sources. Generally, if the first eigenvalue of the decomposition is well separated from the others, its respective partial field represents a dominant, coherent source mechanism. In the case of multiple, competing source mechanisms, if a single reference microphone is located near each source and well separated from all others, PFD methods exist that can result in "physically meaningful" partial fields. Otherwise, the distinction between sources is unclear. Some effort

has been made to develop PFD methods that separate the contributions of individual sources. An important example, in the context of the present work, is that of Kim *et al*.,[64] who developed an optimization scheme to obtain physically meaningful partial fields by placing virtual references in ideal locations (near sources) *after* an initial holographic reconstruction of the sound field. This method is modified for the jet noise application given here, as explained in Chapter 6.

PFD has been employed to simplify the representations of partially coherent jet sources (usually called proper orthogonal decomposition, or POD, in the literature dealing with turbulent flow measurements). A POD procedure was first proposed in 1962 by Lumley[65] to investigate structure in turbulent flow. Glauser *et al*.[66,67] developed a method for performing a POD of directly measured flow structures in the 1980s. Numerous implementations of POD have since been applied to the turbulent flow field, but it should be kept in mind that a very small fraction of turbulent kinetic energy is propagated as acoustic waves. In-flow measurements were impractical at high jet speeds in a study by Long *et al*.,[68] so they extended their POD technique to measured pressures at the outer edge of the jet shear layer (which will be distinguished here as PFD).

In 1997, PFD was applied by Arndt *et al*.[69] to a hydrodynamic pressure measurement, in order to reduce the representation of coherent structures in a turbulent jet. They demonstrated that the decomposed eigenfunctions grow, saturate, and decay within about three wavelengths for any frequency. Suzuki and Colonius[26] sought to represent the near field with partial fields based on an analysis of the flow properties. They showed how the partial field that had the greatest eigenvalue matched their instability-wave model (in the high-amplitude region) when the field was dominated by one coherent source. Freund and Colonius[70] demonstrated a wave-packet structure from a PFD of near-field quantities in simulated jet data.

Some investigations have been performed to better understand the nature of a PFD as it relates to the spatial coherence of jet sources. For example, in works by Shah *et al*.,[60] the general trend was shown that more partial fields are required for decompositions of jet noise fields at

higher frequencies. Vold *et al.*[71] developed a model of a jet using random azimuthal distributions of "sound flares," or single, random, fluidic dynamic events in a turbulent flow. The incoherent superposition of many flare events resulted in the total field. They then performed an eigendecomposition of the autospectral matrix of all channels, and presented the weighted eigenvectors as partial fields. They discuss how partial fields developed in this way can be used directly as quantitative expressions of traveling wave packets, or may be used to fit physics-based reduced-order models.[60,72,73]

PFD can also be used to generate coherent hologram measurements in NAH applications. Lee and Bolton[55] performed a PFD of measured pressures outside a laboratory-scale jet to allow for a SONAH reconstruction of the jet field. In relation to the same study, since the random nature of turbulence leads to a source with some variation in amplitude, a PFD method was developed that accounts for source nonstationarity.[74] The partial fields that resulted from this PFD took on the appearance of dipole, quadrupole, and octupole source configurations.

1.3 Objectives and Scope of Work

In this work, near-field NAH and PFD methods are used to reconstruct the sound field of a full-scale jet. NAH Measurements were made on the jet from an F-22A Raptor. Figure 1.1 demonstrates the relationship between existing methods and the contributions of the current work to the field of jet noise research. Techniques developed in this work are highlighted in red. First, many PFD methods have been applied to simplify the representation of jet sources and generate coherent holograms in preparation for NAH applications. For a scan-based measurement, PFD requires the use of a fixed-location reference array. Few quantitative guidelines for the design of a reference array exist. In 2009, Gardner[75] presented a new figure of merit, references per coherence length, to provide such guidelines. In Section 3.3, this method is refined for application to more general cases of sources with arbitrary coherence. A reference-

per-coherence-length analysis is used to evaluate the design of the reference array for the full-scale jet experiment.

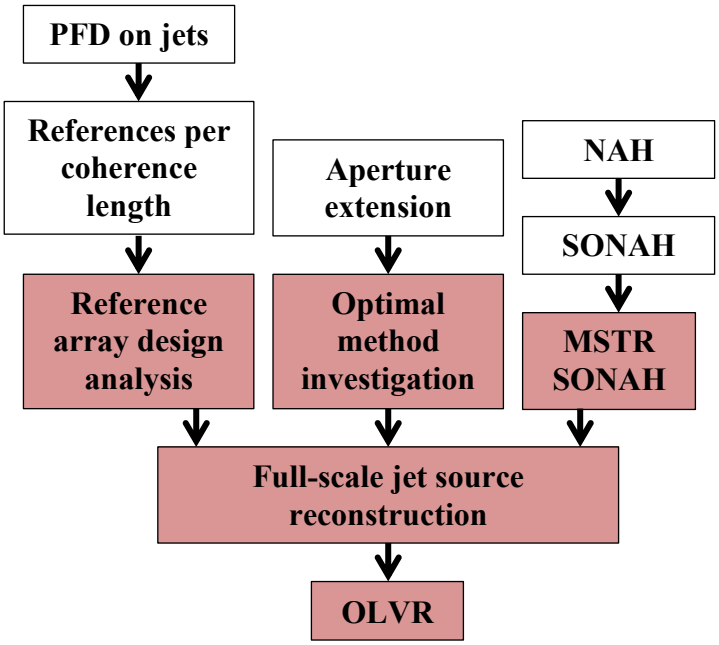

Figure 1.1 Flowchart that shows the relationships between existing methods and the contributions of the current work to jet noise research.

It is found that the measurement aperture used in the full-scale jet experiment is insufficient for NAH applications. Hence, an extrapolation scheme is required to predict data outside the measurement aperture. Several aperture extension methods exist. In Chapter 4, some of these methods are used to extend the aperture of a numerical hologram measurement of an extended source, and their relative merits are discussed in context of the full-scale jet data.

NAH methods were developed for sound field visualizations. In particular, SONAH has proven useful in previous jet noise investigations.[55,56] In Chapter 5, the SONAH algorithm is modified to account for sound fields comprised of multiple, spatially separated sources. This method is called multisource-type representation SONAH (MSTR SONAH) Inasmuch as the elementary wave functions are well adapted for their corresponding source shape, the total

number of functions required to describe the field is relatively low, which leads to an efficient reduced-order EWM for that source configuration. For the specific case of the full-scale jet experiment, the field is modeled with two sets of cylindrical wave functions, one set centered on the jet centerline, and a second centered on its image below the reflecting plane. The sound field reconstructed from this model is shown to be more accurate than reconstructed fields produced by NAH methods that do not incorporate the ground reflection, or do not account for the geometrical spreading of the field.

All of these methods discussed above are combined in the most comprehensive application of NAH performed to date. The full-scale jet experiment also represents the most comprehensive investigation of a full-scale jet, so far. The three-dimensional sound field of the jet is reconstructed to investigate source and radiation properties.

To crown this work, after the application of MSTR SONAH, the reconstructed partial fields are decomposed into new partial fields that closely represent independent source mechanisms, using a PFD method similar to that of Kim *et al*.,[64] called the optimized-location virtual reference method (OLVR). In this approach, the locations of virtual references are determined through an optimization algorithm, and the corresponding partial fields represent individual sources, insomuch as the virtual references are located near what could be called "independent" sources in a turbulent field. The OLVR decomposition of the full-scale jet field represents the most direct attempt to equate independent partial fields to independent source mechanisms.

It is important to understand some of the limitations of this study. The measurements of the full-scale jet represent the first attempt to apply NAH to a source of this complexity. Many meaningful analyses have resulted from this experiment, in spite of the limitations discussed here.

First, the levels in the extreme near field of the full-scale jet were too high to be accurately recorded by the transducer/data acquisition system used. Hence, measurements were

restricted to a distance of about 4.1 m and farther from the jet. Hence, little information from the acoustic near field was captured, and no near-field measurement or modeling of the hydrodynamic pressure signatures are possible here. This also limits the resolution possible in an NAH reconstruction, since NAH reconstructions are limited to one-half wavelength resolution when evanescent (near-field) information is not captured. However, since LST structures are relatively large compared to a wavelength (Arndt[69] suggests three wavelengths long), in the present work, such a limitation is not much of a concern. (No attempt is made to model the radiation of FST in this work.) The measurements were made in the geometric near field, (close relative to the characteristic size of the source), so a reduced-order approach with a limited number of measurement positions is still possible and can provide insight about the distributions of multiple, independent source mechanisms, with a few caveats.

In addition, no attempt is made to equate acoustic pressures, measured or reconstructed, to any turbulent flow quantities. Although there are many experiments that measure flow simultaneously with acoustic data, and correlate the two to illuminate source properties, direct measurement of correlation between turbulence and acoustic radiation in high-speed jets remain elusive.[9] Finally, the current data set of the full-scale jet is not likely the ideal hologram for the source at hand, largely because the measurement aperture is limited in its azimuthal coverage of the jet . Rather, it represents a practical measurement setup and the first attempt to perform NAH on any source of this scale. Despite these limitations, excellent sound field reconstructions are generated through the MSTR SONAH method, and much insight is gained about the full-scale jet noise sources and about improved measurement procedures for future NAH jet noise applications.

Chapter 2 provides a detailed explanation of the measurement procedures of the full-scale jet experiment and of several preliminary, level-based results that lend insight into the jet noise field. The reader of subsequent chapters is directed to Chapter 2 for questions about measurement details, although key components will be repeated in each chapter as necessary.

For a foundational understanding of the key role of PFD, Chapter 3 presents a PFD method based on the use of a singular value decomposition, and describes how it is used in this study. A figure of merit to guide the design of a sufficient reference array, prior to the implementation of PFD and NAH, called references per coherence length (RPL_C),[75] is discussed. In addition, some aspects of the spatial coherence of the jet noise field are presented, which motivated the use and selection of the various PFD methods. Several kinds of numerical aperture-extension techniques, pertinent to the NAH methods used in this work, are discussed and compared in Chapter 4.

In Chapter 5, the theoretical foundation for the MSTR SONAH method is discussed in detail. MSTR SONAH is applied to configurations of multiple numerical sources in two key experiments: (1) a simulation of simple sources confined to a plane, with a conformal hologram measurement, and (2) a simulation of two line sources that mimics the geometry of the full-scale experiment. In both of these numerical studies, planar SONAH and cylindrical SONAH are also applied to contrast the utility of the multisource-type reduced-order representation of the field. Finally, the key investigations of this work are performed in the application of MSTR SONAH to reconstruct the full-scale jet noise field from the measured data at the end of Chapter 6, and in Chapter 7, OLVR is applied to the reconstructed fields in an attempt to isolate the contributions from individual source mechanisms. Important aspects of jet noise source and field properties from the current study are discussed in Chapter 7, in light of past investigations and the ongoing work.

In summary, the objectives of this work include the following.

1. Assess the design of the hologram and reference array used in the current experiment on a full-scale jet, and make recommendations for future NAH experiments.
2. Develop a SONAH-based algorithm that includes the effects of a rigid reflection in the presence of the jet.

3. Reconstruct source distributions (approximated by pressure distributions at the shear layer) of a full-scale jet.
4. Modify and implement a PFD method that generates physically meaningful partial fields of the jet in an automated fashion.
5. Produce spatially distinct, independent source mechanisms, and investigate their individual and combined radiation properties.

1.4 On Nonlinearity

NAH and all inverse methods that rely on the homogeneous wave equation inherently assume linear wave propagation. The high-amplitude noise from full-scale jets is inherently nonlinear, both in the source mechanisms and in propagation. The question therefore arises as to the validity of holographic methods employed on full-scale jets. Well-established models exist for the nonlinear propagation of waveforms subject to planar, cylindrical, or spherical spreading, including the effects of absorption.[76] Gee *et al*.[77] applied such a model to measured waveforms to predict far-field spectra of noise from an F-22AA. However, the application of similar theory in the geometric near field, for a broadband source, where geometrical spreading is ill-defined and signals have limited correlation, is difficult. For example, the calculation of a shock-formation distance based on analytical theory depends on both the initial level of a pure sine wave. Although shock formation can be predicted for a complex initial waveform, no analytical theory exists for defining a characteristic shock-formation distance from a noisy signal based only on statistical characteristics, such as level and spectral content.[78] In future work, it would be insightful to apply nonlinear propagation models to waveforms measured in the geometric near field and compare predicted and measured results, similar to that of Gee *et al*.,[77] which was performed in the far field.

For the purposes of this work, several key findings from past investigations of nonlinearity in full-scale jet noise are important. First, it is clear that nonlinear propagation does play a role in the near field region. Gee *et al*.[79] show nonlinear wave steepening in the near field of the jet on an F-35A and Neilsen *et al*.[80] demonstrate evidence of nonlinearity in spectral measurements of the F-22A. However, the effects of nonlinearity are most evident in the higher frequencies of the spectrum, due to the fact that nonlinear effects are shown to trump absorptive effects in this region.[79] The spectrum is negligibly affected at the low frequencies where NAH is being implemented.[77] In the current work, the difference in errors between reconstructions on plane 1 and on the arc, which are the most spatially separated surfaces of interest, are typically less than 0.5 dB, suggesting that linearity in the geometric near field is a reasonable assumption below at least 1000 Hz. In addition, Morgan *et al*.[43] showed excellent agreement at low frequencies between predicted and measured levels both in the geometric near and mid fields when an ESM and linear propagation model were assumed. Due to these results, it is assumed in this work that the errors associated with nonlinearity are far below those introduced by the current methods, for the frequencies of interest herein.

1.5 Overview of NAH Process for Jet Noise

Each step of the holography process employed in this work is outlined briefly here to guide the reader to an understanding of the role each step takes in the overall NAH implementation. Although variations of each of these steps exist, the overall process is nearly invariant.

6. *Measurement.* The field over the hologram surface is captured by a large array in a simultaneous measurement or in a series of patch-and-scan measurements by a small, dense array.

7. *PFD: Coherent holograms.* The measured field is decomposed into a set of mutually incoherent partial fields.
8. *Aperture extension.* If the hologram aperture does not cover the source (i.e. capture sufficient data to accurately represent all of the basis functions), a numerical extrapolation of the data can restore (predict) the necessary pressure values outside the aperture.
9. *NAH.* Each partial field is expanded, using the basis set, and then projected to predict acoustic quantities at the reconstruction location.
10. *PFD: Isolation of physical source contributions*. The reconstructed partial fields are decomposed (again), this time into partial fields that represent the contributions of independent source mechanisms.

Chapter 2

Near-Field Noise Measurements of a High-performance Military Jet Aircraft

2.1 Introduction

The noise radiated from jets on military aircraft is not well understood because characteristics unique to supersonic, high-temperature, full-scale engines have not previously been widely investigated. A connection must be established between turbulent flow structures in a jet and radiated noise in order to understand and improve the impact of noise control measures. Extensive measurements were made in the geometric near field of a high-performance military aircraft to characterize the acoustic environment of maintainer personnel, and to provide greater understanding of full-scale jet noise phenomena.[81-83] The purpose of this paper is threefold: First, this paper describes the experiment in depth, so it serves as a reference for future work. Second, it provides basic analyses of near-field properties and source characteristics that are inferred from these properties, with a focus on phenomena unique to full-scale jet engine noise. Finally, this paper offers insights into sound field characteristics that are useful for the practical implementation of high-power jet noise experiments. This chapter was modified from a 2012 paper published in the *Noise Control Engineering Journal* under the same title.[61]

The majority of today's jet noise studies have been limited to smaller, laboratory-scale tests. Some acoustical data are available for high Mach number flows,[14,33,84,85] but test facilities are generally scale, temperature and velocity-limited. Several notable studies have been performed of model-scale jets in the near field,[26,86,87] and others of full-scale jets in the far field,[77,88,89] but studies performed in the near field of military-type jets are few.[32] This study reports the experimental procedures of, and addresses some jet noise phenomena observed from measurements made in the geometric near field of the jet produced by an installed engine on an F-22A Raptor.

Section 2.2 of this paper describes the experiment, including details about the aircraft and test environment, the design of the array-based measurements, the data acquisition system and the test procedures. Section 2.3 provides results of measured jet noise quantities, such as overall sound pressure levels (OASPLs), the spatial variation of spectral content, and basic time-waveform properties. From these results characteristics about the maintainer environment are provided, frequency-dependent radiation patterns are observed, two separate spectral peaks unique to full-scale jets are identified and nonlinear acoustic shock content is shown. Throughout the paper, issues concerning technical and logistical challenges encountered in performing full-scale jet noise experiments are addressed.

2.2 Experiment Overview

More than 6000 measurement points and the repetition of the measurement over four engine conditions make this the most extensive near-field measurement of a jet on a high-performance military aircraft to date. The experiment was primarily designed for a near-field acoustical holography analysis,[55,72,83,90,91] although holography results are not presented in this paper. This section summarizes the measurements made. First, details about the aircraft, test environment, microphone arrays and data acquisition system are presented.

Then the test sequence is outlined. Additional details about the experiment are described elsewhere by James *et al*.[81] and by James and Gee.[82]

2.2.1 Aircraft

Researchers at Blue Ridge Research and Consulting and Brigham Young University conducted static run-up tests on the Lockheed Martin/Boeing F-22A Raptor (shown in Figure 2.1) during 27-30 July 2009 at Holloman Air Force Base (HAFB), New Mexico. The F-22A Raptor has two Pratt & Whitney F119-PW-100 turbofan engines that are each in the 160 kN (35,000 lbf) thrust class. The engines have two-dimensional convergent-divergent nozzles capable of ±20° thrust vectoring. The engine closest to the measurement arrays was cycled through four power conditions: idle, intermediate, military, and full afterburner, while the other engine was held at idle.

Figure 2.1 The Lockheed Martin/Boeing F-22A Raptor used in the experiment, shown tied down at the HAFB F-22A ground run-up pad. The measurement team members are shown, including personnel from Blue Ridge Research and Consulting, Brigham Young University and Holloman Air Force Base.

For the purposes of this experiment, the focus is on radiation into the environment of the aircraft maintainer, to the side of the jet. Since all measurements were taken in this region, the noise variation with the change in azimuthal direction is unknown. (For studies on the effects of non-axisymmetric nozzle geometries, the reader is directed to references [92] and [93].) The

nozzle exit of each engine is centered 1.91 m above the ground and has a rectangular aspect ratio of approximately 1:2, although the variable thrust-vectoring components cause the nozzle shape to change with different engine conditions.

2.2.2 Test Environment

During the static run-up measurements, the aircraft was tied down in the center of a 24.4 m (80 ft) wide concrete ground run-up pad. Rain-packed dirt was on either side of the pad, making the terrain very flat. A blast deflector was located approximately 30 m (100 ft) directly behind the aircraft. On the measurement side of the run-up pad, there was also a small building approximately 25 m to the side and slightly forward of the nozzle exit, and a short wall running almost parallel to and 30 m from the jet centerline. These obstructions precluded measurement locations in the far field. Note that some ground-based measurements were made about 3 m from the base of the upward-curving blast deflector.

Over the short propagation distances in this measurement (<23 m) the effects of temperature fluctuations and wind speeds were determined to be minor. Measurements were generally made in the morning and evening to minimize the effects of strong temperature lapses and moderate winds that prevail in the daytime, as well as to minimize temperature effects due to increased heating of the fuel during the day. Meteorological trends near the run-up pad were monitored continuously. The average wind speed during the measurements did not exceed 2.4 m/s, except for a single row of scans in plane 2, during which the average wind speed was 5.0 m/s. Temperatures averaged 30 °C, with a standard deviation of 4° C. The speed of sound was calculated as a function of temperature, and it was found that the largest fluctuation in sound speed was approximately 6 m/s, or about 2% of the mean sound speed.

A temperature probe was mounted to the field array rig to track temperature fluctuations as a result of the engine firing. It was found that the jet did not heat the ambient fluid significantly within the measurement region. It was therefore determined that any refraction

effects due to heating of the air beyond the shear layer were negligible in the measurement region.

2.2.3 Field Array

The field array used in this experiment (see Figure 2.2) allowed for a series of dense, large-aperture, two-dimensional measurements. It was designed and built by Blue Ridge Research and Consulting, and was composed of 90 6.35-mm (0.25-in) GRAS 40BE prepolarized microphones, each coupled with a 26CB preamplifier, arranged in 5 rows and 18 columns (when in the horizontal orientation) with 0.15-m (6.0-in) equal spacing. The array had an optional horizontal or vertical orientation, an adjustable height, and was mounted to an extruded aluminum guide rail.

Figure 2.2 Two views of the 90-channel field array rig mounted to a guide rail. Reference microphone locations on the ground are marked with yellow circles.

Figure 2.3 describes the field measurement locations relative to the aircraft. In addition to the *x* and *z* coordinates marked on the schematic, the vertical axis is represented by *y*, with a positive direction pointing up. The origin of the coordinate system is on the ground directly below the nozzle exit. Red triangles denote the locations of the field array center for each "scan" (see Section. 2.2.6). Planes 1 and 2 were measured parallel to the estimated shear layer boundary, with the array in the horizontal orientation (see Figure 2.2), and with the center row at heights of 0.69, 1.29, and 1.91 m (27.0, 51.0, and 75.0 in) above the ground. This provided an overlap of microphone locations, with the microphone locations of the top row overlapping the microphone locations of the bottom row as the rig was raised from 0.69 to 1.29 m, and again from 1.29 to 1.91 m. Plane 3 was measured parallel to the jet centerline, with the array in the horizontal orientation, at heights of 1.29 and 1.91 m. For planes 1-3 the array was moved in 2.3 m (7.5 ft) increments, so that the locations of the first three and last three columns overlapped from scan to scan. All measurement planes were located sufficiently far from the flow to render flow-induced noise negligible.

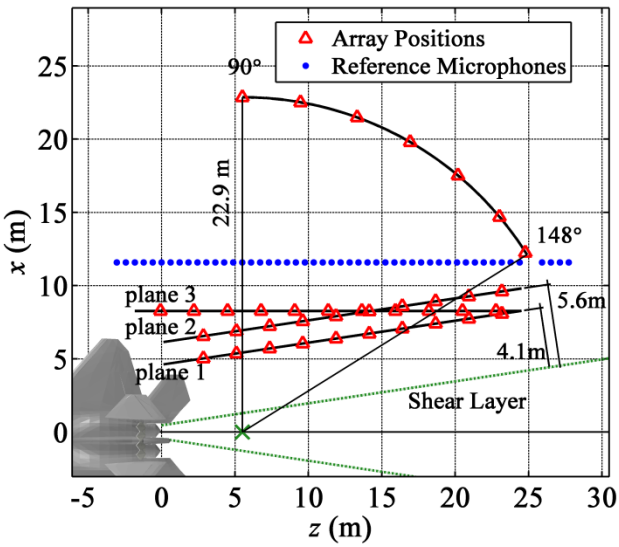

Figure 2.3 Schematic of the measurement locations, relative to the aircraft. The estimated shear layer boundary is marked by green dashed lines, and the green "x" delineates the estimated maximum noise source region and the center of the arc.

In addition to the three planar measurements, an arc-shaped surface was measured in the transition region from the near to the far field by the 90-microphone field array. The arc was centered at a point 5.5 m (18.0 ft) downstream of the nozzle (marked by a green "*x*"), with a radius of 22.9 m (75 .0 ft). The arc center represents an attempt to approximate the location of the dominant noise source region, although it is understood that this region is noncompact and varies as a function of frequency and engine operating conditions.[85] The location of the arc center and the radius of the arc are consistent with measurement locations used by Gee *et al*.[77] in a previous study of the F-22A Raptor. Measurements were made along the arc at a height of 1.91 m and at six locations in 10° increments from 90° to 140°. A seventh location was measured at 148°, because the edge of the concrete pad made a measurement at 150° difficult. All angles reported in this paper are measured relative to the front of the aircraft (inlet axis) and to the arc center at 5.5 m downstream of the nozzle.

2.2.4 Fixed-location Reference Array

An additional 50 microphones (marked by yellow circles in Figure 2.2 and by blue dots in Figure 2.3) were placed in a fixed-location array to allow for the generation of coherent field measurements from temporally distinct scans, for the purposes of performing near-field acoustical holography. The data recorded at these microphones can be used as reference values to tie together magnitude and phase discontinuities of the field array from scan to scan, hence the name "reference array." This is done using a process called partial field decomposition, which also compensates for measurement noise and nonstationarity of the jet noise source.[74,83] Although partial field decomposition and holography results are not given here, in this paper the reference array is used to provide overall levels and show spectral variation over a large spatial region in the near field from measurements made simultaneously.

The reference microphones, shown by the blue dots in Figure 2.3, were placed on the ground 11.6 m (38.0 ft) from the centerline of the jet in the *x*-direction (11.7 m total distance in *x*

and *y*) and spaced 0.61 m (2.0 ft) apart in the *z*-direction. It was 12.0 m from the center of the aircraft in the *x*-direction. With references on the ground, multipath interference due to ground reflections was avoided. Several types of microphones were used in the reference array, including GRAS 6.35-mm (0.25-in) 40BD, 40BE and 40BH prepolarized microphones, and GRAS 3.18-mm (0.125-in) 40DD prepolarized microphones. All reference microphones were laid out according to their sensitivities, taking into account the peak sound-pressure levels that were expected along the array.

2.2.5 Data Acquisition System

The proper design of the data acquisition setup for near-field acoustical measurements of full-scale jet noise is critical. Accurate measurements require the ability to record frequencies that range from the infrasonic to the ultrasonic regimes, and to capture data over a very large spatial aperture and dynamic range. For example, the field array was restricted to distances beyond 4.1 m, where instantaneous sound pressure levels (SPLs) exceeded 170 dB re 20 μPa. This converts to an approximately 6.3 V signal peak for a nominal rig-microphone sensitivity of 1 mV/Pa. (Some of the field array microphones had a sensitivity as high as 1.28 mV/Pa.) With these requirements in mind, a National Instruments (NI) PXI-1045 chassis system with NI PXI-4498 and NI PXI-4462 cards served as the A/D converters, which streamed data to an NI 8353 rackmount controller with a high-power Intel Core 2 Quad processor and four 250-GB hard drives in a RAID-0 configuration. The entire data acquisition system was monitored using a laptop with a Windows Remote Desktop, which allowed for wireless or wired connection to the controller. The software was a custom designed LabVIEW data acquisition program, which provided setup, microphone calibration, real-time level and spectral monitoring and channel overload alerts. BNC cables ran from the microphones to several NI BNC-2144 InfiniBand-to-BNC breakout boxes. Then bundled InfiniBand cables ran from the breakout

boxes to the NI PXI cards. This setup allowed for the simultaneous measurement of 150 channels. The data acquisition setup is pictured in Figure 2.4.

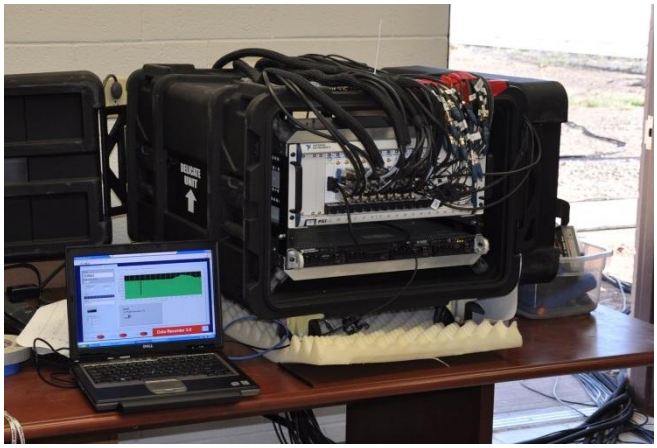

Figure 2.4 Laptop, NI PXI-1045 chassis, and NI 8353 rackmount controller used for data acquisition. The chassis and controller are mounted in a shock mount rack case, and the entire system is in a building located near the run-up pad.

During afterburner conditions, several reference-array channels centered around 100°, corresponding to microphones with the highest sensitivities, experienced infrequent capacitive-like effects in the time waveform. Further investigation has shown that this effect is due to insufficient response time of the on-board constant-current supplies when very rapid rises (i.e., steep shocks) occurred in the pressure field. These capacitive effects, which were manifest as low-frequency spectral noise, were removed from the time waveform data prior to processing. Recommendations for avoiding these effects in future jet and rocket noise measurements are provided by Taylor et al.[94]

Careful vibration isolation measures are necessary for data acquisition systems used during high-power jet noise measurements. In this experiment, while the aircraft engine operated at afterburner conditions, high-amplitude, acoustically induced vibrations caused the hard drives to stop writing temporarily. This caused the on-board memory buffer to fill before writing all the data to disk, precluding the 96-kHz sampling frequency used for lower engine powers. In an attempt to address the problem, the data acquisition system was placed in a nearby

building and mounted in a shock-mount rack case, seen in Figure 2.4. These measures, however, were insufficient, particularly because the energy of the acoustic signatures was dominated by low frequencies (~ 100 Hz). An accelerometer placed directly on the rackmount controller measured rms acceleration values of 1.58 m/s^2 during afterburner conditions. To work around the problem, during afterburner engine firings the measurements were recorded at a sampling frequency of 48 kHz instead of the 96 kHz used for all other conditions. The lower sampling frequency caused the buffer to fill more slowly, allowing it time to write all the data to disk. In future measurements, a solid-state hard drive or more robust vibration isolation methods are recommended.

2.2.6 Test Sequence

Before testing, the aircraft was tied down to the run-up pad, the reference microphones were attached in place, the field array was mounted to the guide rail in the horizontal position and at the desired distance from the jet (see Figure 2.2), and all channels were calibrated and deemed functional. Then, when the meteorological conditions were suitable (as described in Section 2.2.2), the measurements began. The aircraft engine was fired to operate on condition at idle power, and the pilot signaled the measurement team by rotating the horizontal stabilizers on the rear of the aircraft. Then pressure waveforms were recorded by all microphones at a sampling frequency of 96 kHz for 30 s. When the measurement was complete, a member of the team signaled the pilot to go to intermediate engine conditions. With the engine on condition, the measurement process was repeated. Military engine conditions were recorded in the same manner. Then the sampling frequency setting of the data recorder software was decreased to 48 kHz. At this lower sampling frequency the measurement was performed for afterburner engine conditions. The aircraft engines were then returned to idle conditions, the sampling frequency setting was returned to 96 kHz, and two team members moved the field array to the subsequent measurement position. When all measurement scans were taken in a row along the length of the

jet (with the array at a fixed height and offset distance), the aircraft was powered down for cooling and the addition of fuel, while the height of the array or its offset distance was changed.

The sequence of cycling through each of the four engine conditions and recording data with the field array and reference microphones in a single fixed location is referred to as a "scan". Scan locations of the field array are marked by red triangles in Figure 2.3. Each measurement plane shown in Figure 2.3 was composed of a set of scans made along the length of the jet and at several heights. The resulting database after all measurements were performed was approximately 650 GB in size.

2.3 Level-based Results and Discussion

This section presents several results of the near-field experiment described above, with an emphasis on level-based analyses. Specifically, acoustically induced vibrations of the rig, OASPLs, spectral content and the variation of the spectra over space, sound-field stationarity and characteristics of time waveforms are examined for subsets of the data. In each subsection, measurement results are presented, followed by a discussion of the corresponding physical phenomena that are important for understanding full-scale jet noise.

2.3.1 Vibration Measurements

Before showing measured results, it is important to establish the quality of data taken on the rig. Specifically, it is shown that rig vibrations did not appreciably affect measured quantities. Acoustically induced vibrations of the rig led directly to vibrations of the microphones, which increased their effective noise background. Euler's equation, which relates a pressure gradient to particle acceleration, can be used to link the microphone motion directly to a theoretical, false pressure wave. If it is assumed that a time-harmonic plane wave is incident on the microphone diaphragm, then from Euler's equation the false pressure magnitude as a function of frequency is related to the microphone acceleration by

$$|p(f)| = \left|\frac{\rho_0 c a(f)}{2\pi f}\right| \tag{2.1}$$

where $p(f)$ is the false pressure in Pa, f is the frequency in Hz, ρ_0 is the ambient air density, c is the ambient sound speed and $a(f)$ is the acceleration of the microphone in m/s^2. In this formulation it is assumed that the vibration measured by the accelerometer is representative of the vibration of the diaphragm of the nearby microphone (i.e. there was a rigid connection from the rig to the diaphragm).

Accelerometers were placed in several locations on the rig frame during engine run-ups to measure microphone accelerations (along the microphone axis). The data shown are for a microphone within 8 cm of the accelerometer. Using Eq. (2.1) the measured accelerations were converted to false SPLs and compared to the measured SPLs of the nearby microphone. Figure 2.5 shows the measured and false SPLs (in one-third octave band bins) in the case when the rig was at a height of 1.91 m, on plane 2 and in the region of maximum radiation ($z = 9.6$ m downstream) for afterburner conditions. The resulting theoretical noise background ranges from about 20 to 40 dB below the actual measured SPLs over all frequencies of interest. For most engine conditions, frequencies, and locations in the field the theoretical noise background, derived from rig vibrations, are at least 20 dB below the measured SPLs. At idle and intermediate conditions the false SPLs produced approach the measured levels above 10 kHz in several instances, but these frequencies are already ignored in this paper because they contain engine noise components (see Section 3.3.1). Hence, rig vibrations do not play a significant role in the measured acoustic quantities reported through the remainder of Sec. 3.

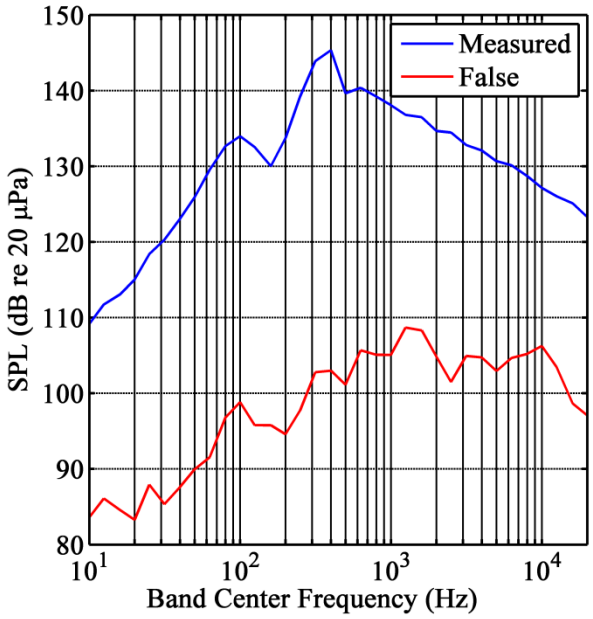

Figure 2.5 One-third octave band SPLs measured by a microphone on the rig, located at z = 9.6 m downstream on the top row of plane 2, with the engine operating at afterburner conditions. Also shown is the corresponding false SPL calculated from acceleration measurements by an accelerometer located near the microphone.

2.3.2 Overall Sound Pressure Levels

In order to characterize the aircraft maintainer environment the OASPLs over the measured spatial aperture are given. Important clues about jet noise radiation characteristics can be obtained by observing the change in overall radiation patterns as a function of engine condition. Figures 2.6 through 2.9 show OASPLs measured by the field array for idle, intermediate, military and afterburner engine conditions, respectively. All figures have a color scale that spans 20 dB. Note that Gee *et al.*[77] measured OASPLs for the F-22A Raptor on the same arc as that shown here (23 m from the arc center). At a height of 1.8 m and at 125°, the OASPL they measured for afterburner conditions was 143.1 dB re 20 μPa, which agrees to within 1 dB of the measured value shown in Figure 2.9.

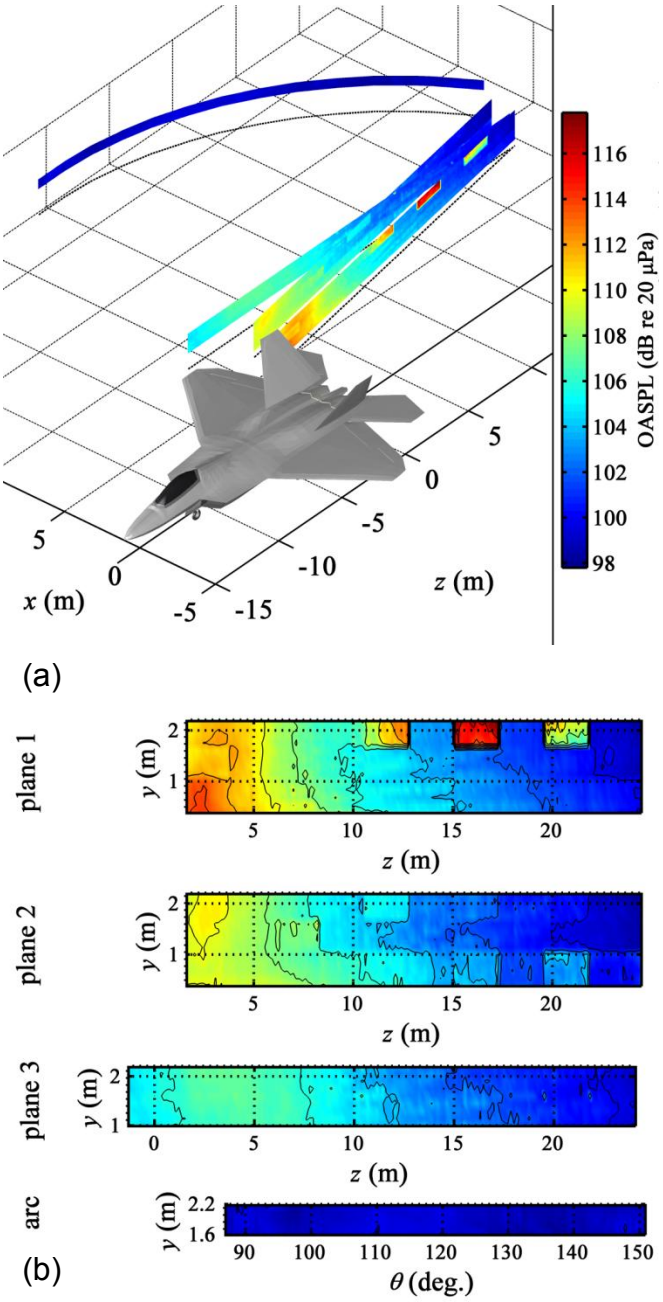

Figure 2.6 OASPLs measured in the geometric near field at idle engine conditions. (a) Levels are plotted at their three-dimensional locations. (b) Levels of measurement planes 1-3 are projected onto the *z*-*y* plane; levels of the measurement arc are plotted as a function of polar angle.

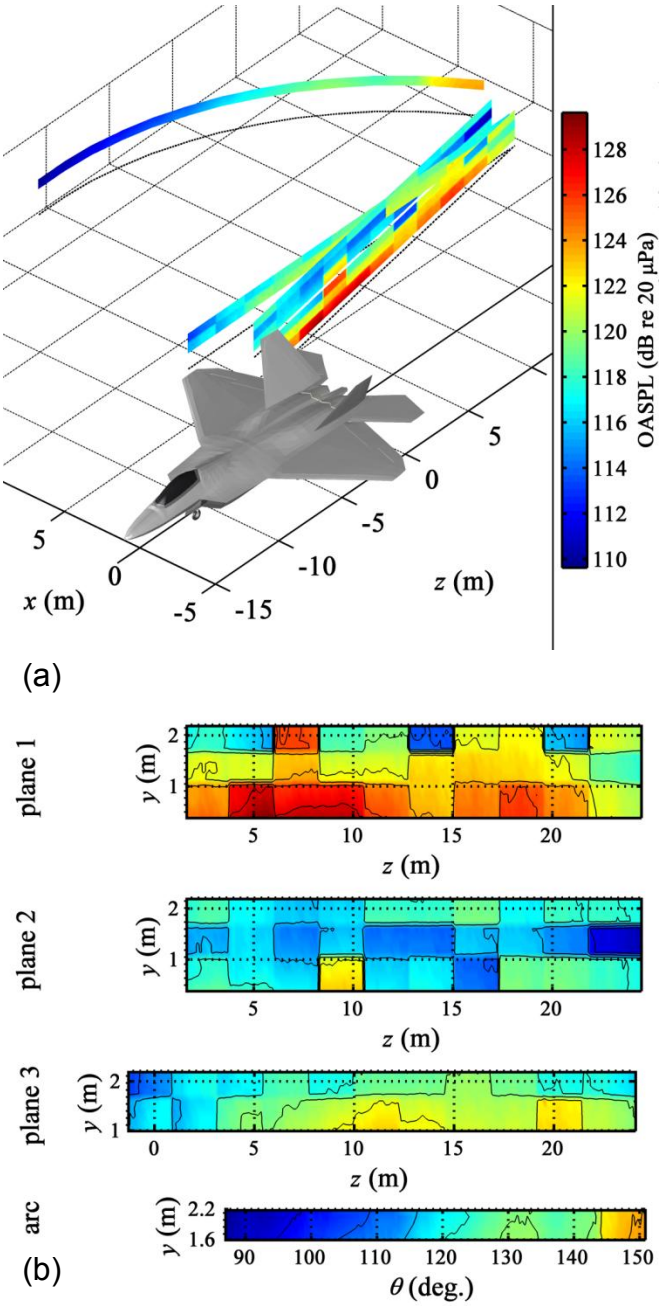

Figure 2.7 OASPLs measured in the geometric near field at intermediate engine conditions. (a) Levels are plotted at their three-dimensional locations. (b) Levels of measurement planes 1-3 are projected onto the *z*-*y* plane; levels of the measurement arc are plotted as a function of polar angle.

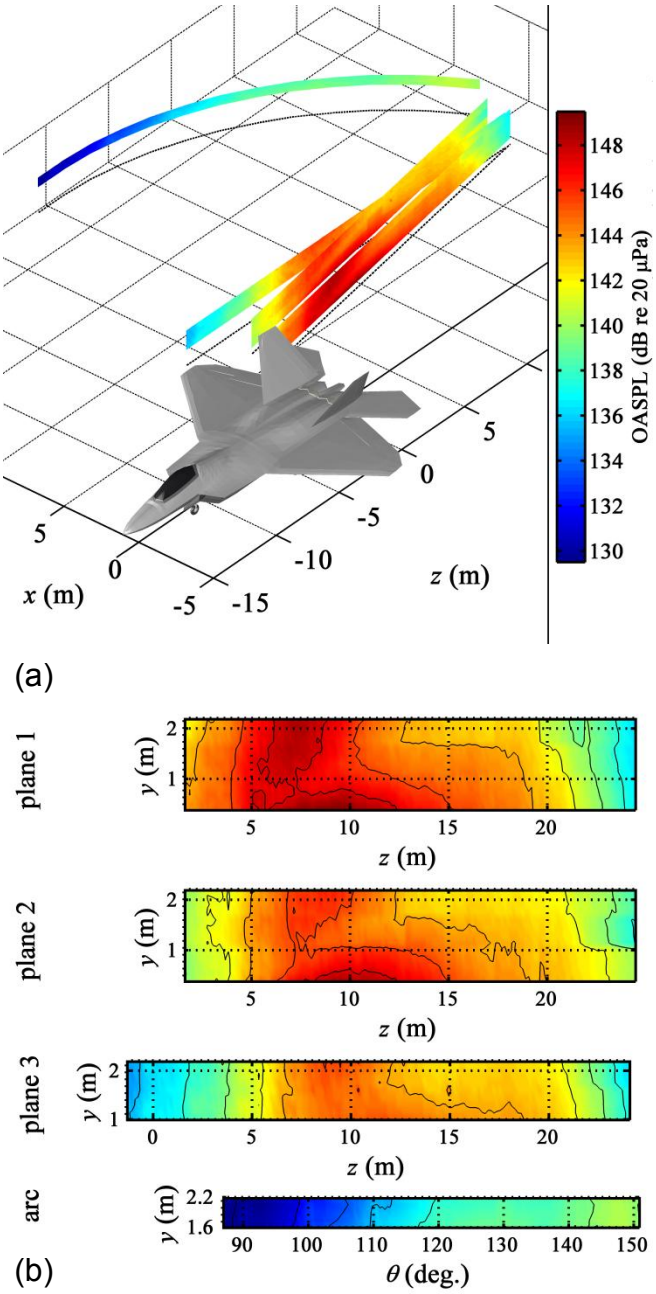

Figure 2.8 OASPLs measured in the geometric near field at military engine conditions. (a) Levels are plotted at their three-dimensional locations. (b) Levels of measurement planes 1-3 are projected onto the *z*-*y* plane; levels of the measurement arc are plotted as a function of polar angle.

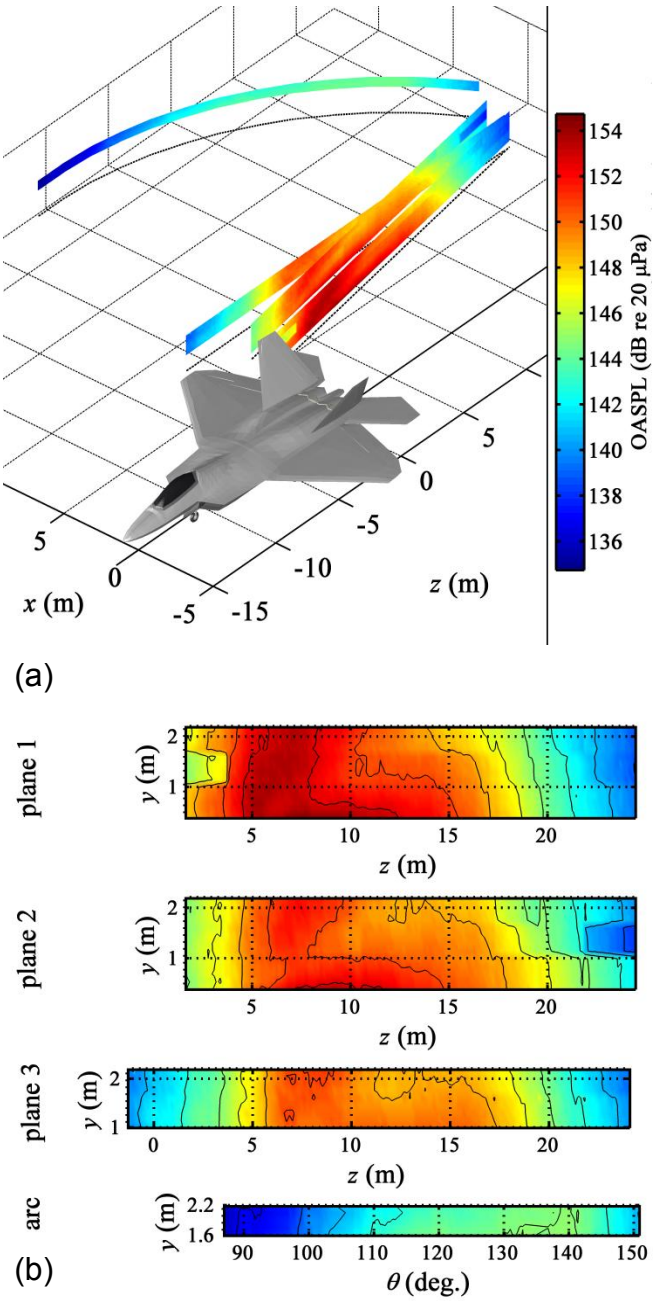

Figure 2.9 OASPLs measured in the geometric near field at afterburner engine conditions. (a) Levels are plotted at their three-dimensional locations. (b) Levels of measurement planes 1-3 are projected onto the *z*-*y* plane; levels of the measurement arc are plotted as a function of polar angle.

The OASPLs measured by the reference microphones, averaged over several scans, for all four engine power conditions are shown in Figure 2.10. The directly measured levels, represented by black dots, show a somewhat "noisy" variation in level along the reference array. These local variations are a result of a slight bias in the field-calibrated microphone sensitivities. They are greater for the 3.18 mm microphones (located between z values of 12.2 and 16.5 m), which had the lowest sensitivities (0.2-0.4 mV/Pa) and are the most difficult to calibrate in the field. To correct for this uncertainty in calibration, a set of weighting factors was derived by visual inspection of the variation in the levels of the intermediate case. The intermediate condition was chosen because it has the flattest spatial distribution. These resulting factors were then applied to all scans and engine conditions, and the resulting "filtered" results are represented by the solid lines. (The dashed lines represent ±1 standard deviation of the OASPL at each location and are used to explore the stationarity of the source from scan to scan in Sec. 3.2.1.)

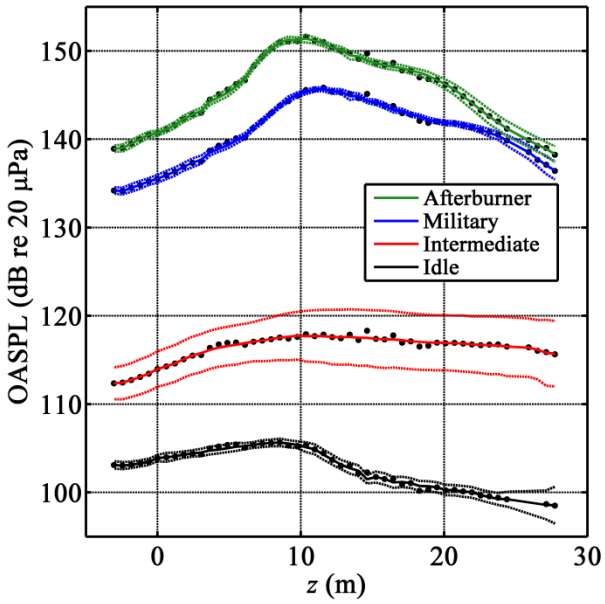

Figure 2.10 OASPLs measured along the ground 12.0 m from the jet centerline by the reference array, for all engine power conditions. Black dots indicate averages of directly measured values and exhibit slight spatial noise due to microphone-sensitivity biases. Smoothed data are shown by a solid colored line, and ± 1 standard deviation over all scans is represented by colored dashed lines.

The reference microphone array, placed along the ground at a perpendicular distance of 12.0 m (39.5 ft) from the center of the aircraft, was near the 42-ft "foul line" position where aircraft maintainer personnel often stand in relation to the jet on the deck of an aircraft carrier. Figure 2.10 shows that, at afterburner conditions, there is a 25-m region where the OASPL exceeds 140 dB re 20 μPa, and a 5-m region where the OASPL exceeds 150 dB re 20 μPa. The levels at the head of an aircraft maintainer are expected to be slightly lower, since the measurements here experienced a level boost due to the ground reflection, and were taken 0.76 m closer to the jet than the foul line position. Also note that the OASPL difference between military and afterburner conditions ranges from about 5 to 6 dB over most of the measurement aperture ($z \leq 19$ m).

The relative locations of maximum-level regions from one measurement plane to the next, shown in Figure 2.8a and 2.9a, as well as the distinct maximum-level regions in Figure

2.10, demonstrate a strong lobing of the overall radiation in the aft direction for military and afterburner conditions. However, an important distinction between military and afterburner conditions exist in the results. The maximum region measured along the reference array in Figure 2.10 shifts forward two or three meters as engine condition increases from military to afterburner. This corresponds to a forward shift of about 10° and is likely due to an increase in the convective speed of large-scale turbulence structures (see Figures. 2.2.9 and 2.2.10 of reference [1].

2.3.3 Spectral Analysis

Turbulent structures within a jet vary greatly in their length and time scales. This manifests itself in the broadband spectra of measured jet noise. In this subsection an examination of the measured spectra, an assessment of the sound field stationarity and a spatio/spectral analysis of the near field radiation lead to insights regarding the frequency dependence of jet noise.

2.3.3.1 Spectral Content

The spectral content in the geometric near field is represented here by the frequency-dependent sound pressure levels (SPLs) measured for all four engine conditions at two key locations within the field. The first, at $z = 5.5$ m downstream (corresponding to an angle of 90° with respect to the front of the aircraft) is shown in Figure 2.11, and a second at $z = 15.2$ m downstream (corresponding to 130°) is shown in Figure 2.12. These locations are important because previous studies often indicate that jet noise is composed of two distinct source components: fine-scale turbulence that dominates the sideline radiation, and large-scale turbulence structures that dominate the downstream radiation.[10,15] The one-third octave SPLs represented by solid lines in Figure 2.11 and 2.12 have been averaged over all scans. The dashed lines show ±1 standard deviation of the SPLs at each frequency and engine condition, and are used to assess stationarity in Sec. 3.2.2. Data for the upper frequencies of the idle and

intermediate conditions are not included because they are contaminated by engine noise components. The legends of Figure 2.11 and 2.12 list the mean values and standard deviations of the OASPLs corresponding to each condition. Note that there is significant spectral energy below 10 Hz and above 20 kHz at some conditions, reaffirming the need for broadband data acquisition and instrumentation capabilities.

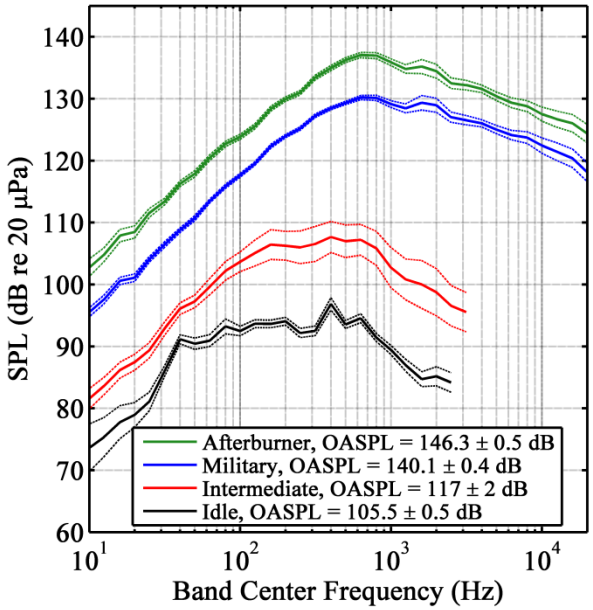

Figure 2.11 One-third octave spectra measured along the reference array at z = 5.5 downstream (90°). Solid lines represent SPL values averaged over all scans. Dashed lines represent ±1 standard deviation. The legend includes the mean values and standard deviations of the respective OASPLs. The upper frequencies of idle and intermediate are not shown due to engine-noise components.

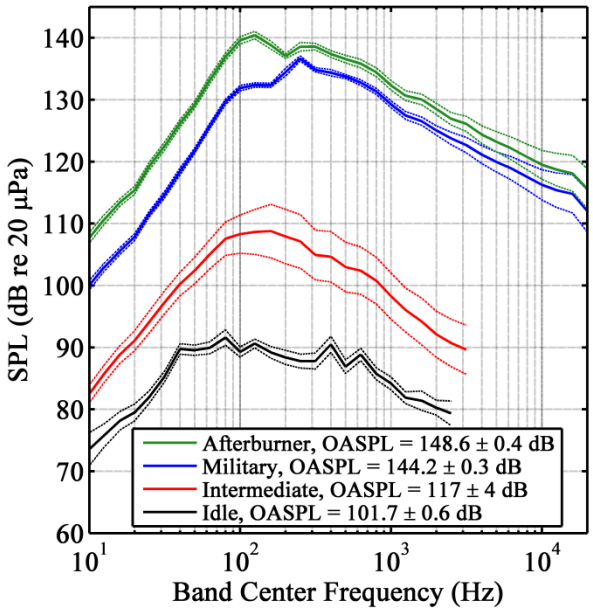

Figure 2.12 One-third octave spectra measured along the reference array at z = 15.2 m downstream (130°). Solid lines represent SPL values averaged over all scans. Dashed lines represent ±1 standard deviation. The legend includes the mean values and standard deviations of the respective OASPLs. The upper frequencies of idle and intermediate are not shown due to engine-noise components.

A comparison of Figure 2.11 and 2.12 indicates that the higher frequencies tend to dominate the noise to the sideline, while lower frequencies dominate in the downstream direction. For example, at $z = 5.5$ m downstream the maximum frequencies are within the 400-Hz one-third octave band for intermediate engine conditions, the 630-Hz band for military conditions, and the 800-Hz band for afterburner conditions. However, at $z = 15.2$ m, the maximum-frequency bands are 100 Hz for intermediate, 250 Hz for military, and 125 Hz for afterburner conditions. Note that the spectra for idle engine power at both locations do not have as well defined of a characteristic "haystack" shape; hence it is more difficult to draw conclusions about the dependence of dominant frequencies on location with these data.

The spectral dependence on location is qualitatively consistent with the popular two-source jet noise model. Schlinker[14] and Laufer *et al.*[15] were the first to observe that there are two independent sources of jet noise: one source generated by large-scale turbulent structures

that radiates preferentially in the aft direction and generates Mach waves, and a source generated by the fine-scale turbulence that dominates to the sideline of the jet. Tam *et al*.[10,16] developed empirically determined similarity spectra to characterize the noise radiated by these two sources for any jet. The application of the two-source similarity spectra to high-power jet noise is under investigation.[95]

It is interesting to compare the spectral shapes shown in Figure 2.12 for military and afterburner engine conditions measured at $z = 15.2$ m. With the increase in power from military to afterburner, high frequencies are boosted by about 3 dB, while low frequencies are boosted by about 8 dB. This is accompanied by a double-peak near the dominant frequencies. The double-peak is not found in laboratory-scale jet noise, but is observed in other full-scale jet ground run-up measurements.[32,77,96] The lower-frequency spectral peak might, in part, be due to the impingement of the jet flow on the ground as it expands downstream of the nozzle, which is referred to as "scrubbing."[97] However, Greska and Krothapalli[89] show a double-peak in the spectrum of an F404-GE-402 jet engine mounted 5.5 m above the ground, which virtually eliminated scrubbing effects. Evidence of a double-peak also appears in flyover measurements of the F-15 ACTIVE Aircraft[98] and in flyover measurements of a military jet by McInerny *et al*.[99] The presence of this feature in full-scale jet noise merits further study.

2.3.3.2 Sound-field Stationarity

To create accurate representations of the sound field over the large measurement planes described in Figure 2.3, it is important to determine stationarity of the noise field produced for each engine run-up. Consequently, frequency and spatial-based stationarity evaluations are performed here to determine how consistent the measurements were from scan to scan. To address stationarity of the sound field for each frequency, the ±1 standard deviation values of the one-third octave SPLs were calculated for all four engine conditions and are shown as the dashed lines in Figure 2.11 and 2.12. For most engine operating conditions and frequencies below about

3 kHz the standard deviations from scan to scan of the power spectra were less than 1 dB, and were less than 2 dB below 10 kHz. Intermediate engine conditions were less consistent than other conditions because there is no "intermediate" set throttle position for the F-22A as there is for the other conditions.

The stationarity of the sound field over space was evaluated by including the standard deviations of the reference array-measured OASPLs in Figure 2.10, also as dashed lines. The OASPL standard deviations measured at most reference microphones were less than about 0.3 dB for idle, military, and afterburner conditions. However, the levels in the extreme aft locations varied by as much as 1 dB. The effects of this aft fluctuation may also be seen in the highly discontinuous scans at the right in Figure 2.8 and 2.9. Possible causes for this greater variability include wave propagation in the near-axial direction through fluctuating turbulent flow, a particularly strong variation in the sources that radiate in the far aft direction, scrubbing of the flow on the ground, or interference by the blast deflector. Recall that the reference microphone farthest downstream was located about 3 m from the bottom of the deflector. The lower stationarity in this region requires further investigation.

Each measurement of the jet noise data was recorded for 30 s. In addition to the source stationarity over the duration of the entire experiment, demonstrated above, it is desirable to understand how stationary the jet was over each 30 s measurement. To quantify sound-field stationarity over each time record the mean and standard deviation of each spectra were calculated. First, the 30 s records were broken up into blocks of equal length. A Hanning window was applied to each block, and adjacent time blocks were overlapped by 50%, according to established Fourier analysis procedures. The complex spectra were calculated for each block and then converted to spectral levels. Finally, the mean and standard deviations of the spectral levels, across the blocks, were calculated.

Figure 2.13 shows the spectra at the sideline of the jet. These data were measured along the ground-based array at 5.5 m downstream of the nozzle exit (11.7 m from the jet centerline).

This corresponds to a polar-angle location of 90°. The solid lines represent the mean SPLs, and the dashed lines show the values of the ±1 standard deviation over the blocks, and indicate source stationarity. (The upper frequencies of idle and intermediate are not shown due to contamination by components unrelated to jet noise.) The time blocks used in generating Figure 2.13 had a length of 250 ms. The standard deviations varied from about 5 decibels for the lowest frequencies (~20 Hz), and gradually decreased to about 1 decibel for higher frequencies (~20 kHz).

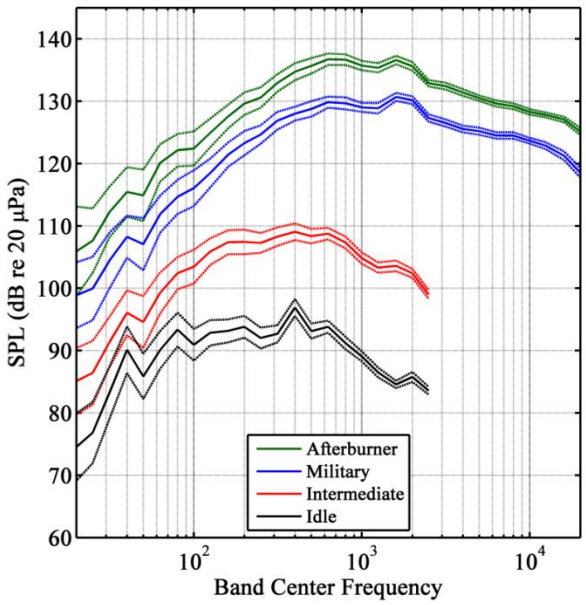

Figure 2.13 One-third octave band spectral levels for all four engine conditions, measured on the ground 11.7 m from the jet centerline and 5.5 m downstream of the nozzle exit (90°). Time blocks of 250 ms were used in the Fourier transform analysis. Solid lines represent the SPL values averaged over all blocks. Dashed lines represent ±1 standard deviation.

This analysis was repeated for time blocks of 1000 ms, and the results are shown in Figure 2.14. Note how the standard deviations are now significantly smaller. This is because longer time blocks allow for more of the sound-field variations to be "averaged out" in the Fourier analysis. Hence, the choice of block size has a significant impact on the quantization of stationarity. This should be recognized when performing further data analyses.

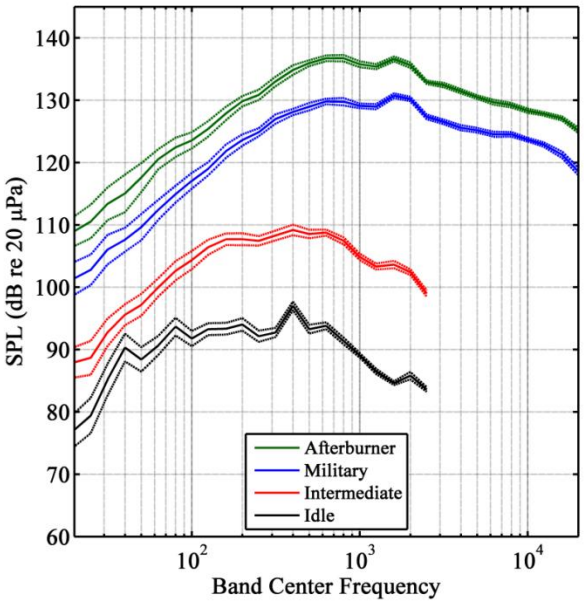

Figure 2.14 One-third octave band spectral levels for all four engine conditions, measured on the ground 11.7 m from the jet centerline and 5.5 m downstream of the nozzle exit (90°). Time blocks of 1000 ms were used in the Fourier transform analysis. Solid lines represent the SPL values averaged over all blocks. The upper frequencies of idle and intermediate are not shown due to contamination by components unrelated to jet noise.

The analysis was performed for a second location 15.2 m downstream of the nozzle exit, corresponding to a polar angle location of 130°. Figures Figure 2.15 and Figure 2.16 show the results for time blocks of 250 ms and 1000 ms, respectively. Although spectral shapes differ significantly at this location, the trends in sound-field stationarity are quantitatively similar.

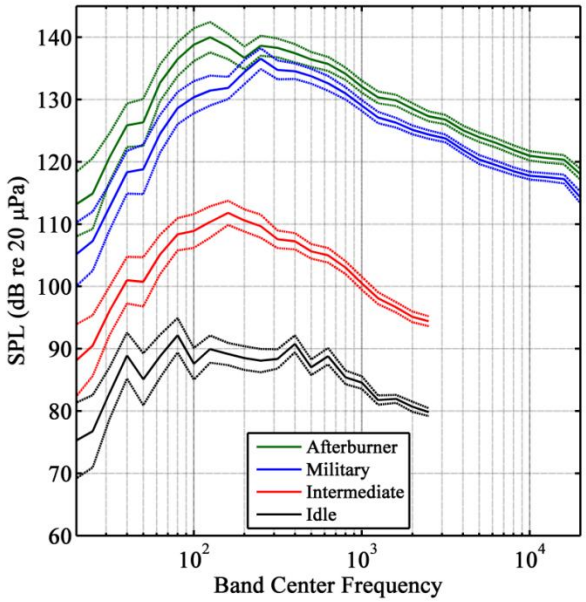

Figure 2.15 One-third octave band spectral levels for all four engine conditions, measured on the ground 11.7 m from the jet centerline and 15.2 m downstream of the nozzle exit (90°). Time blocks of 250 ms were used in the Fourier transform analysis. Solid lines represent the SPL values averaged over all blocks. Dashed lines represent ±1 standard deviation.

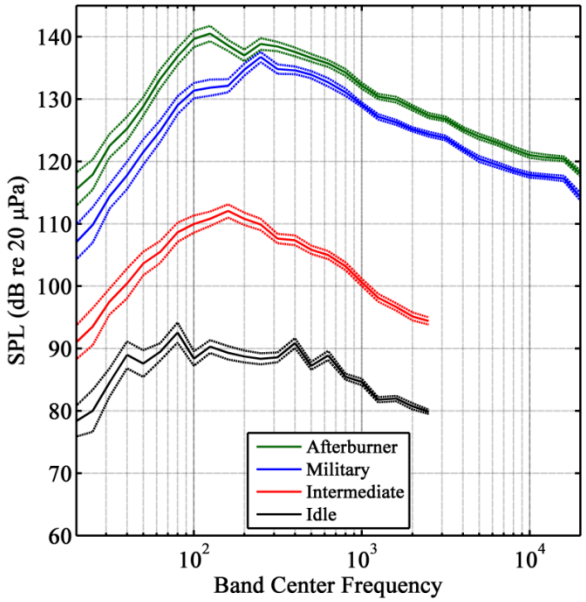

Figure 2.16 One-third octave band spectral levels for all four engine conditions, measured on the ground 11.7 m from the jet centerline and 15.2 m downstream of the nozzle exit (90°). Time blocks of 1000 ms were used in the Fourier transform analysis. Solid lines represent the SPL values averaged over all blocks. The upper frequencies of idle and intermediate are not shown due to contamination by components unrelated to jet noise.

2.3.3.3 Spatial/Band-Level Maps

The spectral variation along the rig planes and the reference array may be used to indirectly infer source characteristics. First, Figures 2.17 through 2.20 show SPL maps of several one-third octave bands measured using the field array at plane 2 (see Figure 2.3), for idle, intermediate, military and afterburner conditions, respectively. The corresponding one-third-octave band center frequency in Hz is displayed in the bottom right corner of each map. A color axis that spans 20 dB is used in each map for consistency. Vertical black lines in both figures mark the edges of the regions where all SPLs in the column drop at least 3 dB below the maximum SPL. Note that the variability of the field for intermediate engine conditions (see Figure 2.10-2.12) reduces the utility of similar maps for that engine power.

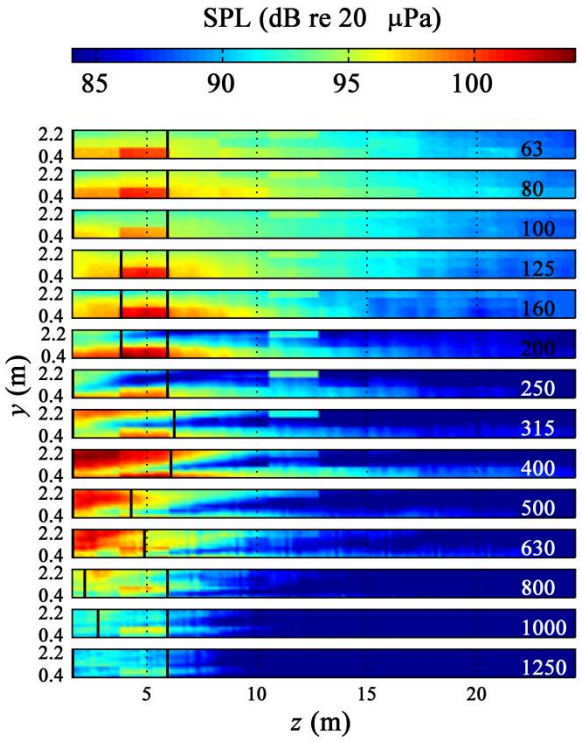

Figure 2.17 SPLs measured at plane 2 for several one-third octave bands at idle engine power conditions. Vertical black lines indicate the regions where SPLs are within 3 dB of the maximum SPL. The number at the right of each plot is the band center frequency in Hz.

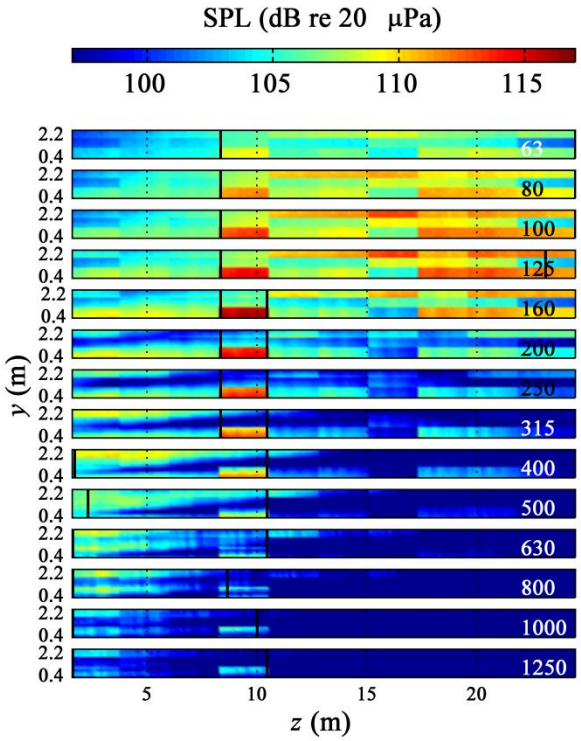

Figure 2.18 SPLs measured at plane 2 for several one-third octave bands at intermediate engine power conditions. Vertical black lines indicate the regions where SPLs are within 3 dB of the maximum SPL. The number at the right of each plot is the band center frequency in Hz.

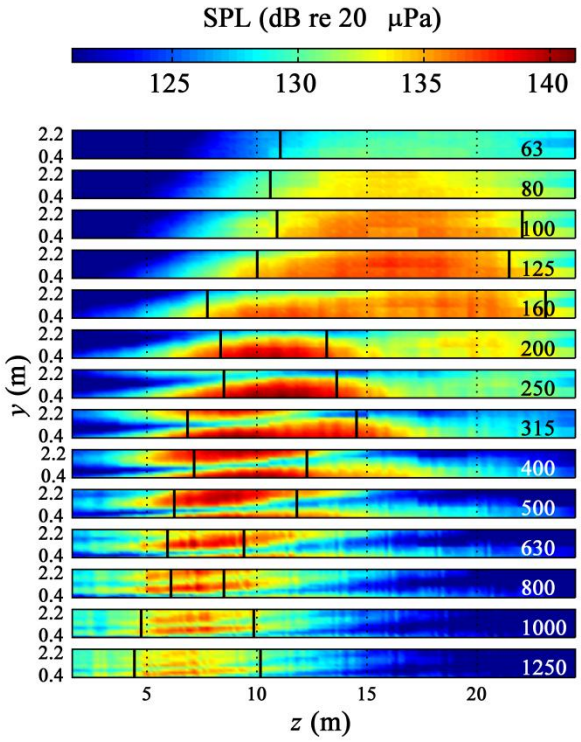

Figure 2.19 SPLs measured at plane 2 for several one-third octave bands at military engine power conditions. Vertical black lines indicate the regions where SPLs are within 3 dB of the maximum SPL. The number at the right of each plot is the band center frequency in Hz.

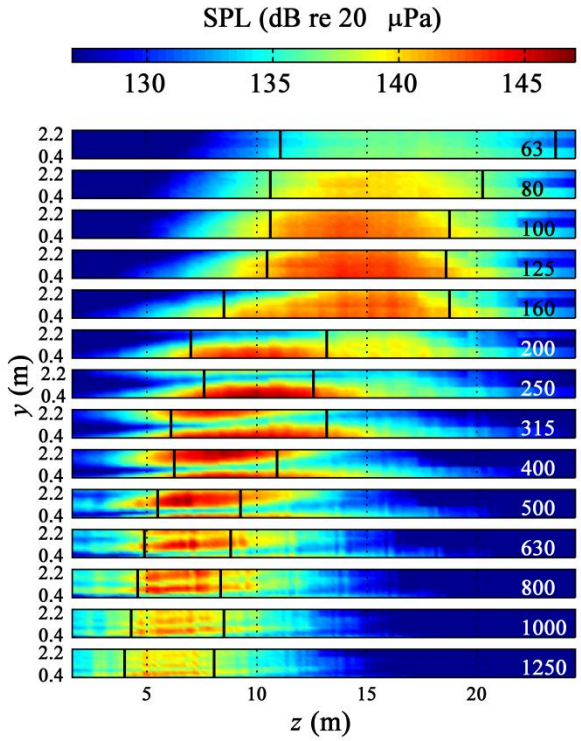

Figure 2.20 SPLs measured at plane 2 for several one-third octave bands at afterburner engine power conditions. Vertical black lines indicate the regions where SPLs are within 3 dB of the maximum SPL. The number at the right of each plot is the band center frequency in Hz.

Before proceeding to level-based maps for the reference array, some comments about what is readily learned from Figure 2.19 and Figure 2.20 are merited. First, as is characteristic of jet noise, both the maps for military and afterburner show that the maximum-level region (demarcated by the 3-dB down points) moves upstream and generally becomes more compact as frequency increases. Second, there is also some indication that the location of this dominant region is asymptotically approaching some limit downstream of the nozzle for these conditions. This is supported by the level maps of higher frequencies (not shown). Although this is a field measurement rather than a source measurement, the upstream movement and spatial constriction of the maximum-level region with increasing frequency agrees, in principle, with Lee and

Bridge's[33] phased-array estimates of the dominant aeroacoustic source region in heated model-scale jets.

The rig-based SPL maps in Figure 2.17 through Figure 2.20 contain horizontal null regions due to multipath interference effects from reflections off the run-up pad. Although these interference nulls are present in realistic run-up and take-off environments, and can be useful in understanding source characteristics,[42,100] the additional spatial variation of spectral levels due to the presence of a reflecting plane can make examination of spectral trends more difficult. Therefore, it is useful to examine level-based maps measured by the reference array, which was placed on the ground. SPLs as a function of one-third-octave band center frequency and location in z are displayed in Figure 2.21 through Figure 2.24 for idle, intermediate, military, and afterburner engine conditions, respectively. The contour lines represent step sizes of 1 dB, and all color axes span a range of 20 dB.

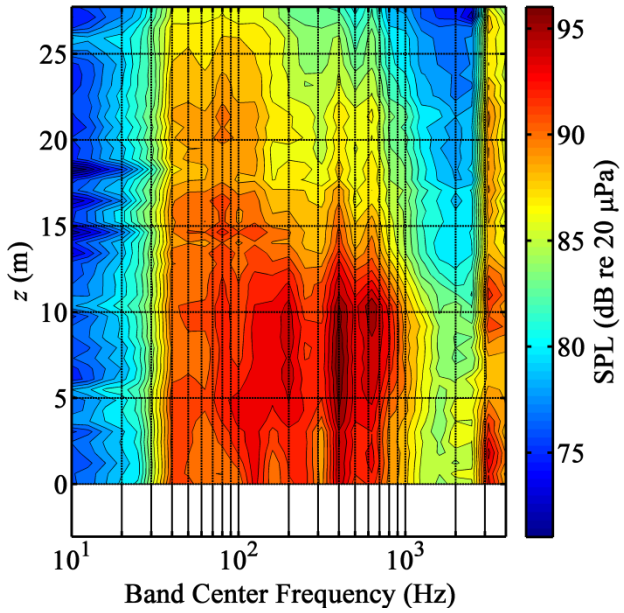

Figure 2.21 One-third octave spectral variation over location along reference array at idle engine conditions. Each contour line represents a step size of 1dB.

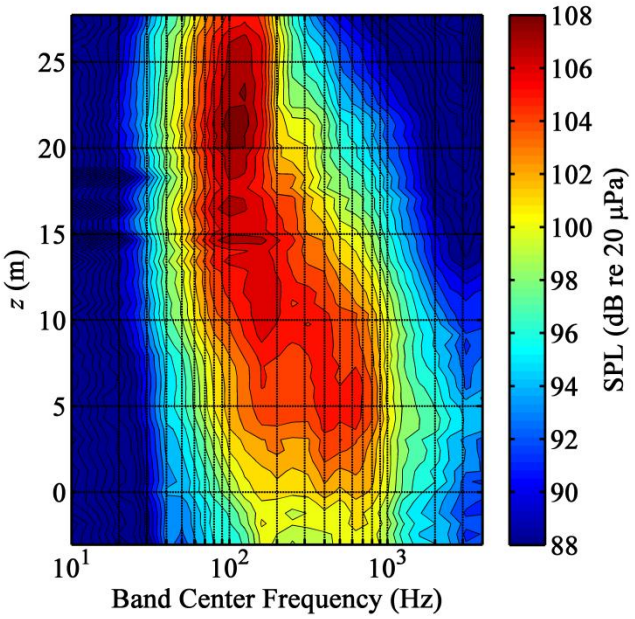

Figure 2.22 One-third octave spectral variation over location along reference array at intermediate engine conditions. Each contour line represents a step size of 1dB.

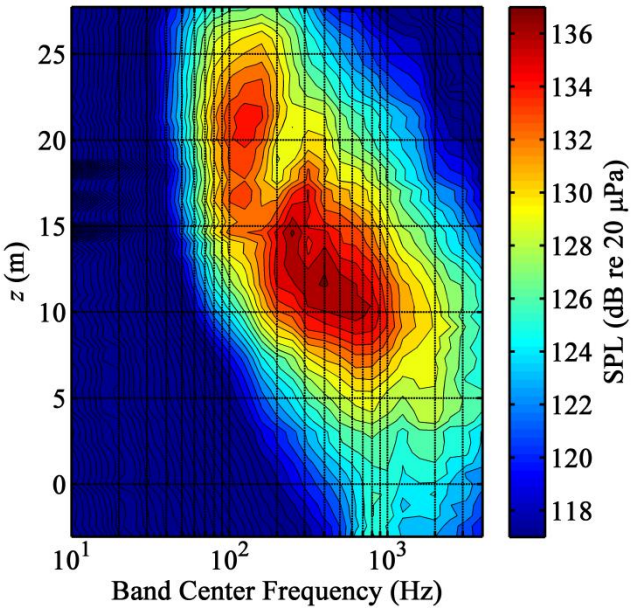

Figure 2.23 One-third octave spectral variation over location along reference array at military engine conditions. Each contour line represents a step size of 1dB.

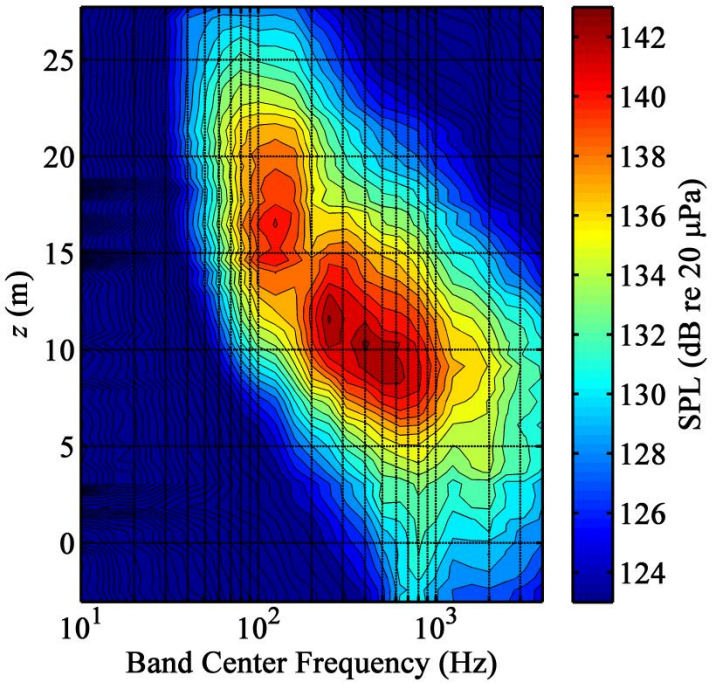

Figure 2.24 One-third octave spectral variation over location along reference array at afterburner engine conditions. Each contour line represents a step size of 1dB.

Figure 2.22 through Figure 2.24 reveal the trend that the region of maximum level in the geometric near field moves upstream and constricts spatially with an increase in frequency for these three engine conditions. Some evidence of this trend is visible in Figure 2.21, although jet noise may not be the dominant source at all frequencies. These figures also demonstrate further the two-peak phenomenon seen at afterburner and military powers in Figure 2.12 (the data shown in Figure 2.11 could be considered "slices" through Figure 2.21-2.24 at z = 15.2 m). In Figure 2.23 and 2.24, there appear to be two distinct, dominant, spatio/spectral components, or regions of local maximum level. The high-frequency component dominates farther upstream and the low-frequency component dominates in the downstream direction. For the afterburner conditions shown in Figure 2.24, the spectra between $z = 13$ m and $z = 22$ m all contain a local maximum frequency near 125 Hz. However, the local frequency maxima of the second component are spatially dependent. Near $z = 14$ m the dominant frequency is about 250 Hz, but

shifts gradually to 800 Hz near $z = 5$ m. The results of military conditions are qualitatively similar in Figure 2.23, and although the distinction between two peaks does not occur in the intermediate case (see Figure 2.22), there is a downstream region where the dominant frequencies (near 160 Hz) do not depend on *z,* and a region upstream where the dominant frequency is spatially dependent.

Caution should be used in drawing conclusions about far-field directivity from the spatial maps in Figure 2.10 and Figure 2.17 through Figure 2.24, since the measurements were taken in the geometric near field. For example, note that the farthest-aft portion of the arc is only about 8 m from the estimated shear layer location. In addition, although the features are similar, when the angular locations of either the arc or the reference microphones are used, similar features for the afterburner spectra are farther aft by 5-10° relative to far-field F-22A spectra shown previously by Gee *et al*.[77]

The question arises, in light of the presence of multiple localized maxima in the spatial/frequency maps shown here: *Are the apparent distinct source mechanisms related to the influence of both fine-scale and large-scale turbulence?* Neilsen *et al*.[80] performed a decomposition of the measured spectra along the reference array. They show that the radiation from large-scale turbulence dominates the spectra as far forward as 90° for the military conditions, and 100° for the afterburner case, which correspond to downstream locations of $z = 5.5$ and 7.3 m, respectively. Since the majority of the energy along the reference array is found farther downstream than these locations in Figure 2.23 and Figure 2.24, it may be concluded that LST dominates a large majority of the field as a whole. In addition, there is energy within 10 dB of the maximum levels (the turquoise regions) at 4 kHz spanning about 10 m of the LST-dominated region for the military conditions, and about 5 m for the afterburner conditions. This suggests that significant information about the radiation from LST structures is contained in frequencies as high as the low kHz range.

2.3.4 Time Waveforms

An examination of directly recorded time waveforms reveals the presence of acoustic shocks and helps to explain important spectral characteristics. Figure 2.25 shows pressure waveform data measured at $z = 5.5$ m on the reference array for all engine conditions, and Figure 2.26 shows waveforms measured at $z = 15.2$ m. These are the same respective locations for which the spectra are plotted in Figure 2.11 and Figure 2.12. For each waveform, the peak amplitude of the entire 30 s time record is shifted to the 10 ms position. Note the presence of shocks in both the sideline and downstream directions for military and afterburner conditions.

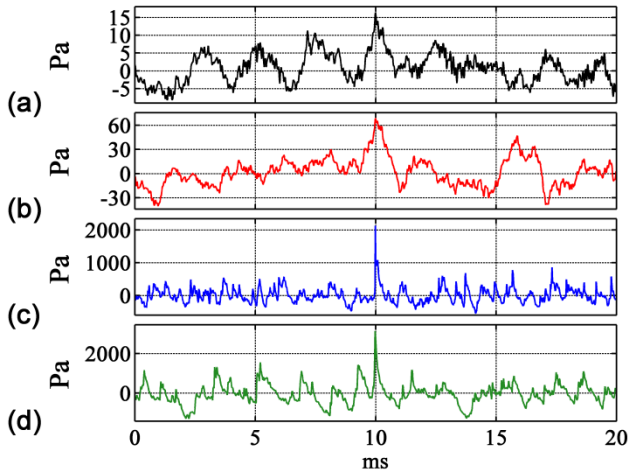

Figure 2.25 Pressure waveforms measured at z = 5.5 m (90°) for (a) idle, (b) intermediate, (c) military and (d) afterburner engine conditions.

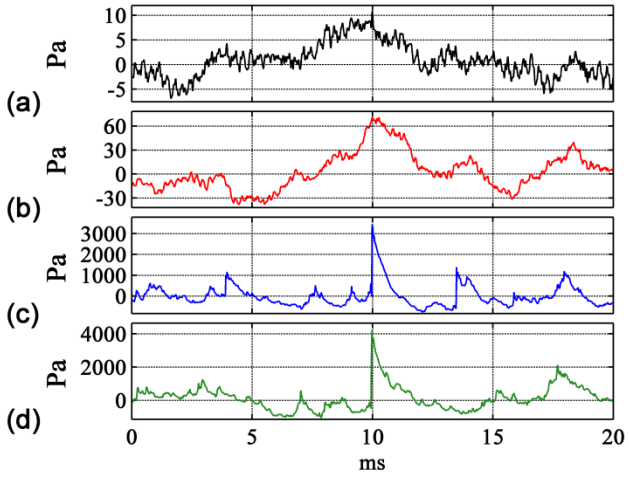

Figure 2.26 Pressure waveforms measured at z = 15.2 m (130°) for (a) idle, (b) intermediate, (c) military and (d) afterburner engine conditions.

An important difference between the sideline and downstream jet noise may be observed by comparing the waveforms shown in Figure 2.25 and Figure 2.26 for each engine condition individually. The waveforms in the downstream location, for both military and afterburner conditions, are broader in time and have fewer zero crossings than those measured to the side. This accounts for the spectral maxima occurring at lower frequencies in Figure 2.12 than those given in Figure 2.11. A likely reason for this is that the sideline radiation is dominated by noise from the fine-scale turbulence structures, which are inherently higher in frequency to begin with, while the aft measurement is dominated by directional noise from large-scale structures.[10,16]

Acoustic shock structures with sharp rise times are present in both the military and afterburner waveforms to the sideline [see Figure 2.25(c)-(d)] and in the downstream direction [see Figure 2.26(c)-(d)]. The formation of shocks due to nonlinear propagation induces a shift of spectral energy toward higher frequencies.[77,96] The presence of shocks in the near field[32,95,101] requires further investigation.

2.3.5 Crest Factor

The crest factor, or the difference between peak and rms overall levels, is an essential measure when designing a high-amplitude jet noise measurement. Not only must measurements be made over a large dynamic range, it is the peak pressures, rather than the rms pressures, that limit the proximity of microphones to the jet. In this analysis, the crest factor was found along both the rig and reference arrays as a function of engine condition and location. A 99.999th percentile criterion was used; i.e., 99.999% of all instantaneous pressure amplitudes in a waveform were below the peak value found. This essentially corresponds to one pressure value above the calculated peak value every two seconds at afterburner conditions, or every one second at other conditions.

The largest peak pressure measured on the array at plane 1 for afterburner conditions was 6443 Pa (170.2 dB re 20 μPa). The corresponding crest factor was 16.7 dB. Peak pressures at the reference array (which was placed on the ground to avoid multi-path interference but, therefore, experienced a pressure boost) for afterburner engine conditions reached 6183 Pa (169.8 dB re 20 μPa). The crest factor at this location was 18.1 dB. Both maximum crest factor estimates agree with previous works by Gabrielson *et al*. [101] and by McInerny[102] where they indicated that peak pressures can be five to ten times (or 14-20 dB) greater than rms pressures for high-power aeroacoustic noise. This information should prove useful in the future design of near-field experiments on full-scale jet noise.

2.4 Conclusions

Turbulent jets from full-scale engines on military aircraft are some of the largest and most complicated noise sources of interest in aeroacoustics. Near-field experiments on these sources require measurements to be made over tens of meters in length, for noise over a very large dynamic range and with significant spectral content from the infrasonic to the ultrasonic

regimes. This paper describes basic results of measurements made in the geometric near field of the jet on an F-22A Raptor. It is shown here that an increase in engine power from military to afterburner conditions results in a forward-shifting of the noise radiation and a possible increased lobing effect. It is also shown that, in the downstream direction, as engine power increases from military to afterburner engine conditions the low-frequency noise components increases much more rapidly than high-frequency components. This is coupled with the occurrence of two distinct maximum regions in the level maps as a function of frequency and location: a low-frequency component that dominates downstream and where the maximum frequency is nearly independent of location, and a high-frequency component that dominates upstream with a location-dependent maximum frequency. It is also shown that the noise measured in the far downstream locations is less stationary than the noise measured elsewhere.

The scope of the measurements made in this experiment provides for a detailed characterization of full-scale jet noise sources and the near sound field using near-field acoustical holography methods. The extensive measurements should also allow for future beamforming, near-field correlation and coherence, vector acoustic intensity, partial field decomposition and nonlinear propagation analyses. These analyses can expand the understanding of high-power jet noise properties in the near field and help to determine important jet noise source characteristics.

Chapter 3

Partial Field Decomposition of Jet Noise

3.1 Introduction

Accurate characterization of the spatial distribution of noise sources within a jet provides insight into physical noise generation mechanisms in the turbulent flow field. This characterization can help lead to reduction schemes of the noise that can cause significant hearing loss for military personnel and is a disturbance to communities. We wish to use near-field acoustical holography (NAH) to localize noise sources within the jet of a full-scale military aircraft. We explore acoustical inverse methods because they employ a non-intrusive measurement of the sound field outside of the flow field and then use the wave nature of sound to obtain sound field information at the source.

Partial field decompositions (PFDs) are an integral part of near-field acoustical holography (NAH) methods. To understand why, it is helpful to discuss the nature of coherent and incoherent sound fields.[63] A coherent wave field, defined for a single frequency, is a field with perfect coherence between every pair of points. The propagation of sound waves in a homogeneous source free medium is based on solutions to the homogeneous Helmholtz equation. These solutions define complex sound pressures with assumed time harmonicity,

which are obtained from a Fourier transform of time signals of theoretically infinite length. The time harmonic field represented by a single set of pressure values (i.e. one complex pressure at any given location) is perfectly coherent. A coherence less than one cannot be represented by a single time harmonic field. Multiple independent Fourier transformed time records are required to predict coherences of less than one.

For NAH to be successful, the holograms used must be coherent. Jet noise sources are comprised of multiple independent source mechanisms. Hence, the complex pressure field will not be coherent and cannot be represented by the Fourier transform of a single time record. Therefore, multiple recordings must be made at the hologram array, even in a snapshot measurement, where all measurements are made simultaneously. A PFD uses the multiple measurements to decompose a sound field into linearly independent components, or "partial fields." Each of these partial fields is self-coherent, yet independent of the other partial fields. They can be processed individually with NAH, and the result is a set of field reconstructions, one for each partial field. Since they are mutually incoherent, they are then summed on an energy basis to provide the total field reconstruction.

It is often necessary to measure a source in a holography application with a large measurement aperture and dense spatial sampling. This often requires an inordinate number of transducers. In such cases, the overall field can be measured in a series of scans with a small, dense microphone array. However, the phase information between scan locations is lost, since measurements are not taken simultaneously. In a hologram measurement that is made of a series of incoherent scans, a set of reference microphones with fixed locations must record the sound field simultaneously with each scan. These reference measurements can be used to tie together the incoherent scans into coherent holograms.

In such a measurement there must be at least as many reference microphones as there are independent sources (and more if noise is present in the measurement), if the total energy of all sources is to be represented. However, the number of sources in a turbulent field is ambiguous.

In general, there are more independent (incoherent) sources for higher frequencies, but predicting the number of sources *a priori* is not feasible. Qualitative guidelines for reference deployment exist, as do methods for verifying the reference array sufficiency after the hologram has been measured. In this chapter, it is shown that spatial coherence measurements in the geometric near field can be used to quantitatively guide the design of a sufficient reference array.

Two PFD methods are presented in this work. The method explored in the current chapter is a commonly used PFD method for jet noise analyses and other multi-source acoustic problems, which is based on the use of singular value decomposition (SVD-based PFD). It is a means to generate mutually incoherent partial fields and estimate the number of independent sources in a jet. Since use is made of an SVD, the partial fields generated here do not generally represent physically meaningful sources—each partial field cannot be exclusively assigned to one independent source mechanism. In Chapter 6, an additional PFD method is discussed that breaks up a total sound field into partial fields that can correspond to physically meaningful source mechanisms.

Section 3.2 of this chapter describes the basic theory of SVD-based PFD algorithms. The virtual coherence method is discussed, which provides a way to verify the sufficiency of a reference array used in the PFD. Results of the PFD, including the resulting partial fields, are presented. References per coherence length (RPL_C), a figure of merit for determining a sufficient number of reference microphones *a priori*, is presented in Section 3.3. This method relies on the measurement of coherence lengths of a source and can predict the sufficiency of a reference array before PFD or NAH is implemented. Numerical and physical experiments are described to demonstrate the utility of RPL_C. In Section 3.4, measured coherence lengths are shown for the full-scale jet, and an RPL_C analysis of the jet data is performed to validate the use of this figure of merit and to demonstrate limitations in the reference array of the jet experiment.

3.2 SVD-based PFD

3.2.1 Introduction

Before performing NAH to localize sources, a coherent measurement plane is required. This requirement will be met through the use of fixed reference microphones and a partial field decomposition (PFD). Section 3.2 demonstrates a commonly employed multireference PFD method for the full-scale jet data used in this work (see Section 2.2). This method was initially presented under the name Spatial Transformation of Sound Fields,[63] but it is often discussed in the literature in the context of its association with the singular value decomposition process (SVD). Hence, in this work it will be referred to as SVD-based PFD. Section 3.2 was modified from a 2011 publication in *Proceedings of Meetings on Acoustics* under the name, "Near-field acoustical holography applied to high-performance jet aircraft noise."[83]

In Section 3.2.2, the spectra and spatial coherence of aeroacoustic sources are discussed. This provides some context for the PFD methods investigated here. Section 3.2.3 describes the theory of SVD-based PFD, in conjunction with the virtual coherence function. Section 3.2.4 gives details of the physical experiment on a full-scale military aircraft. Results of the application of SVD-based PFD and virtual coherence on the full-scale jet data are provided in Section 3.2.5. In Section 3.2.6, implications of the PFD results are discussed for the NAH problem.

3.2.2 Sound Radiation from Aeroacoustic Sources

The noise sources of a jet are not well understood. For high-power jets from the engines of military aircraft, sources are particularly complicated. Typical spectra of radiated sound pressures follow the trends of those shown in Figure 3.1. These one-third-octave sound pressure levels (SPLs) are calculated from sound pressure measurements of an F-22A Raptor, approximately 11.7 m from the jet centerline and on the ground. Note that the noise is broadband with peak frequencies around 100-900 Hz.

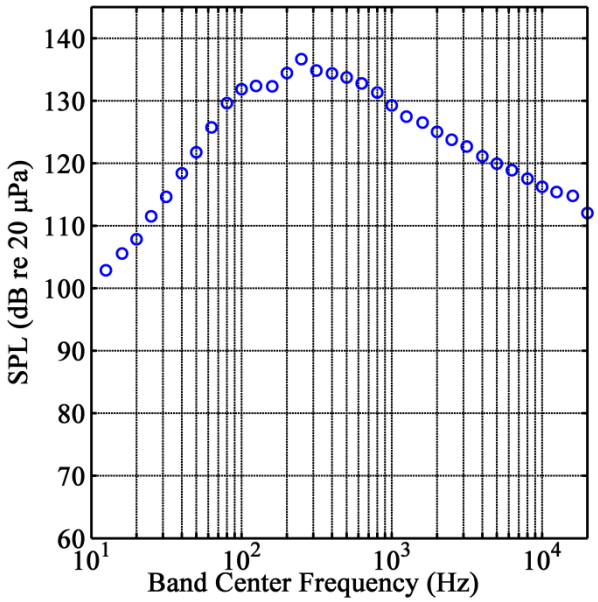

Figure 3.1 One-third-octave SPL at 11.7 m from the centerline of the jet on an F-22A Raptor at afterburner engine conditions.

Many noise sources, especially those with characteristic lengths larger than a wavelength, do not radiate like simple sources. For example, a large vibrating plate will have significantly different radiation properties than will a point source. We may consider a vibrating plate as a distribution of radiating monopoles. The phase relationships between each monopole on the plate are not random, but fixed. Note that we are considering here complex pressures on a frequency-by-frequency basis. This fixed-phase relationship causes all the point sources that make up the plate to be coupled in such a way as to generate acoustic radiation into the surrounding fluid very differently from that which would be generated by a similar distribution of monopoles all vibrating independently. This fixed-phase relationship may be described by the *coherence* between each monopole.[103] The coherence between two complex pressure measurements describes the degree to which the two measurements are related. If the two measurements are perfectly related, then the coherence function will have a value of unity. Two fully independent measurements will have a coherence of zero. Signals that are somewhat

related will have a coherence somewhere in between zero and unity. For example, vibrations in a solid structure, such as a plate, are fully coherent, and hence they radiate a coherent sound field. It is well established that aeroacoustic sources are partially coherent over finite distances, and therefore radiate somewhat coherently.[85,104]

3.2.3 Theory

NAH requires a coherent measurement over the hologram to propagate the sound field in toward the source. This means that there must be a fixed phase relationship between every set of two points on the hologram. For this work, consider the use of a patch-and-scan measurement with simultaneous measurements by an array of fixed-location reference microphones. The discontinuities in phase information between scans may be removed with the use of PFD.

In this work, SVD-based PFD is used in conjunction with the virtual coherence function.[105,106] First, for a chosen frequency we calculate the cross-spectral matrix of the reference array measurements, $\mathbf{C}_{rr}$. A decomposition of this matrix is performed using SVD, i.e.,

$$\mathbf{C}_{rr} = \mathbf{U}\boldsymbol{\Sigma}\mathbf{V}^{\mathrm{H}} = \mathbf{U}\boldsymbol{\Sigma}\mathbf{U}^{\mathrm{H}}, \tag{3.1}$$

where $\boldsymbol{\Sigma}$ is a diagonal matrix of singular values, $\mathbf{U}$ and $\mathbf{V}$ are unitary matrices of the left and right singular vectors, respectively, and $\mathbf{U}$ and $\mathbf{V}$ are identical since $\mathbf{C}_{rr}$ is a positive semi-definite Hermitian matrix. The superscript H indicates the Hermitian transpose. This generates an orthogonal basis of "virtual references," each virtual reference containing information from all the individual physical references. It is actually the singular values in $\boldsymbol{\Sigma}$ that represent the autospectral amplitudes of the virtual references, so we can write the virtual reference cross-spectral vector

$$\mathbf{C}_{vv} = \boldsymbol{\Sigma}. \tag{3.2}$$

The singular values that describe the strength of each of these virtual references are sorted in descending order. The first singular values contain information relevant to the source, and the rest contain lower amplitude noise. Therefore, a sufficient number of singular values must be selected to represent the total energy of the sound field at the field array in the partial fields, and the rest filtered out. This is only possible if there are more reference measurements than independent source mechanisms. In a noiseless case, no filtering is required, and the number of references can be equal to the number of sources. However, as noise in the measurement increases, more references are needed to filter that noise.

The noise-related singular values can be estimated with the virtual coherence method. We calculate two additional cross-spectral matrices, including the cross spectra between all field measurements in a scan, $\mathbf{C}_{pp}$, and the cross spectra between virtual references and field measurements, $\mathbf{C}_{vp}$. The virtual coherence function between the *i*th virtual reference and the *j*th measurement position in each scan is given by

$$\gamma_{j,i}^2 = \frac{\left|\mathbf{C}_{v_i p_j}\right|^2}{\mathbf{C}_{v_i v_i}\mathbf{C}_{p_j p_j}} \tag{3.3}$$

This virtual coherence is summed over the first *R* elements of *i*, iteratively increasing *R* until the coherence criterion is met, namely

$$\sum_{i=1}^{R} \gamma_{j,i}^2 \geq \text{coherence criterion} \tag{3.4}$$

Once the coherence criterion is reached for every measurement position *j* in a scan, the corresponding *R* value is the necessary number of singular values for that scan. The median of these *R* values is selected as the number of singular values retained, while the remainder of singular values in $\mathbf{\Sigma}$ are filtered out. This number may also be considered the effective number of sources in the field. In practice, a coherence of unity is nearly impossible to achieve. We

have therefore chosen a coherence criterion of 0.9 for the purposes of this chapter. This corresponds to a signal-to-noise ratio of approximately 10 dB by the relation

$$\mathrm{SNR} = 10\log_{10}\left(\frac{\gamma^2}{1-\gamma^2}\right), \tag{3.5}$$

where the numerator in the log function represents the coherent power, and the denominator corresponds to noise, or incoherent power.

With the important singular values chosen, the partial fields can then be calculated as described by Lee and Bolton.[74] Their calculation accounts for variation in source level. The total number of partial fields produced by the decomposition equals the number of reference microphones. These partial fields are also sorted by strength. This is mathematically the "ideal" decomposition, since as much of the sound field as is possible is packed into the first partial fields, and the noise is filtered out of the singular values. These partial fields form an orthogonal basis set for the sound field. The energy-based summation of these partial fields returns the total measured hologram surface magnitude.

Returning to the example of a vibrating plate, because the entire source is coherent, only one singular vector contains relevant information. Consequently, only one reference microphone is needed to perform PFD (assuming noise is negligible). A sound field generated by N independent sources requires at least N reference microphones. If the number of sources is unknown, the singular values of the SVD on the reference microphones give clues about estimating the number of sources. For a system with N well-defined independent sources and a large signal-to-noise ratio, there will be a sharp drop from the singular value N to the N+1 singular value. For a jet, where the number of independent sources is unclear, the singular values tend to decrease somewhat steadily. Thus, the number of reference microphones required to fully measure the source must be determined. A figure of merit, based on spatial coherence

measurements, that provides a method for estimating the necessary number of references is provided in Section 3.3.

3.2.4 Experiment

In July 2009, near-field measurements of the jet on a Lockheed Martin/Boeing F-22 Raptor were taken at Holloman Air Force Base in New Mexico. A 5 by 18 array of G.R.A.S ¼" microphones, with 0.15 cm spacing (Figure 3.2), scanned an approximately 2 m by 24 m region (Figure 3.3) as near to the jet as transducer limitations would allow (see Section 2.3.5). This was repeated for three more measurement planes some distance farther from the jet. In addition, 50 fixed reference microphones were placed on the ground with 0.6 m spacing, spanning more than 30 m, (shown in Figure 3.4). Measurements were repeated for four engine conditions ranging from idle to full afterburner. Figure 3.5 shows the overall sound pressure levels measured in relation to the aircraft location for the afterburner engine condition. There were a total of more than 6000 measurement positions, making this the largest-scale acoustic measurement of a high-power jet ever performed.

Figure 3.2 Blue Ridge Research and Consulting 90-microphone array, scanning the near field of the jet on an F-22 Raptor.

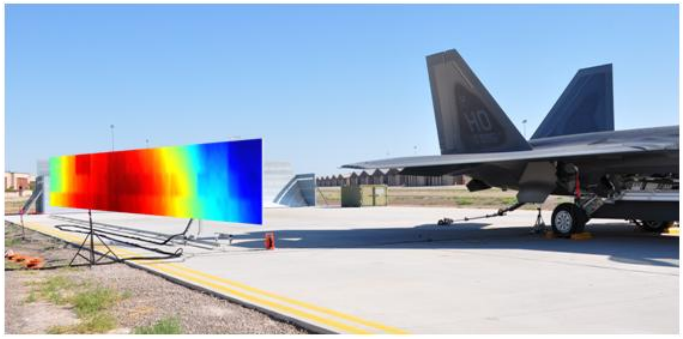

Figure 3.3 An example sound pressure level map overlaid with the jet photo at the approximate measurement location.

Figure 3.4 Fifty reference microphones were placed on the ground 11.7 m from the jet centerline, which measured sound pressures simultaneously with each scan.

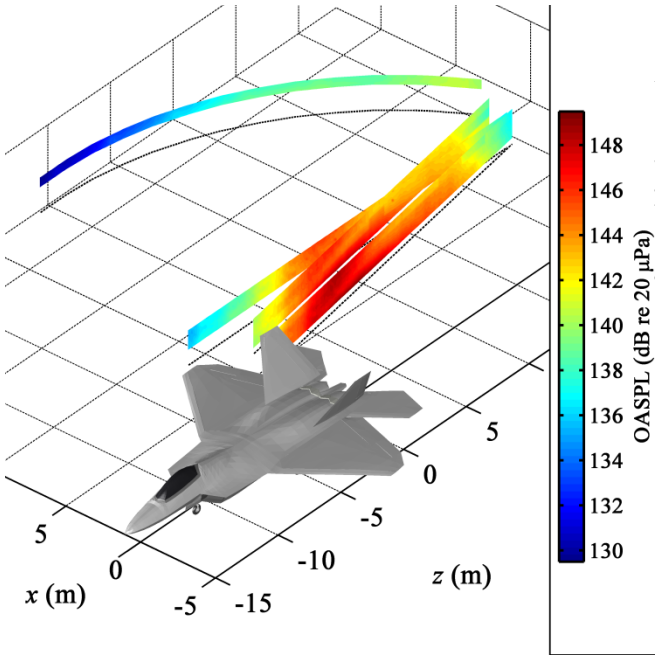

Figure 3.5 Overall sound pressure levels measured in the jet vicinity for military engine conditions.

3.2.5 Results

Results of SVD-based PFD performed on the measured hologram data at plane 2 and reference array data (see Figure 2.3) are shown for military engine conditions. First, Figure 3.6 shows all 50 singular values of the reference array decomposition as a function of one-third-octave band center frequency. Note that the first (highest-amplitude) singular value at 10 Hz is about 10 dB larger than the second singular value. In fact, the first 10 singular values at 10 Hz are characterized by typical separations of 3-10 dB, and the remaining singular values are much more closely spaced. As frequency increases, separations gradually diminish further. This indicates that the number of effective independent sources in the field increases with frequency.

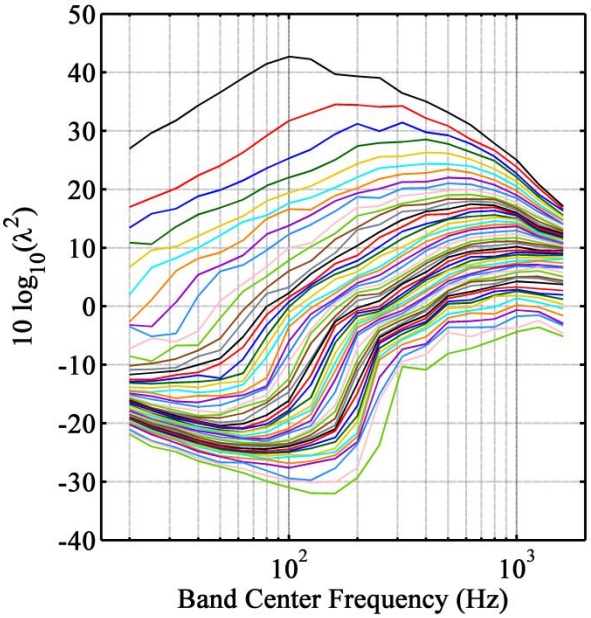

Figure 3.6 Singular values of the reference array decomposition for military power.

To demonstrate how the number of singular values retained affects the virtual coherence results, values of the virtual coherence function summed over partial fields ($\Sigma\gamma^2$) are plotted as a function of location on measurement plane 2 for four select frequencies: 125 Hz, 250 Hz, 500 Hz, and 1000 Hz, and for military power. These are shown in Figure 3.7 through Figure 3.10, respectively. Recall that the sum of virtual coherence values indicates the ability of the combined partial fields to represent the total field energy. In each figure, part (a) shows the virtual coherence corresponding only to the first partial field. Parts (b) are summations of virtual coherence over the first 5 partial fields, and parts (c) are the summations over all 50 partial fields. For 125 Hz in Figure 3.7a, the virtual coherence of the first partial field approaches unity over a large region near $z = 16$ m. This suggests that one partial field contains the majority of information near $z = 16$ m, which is the location of maximum amplitude in the total field. However, $\Sigma\gamma^2$ drops away from this location, approaching zero for the lowest values of z. The inclusion of 5 partial fields in Figure 3.7b brings $\Sigma\gamma^2$ toward unity for all locations of $z > 10$, and the inclusion of all 50 in Figure 3.7c brings $\Sigma\gamma^2$ toward unity over the majority of locations,

excluding those that correspond to locations of low magnitude. Figure 3.8 and Figure 3.9 show similar trends for the 250 Hz and 500 Hz cases, respectively, but note that, as frequency increases, $\Sigma\gamma^2$ values approach unity for smaller portions of the field with the same R values.

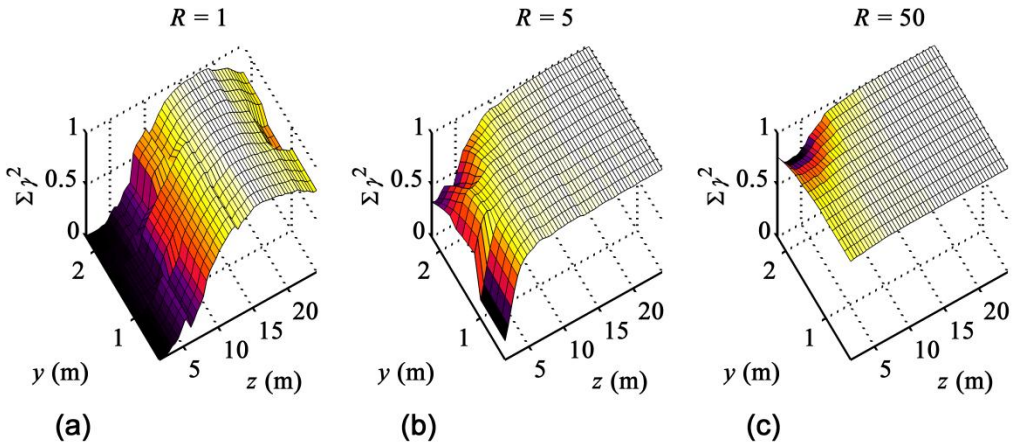

Figure 3.7 Sum of the first *R* virtual coherence function values for various values of *R*, as a function of location in measurement plane 2, for military power, 125 Hz.

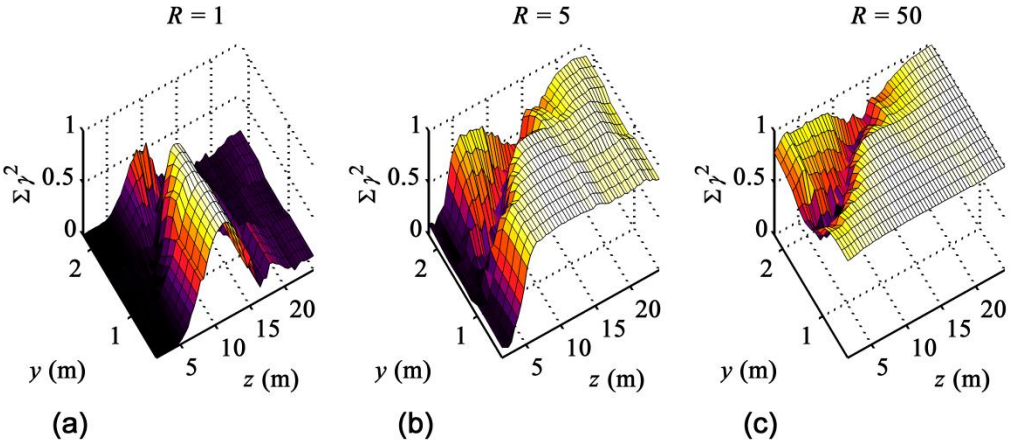

Figure 3.8 Sum of the first *R* virtual coherence function values for various values of *R*, as a function of location in measurement plane 2, for military power, 250 Hz.

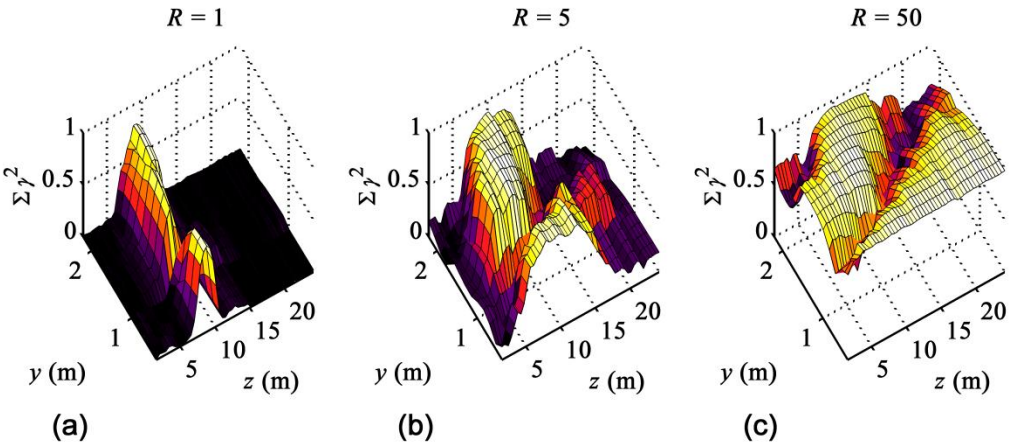

Figure 3.9 Sum of the first *R* virtual coherence function values for various values of *R*, as a function of location in measurement plane 2, for military power, 500 Hz.

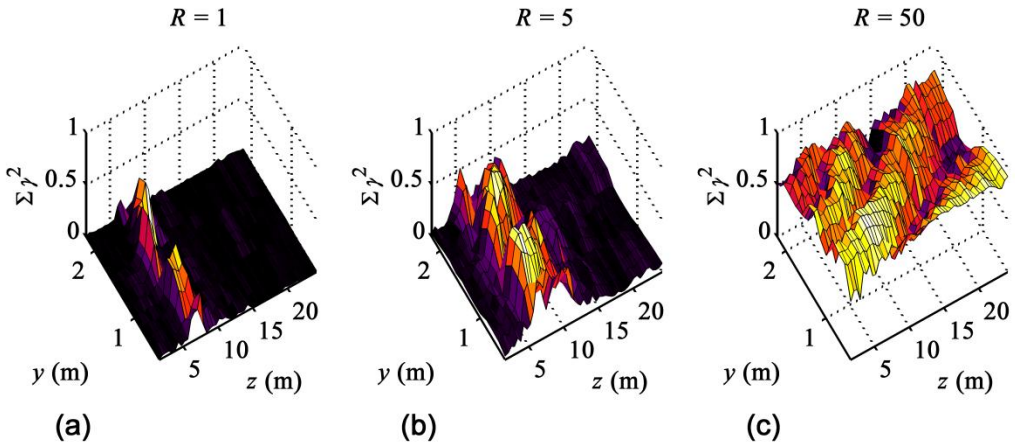

Figure 3.10 Sum of the first *R* virtual coherence function values for various values of *R*, as a function of location in measurement plane 2, for military power, 1000 Hz.

The virtual coherence summation for 1000 Hz, shown in Figure 3.10, is a special case. Note that, even with all 50 partial fields, $\Sigma\gamma^2$ is well below unity for the majority of locations. The reference array was insufficient to accurately capture the information that is coherent with that of the field measurement above about 500 Hz.

The partial fields that result from SVD-based PFD for military power are now presented. Figure 3.11 shows the total SPLs measured at plane 2 and at 125 Hz, and Figure 3.12 shows the SPLs of the first six partial fields. Note that the majority of the energy in the total field is represented in the first partial field. There is an approximately 10 dB difference in maximum levels between the first and second partial fields, with gradually decreasing energy in the partial fields 3 through 6..

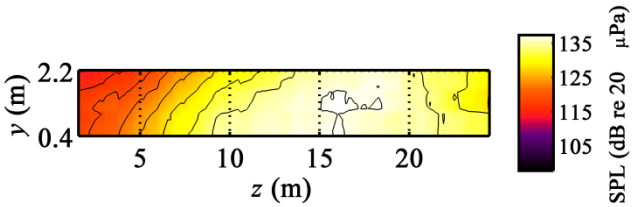

Figure 3.11 Total measured SPLs in the 125 Hz one-third-octave band at plane 2 for military power.

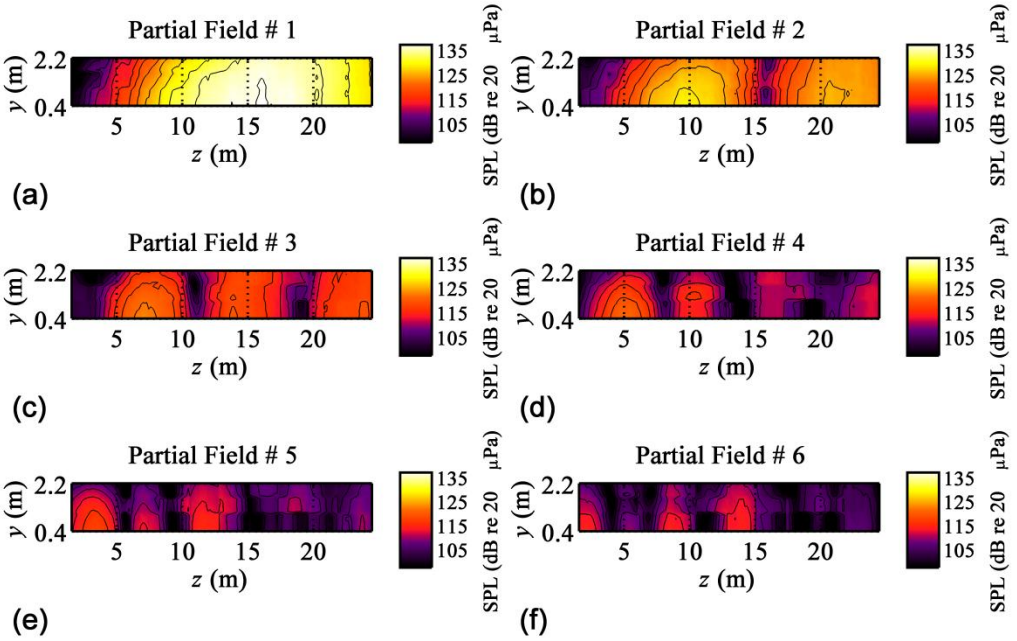

Figure 3.12 SPLs of the first six partial fields in the 125 Hz one-third-octave band at plane 2 for military power, after SVD-based PFD.

To demonstrate the ability of SVD-based PFD to generate self-coherent partial fields, the phase information of the original scan-based measurement is compared to the phases of the partial fields. Figure 3.13 shows measured phases for 125 Hz, military power , which are discontinuous at the boundaries between scans. However, the phase information is made continuous in the PFD process, as shown in Figure 3.14. Some discontinuities remain at select

locations in each partial field, which correspond to low-amplitude regions of the magnitude of the respective partial fields.

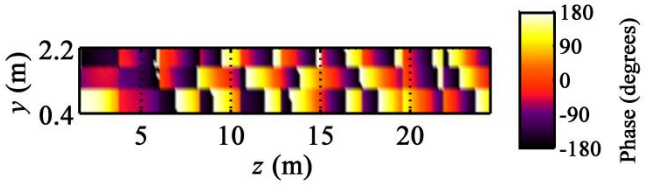

Figure 3.13 Measured phases for 125 Hz at plane 2 for military power.

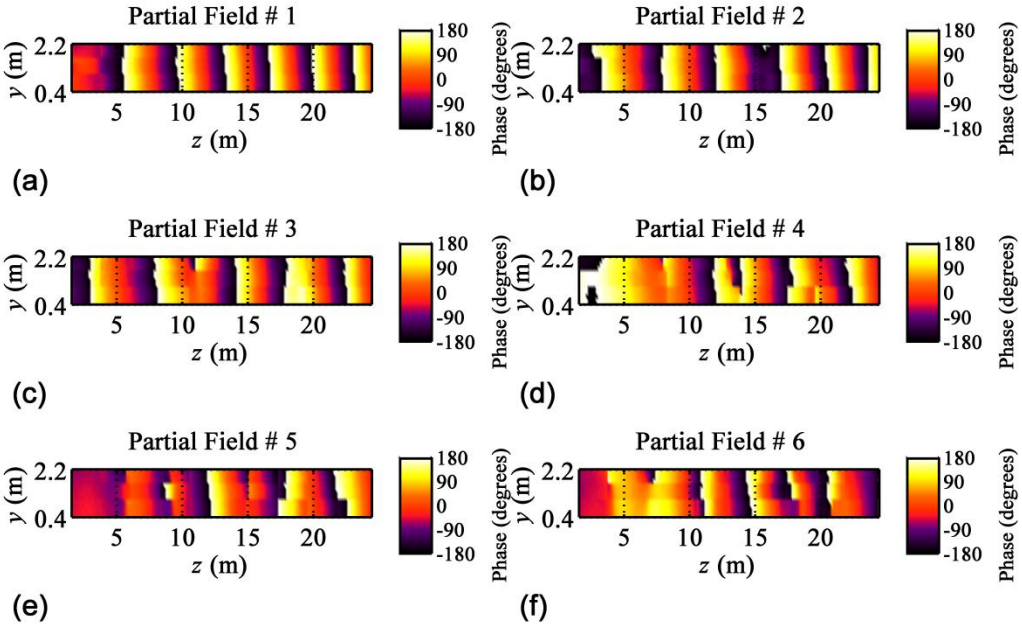

Figure 3.14 Phases of the first six partial fields for 125 Hz at plane 2 for military power, after SVD-based PFD.

Total measured levels and the levels of the first six partial fields at plane 2 for military power are shown in Figure 3.15 through Figure 3.20 for the additional frequencies of 250 Hz, 500 Hz, and 1000 Hz. In general, as frequency increases, energy becomes more uniformly distributed over more partial fields. For example, the difference in the maximum amplitudes of partial fields 1 and 2 at 500 Hz (see Figure 3.18) is less than 3 dB, as opposed to the 10 dB

difference in the 125 Hz case. This is related to the trend that the number of effective sources in the field is also increasing with frequency.

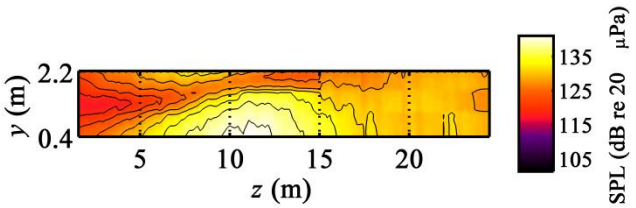

Figure 3.15 Total measured SPLs in the 250 Hz one-third-octave band at plane 2 for military power.

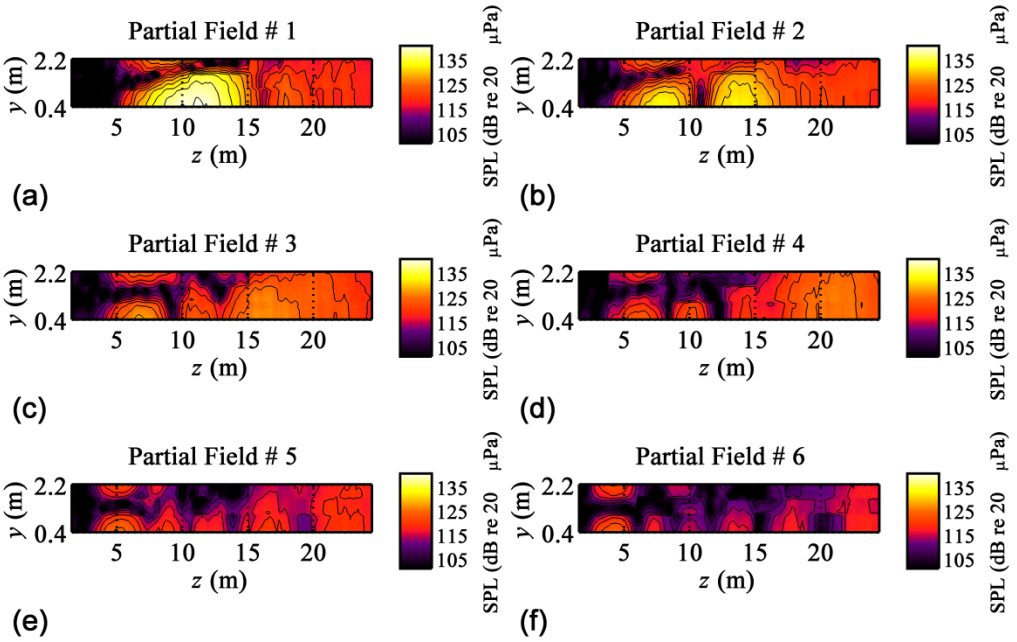

Figure 3.16 SPLs of the first six partial fields in the 250 Hz one-third-octave band at plane 2 for military power, after SVD-based PFD.

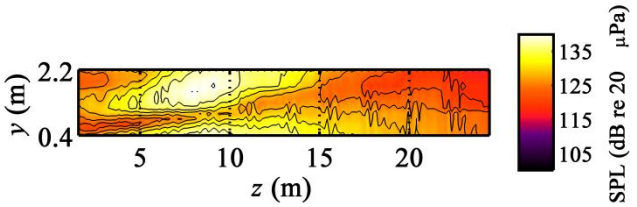

Figure 3.17 Total measured SPLs in the 500 Hz one-third-octave band at plane 2 for military power.

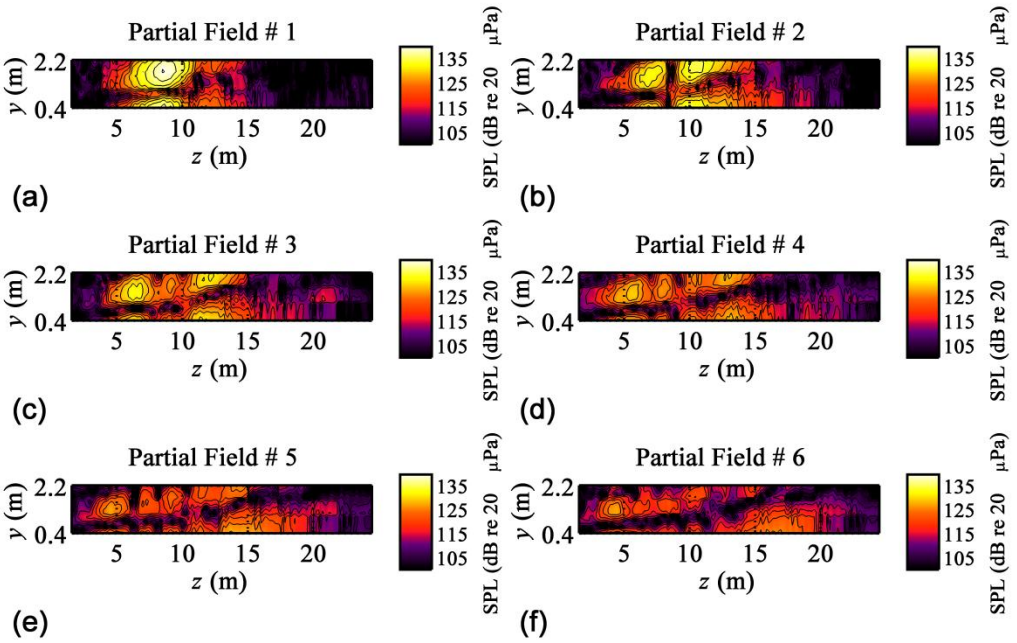

Figure 3.18 SPLs of the first six partial fields in the 500 Hz one-third-octave band at plane 2 for military power, after SVD-based PFD.

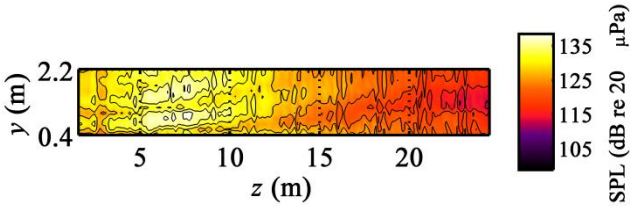

Figure 3.19 Total measured SPLs in the 1000 Hz one-third-octave band at plane 2 for military power.

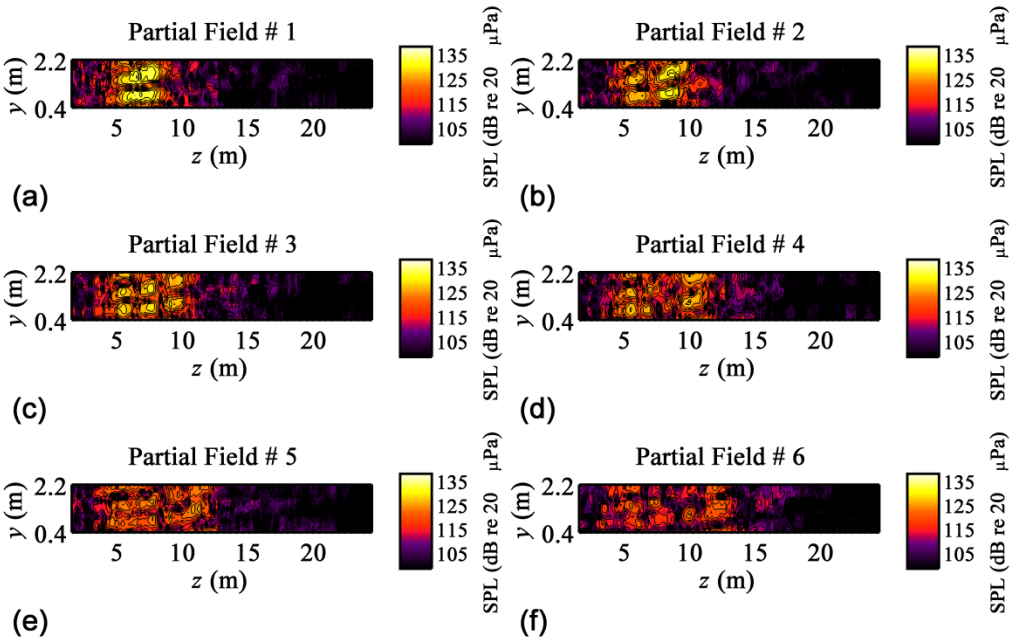

Figure 3.20 SPLs of the first six partial fields in the 1000 Hz one-third-octave band at plane 2 for military power, after SVD-based PFD.

There is one important feature of the partial fields that is found at every frequency: the distributions of levels in the *z*-direction across each partial field take on the appearance of a "modal decomposition," similar to that seen on a vibrating string or plate. For all frequencies shown here, in Figure 3.12, Figure 3.16, Figure 3.18, and Figure 3.20, the first partial fields have the appearance of a first mode, or "breathing mode," with one broad maximum region. The second partial fields are divided by a nearly vertical null, with two local maxima on either side. The third partial fields have three local maxima, and so on. (All of the nearly-horizontal nulls at and above 250 Hz are due to interference from the ground reflection, not the PFD.) Recall that the reference array used in this PFD is restricted to a linear region along the ground. When an SVD is taken of the cross-spectral matrix of a linear array, the overall shapes of the singular vectors take on modal characteristics, similar to the shapes of standing waves on a string.[107]

These modal-like shapes are reflected in the partial fields as well. A similar effect was seen in the SVD-based PFD of a jet by Lee and Bolton,[55], where the partial fields took on the appearance of dipole, quadrupole, and octupole sources. This does not necessarily signify that jet sources are actually distributions of mutually incoherent multipoles, but jet noise fields have often been modeled with equivalent source distributions of multipoles since the acoustic analogy model of Lighthill.[3]

3.2.6 Discussion

It has been shown how SVD-based PFD, in conjunction with the virtual coherence function, can be used to estimate the number of independent sources in a field. This is related to the number of reference microphones necessary to perform PFD on measured hologram data prior to the implementation of NAH. Further development of reference microphone requirements is provided in Section 3.3.

The fact that the reference array was insufficient to represent all the information in the field measurement above about 500 Hz limits the accuracy of NAH methods. NAH cannot be used to reconstruct field energy that is missing from the hologram, no matter how accurate the propagation. Hence, NAH results in following chapters are performed at frequencies of 500 Hz and below. It is likely that a distribution of reference microphones around the jet azimuthally, instead of limiting them to a linear array, would improve the results in future measurements.

Finally, although the partial fields from an SVD-based PFD are valid, mutually incoherent components that, in total, represent the sound field, the physical interpretation of these individual fields is tenuous. The sound fields of sources that are characterized by decaying spatial coherence are represented by a modal-like decomposition, rather than a decomposition involving spatial separation of source components. This motivates the use of a secondary PFD method, developed in Chapter 6, which re-decomposes the reconstructed field into partial fields that are physically meaningful.

3.3 Coherence Length as a Figure of Merit

3.3.1 Introduction

Near-field acoustical holography (NAH) requires a spatially coherent hologram to give a successful reconstruction of the sound field. This may be obtained from a simultaneous measurement of all field points. However, hologram measurements often consist of hundreds or thousands of measurement grid points, making the number of field microphones required impractical. In these cases, a scan-based measurement with a small, dense, field array, in combination with a fixed-location reference array, is used. When a sound field is generated by a single, coherent source, only one reference microphone is required to tie the scans together. Hald[63] developed a multireference procedure called Spatial Transformation of Sound Fields (STSF), which is a PFD method to accommodate sound fields of multiple independent (incoherent) subsources. In STSF, a singular value decomposition (SVD) of the cross-spectral matrix of reference pressures can be used as the basis for a linear projection of the field measurement, which results in a set of mutually incoherent partial fields. The incoherent sum of these partial fields represents the total field. Each partial field may then be projected individually using NAH, and summed to provide the total reconstruction. STSF is the method on which the SVD-based PFD method is based, as presented in Section 3.2.

Additional PFD methods have been developed to generate partial fields that can be associated with physical subsources.[108,109] These are most successful when each reference is located as closely as possible to each individual subsource. Kim et al.[64] introduced a method that uses holographic projection to determine the optimal reference locations, and then places a set of virtual references at those locations. However, in the STSF, virtual reference, and all PFD methods, it is important to understand that the physical reference array must completely sense all independent sources to begin with—the number of reference microphones must equal or exceed the number of subsources and each subsource must be sensed by at least one reference—if the

total energy at the hologram is to be represented in the decomposition.[64] In practice, when the subsources are localized or spatially distinct, this requirement is simple to meet.

What is to be done when independent subsources are not localized, such as in the case of an aeroacoustic source? An aeroacoustic source may be considered a continuum of partially coherent subsources, where the number of subsources is ambiguous. Lee and Bolton,[55] Shah *et al.*,[60] Wall *et al.*,[56] and others performed scan-based NAH on jet noise sources. In each of these experiments, the sufficiency of the reference array in completely sensing all subsources was verified after the measurement was taken, using the virtual coherence method.[74,83,110] However, no quantitative guidelines exist in current literature to predict reference-array sufficiency a priori, or guide the design of a reference array when the number and locations of independent subsources are unknown. Although this study is directed toward an application in aeroacoustic measurements, no attempt is made here to model the sound field of an actual aeroacoustic source. Rather, the partial spatial coherence of an aeroacoustic source is represented by a simple array of partially coherent point monopoles.

The purpose of this paper is to present a simple, quantitative figure of merit that yields the inter-microphone spacing necessary, given an array aperture, for the deployment of a sufficient reference array near partially coherent complex sources. This guideline is based on a spatial analysis of the (ordinary) coherence in the region of the source, such as those performed by Wall *et al.*[111] (see Section 3.4), which can be performed with relatively few sensors. From such coherence measurements, an average spatial coherence length in the sound field is determined. The spatial density of microphones in the reference array dictates how many references, on average, are located within an average coherence length. This figure of merit is called "references per coherence length" (RPL_C). Section 3.3 was modified from a 2012 publication in JASA-EL under the title "Coherence length as a figure of merit in multireference near-field acoustical holography."[112]

Section 3.3.2 provides the theoretical basis for the quantity RPL_C. It also provides an explanation of the virtual coherence function, which is used to validate the use of this figure of merit. Section 3.3.3 presents a laboratory experiment. Here, to help the reader develop an intuition for reference array design, some of the effects of reference deployment for a partially coherent source are developed. A numerical experiment, which examines the relation between RPL_C and a sufficient array is described in Section 3.3.4, and the guideline for reference array deployment, based on this experiment, is discussed in Section 3.3.5.

3.3.2 Theory: References per Coherence Length

An analysis of the spatial coherence measured in the geometric near field of partially spatially coherent sources leads to the definition of RPL_C.[75] To obtain a spatial coherence measurement, a linear sensor array (collinear with the eventual location of the reference array) is placed near and along the length of an extended source. Coherence values,[103] $\gamma^2_{z_m,z}$,between a given sensor at a location z_m and all sensors along the array are calculated. From these data, the coherence length, L_C, is determined. Although the term "coherence length" is used in other studies, such as in optical holography applications[113] and underwater acoustics,[114] here it is defined as the spatial distance L_C along the array over which $\gamma^2_{z_m,z}$ drops from unity to some desired threshold. In this paper a coherence threshold of $\gamma^2_{z_m,z} = 0.5$ is used. The value of L_C is assigned to the location z_m of the given sensor. This process is repeated for all N_R sensor locations, resulting in an array of coherence length values, $L_C(z_m)$. The mean of $L_C(z_m)$ over all locations yields the mean coherence length,

$$\langle L_C \rangle = \frac{1}{N_R} \sum_m L_C(z_m)\,, \tag{3.6}$$

which summarizes the spatial coherence of the sound field into a single quantity.

Note that $\gamma^2_{z_m,z}$ generally drops off in both directions of increasing and decreasing z away from z_m, so $L_C(z_m)$ may be calculated in either direction. If the source radiates symmetrically,

then $\langle L_C \rangle$ is the same for either direction chosen. This may not be the case when the sound field is asymmetric.[111]

With $\langle L_C \rangle$ established, references per coherence length is defined as

$$\mathrm{RPL}_C = \frac{\langle L_C \rangle}{\Delta z_R}, \tag{3.7}$$

where the distance Δz_R is the physical spacing between sensors in a reference array. The figure of merit RPL_C quantifies the spatial density of sensors in the reference array in terms of spatial field coherence. As spatial source coherence decreases, $\langle L_C \rangle$ decreases and the number of effective independent subsources increases. A greater number of reference sensors are required to completely sense these subsources so the inter-reference spacing must be more dense (i.e. for a reference array of fixed aperture length, the sensor spacing Δz_R must decrease). The quantity RPL_C takes advantage of the fact that information about the number of independent subsources is contained in $\langle L_C \rangle$. One might expect that the value of RPL_C required for a sufficient reference array is invariant with source coherence, since the necessary Δz_R decreases with decreasing $\langle L_C \rangle$. Such a relationship is demonstrated in this section.

To assess the utility of RPL_C, a quantitative method of determining the sufficiency of a reference array is desired. Therefore, the quantity "mean virtual coherence sum", $\langle \Sigma \tilde{\gamma}^2 \rangle$, is defined. This quantity is calculated after application of the virtual coherence method.[74] In a PFD based on the SVD of the reference cross-spectral matrix, information about noise sources is contained in the ordered, monotonically decreasing singular values, and the remainder contain noise. Theoretically, when there are *S* independent subsources and low measurement noise there will be *S* large source-related singular values. The *S*+1 and subsequent singular values will be relatively small, and are filtered out.

However, in aeroacoustic sources the number of subsources is ambiguous. This is reflected in a more gradual decrease of the ordered singular values with no clear distinction

between source and noise-related singular values.[74,83] Virtual coherence, in conjunction with the STSF method, provides a way to estimate the number of significant partial fields.[63,74] The virtual coherence function,

$$\tilde{\gamma}_{i,j}^2 = \frac{\left|C_{v_i p_j}\right|^2}{C_{v_i v_i} C_{p_j p_j}} \tag{3.8}$$

quantifies the amount of (normalized) coherent energy in the *i*th partial field at the *j*th measurement location. The quantity $C_{v_i p_j}$ is the cross spectrum between the virtual reference pressure, v_i and the field pressure, p_j; $C_{v_i v_i}$ is the autospectrum of the virtual reference pressure; and $C_{p_j p_j}$ is the autospectrum of the field pressure. If the sum of the virtual coherence function over all the partial fields, $\sum_i \tilde{\gamma}_{i,j}^2$, approaches unity for each field location *j*, then the reference array has sufficiently sensed all of the subsources. If a subset of the first *K* partial fields returns a sum that approaches unity for each *j*, then these *K* partial fields fully contain the source information (i.e. $K \geq S$), and the remaining partial fields are discarded. Examples of $\sum_i \tilde{\gamma}_{i,j}^2$ plotted over all *j* are shown by Lee and Bolton (see Ref. 74, Figs. 15 and 17), as well as in Section 3.2.5.

It is useful to collapse the information in the spatial maps of maps of $\sum_i \tilde{\gamma}_{i,j}^2$ to a single number, which has not been done previously. Taking the average over field locations, the "mean virtual coherence sum" is obtained, i.e.,

$$\langle \Sigma \tilde{\gamma}^2 \rangle = \frac{1}{J} \sum_j \sum_i \tilde{\gamma}_{i,j}^2 , \tag{3.9}$$

where *J* is the total number of field measurements. If $\langle \Sigma \tilde{\gamma}^2 \rangle$ approaches unity then it is likely $\sum_i \tilde{\gamma}_{i,j}^2$ is nearly unity for all *j*. Hence, $\langle \Sigma \tilde{\gamma}^2 \rangle$ quantifies the sufficiency of a reference array in this paper. A calculation of $\langle \Sigma \tilde{\gamma}^2 \rangle$ as a function of RPL_C results in an RPL_C criterion for a sufficiently dense reference array regardless of frequency and spatial coherence.

3.3.3 Controlled Physical Experiment

A laboratory experiment was performed to explore the effects of reference microphone number and placement on the ability of a partial field decomposition (PFD) to fully determine source components. The number of discrete sources is represented here by N_Q, and N_R is the number of reference microphones in the array. Recall, in the theory of PFD, that if all N_Q sources are completely uncorrelated, then N_R must be at least equal to N_Q to fully represent the sources. However, if the sources are partially correlated, then it stands to reason that $N_R \leq N_Q$ reference microphones may be required. The following laboratory experiment was performed on carefully controlled discrete sources with varying correlations to test this hypothesis and to develop an intuition for the effect of reference-microphone array design on the quality of NAH source visualization.

3.3.3.1 Experimental Details

Four Mackie HR824 loudspeakers were placed end-to-end and facing upward in the fully anechoic (>80 Hz) chamber at Brigham Young University, which has working dimensions of 8.71 x 5.66 x 5.74 m (see Figure 3.21). The woofers are considered to be the sources, since the frequencies of interest are well below the woofer-to-tweeter crossover frequency of 1800 Hz. The loudspeaker gains were set such that the overall sound pressure levels measured 2 cm above the woofer centers were equal to within a fraction of a decibel. The signal input to the *i*th loudspeaker is represented by q_i. To generate the input signals, four bandlimited white noise signals with normalized distributions, called the "primary" signals and denoted by s_i, were mixed according to the following formula:

$$q_1 = s_1 ,$$

$$q_i = \frac{q_{i-1} + b \times s_i}{1 + b}, \text{for } i = 2, \ldots, N_Q , \tag{3.10}$$

where b is called the correlation factor. The relationships among the loudspeaker input signals could therefore be varied from fully correlated ($b = 0$) to uncorrelated ($b \to \infty$, such that $q_i = s_i$). Allowing b to have a finite value resulted in a set of sources with partial correlation. Several different source correlation conditions were explored: fully correlated ($b = 0$), highly correlated ($b = 0.3$), moderately correlated ($b = 1$), and uncorrelated (all source input signals were independent). To illustrate the effect of b on source correlations, Figure 3.22 shows the correlation coefficients, ρ_{1i},[63] between the first input signal, q_1, and all other input signals as b is varied. Each curve gives a sense of how related all the sources are to the first source.

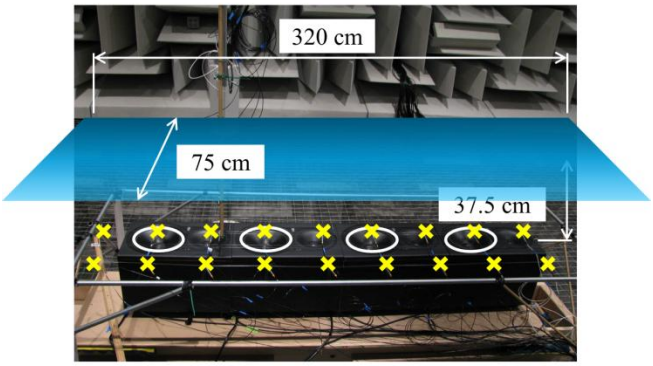

Figure 3.21 Physical experimental setup showing woofers (circles), the hologram surface 37.5 cm above the loudspeaker box faces (not to scale), and the reference microphone array 2 cm above the loudspeaker box faces (each reference is denoted by an "x").

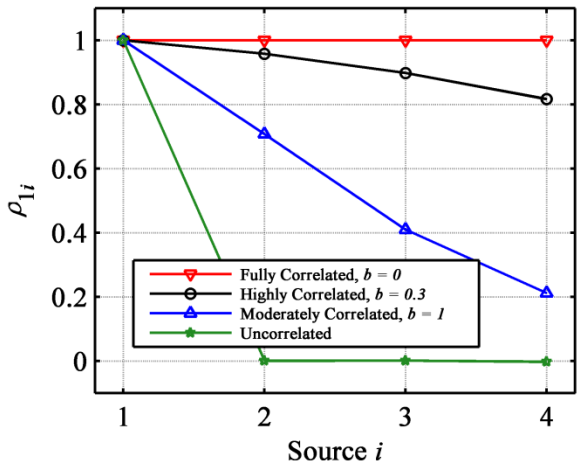

Figure 3.22 Correlation coefficient between the first loudspeaker input signal and all other input signals, for several correlation conditions.

The transducers used in the hologram measurement and reference array were 6.35 mm (1/4 in) G.R.A.S Type-1 prepolarized microphones. A single microphone, controlled by an automated scanning system, traversed an 11 x 13 grid with equal 7.62 cm (3 in.) spacing to record time waveforms of sound pressures on a horizontal plane 37.5 cm above the faces of the loudspeakers. This scan-based measurement was used as the hologram surface. A second microphone recorded sound pressures on an equivalent grid, but at a distance of 7.5 cm above the loudspeaker faces. These pressure values were used for a benchmark comparison. A set of fixed reference microphones recorded sound pressures simultaneously with each scan. One reference microphone was placed directly over the center of each woofer in a plane 2 cm above the faces of the loudspeaker boxes. An additional 14 reference microphones were placed in the same horizontal plane to give the overall 2 x 9 reference array shown in Figure 3.21. All time data were recorded at a sampling frequency of 16,384 Hz with five seconds per scan. The time data were then broken up into 18 blocks (to allow for coherence calculations[103]), an eight-point Tukey window was applied to each block, and a Fourier transform of each block was calculated to obtain complex pressure values as a function of frequency.

On a single-frequency basis, a PFD of the complex pressures from each scan was used to generate a coherent hologram, using SVD-based PFD. This provides insight on the number of subsources in an extended, partially correlated source, for which such information is ambiguous (i.e. in a jet). All or some subset of the reference array described above was used in this decomposition. (Important details of the reference selection are discussed in Section 3.3.3.2.) Cross-correlations between the virtual references and the scan-based hologram measurements were used to generate a set of self-coherent partial fields, the sum of which make up the total hologram. Because these partial fields are mutually incoherent, the summation of partial fields is carried out on an energy basis.

A projection was made of each partial field individually from the hologram plane to the reconstruction plane, 7.5 cm above the loudspeakers, using planar statistically optimized near-field acoustical holography (SONAH).[54] SONAH was chosen because it avoids the requirements that the hologram measurement fully cover the source area and that the measurement grid be regularly spaced. These requirements were easily met for the sources measured in this study but are often impractical for large sources such as jets. To remove high wavenumber components below the measurement noise floor, modified Tikhonov regularization with generalized cross validation was employed.[115] The reconstructed partial fields were then summed on an energy basis and the total reconstruction was compared with the benchmark measurement at that location.

An illustration of the experimental process is given in Figure 3.23 for the 900 Hz uncorrelated source condition. In Figure 3.23a the measured sound pressure levels (SPLs) at the hologram plane are shown, averaged over all blocks. Notice that the data are rather noisy due to source nonstationarity and the limited number of averages used. This was done intentionally to test the source nonstationarity compensation method described by Lee and Bolton.[74] Figure 3.23b shows the sum of the partial fields generated with the virtual coherence method. All 18 reference microphones were used. The SPLs resulting from SONAH propagation to the

reconstruction plane are shown in Figure 3.23c. Figure 3.23d is the benchmark measurement of SPLs made at the same location as the reconstruction plane, calculated as the sum of the partial fields generated from the direct measurement at 7.5 cm. The purpose of using the partial-field sum as a benchmark was to remove source nonstationarity effects. The SPLs along the horizontal centerlines ($y = 0.46$ m) of Figure 3.23a-d are given in Figure 3.23e. The results show that with a suitable reference array (and having met the requirements for NAH) the processing methods used may produce an accurate source visualization. This allows for investigation of the effects of varying the reference array design.

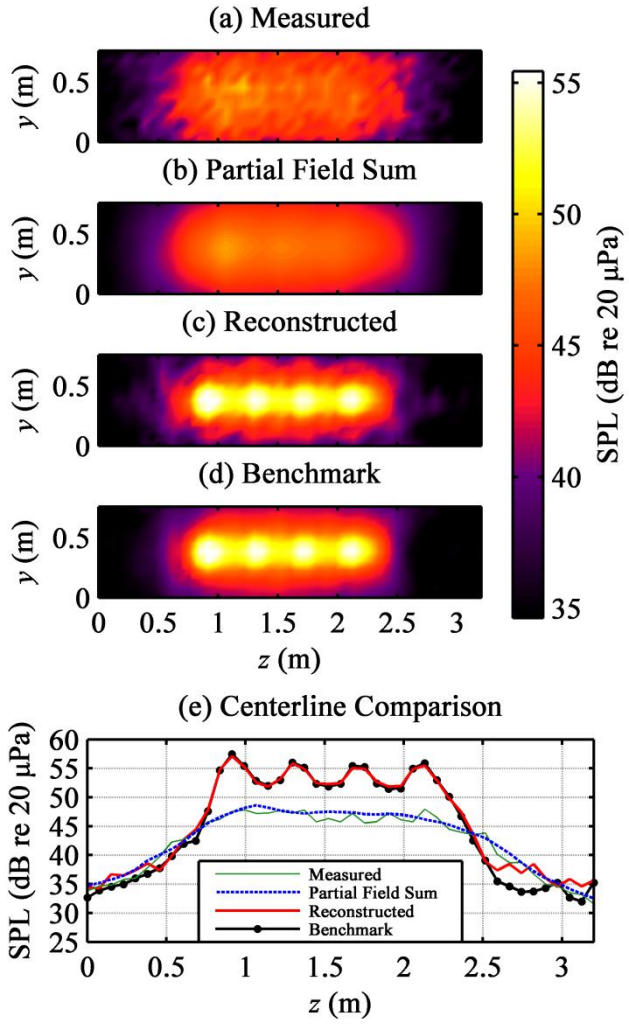

Figure 3.23 Holographic visualization of four uncorrelated loudspeakers at 900 Hz. (a) Measured SPLs at the hologram plane, averaged over all blocks. (b) Sum of the partial fields calculated at the hologram plane. (c) Total SPLs propagated to the reconstruction plane. (d) Sum of partial fields calculated from direct measurements at the reconstruction plane (benchmark). (e) Comparison of the above results at y = 0.46 m (1.5 ft.).

3.3.3.2 Reference Microphone Number and Locations

It is critical to understand that the reference array must be adequately designed such that all subsources are accounted for (i.e. the basis set of partial fields must be complete). The virtual coherence function is a useful metric for evaluating the reference-array design (see Section 3.3.2). If there are enough partial fields to fully determine the sound field at a given location,

then the sum of the virtual coherence function over all partial fields approaches unity at that location. In theory, if N_R is sufficiently large, and if the members of the reference set together sense all sources, then there are a sufficient number of partial fields for all locations.

This laboratory experiment was designed to allow for an investigation of reference-microphone number and location requirements for given source correlation properties. The experimental process explained in the previous section was repeated for the four degrees of correlation shown in Figure 3.22, and for different values of N_R. Instead of using all 18 reference microphones, subsets of one, two, three, and four microphones were selected in all possible combinations, and the resulting PFD was applied to the scan-based hologram measurement. Table 3.1 gives the $\langle \Sigma \tilde{\gamma}^2 \rangle$ values averaged over all combinations, as well as the lowest and highest values of $\langle \Sigma \tilde{\gamma}^2 \rangle$, as a function of correlation condition and N_R. If the sources are fully correlated, or if $N_R = 4$, then $\langle \Sigma \tilde{\gamma}^2 \rangle$ is close to unity. As source correlation drops and as N_R is decreased, $\langle \Sigma \tilde{\gamma}^2 \rangle$ decreases.

Table 3.1 Mean virtual coherence sum values $\langle \Sigma \tilde{\gamma}^2 \rangle$ averaged over all possible reference microphone combinations, as a function of number of references N_R and correlation condition b, for 900 Hz. Shown in parenthesis are the lowest and highest $\langle \Sigma \tilde{\gamma}^2 \rangle$ values resulting from all possible combinations.

N_R	Uncorrelated	Moderately correlated $b = 1$	Highly correlated $b = 0.3$	Fully Correlated $b = 0$
1	0.354 (0.223,0.431)	0.595 (0.410,0.697)	0.882 (0.812,0.910)	0.998 (0.997,0.998)
2	0.620 (0.456,0.724)	0.811 (0.670,0.892)	0.951 (0.907,0.975)	0.999 (0.998,1.000)
3	0.829 (0.718,0.894)	0.928 (0.819,0.968)	0.980 (0.949,0.992)	0.999 (0.999,1.000)
4	0.988 (0.823,0.999)	0.988 (0.902,0.999)	0.993 (0.966,0.999)	0.999 (0.999,1.000)

These trends are insightful, but the results may be extended to give an indication of the quality of NAH reconstruction as a function of reference array design. To demonstrate how NAH results relate to reference selection, centerline reconstructions generated with the use of

several reference configurations are shown in Figure 3.24, along with their respective benchmark measurements. Figure 3.24a is a simplified schematic of the four woofers and the relative locations of the eighteen reference microphones (see also Figure 3.21) to assist the reader in the discussion of reference configurations below. Figure 3.24b-d show the centerline reconstruction SPLs related to select reference configurations for uncorrelated, moderately correlated, and highly correlated loudspeaker conditions, respectively.

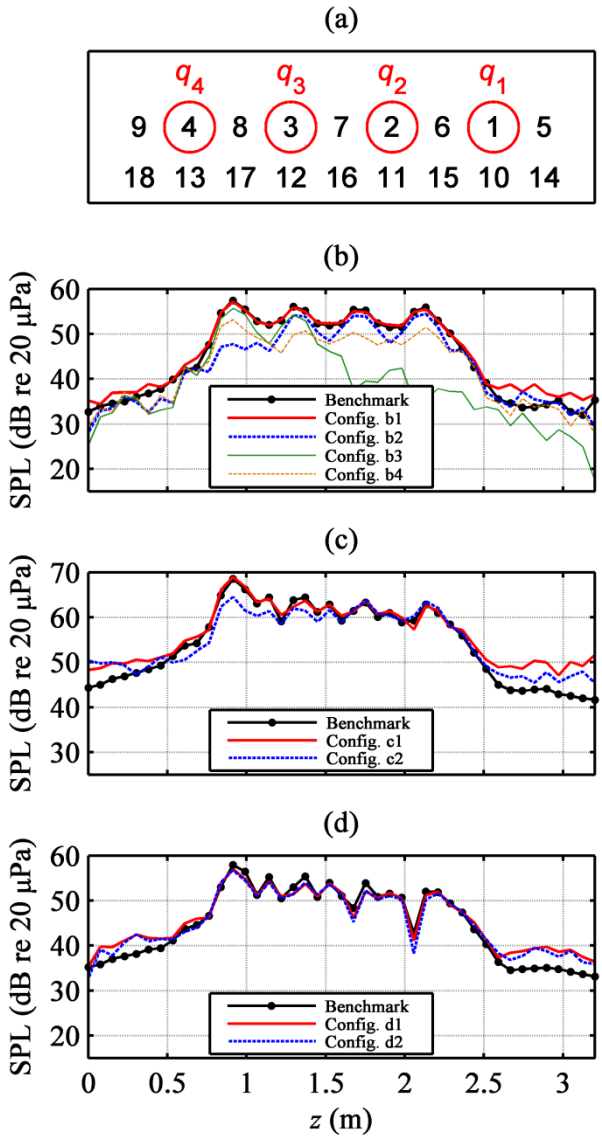

Figure 3.24 (a) Top-view schematic of microphone locations relative to four woofers (not to scale). Reconstructed centerline SPLs at 900 Hz are shown for the (b) uncorrelated, (c) moderately correlated, and (d) highly correlated loudspeakers, each with benchmark measurements. Each configuration represents select combinations of reference microphones as explained in the text.

In Figure 3.24b, reference configuration b1 might be considered an ideal reference array for four uncorrelated sources: it consisted of reference microphones 1, 2, 3, and 4, which were placed directly above each woofer. The corresponding reconstruction matches the benchmark closely in both source location and level. Many combinations of four references give similar

results, but, due to the finite spatial coherence of the uncorrelated loudspeakers, not all configurations are acceptable. Configuration b2 represents reference microphones 2, 11, 14 and 15, which returned the lowest $\langle \Sigma \tilde{\gamma}^2 \rangle$ value reported in Table 3.1 for the uncorrelated-loudspeaker, four-reference case. All these references were located on one side of the sources. With this configuration the holographic projection successfully located three woofers, but almost completely missed the woofer with input signal q_4.

Selecting fewer than four references when the loudspeakers are uncorrelated provides some insight about the effect of reference locations when N_R is insufficient. In Figure 3.24b, only references 3 and 4 were used for configuration b3. Thus, the woofers with input signals q_3 and q_4 were well localized. Two reference microphones were also chosen for configuration b4, namely 6 and 8. Each of these was placed between two woofers and it seems they captured nearly equal amounts of energy radiating from all four sources. The source levels were underestimated, but all sources were localized.

Reconstructions shown in Figure 3.24c-d demonstrate that references numbering fewer than the discrete physical sources are able to sufficiently decompose the subsources if they are partially correlated. This means there are fewer independent subsources than physical sources. Figure 3.24c gives reconstructions of the moderately correlated woofers. (Note that there are SPL peaks between the main source peaks, due to partially coherent interference.) Configuration c1 consisted of reference microphones 6 and 18, and returned the highest $\langle \Sigma \tilde{\gamma}^2 \rangle$ value for two references, reported in Table 3.1. These microphones seem to have been located well enough to capture energy from all sources, and they reconstructed most peak locations with accurate levels. The lowest value of $\langle \Sigma \tilde{\gamma}^2 \rangle$ calculated using two references was returned by reference microphones 1 and 2, represented by configuration c2. Figure 3.24d shows reconstructed SPLs of the highly-correlated woofers. Configuration d1 (reference microphones 6 and 8) and configuration d2 (reference microphones 10 and 11) returned the highest and lowest $\langle \Sigma \tilde{\gamma}^2 \rangle$ values generated with two references, respectively. Here, the difference between the two

reconstructions is quite small. The results of Figure 3.24c-4d show that the partially correlated loudspeakers may be accurately visualized using only two references in the PFD in spite of the fact that four independent signals were mixed to generate the source.

3.3.3.3 Numerical Validation

A numerical experiment was performed that was identical in every way to the physical experiment described above, except that the loudspeakers (woofers) were replaced with ideal point sources. When the references were placed in the same locations as those in the physical experiment, $\langle \Sigma \tilde{\gamma}^2 \rangle$ value trends were very similar to those reported in Table 3.1. This verified that numerical experiments involving arbitrarily correlated sources reflect physical results. Multiple simulations of a large number of sources can therefore be carried out much more efficiently than additional laboratory experiments, and these are discussed in Section 3.3.4, where quantitative guidelines for reference arrays are developed.

In additional numerical experiments the locations of four simulated reference microphones were varied to extremes with respect to the sources. In the limit as the combined distance between microphones went to zero, the one-reference-microphone configuration was approached (i.e. all the measured pressures became too correlated). In this limit, the PFD could not decompose the source into more than one independent subsource, and results were poor. Results were also poor when the references were at great distances from each other and from the source, because in this limit the four subsources appeared to be a single point source from the perspective of the references. Therefore, the necessary guidelines for successful PFD are that the references should not be placed so far from the source that the source appears point-like to the references, nor should the references be placed so close together that they approach a single point measurement. In holographic measurements of discrete sources, these requirements are likely easily satisfied. For application to noncompact, partially correlated sources, further investigations are required to develop quantitative reference array guidelines.

3.3.4 Numerical Experiment Setup: A Spatially Noncompact Source

To investigate the relationship between RPL_C and $\langle \Sigma \tilde{\gamma}^2 \rangle$, a numerical experiment was performed in which an approximately continuous, partially coherent source was generated one frequency at a time. See Figure 3.25 for a schematic. An array of $N_Q = 1000$ point monopoles, marked by red circles, were spaced evenly along the *z*-axis between $z = 0.9$ and 2.1 m with an inter-source separation of *d* such that $kd \ll 1$, *k* being the acoustic wavenumber. A "primary" complex vector, $\hat{s}_1$, was generated of complex numbers with unit magnitude and random phase. This vector defined the amplitude of the first monopole source, i.e., $\hat{q}_1 = \hat{s}_1$. Subsequent source amplitudes were defined by

$$\hat{q}_n = \frac{\hat{q}_{n-1} + b \times \hat{s}_n}{\|\hat{q}_{n-1} + b \times \hat{s}_n\|_2}, \text{ for } n = 2, \ldots, N_Q \tag{3.11}$$

where $\hat{q}_{n-1}$ were the complex amplitudes of the previous source, $\hat{s}_n$ were newly generated random complex values, and the coherence factor *b* dictated the portion of new, random energy that was added to the previous source vector. Division by the L2 norm, $\|\cdot\|_2$, of the total complex vector ensured that all monopole magnitudes were unity. The result was a line array of monopoles with normalized magnitude, comprising a partially coherent source. The spatial coherence properties of this source, and consequently the radiated field, depend on the coherence factor, *b*, and on frequency, *f*. For example, a *b* value of zero results in a perfectly coherent source, and as *b* approaches infinity the sources becomes completely incoherent.

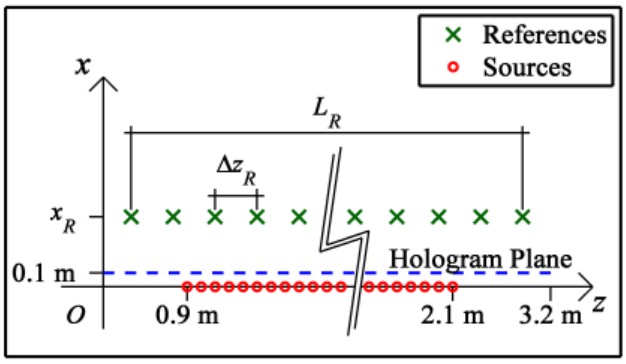

Figure 3.25 Schematic of relative locations of sources, references, and the hologram plane for the numerical experiment (not to scale).

A scan-based measurement of the sound field was simulated by propagating sound pressures from the monopoles to the measured hologram using the free-space Green's function. The measurement grid was 10 cm from the sources and consisted of a linear array of 11 receivers, placed at 43 locations, to generate a hologram of 11 x 43 points with equal 7.62 cm (3 in.) spacing. Its location is marked by the blue dashed line in Figure 3.25. An infinite signal-to-noise ratio (SNR) was assumed in the measurement. The holographic projection of these data was not carried out in this work. Rather, the hologram data serve as the field pressures for which the reference array sufficiency is determined. When a reference array sufficiently senses all sources, then all energy in the field measurements is represented in the partial field decomposition.

The reference array, shown by the green "x" symbols in Figure 3.25, was placed at a standoff distance of $x_R = 0.3$ m from the source, with an aperture that spanned from $z =$ 0.3 to 2.7 m (twice the length of the source), and with variable spacing, Δz_R, as illustrated in Figure 3.25. With the fixed aperture length, L_R, Δz_R depended on the number of references, N_R.

The simulated scan-based measurement of the partially coherent source was repeated as f was varied from 0.1 to 10 kHz, b was varied from 0.01 to 10, and RPL_C was varied from 0.2 to 2. The analysis for each parameter set proceeded as follows. 1) From the L_C values found in the

direction of increasing z, $\langle L_C \rangle$ was calculated. 2) Reference sensor spacing Δz_R was determined for a given RPL_C value using Eq. (3.7). 3) A PFD of the sound field was performed using a reference array with spacing Δz_R. 4) The mean virtual coherence sum, $\langle \Sigma \tilde{\gamma}^2 \rangle$, was calculated to determine reference-array sufficiency. Results of this experiment are reported in the following section.

3.3.5 Results

Figure 3.26 shows examples of coherence $\gamma^2_{z_m,z}$ as a function of z, referenced to two values of z_m, and for 300 Hz and 900 Hz. The coherence factor was $b = 0.05$. Note the locations where $\gamma^2_{z_m,z} = 0.5$, which value was used previously to define L_C. The values of L_C tend to be smaller for large f and lower b. This trend also holds true for $\langle L_C \rangle$. It is also important to note that $\langle L_C \rangle$ depends somewhat on the reference-array aperture; calculated coherence lengths vary over location and can become large far from the source.

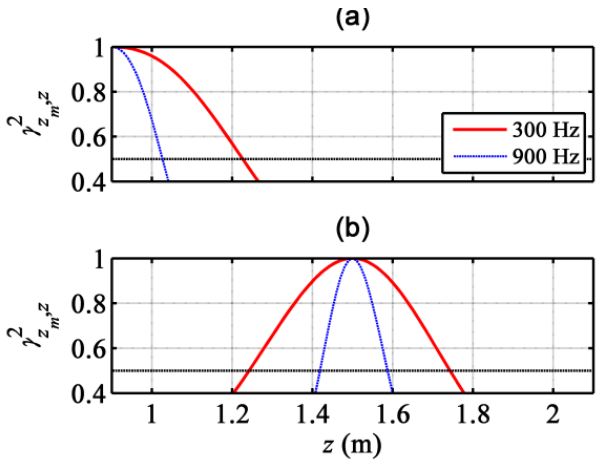

Figure 3.26 Near-field coherence values (along the reference array) for a source with a coherence factor b = 0.05 (a) calculated between z_m = 0.9 m and all other z values, and (b) calculated between z_m = 1.5 m and all other z values. Also shown are dashed horizontal lines denoting a coherence value of 0.5.

The values of $\langle \Sigma \tilde{\gamma}^2 \rangle$ are plotted against N_R in Figure 3.27a for two frequencies (300 Hz and 900 Hz), and two b values: 0.05 for the highly coherent case and 10 for the highly incoherent

case. For the purpose of comparison, $\langle \Sigma \tilde{\gamma}^2 \rangle \geq 0.99$ is considered to be "sufficient" in sensing all subsources. The minimum N_R at which this occurs is represented by $\widetilde{N}_R$, the critical number of reference microphones. Figure 3.27a illustrates how $\widetilde{N}_R$ depends on both *b* and *f*, although it is far more sensitive to *f* than to *b* in this case. In general, it is difficult to predict the sufficiency of a reference array for an arbitrary source configuration based on an analysis of $\langle \Sigma \tilde{\gamma}^2 \rangle$ as a function of N_R.

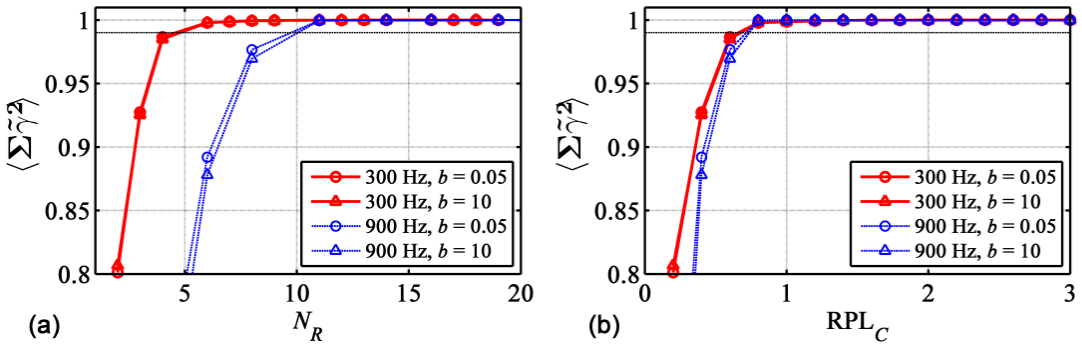

Figure 3.27 The mean virtual coherence sum, (a) as a function of the number of references, N_R, for two frequencies and two different coherence factors, b, and (b) the mean virtual coherence sum as a function of the new figure of merit, reference microphones per coherence length, RPL_C, for the same parameters.

The figure of merit RPL_C provides an alternative way to view these data that shows a more consistent trend. The data in Figure 3.27a are shown again in Figure 3.27b, but this time they are plotted against RPL_C. Note how the curves now more closely collapse, and $\langle \Sigma \tilde{\gamma}^2 \rangle$ exceeds 0.99 above $\mathrm{RPL}_C \approx 1$. For all *f* and *b* tested in this work, with the definition of $\langle L_C \rangle$ given in Sec. II, one reference microphone per coherence length ($\mathrm{RPL}_C = 1$) is considered sufficient to fully decompose the subsources.[75,116] Hence, RPL_C, as defined in Sec. II, is a useful figure of merit when source coherence properties or the number of independent subsources is ambiguous. It should be noted that, although the criterion $\mathrm{RPL}_C = 1$ may be intuitive, it is dictated by the definition of the coherence length, L_C, which in turn is dictated by the coherence threshold. For example, a coherence threshold of $\gamma^2_{z_m,z} = 0.8$ resulted in a criterion of $\mathrm{RPL}_C =$

0.2 for the same experiment.

It is important to understand the extent to which $\mathrm{RPL}_C = 1$ is a reasonable guideline. This guideline can become invalid when test parameters are varied to the extreme. As one example, decreasing b to smaller orders of magnitude than those shown here results in a highly coherent source, with long coherence lengths, and the calculation of RPL_C becomes unreliable. However, in this case, only one or two references are needed, eliminating the utility of such an analysis. For all practical realizations of source coherence and frequency $\mathrm{RPL}_C = 1$ is quite robust.

To test the robustness of $\mathrm{RPL}_C = 1$, the experiment was repeated with $b = 0.05$, $f = 900$ Hz, and with a varying reference array aperture and standoff distance. The criterion $\mathrm{RPL}_C = 1$ was used to determine Δz_R. First, $\langle \Sigma \tilde{\gamma}^2 \rangle$ was calculated as a function of x_R for $L_R = 2.4$ m (twice the source length) and then as a function of L_R for $x_R = 0.3$ m. The results are shown in Figure 3.28. Note that $\langle \Sigma \tilde{\gamma}^2 \rangle > 0.99$ for a range of $x_R = 0.1$ to 1.1 m in Figure 3.28a and for a range of $L_R = 1.2$ to 4.0 m in Figure 3.28b. This suggests that $\mathrm{RPL}_C = 1$ results in a sufficient reference array for a wide range of apertures and standoff distances. Extreme values of L_R and x_R can cause the $\mathrm{RPL}_C = 1$ guideline to break down, such as moving the reference array far from the source. However, this experiment shows that a reference-array design that satisfies $\mathrm{RPL}_C = 1$ based on a rudimentary knowledge of the source location and extent sufficiently senses all subsources.

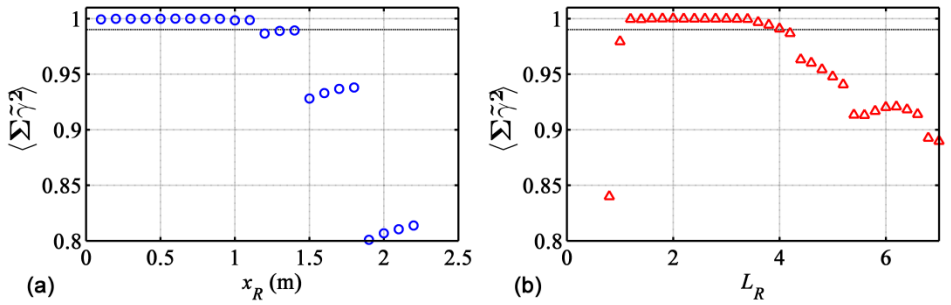

Figure 3.28 The mean virtual coherence sum, for f = 900 Hz and b = 0.05 (a) as a function of standoff distance of the reference array from the source, x_R, with a fixed reference aperture L_R = 2.4 m, and (b) as a function of L_R with a fixed x_R = 0.3 m. Reference spacing Δz_R was always determined such that $\mathrm{RPL}_C = 1$.

3.3.6 Discussion

A useful figure of merit for predicting a sufficient inter-microphone spacing of a reference array, deployed near a partially spatially coherent, extended source for the application of partial field decomposition (PFD) and near-field acoustical holography (NAH) methods, has been introduced. This quantity, "references per coherence length" (RPL_C) can be calculated from simple coherence measurements near the source. It has been shown that if microphones are placed such that there is one reference per coherence length, according to the definition of RPL_C given here, all independent subsources will be sufficiently sensed. This has been shown to be a robust guideline regardless of frequency, spatial source coherence, reference aperture, and standoff distance, over a broad range of these parameters.

There exist a myriad of additional source and measurement configurations to which such an RPL_C study can be applied to further ensure that $\mathrm{RPL}_C = 1$ is a robust criterion. Future investigations could include the effects of amplitude-weighted sources and the directional radiation due to phase shading, and measurement noise. In addition, the validity of $\mathrm{RPL}_C = 1$ to aeroacoustic or other physical, partially coherent sources needs to be investigated. This is performed for the full-scale jet experiment in the following section.

3.4 On Coherence Lengths and Reference Array for the Full-scale Jet

3.4.1 Introduction

Near-field coherence measurements can lead to a greater understanding of a source when its properties are unknown, such as in aeroacoustic noise. Jet noise is predominantly represented with two distinct source types: fine-scale turbulence structures and large-scale turbulence structures.[7,15,17] The fine-scale turbulence tends to be made of many independent structures that radiate sound omnidirectionally. However, there is significant spatial coherence along the jet axis due to the physical extent of the large-scale structures, particularly at low frequencies.[10] This leads to highly coherent, directional noise radiation.

The large spatial extent of these sources has important implications for the type of acoustic measurement performed. Acoustical inverse methods, such beamforming[23,32] and other far-field methods,[15,27,28] have often been employed to measure source strengths, size, and distribution within the turbulent flow. However, these methods have been shown to perform poorly for spatially noncompact, correlated sources.[30,31] This is why NAH is being explored as a jet noise visualization technique in the current work.

The purpose of this section is to address the utility of measuring coherence length—a metric that summarizes spatial coherence information—in the geometric near field of jet noise sources. This section also serves to validate the utility of the figure of merit references per coherence length, discussed in the previous section, in the assessment of the reference array design for a full-scale jet. Section 3.4 was modified from a 2011 publication in *Proceedings of Meetings on Acoustics* under the name, "On near-field acoustical inverse measurements of partially coherent sources."[111]

Section 3.4.2 reviews the theory of coherence length measured in the geometric near field. A brief summary of the full-scale jet experiment, which focuses on the reference array measurements, is given in Section 3.4.3. In addition, a numerical experiment in which coherence

lengths are measured near a line array of uncorrelated monopoles is described. Results of the coherence length measurements for the full-scale jet and for the numerical source are compared, and an analysis of the references per coherence length metric is provided in Section 3.4.4. Section 3.4.5 discusses the implications of these results on the NAH experiment of the jet.

3.4.2 Theory

A useful metric for examining near-field coherence is the coherence length, here defined as the distance (parallel to the extent of a long source) over which the coherence function, γ^2,[103] drops from unity to a value of 0.5.[75,114] To determine the coherence length, L_C, the coherence between a single reference transducer and all other transducers in a linear array are calculated. The physical distance between the reference transducer and the transducer (in the upstream direction of propagation) at which coherence falls below 0.5 is L_C, and this value is assigned to the physical location of the reference transducer.

For example, if the coherence function across an array varies like a Rayleigh curve, as shown in Figure 3.29, then L_C is given by the distance indicated, which is about 2 m. As is often the case, a coherence length can be calculated in the two opposite directions. When this occurs, the value measured in one direction or the other, or an average of these two values can be used to determine the coherence length.[116] Here, in this work, L_C is defined in the direction of decreasing *x*.

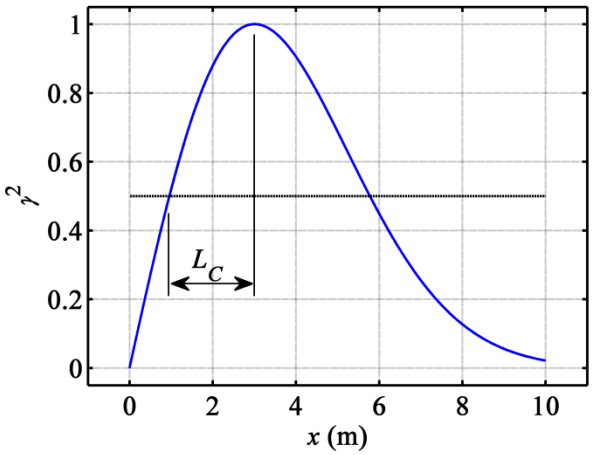

Figure 3.29 An example coherence length measurement, L_C, for an arbitrary spatial coherence measurement referenced to a pressure at x = 3 m.

3.4.3 Experiment

A brief summary of the measurement—focusing on the ground-based microphone array—is given here. A more complete description of the holographic measurement is provided in Section 2.2. Fifty microphones (shown in Figure 3.4) were placed on the ground with 0.61 m (2 ft.) spacing, spanning more than 30 m and running parallel to the jet flow of an F-22A Raptor, at a perpendicular distance of 11.7 m from the jet centerline. A top-view schematic of the location of the reference microphone array relative to the aircraft and jet is shown by the blue dots in Figure 3.30. Complex sound pressures were measured over a broad range of frequencies, and from these L_C values were calculated at all measurement locations along the array. In addition, planar measurements of sound pressures were taken in the vicinity of the jet. For this section, the surface called "plane 2" in Figure 3.30 is of particular interest.

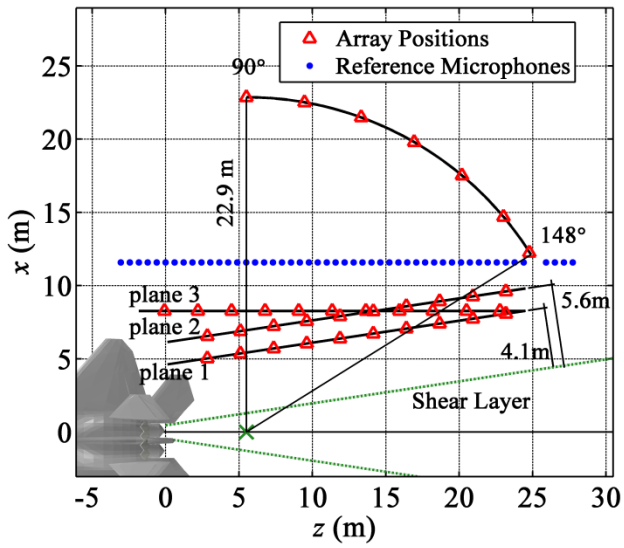

Figure 3.30 Schematic of the measurement locations, relative to the aircraft. The estimated shear layer boundary is marked by green dashed lines, and the green "x" delineates the estimated maximum-noise-source region and the center of the arc.

A second experiment was performed on an extended numerical source. This source was not designed to model actual jet noise, but rather to draw a comparison between near-field coherence properties of the jet and an uncorrelated source array. The source was comprised of a line array of 151 uncorrelated monopoles at a height of $y = 1.9$ m, spaced 0.1 m apart (closely spaced relative to wavelengths of interest) and extending from 0 to 15 m in the positive z direction. This corresponds to the location of the jet centerline on the F-22A Raptor, as shown in Figure 3.31. The measured sound pressures were simulated in the same relative locations as the ground-based microphone array using propagation via the free-space Green's function. Similar to the physical experiment, L_C values were calculated at all measurement locations along the simulated array.

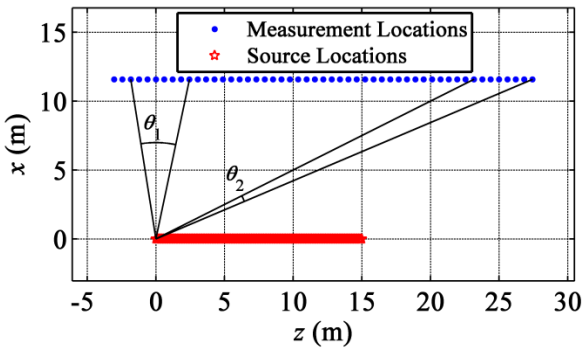

Figure 3.31 Top view schematic of the measurement array location relative to the uncorrelated line array of 151 monopoles. Measurement locations are marked by blue dots. The array is located 11.7 m from the source array.

3.4.4 Results

Coherence function values, γ^2, were calculated across the reference array for the jet experiment, referenced to the pressure measured by a single transducer on the array at $z = 14.6$ m. The aircraft was operating at military engine conditions. The values calculated for γ^2 at 120 Hz are shown in Figure 3.32. These data represent well the trends seen in all geometric near-field γ^2 measurements of the jet: coherence decays away from the reference location and the curve is typically asymmetric. The resulting coherence length of $L_C = 5.7$ m, assigned to this frequency and location, is also illustrated.

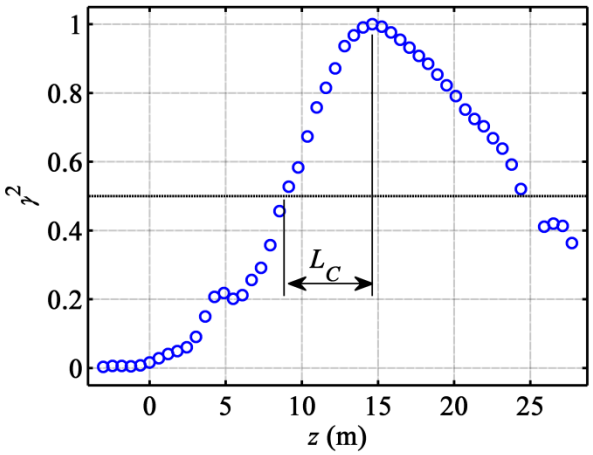

Figure 3.32 Coherence values at 120 Hz calculated between the pressure measured at z = 14.6 m and all measurements along the microphone array with the aircraft operating at military engine conditions. The physical distance representing the coherence length of 5.7 m, assigned to the transducer at z = 14.6 m, is marked.

The sound pressure levels (SPLs) over a broad range of narrowband frequencies, measured along the microphone array, are shown in Figure 3.33a. The respective L_C values are plotted in Figure 3.33b. Note that the L_C values tend to increase both with decreasing frequency and greater distance downstream (larger z). This is consistent with the idea that the jet is comprised of a greater number of independent sources with increasing frequency; information about the number of sources is contained in the comparison of a coherence length to the spatial extent of the high-amplitude region. Coherence lengths are very large—greater than 10 m—beyond $z = 20$ m and below about 100 Hz. The regions of largest L_C values in Figure 3.33b tend to correspond to the regions of highest SPL in Figure 3.33a.

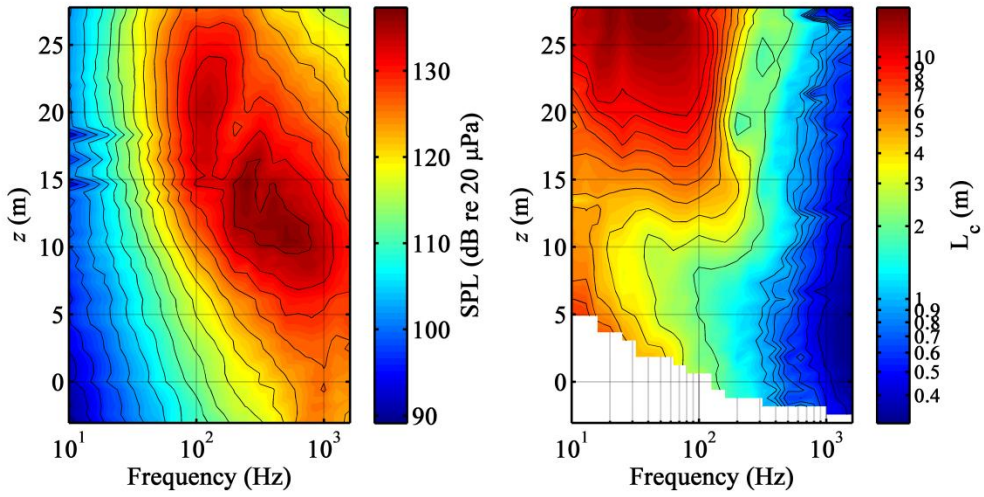

Figure 3.33 (a) SPLs measured by the ground-based microphone array running parallel to and 11.7 m from the centerline of the jet on the F-22 Raptor, operating at military engine conditions. (b) Calculated coherence lengths along the microphone array.

Long, coherent sources lead to large coherence length measurements in the geometric near field. The high spatial extent of the large-scale turbulence structures predicted in the two-source model[10] is therefore reflected in the regions of large L_C at low frequencies, shown in Figure 3.33b. This suggests that the lowest frequency sources, likely generated by the large-scale turbulence structures, exhibit the highest spatial coherence.

While the general trend is that L_C increases gradually with distance downstream, there is a sharp rise in L_C near $z = 15$ m for all frequencies below 200 Hz in Figure 3.33b. There are also high levels measured below 200 Hz and past $z = 15$ m, displayed in Figure 3.33a. This is because the large-scale structures tend to radiate in a preferred downstream direction that is fairly constant over this frequency range.[117]

It is instructive to consider the two limits of spatial source coherence, and their effect on the radiated sound field. First, a perfectly coherent source produces a perfectly coherent field, resulting in an infinite coherence length at all locations. The numerical experiment on an array of completely independent sources provides an example of the opposite limiting case. The L_C values are plotted as a function of frequency and location in Figure 3.34b. (Between these two

extremes lies the case of a partially coherent source.) As with the jet data, L_C for the numerical source tends to increase as frequency decreases and with increasing distance "downstream." Since the overall trends in L_C values for the uncorrelated numerical case match those of the jet data, the majority of the radiated jet noise field above about 200 Hz and upstream of $z =$ 5 or 10 m is probably generated by sources of low spatial coherence, i.e. fine-scale turbulence.

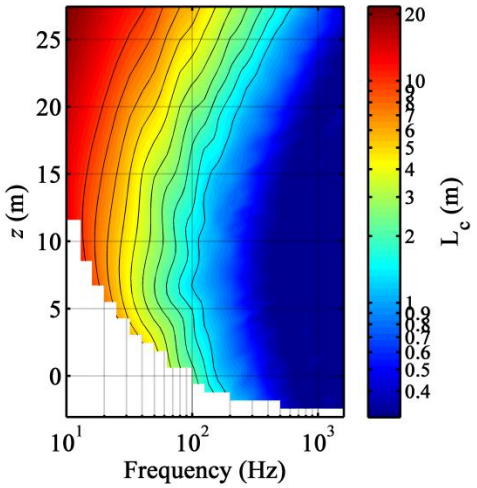

Figure 3.34 Calculated coherence lengths along the simulated measurement array.

An important difference in the numerical experiment is that there is no abrupt onset of high L_C values at $z = 15$ m. Trends over all frequencies and locations vary smoothly. Since the numerical source is spatially incoherent, this further supports the idea that the locations and frequencies with high amplitudes in Figure 3.33a, which correspond to relatively high L_C values Figure 3.33b, are dominated by radiation from a spatially coherent source, i.e. large-scale turbulence structures.

Note that regions of small L_C values in Figure 3.34 occur at $z = 7.5$ m, which location corresponds to the center of the source array. All levels and coherence lengths at other locations are symmetric about this central distance. Thus, small coherence lengths give an indication of

the center of a distribution of incoherent sources. An important factor that influences the values of L_C is the fact that microphones near the end of the array are receiving the sound wave "end on" from a long, narrow source region. In other words, the arriving wave approaches a grazing incidence along the array far downstream. Figure 3.31 illustrates this concept. Here, two sets of eight microphones are selected from the simulated measurement array: one set near the first source and another far downstream. The angle θ_2 "covered" by the latter set is significantly smaller than the angle θ_1 covered by the former. The result is that L_C values increase with distance from the source region as a result of simple geometry, independent of source coherence.

The effects of measurement geometry—isolated from the effects of source coherence—are further demonstrated by the numerical experiment. Recall that the source is composed of a series of uncorrelated monopoles. Therefore, the increase of L_C with distance downstream in Figure 3.34b is a result of geometry. It is important to realize that measurement geometry effects must be carefully considered when using near-field coherence lengths to make inferences about source coherence properties. This does not rule out using L_C as an indicator of source coherence. On the contrary, the relatively large yet finite coherence lengths in Figure 3.33b, compared to those in the numerical experiment, point directly to a partially coherent source.

The final investigation of this chapter is to verify the guideline of one reference microphone per coherence length as developed in Section 3.3. Figure 3.35a shows the mean virtual coherence sum, $\langle \Sigma \tilde{\gamma}^2 \rangle$, as a function of frequency and the number of reference microphones used in the PFD, for military power. In the calculation of these values it was always ensured that the subset of references chosen from the 50-channel array were spaced as close to evenly as possible, and spanned the extent of the entire array. Note that between 10 Hz and 100 Hz, an increase in reference microphones from 2 to 4 results in an increase of $\langle \Sigma \tilde{\gamma}^2 \rangle$ from near zero to more than 0.9. With a further increase in the number of references $\langle \Sigma \tilde{\gamma}^2 \rangle$ "plateaus," gradually increasing toward unity. This suggests that, at low frequencies, the jet may be considered to consist of about four sources, based on the $\langle \Sigma \tilde{\gamma}^2 \rangle$ criterion of 0.9. For the same

data, plotted against frequency and RPL_C in Figure 3.35b, $\langle \Sigma \tilde{\gamma}^2 \rangle$ is near 0.9 at $\mathrm{RPL}_C = 1$ for the same low frequencies, 10 to 100 Hz. Hence, the guideline that one reference microphone should be deployed within each coherence length remains robust.

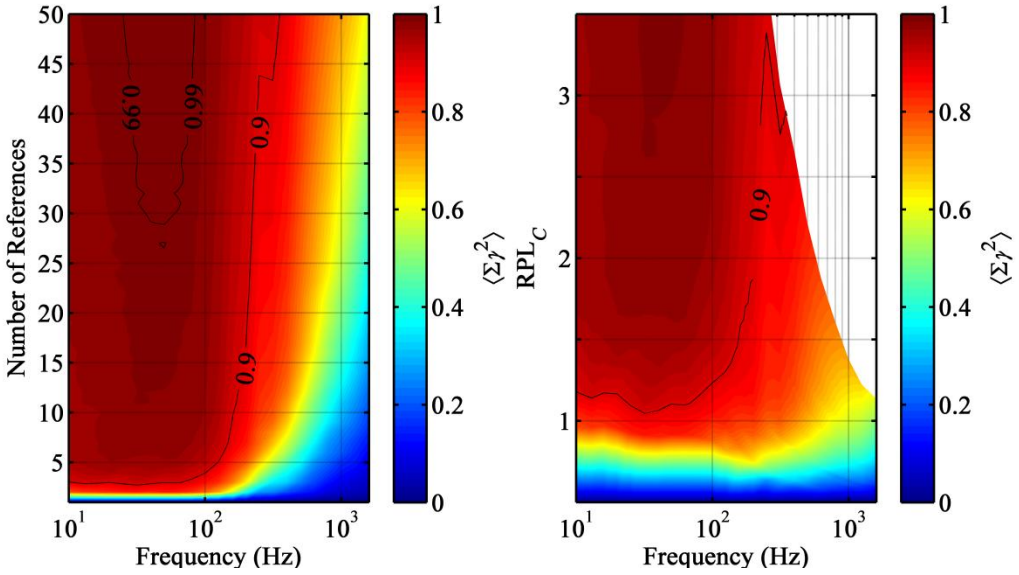

Figure 3.35 Mean virtual coherence sum values for the jet at military power, (a) as a function of frequency and the number of reference microphones, and (b) as a function of frequency and references per coherence length, RPL_C.

Between 100 and 400 Hz in Figure 3.35a, the number of references required to cause $\langle \Sigma \tilde{\gamma}^2 \rangle$ to reach 0.9 grows rapidly from 4 to 50. This means that above 100 Hz, the linear reference array is less able to represent the coherent energy of the hologram measurement due to azimuthally decaying coherence. Below 400 Hz, if the entire array of references is used in the PFD, most of the energy is captured, based on the 0.9 criterion. Again, 400 or 500 Hz is the approximate "cutoff" frequency, above which not even the entire reference array is sufficient. Further evidence of this is seen in the fact that the contour line that marks $\langle \Sigma \tilde{\gamma}^2 \rangle = 0.9$ in Figure 3.35b diverges from the $\mathrm{RPL}_C = 1$ region between 100 and 400 Hz, and is not captured beyond 400 Hz.

3.4.5 Discussion

Coherence length values have been reported for a full-scale jet from an engine on a military aircraft. Comparisons between the measured coherence lengths for the jet and those of a numerically generated line array of incoherent monopoles provides evidence that most of the energy in the high-amplitude regions for all frequencies (10 Hz to 1600 Hz shown here) is dominated by contributions from the spatially coherent large-scale turbulence structures. Values of L_C are relatively large in the high-amplitude regions for all frequencies, but are similar to those of an array of incoherent sources in the low-amplitude regions, where the radiation from fine-scale turbulence dominates. The analyses presented demonstrate the utility of the coherence length L_C, as it is defined here, in summarizing near-field spatial coherence and in making inferences about spatial source coherence.

In addition, it has been demonstrated that $\mathrm{RPL}_C = 1$ in the axial direction is a robust guideline for jet sources with high azimuthal coherence, which include sources below 100 Hz in the present measurement. Above 100 Hz, due to the large number of transducers, the array is sufficient to represent most of the energy coherent with the hologram measurement up to about 400 or 500 Hz. Hence, the NAH results presented in future chapters are limited to reconstructions up to 500 Hz. In future measurements, a reference array that covers more of the jet in the azimuthal direction will improve results. It is likely that the $\mathrm{RPL}_C = 1$ guideline for the axial direction could then be supplemented with a similar guideline for the azimuthal distribution of references.

Chapter 4

Aperture Extension

4.1 Introduction

The apertures of array-based sound field measurements are, by their nature, discretized and spatially limited in extent. Near-field acoustical holography (NAH) is an inverse method, by which a sound field in three-dimensional space is reconstructed from data on a two-dimensional measurement surface (the hologram). In general, an increase in the hologram aperture leads to a more accurate reconstruction. However, in some instances, large-aperture measurements can be expensive and difficult to obtain. The number of measurements required to ensure the same solid-angle coverage of source radiation increases with distance between the hologram and source (standoff distance). This can be especially problematic when proximity to the source is limited by transducer capabilities in the presence of high-amplitude sources. If a hologram aperture is too small to avoid significant reconstruction errors, it is desirable to numerically extend (extrapolate) the data outward, tangent to the measurement surface, effectively increasing the aperture size. Analytic continuation is an extrapolation method that has been used to successfully extend measured pressure fields into an area nearly double that of the original field, with high accuracy near the boundary of the original measurement.[118] This allowed for an

accurate reconstruction of a vibrating plate from a close-proximity hologram measurement. However, in a measurement with a larger standoff distance, it is desirable to obtain an accurate prediction of data farther outside the measurement aperture than analytic continuation can provide.

The extrapolation of data is a useful problem-solving technique in any field where information is desired outside the range of a given data set. NAH is, in fact, an extrapolation. For each iteration in the analytic continuation method, a two-dimensional spatial Fourier transform of the data is taken, a filter is applied, and the inverse Fourier transform is taken. Only the lack of a spatial propagator separates the algorithm of analytic continuation from that of traditional NAH.[22] Restoration (extrapolation) of missing (damaged) data is a common signal processing problem. Often, an autoregressive model is used to provide a linear prediction (LP) of data in the missing portion.[119-121] Metrics for a comparison of data extrapolation methods for an NAH application include a graceful (gradual) taper of pressure amplitudes from the boundary of the measurement toward zero and an accurate (physical) prediction of values outside the measurement.

The characterization of jet noise sources with NAH assists in the development and verification of noise reduction technologies. Holographic measurements of full-scale jets (tens of meters in length and up to meters in diameter) require thousands of data points, and an aperture that fully covers the source region is difficult to obtain. Coverage of the source region is made more difficult by the fact that measurements must be taken at a relatively large standoff distance, due to microphone limitations in the high-amplitude sound fields of full-scale jets. Hence, three extrapolation methods are implemented in a numerical experiment, in which the relative locations of the sources and the simulated measurement surface mimic those of the full-scale jet experiment (see Section 2.2). It is not within the scope of this section to propagate the extended fields using NAH, nor to substantiate the effectiveness of any extrapolation method by the accuracy of its NAH projection. Rather, the success of each method is quantified by the

accuracy of the data predicted outside the simulated measurement boundary in the numerical experiment. This chapter was modified from a 2012 publication in *Proceedings of Meetings on Acoustics* under the name, "Aperture extension for near-field acoustical holography of jet noise."[122]

This chapter is organized as follows. The details of the physical experiment that motivate this investigation are briefly described in Section 4.2. Each step of the aperture extension process is illustrated with physical data. The numerical experiment which mimics the geometry of the physical experiment is provided. In Section 4.3, the numerical data are extrapolated using three different methods: analytic continuation, a method based on statistically optimized near-field acoustical holography (SONAH), and linear prediction. The relative merits of these methods are discussed, and a quantitative comparison is made of the accuracy of their respective extended fields. Conclusions are presented in Section 4.4.

4.2 Experiment

Sound pressures were measured in the geometric near field of the jet from one of the two engines installed on a Lockheed Martin/Boeing F-22A Raptor. The centerline of the jet was located 1.9 m above the surface of a concrete run-up pad. Pressures were recorded on several planar surfaces. The measurement used in this study is called plane 2, and its location relative to the jet is shown in the schematic in Figure 4.1. (Plane 1, the arc measurement, and the reference array apply to NAH experiments and are not used in this chapter.) Plane 2 was a 2 m x 24 m grid with regular 0.15 m (6 in) spacing, which ran parallel to, and was located 5.6 m from, the estimated shear layer boundary.

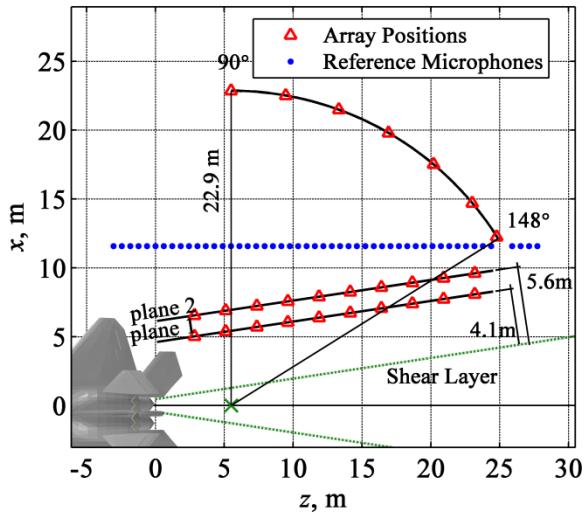

Figure 4.1 Schematic of the measurement locations, relative to the aircraft. The estimated shear layer boundary is marked by green dashed lines, and the green "x" delineates the estimated maximum noise source region and the center of the arc.

The concrete pad introduced a reflecting surface to the sound field, which may be considered perfectly rigid for the frequencies of interest. Based on the theory of the method of images, it is therefore assumed that the sound field was generated by the jet noise source and an equivalent, inverted image source below the ground. By the same principles, the data on the measurement surface are inverted and copied below the reflecting plane (mirrored). The result is a real and image source with two separate planar measurements in a free field, as shown in Figure 4.2 (for measured jet noise at 105 Hz, military engine power). Then, as shown in Figure 4.2b, pressure values are interpolated between the original and reflected data. Finally, in Figure 4.2c, numerical data extrapolation methods (analytic continuation shown here) are applied to estimate pressure values outside the new aperture.

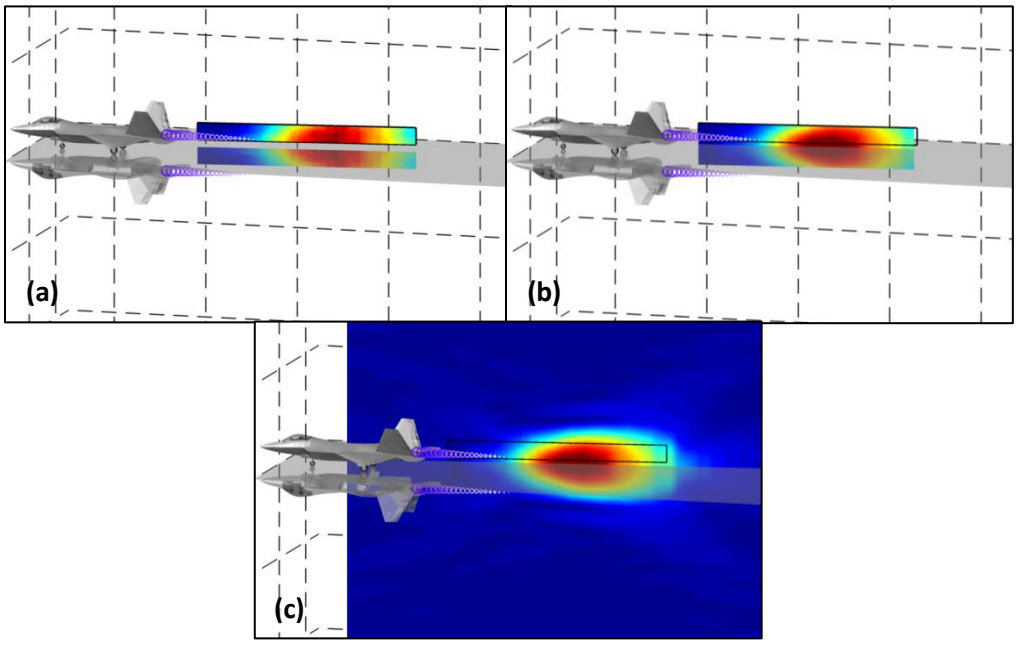

Figure 4.2 Visual representation of a data-extrapolation process. A rigid reflecting plane along the ground is assumed, and the measured pressures are (a) mirrored over the reflecting plane, (b) interpolated between the two surfaces, and (c) extrapolated outward using one of several methods (analytic continuation shown here).

The numerical experiment of this chapter is designed to mimic the measurement geometry of the jet noise experiment, relative to the source region. Two coherent line arrays of point monopoles are located parallel to each other and separated by 3.8 m, representing the same locations of the original and image sources in a free-field environment. Each source array consists of 100 monopoles spaced evenly between $z = 2.0$ m and 9.9 m (downstream of the nozzle exit). The phase of each monopole is adjusted to give the source arrays a directivity of 135° (downstream) relative to the front of the aircraft. (No equivalent jet noise source model is attempted here.) These are shown relative to the assumed aircraft location in Figure 4.3. A mirroring of the data and gap interpolation are bypassed, in favor of a direct measurement of the entire (limited) aperture at the same locations as the data shown in Figure 4.2. This simulated measurement shown in Figure 4.3, which is for sources radiating at 315 Hz, is marked by a black dashed outline. The extrapolation methods investigated here are performed on these data. The

pressure values outside of the dashed box in Figure 4.3 are the benchmark measurements for comparison and extrapolation-error calculation.

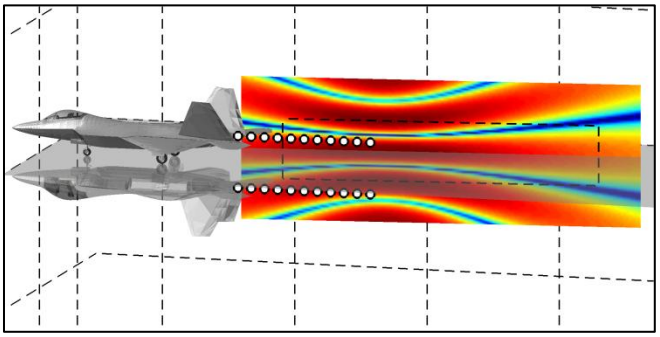

Figure 4.3 The relative locations of the numerical source array (jet centerline and centerline image locations), the simulated measurement surface (inside the black dashed rectangle), and the benchmark measurement for comparison to extrapolations (outside the black dashed rectangle).

4.3 Numerical Data Extrapolation

Analytic continuation[118] is a relatively robust and simple data extrapolation method. It is based on the Green's functions (transfer functions) relating acoustic quantities on the measurement surface to those on the extended surface. The resulting field after the application of analytic continuation for the sources at 315 Hz is shown in Figure 4.4. Note first that the data within the measurement aperture (inside the dashed line) are well preserved. A benchmark measurement is provided in Figure 4.5. In the extended region, levels are predicted with physical accuracy very close to the boundary, and then taper away (toward some low-amplitude artifacts) within about the distance of one wavelength (1.1 m for this frequency). Such an extrapolation is characteristic of the same field for different frequencies tested, with the boundary tapering away within about one wavelength.

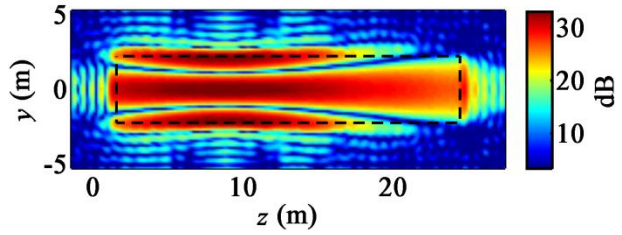

Figure 4.4 Numerical extrapolation of the measured field of a correlated line array source and its image, radiating at 315 Hz, using analytic continuation.

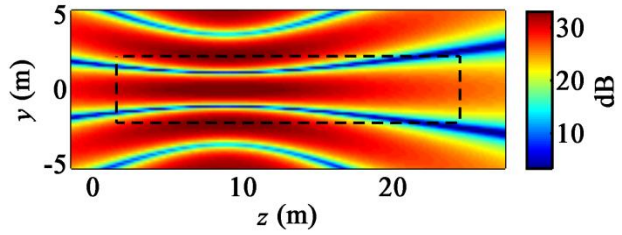

Figure 4.5 The benchmark radiation pattern measured near a correlated line array source and its images source (315 Hz). The black dashed line shows the boundary of the original measurement surface, from which data the field is extrapolated outwards, numerically.

The second method applied is based on the holography method, SONAH.[54] SONAH is designed for reconstructing sound fields when the aperture is limited. It is also based on Green's functions, directly calculating the transfer functions between the measurement and reconstruction locations in a field prior to prediction. These predictions are typically made out-of-plane (not tangent to the measurement surface), but a Green's function (wave function) representation of the field allows SONAH to predict values in any desired location in the field vicinity, so long as the necessary wave functions are sufficiently represented at the measurement in a least-squares sense. Hence, it is applied here to project outward (extrapolate) the data.

Here, the functions used to represent this field are plane-wave functions. As is typical, regularization is required to filter high-wavenumber components.[54] SONAH results are shown (for 315 Hz) in Figure 4.6. Spatial features of the levels in the field are predicted with higher

accuracy, farther out than those from the analytic continuation method, but the artifacts beyond this region are of higher amplitude. The sacrifice for accuracy in this SONAH-based method is mainly in the computational cost.

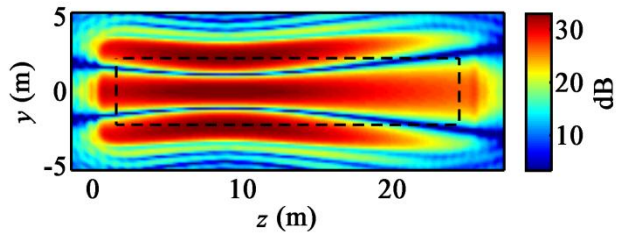

Figure 4.6 Numerical extrapolation of the measured field of a correlated line array source and its image, radiating at 315 Hz, using a SONAH-based in-plane projection.

The final method investigated here is linear prediction.[119,123] In signal processing, linear prediction is used to predict future values of a discrete signal based on a linear function of previous (measured) values. In this experiment, the prediction is performed first in the horizontal direction (row by row) to extrapolate the data in the directions of increasing and decreasing *z*. Then, prediction is performed in the vertical direction (*y*, column by column). The extrapolated field is shown in Figure 4.7. Of particular note is that linear prediction is able to capture the shapes of the interference patterns of the sound field out to 3 m (vertical direction), with a gradual taper in level. Its success in the horizontal direction is comparable to that of both the analytic continuation and SONAH-based methods.

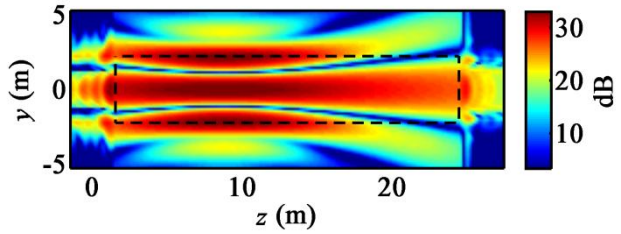

Figure 4.7 Numerical extrapolation of the measured field of a correlated line array source and its image, radiating at 315 Hz, using linear prediction.

To quantify the quality of extrapolation for each method, the normalized L_2 errors are calculated for concentric square rings, one point wide, as a function of distance from the measurement boundary, with the formula

$$\% \, Error = 100 \times \frac{\left\| p_{\text{exact}} - p_{\text{extrapolated}} \right\|_2}{\left\| p_{\text{exact}} \right\|}, \tag{4.1}$$

where p_{exact} are the complex pressure values of the benchmark measurement, and $p_{\text{extrapolated}}$ are the extrapolated pressures. The errors for each method are shown in Figure 4.8, as a function of distance from the measurement boundary. Note that a taper toward zero results in $p_{\text{extrapolated}}$ values of zero, so error near 100% is expected far from the measurement. Within about 1-2 m of the measurement, it is clear that the SONAH-based method provides an extrapolation with the least error. The low error within 0.5 m is due to the fact that levels do not taper off dramatically with distance. Accordingly, the error of the linear prediction rises rapidly with the faster level tapering, even though many of the interference pattern features are represented. Once again, it can be seen that the analytic continuation error reaches 100% within about 1 m, which is on the order of a wavelength.

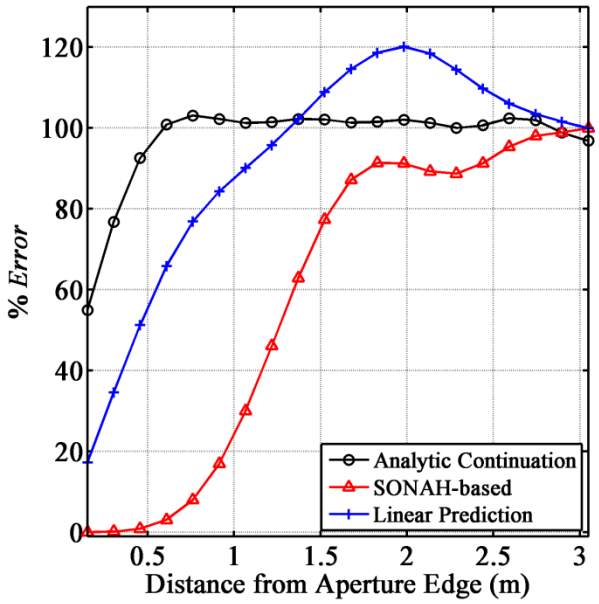

Figure 4.8 Percent error of each concentric (rectangular) ring of data in the extrapolated region as a function of distance from the measurement boundary (315 Hz).

4.4 Conclusion

In this paper, three methods for numerically extending the aperture of a spatially finite sound field measurement are investigated for a simulated experiment where the measurement surface was far from the sources. Based strictly on an error calculation as a function of distance from the original measurement boundary, a SONAH-based projection of the field produces the most accurate extrapolation close to the measurement, for this experiment. Linear prediction represents more of the interference pattern features far from the measurement boundary than do the SONAH-based and analytic continuation methods, although its levels taper more rapidly away. For future data extrapolations, it might be instructive to investigate the accuracy of extrapolation and near-field acoustical holography reconstruction with the variation of solid-angle coverage of the source, which is influenced by all aspects of the measurement geometry, including measurement aperture size, source distribution, and standoff distance. It might also be

instructive to explore the ranges of acoustic wavelengths (or frequencies), relative to the size of the measurement aperture, over which the various methods provide sufficiently accurate extrapolations. In general, the optimal data extrapolation method depends on several factors, including frequency, measurement geometry, and source properties.

Chapter 5

Multisource-type Representation Statistically Optimized Near-Field Acoustical Holography

5.1 Introduction

Statistically optimized near-field acoustical holography (SONAH)[51-54] is the equivalent wave model (EWM) inverse method that serves as the starting point for the primary NAH method employed in this work. The SONAH algorithm calculates a transfer function matrix between all hologram locations and reconstruction locations, then applies the transfer functions to the measured sound pressures. Lee and Bolton[55] applied SONAH to reconstruct the sound field of a laboratory scale jet. A planar SONAH formulation was applied to the current data set for full-scale jet measurements as a first attempt at holographic reconstruction.[56] To the author's knowledge, prior to the current investigation it has never been applied to represent independent components of a sound field generated by spatially separated sources. The closest example is that of Hald,[57] who developed a SONAH method that relied on measurements of two parallel planar arrays to separate incoming and outgoing waves, by concatenating two matrices of wave functions, one for each direction.

The transfer-function approach of SONAH allows flexibility in the selection of the locations of hologram microphones (i.e. they are not restricted to a regular grid, and need not completely cover the source). In addition, it allows for a more convenient representation of the sound field than other NAH algorithms, because multiple sets of wave functions can be included in the generation of the transfer function matrix through a concatenation scheme similar to that of Hald.[57] The most comparable methods are the distributed point sources method (DPS)[49,58,60] and the distributed spherical waves method (DSW),[49,59] (so called by Semenova and Wu[49]) in that these both allow for a user-defined set of elementary wave functions, based on a rudimentary estimate of source location and shape. The flexibility of the SONAH methods in allowing for multiple sets of elementary wave functions is the basis for the NAH method developed here.

In this work, a modified approach to SONAH, using a set of cylindrical functions for both the jet and its image source, is employed to represent the total field. The sound field reconstructed from this model is more accurate than the fields produced by NAH methods that do not incorporate a model of the ground reflection,[106,124] or do not account for the geometrical spreading of the field.[56] In the general case, this method, called multisource-type representation SONAH (MSTR SONAH),[125] employs an EWM where the field is represented as a combination of multiple sets of elementary wave functions, each set for a single source shape and location. Inasmuch as the elementary wave functions conform well to each source shape, the total EWM approaches an ideal reduced-order model for that source configuration. The development of MSTR SONAH and its implementation on the full-scale jet data are the focus of the work presented in this dissertation.

This chapter provides the theory, numerical verification, and experimental implementation of MSTR SONAH. In Section 5.2, the underlying theory of SONAH is presented in detail, as well as the modification to the SONAH algorithm that incorporates a flexible EWM and makes MSTR SONAH possible. A numerical experiment is performed for configurations of multiple sources in Section 5.3, which demonstrates the implementation and

the advantages of MSTR SONAH. A comparison is made to planar SONAH and cylindrical SONAH approaches to the same problem, and the advantages of MSTR SONAH are demonstrated. A second numerical experiment is performed in Section 5.4. The geometry of the full-scale experiment, including the approximate source locations and distributions, as well as the measurement locations, is modeled for the most important frequencies of the jet noise problem. Again, the advantages of MSTR SONAH to alternative NAH methods are demonstrated.

Finally, MSTR SONAH is used to reconstruct the near-field sound environment of the jet from the installed engine on an F-22A Raptor in Section 5.5. A description of the processing required prior to MSTR SONAH, such as partial field decomposition (see Section 3.2) and aperture extension (see Section 4.3) is included. Considerations for the optimization of the expansion terms and the effects of the hologram grid spacing and aperture on reconstruction accuracy are included. Reconstructed fields are compared to benchmark measurements in the geometric near field to quantify the accuracy of the MSTR SONAH method. The accuracy of the method for the full-scale jet data is investigated as a function of frequency.

The focus of this chapter is on the development and implementation of the MSTR SONAH method, culminating in its application to the full-scale jet data. Details about the jet sources and sound field are only briefly discussed, where they pertain to the MSTR SONAH method. A comprehensive discussion of the reconstructed field and source properties is reserved for Chapter 7.

5.2 Theory

5.2.1 Statistically Optimized Near-Field Acoustical Holography (SONAH)

The general theory of SONAH is presented here to provide context for the jet noise reconstructions shown in this work.[52,54] This theoretical development also provides a foundation for the modification to the algorithm discussed below. It is assumed that the complex, time-

harmonic sound field has been measured at a set of locations $\mathbf{r}_h, h = 1,2,\dots,I$, on the hologram surface Ω, in a homogeneous, source-free region that obeys the Helmholtz equation. The problem of reconstructing sound pressures at another set of locations in the field, $\mathbf{r}_r, r = 1,2,\dots,R$, over the reconstruction surface Γ, based on the hologram pressures, is considered. A set of wave functions, $\Psi_n, n = 1,2,\dots,N$ are chosen, which fulfill the homogeneous Helmholtz equation in the source-free field, defined for a single frequency. The wave functions can be elementary functions of plane, cylindrical, or spherical waves, or they can be derived from knowledge of the source properties (outside the source-free region). In light of such an EWM representation, it is desirable to be able to express complex pressures at both the hologram locations and at the reconstruction locations as linear combinations of the same basis functions, Ψ_n. The complex hologram pressures on Ω may be expanded in terms of these basis functions as

$$p(\mathbf{r}_h) = \sum_{n=1}^{N} c_n \Psi_n(\mathbf{r}_h) \ , \quad h = 1,\dots,I, \tag{5.1}$$

where c_n are the complex expansion coefficients for the wave functions. Thus, the first step of a typical NAH process is to determine the amplitude and phase of each wave function (the complex coefficients) that provides the best match to the measured pressures.

To determine the coefficients, it is convenient to represent Eq. (5.1) in matrix form,

$$\mathbf{D}\mathbf{c} = \mathbf{p}(\mathbf{r}_h) \, . \tag{5.2}$$

The matrices of measured pressures on Ω and complex coefficients are, respectively,

$$\mathbf{p}(\mathbf{r}_h) \equiv [p(\mathbf{r}_h)] \equiv \begin{bmatrix} p(\mathbf{r}_1) \\ p(\mathbf{r}_2) \\ \vdots \\ p(\mathbf{r}_I) \end{bmatrix} \ , \quad \mathbf{c} \equiv [c_n] \equiv \begin{bmatrix} c_1 \\ c_2 \\ \vdots \\ c_N \end{bmatrix} . \tag{5.3}$$

The matrix of wave function values at the measurement positions is the transpose of **D**, ($\mathbf{A} = \mathbf{D}^{\mathrm{T}}$), and is written

$$\mathbf{A} \equiv [\Psi_n(\mathbf{r}_h)] \equiv \begin{bmatrix} \Psi_1(\mathbf{r}_1) & \Psi_1(\mathbf{r}_2) & \cdots & \Psi_1(\mathbf{r}_I) \\ \Psi_2(\mathbf{r}_1) & \Psi_2(\mathbf{r}_2) & & \Psi_2(\mathbf{r}_I) \\ \vdots & & \ddots & \vdots \\ \Psi_N(\mathbf{r}_1) & \Psi_N(\mathbf{r}_2) & \cdots & \Psi_N(\mathbf{r}_I) \end{bmatrix}. \tag{5.4}$$

The problem of solving Eq. (5.2) is akin to solving I equations with N unknowns. If $I > N$, the problem is over-determined, and generally no exact solution can be found. In such a case, the solution that approximates the exact solution with the least error is called the least-squares solution,[126] the coefficients for which are

$$\mathbf{c} = (\mathbf{D}^{\mathrm{H}}\mathbf{D})^{-1}\mathbf{D}^{\mathrm{H}}\mathbf{p}(\mathbf{r}_h)\,, \tag{5.5}$$

where H represents the Hermitian transpose. If $I < N$, there are an infinite number of solutions, and the problem is under-determined. In order to solve the problem uniquely, a reasonable criterion is to find the solution of smallest norm, called the least-norm solution,[126] for which the coefficients are

$$\mathbf{c} = \mathbf{D}^{\mathrm{H}}(\mathbf{D}\mathbf{D}^{\mathrm{H}})^{-1}\mathbf{p}(\mathbf{r}_h)\,. \tag{5.6}$$

Proceeding with the least-norm solution (the least-squares solution is addressed below), Eq. (5.6) may be written equivalently as

$$\mathbf{c} = \mathbf{A}^{*}(\mathbf{A}^{\mathrm{T}}\mathbf{A}^{*})^{-1}\mathbf{p}(\mathbf{r}_h)\,, \tag{5.7}$$

where * signifies the complex conjugate, or,

$$\mathbf{c}^{\mathrm{T}} = \mathbf{p}(\mathbf{r}_h)^{\mathrm{T}}(\mathbf{A}^{\mathrm{H}}\mathbf{A})^{-1}\mathbf{A}^{\mathrm{H}}\,. \tag{5.8}$$

In practice, $\mathbf{p}(\mathbf{r}_h)$ contains spatial noise that results, for example, from slight mispositioning of field microphones during a measurement or from variations in the source level from scan to scan. This produces a "noise floor" in the wave number domain that extends into the region of high-order wave functions associated with evanescently decaying components. For

sufficiently high order wave functions the noise components exceed the amplitude of the signals that are linearly related to the sources. This causes the coefficients calculated in Eq. (5.8) to diverge, introducing large errors into the field reconstruction. Hence, regularization, or the truncation of these wave functions at the point where the noise floor begins to dominate is necessary prior to calculation of the inverse in Eq. (5.8). There is no holy grail with respect to the best regularization technique. Due to the fact that modified Tikhonov regularization in conjunction with the generalized cross-validation (GCV) procedure (for determining the optimal regularization parameter) had the best performance for many realizations of an NAH problem investigated by Williams,[115] it is commonly employed in NAH applications, including in the SONAH formulation by Cho *et al*.[52] Thus, it is the regularization method used in this work, and is summarized here.

The matrix $\mathbf{A}^{\mathrm{H}}\mathbf{A}$ is positive semi-definite Hermitian, so it may be represented by the singular value decomposition (SVD)

$$\mathbf{A}^{\mathrm{H}}\mathbf{A} = \mathbf{V}\mathbf{G}\mathbf{V}^{\mathrm{H}}, \tag{5.9}$$

where $\mathbf{V}$ is a matrix of singular vectors and the diagonal elements of $\mathbf{G}$ are the singular values. Then, the regularized inverse of $\mathbf{A}^{\mathrm{H}}\mathbf{A}$ is

$$\mathbf{R}_{\mathbf{A}^{\mathrm{H}}\mathbf{A}} = \mathbf{V}(\alpha(\mathbf{F}_1^{\alpha})^2 + \mathbf{G}^{\mathrm{H}}\mathbf{G})^{-1}\mathbf{G}^{\mathrm{H}}\mathbf{V}^{\mathrm{H}} \ . \tag{5.10}$$

where the singular values are high-pass filtered by the modified Tikhonov filter,

$$\mathbf{F}_1^{\alpha} = \mathrm{diag}\left[\ldots, \alpha \Big/ \left[\alpha + |\lambda_i|^2 \left(\frac{\alpha + |\lambda_i|^2}{\alpha}\right)^2\right], \ldots\right], \tag{5.11}$$

and where the terms λ_i are the singular values (diagonal elements of $\mathbf{G}$). The GCV method is used to find the regularization parameter α, which minimizes the cost function

$$J(\alpha) \equiv \frac{\|\mathbf{F}_1^{\alpha}\mathbf{V}^{\mathrm{H}}\mathbf{p}(\mathbf{r}_h)\|^2}{[\mathrm{trace}(\mathbf{F}_1^{\alpha})]^2}. \tag{5.12}$$

With the regularization complete, Eq. (5.8) may be combined with the regularized inverse, and the expansion coefficients are given by

$$\tilde{\mathbf{c}}^{\mathrm{T}} = \mathbf{p}^{\mathrm{T}}(\mathbf{r}_h)\mathbf{R}_{\mathbf{A}^{\mathrm{H}}\mathbf{A}}\mathbf{A}^{\mathrm{H}}. \tag{5.13}$$

These regularized coefficients can now be used to represent the pressure of the field in terms of the wave functions. Hence, the reconstructed pressure at a desired location on Γ can be written as the linear combination of wave functions,

$$p(\mathbf{r}_r) = \sum_{n=1}^{N} \tilde{c}_n \Psi_n(\mathbf{r}_r)\ ,\ \ r = 1,2,\dots,R. \tag{5.14}$$

Since all the expansion functions of Eq. (5.14) fulfill the Helmholtz equation, the reconstructed pressure field does also. Equation (5.14) can be recast in matrix form as

$$\mathbf{p}(\mathbf{r}_r) = \tilde{\mathbf{c}}^{\mathrm{T}}\boldsymbol{\alpha}, \tag{5.15}$$

where $\boldsymbol{\alpha}$ is the matrix of wave function values over Γ, and is defined

$$\boldsymbol{\alpha} \equiv [\Psi_n(\mathbf{r}_r)] \equiv \begin{bmatrix} \Psi_1(\mathbf{r}_1) & \Psi_1(\mathbf{r}_2) & \cdots & \Psi_1(\mathbf{r}_R) \\ \Psi_2(\mathbf{r}_1) & \Psi_2(\mathbf{r}_2) & & \Psi_2(\mathbf{r}_R) \\ \vdots & & \ddots & \vdots \\ \Psi_N(\mathbf{r}_1) & \Psi_N(\mathbf{r}_2) & \cdots & \Psi_N(\mathbf{r}_R) \end{bmatrix}. \tag{5.16}$$

Finally, the SONAH formulation for the reconstructed pressures, in matrix form, is written by combining Eq. (5.13) with (5.15) to obtain

$$\mathbf{p}(\mathbf{r}_r) = \mathbf{p}^{\mathrm{T}}(\mathbf{r}_h)\mathbf{R}_{\mathbf{A}^{\mathrm{H}}\mathbf{A}}\,\mathbf{A}^{\mathrm{H}}\boldsymbol{\alpha}, \tag{5.17}$$

where $\mathbf{p}^{\mathrm{T}}(\mathbf{r}_h)$ is a vector of dimensions $1 \times I$, $\mathbf{R}_{\mathbf{A}^{\mathrm{H}}\mathbf{A}}$ is $I \times I$, $\mathbf{A}^{\mathrm{H}}$ is $I \times N$, and $\boldsymbol{\alpha}$ is $N \times R$, resulting in the reconstruction matrix $\mathbf{p}(\mathbf{r}_r)$ of size $1 \times R$.

Another way to consider Eq. (5.17) is to view the reconstructed pressures as a linear combination of the measured complex pressure values,

$$\mathbf{p}(\mathbf{r}_r) = \mathbf{p}^{\mathrm{T}}(\mathbf{r}_h)\mathbf{a}\,, \tag{5.18}$$

in terms of the transfer function matrix (complex estimation weights)

$$\mathbf{a} \equiv \mathbf{R}_{\mathbf{A}^{\mathrm{H}}\mathbf{A}}\,\mathbf{A}^{\mathrm{H}}\,\boldsymbol{\alpha}\,. \tag{5.19}$$

Such a consideration sheds light on an important aspect of SONAH: the transfer function matrix between hologram and reconstructed pressures is data independent. The matrix is calculated with only the information about the EWM and the geometry of the propagation, fitting the model to the data implicitly, whereas a different type of NAH method called the Helmholtz equation least-squares method (HELS)[36] does so explicitly.[54]

The derivation here incorporates the least-norm solution of Eq. (5.6). In his comprehensive presentation of the SONAH algorithm, Hald[54] demonstrates that the regularized least-norm and regularized least-squares coefficients actually provide the same solution, independent of the relative values of I and N. However, this formulation does not rely on the SVD (or any other eigenvalue decomposition) of the matrices $\mathbf{D}\mathbf{D}^{\mathrm{H}}$ and $\mathbf{D}^{\mathrm{H}}\mathbf{D}$. It is unclear whether a similar equivalence can be ascribed to the least-norm and least-squares solutions presented here. Further investigation, including a mathematical proof or disproof and the implementation of SONAH with both solutions for the same data set would serve to illuminate this topic. Equivalence aside, when $I < N$, the matrix $\mathbf{D}\mathbf{D}^{\mathrm{H}}$ has smaller dimensions that $\mathbf{D}^{\mathrm{H}}\mathbf{D}$, so it is computationally advantageous to compute the (regularized) inverse of the least-norm solution. In the case where $I > N$, the algorithm could be reformulated with the least-squares solution for computational efficiency. In the current study, for frequencies above about 200 Hz,

$I < N$. The relatively large number of wave functions and grid points required make the higher frequencies more computationally expensive. Hence, the least-norm solution is adhered to.

5.2.2 Multisource-Type Representation SONAH (MSTR SONAH)

The basis functions, Ψ_n, that are typically employed in the EWM used in SONAH are elementary wave functions, which represent radiation from simple sources, such as plane waves,[54] cylindrical waves,[52,55] or spherical waves. When a more complex source is being investigated, it may not lend itself to such a convenient representation. Although the basis sets of elementary wave functions could theoretically be used to model any sound field that obeys the homogeneous wave equation (i.e. it is complete in the subspace of the source-free region), a complex source could require the use of many high-order functions, which can only be captured by a large number of measurement points (e.g. an increase in aperture size and/or density). Hence, it is desirable to find a low-order representation of a sound field.

The transfer-function formulation of SONAH allows for a reduced-order approach for complex sources. Unlike an NAH algorithm based on a discrete Fourier transform (DFT-based NAH), where the basis of wave functions is determined automatically by the acoustic frequency and the hologram grid spacing and aperture,[35] SONAH allows the user to manually select the wave functions included in the expansion. Recommendations for optimal bases exist. For example, since the set of wave functions that represent the field must be discretized for computational purposes, wraparound errors can still be a concern. To mitigate this for a plane-wave basis, it is recommended that the "wave-number domain sampling spacing should therefore be smaller than 2π divided by the smallest acceptable distance between the periodic replica in the represented sound field."[54] In addition, the hologram grid spacing determines the highest wave number that can be represented accurately (a "spatial Nyquist frequency"). Thus, it is recommended that the highest wavenumbers included be those that correspond to two microphones per spatial wavelength.

The inclusion of higher wave numbers will only make the problem more ill-posed. Although such recommendations help to guide the user in obtaining an accurate reconstruction, the flexibility of the user-determined wave functions allows the expansion to be tailored to accommodate source configurations that are not easily represented in a DFT-based approach. For example, if multiple components of a source, or even multiple sources of various shapes exist, then multiple sets of elementary wave functions that conform to each source individually can be included in the EWM. These can include multiple types of wave functions, such as combinations of planar, cylindrical, and spherical functions.

Many wave functions can be required to accurately represent a source that does not conform to the type of wave function used (e.g. reconstructing a point source with a set of plane waves). The selection of wave functions that conform to the shapes and locations of multiple types of sources can dramatically reduce the number of wave functions required to describe each source, and hence the total field, as well as streamline the measurement process. This method derives its name from the ability to represent a sound field generated by multiple types of sources with multiple sets of wave functions: multisource-type representation SONAH.

In this formulation, reconsider the wave function matrices of Eqs. (5.4) and (5.16). A set of wave function values at all positions on Ω can be defined for the *m*th source, and formulated as the matrix

$$\mathbf{B}_m \equiv [\Psi_n^m(\mathbf{r}_h)] \equiv \begin{bmatrix} \Psi_1^m(\mathbf{r}_1) & \Psi_1^m(\mathbf{r}_2) & \cdots & \Psi_1^m(\mathbf{r}_I) \\ \Psi_2^m(\mathbf{r}_1) & \Psi_2^m(\mathbf{r}_2) & & \Psi_2^m(\mathbf{r}_I) \\ \vdots & & \ddots & \vdots \\ \Psi_N^m(\mathbf{r}_1) & \Psi_N^m(\mathbf{r}_2) & \cdots & \Psi_N^m(\mathbf{r}_I) \end{bmatrix}. \tag{5.20}$$

The wave-function matrix for the locations on Γ is similarly written

$$\boldsymbol{\beta}_m \equiv [\Psi_n^m(\mathbf{r}_r)] \equiv \begin{bmatrix} \Psi_1^m(\mathbf{r}_1) & \Psi_1^m(\mathbf{r}_2) & \cdots & \Psi_1^m(\mathbf{r}_R) \\ \Psi_2^m(\mathbf{r}_1) & \Psi_2^m(\mathbf{r}_2) & & \Psi_2^m(\mathbf{r}_R) \\ \vdots & & \ddots & \vdots \\ \Psi_N^m(\mathbf{r}_1) & \Psi_N^m(\mathbf{r}_2) & \cdots & \Psi_N^m(\mathbf{r}_R) \end{bmatrix}. \tag{5.21}$$

The wave function matrices for all M sources are then concatenated vertically to obtain composite matrices:

$$\mathbf{A}' = \begin{bmatrix} \mathbf{B}_1 \\ \mathbf{B}_2 \\ \vdots \\ \mathbf{B}_M \end{bmatrix}, \text{and} \quad \boldsymbol{\alpha}' = \begin{bmatrix} \boldsymbol{\beta}_1 \\ \boldsymbol{\beta}_2 \\ \vdots \\ \boldsymbol{\beta}_M \end{bmatrix}. \tag{5.22}$$

These complete wave function matrices are then processed, using the traditional SONAH algorithm outlined in Section 5.2.1. After the complete matrices are defined, the regularized inverse $\mathbf{R}_{\mathbf{A}'^{\mathrm{H}}\mathbf{A}'}$ is found using the same method represented by Eq. (5.10), and the projection to the reconstruction locations is performed using Eq. (5.17).

An important question arises with such a formulation: *What are the consequences of using a basis that is not orthogonal?* In short, none. Completeness (or an approximation thereof) is a sufficient requirement for the basis. Orthogonal bases are often employed because of their convenient representation of a vector or function space, and because of the ease of implementation in computational processes, but orthogonality is not requisite in an EWM.

5.2.3 Advantages of and Considerations for MSTR SONAH

It is beneficial to consider some of the advantages of the MSTR SONAH method, as well as some considerations that can guide the reader in its appropriate use. The first advantage is that this method definitely provides for a convenient (reduced-order) representation of the sound fields from multiple sources of various shapes and locations, with which traditional NAH methods could struggle to succeed. However, it should be noted that MSTR SONAH can be successful insomuch as *each source* can be represented independently by a reduced-order model. If any single source is shaped too irregularly to be represented by known wave functions, this process is limited in the same way more conventional NAH methods are. It might be necessary to incorporate some of the HELS-type approaches to sources of irregular shape[127] in the MSTR SONAH EWM. It is also important to understand that much of the wave information in a field

can be represented with high accuracy, using a non-optimal basis set, if the near-field evanescent wave information is captured. For example, planar DFT-based NAH remains a simple, straightforward, and fast way to reconstruct the fields of arbitrary source distributions, so long as they are restricted to a planar region. MSTR SONAH provides a feasible alternative when this near-field data are not available.

5.2.4 Some Notes on Computational Implementation

Some problems have been encountered in the implementation of SONAH methods in the mathematical computation package MATLAB, and tips for avoiding these problems are provided here. First, due to the way MATLAB defines the imaginary unit, it is necessary to represent outgoing cylindrical waves using Hankel functions of the second kind, instead of the first kind, as is common in most literature, and which is the convention used here (see Sections 5.3, 5.4, and 5.5). Second, in the numerical implementation, the calculation of Hankel functions with large imaginary arguments can numerically diverge. This is especially problematic when attempting to propagate pressures to the far field. To mitigate these problems, it is helpful to use the expanded form in terms of the Bessel functions,

$$H_n^{(2)}(z) = J_n(z) - i\,Y_n(z)\,, \tag{5.23}$$

where J_n is the Bessel function of the first kind, and Y_n is the Bessel function of the second kind, instead of using the Hankel function ('`besselh`' in MATLAB) directly. It is also helpful to implement the asymptotic expansion functionality of the Bessel functions, written '`besselj(nu,Z,1)`' and '`bessely(nu,Z,1)`.'

5.3 Simple Numerical Study

A numerical experiment was performed to validate the use of the MSTR SONAH algorithm. MSTR SONAH was implemented, as well as traditional planar SONAH[54] and

cylindrical SONAH[52] to reconstruct the near field of configurations of multiple, simple sources. The reconstruction accuracies of these various methods are compared. This section was modified from a 2013 publication in *Proceedings of Meetings on Acoustics* under the name, "Modified statistically optimized near-field acoustical holography for multi-source fields."[125]

5.3.1 Numerical Experiment

The first source configuration explored is comprised of two parallel, coherent, finite line radiators a distance of 1 m apart (see Figure 5.1). Each line array was made of 51 monopoles spanning 1 m in length, all located in the source plane, and radiating at 1 kHz. A Gaussian weighting was applied to the amplitudes of the monopoles along each array. The hologram surface, Ω, was located 1 m above the source plane, and consisted of a regular grid of measurements with equal 0.15 m spacing. It spanned a 2 m by 2 m area, and was centered on the point directly above the center of the sources. Pressures at the hologram points were simulated by propagating pressures from the sources with the free-space Green's function for point monopoles. A secondary measurement was simulated at a height of 0.01 m above the sources and is illustrated as the surface Γ.

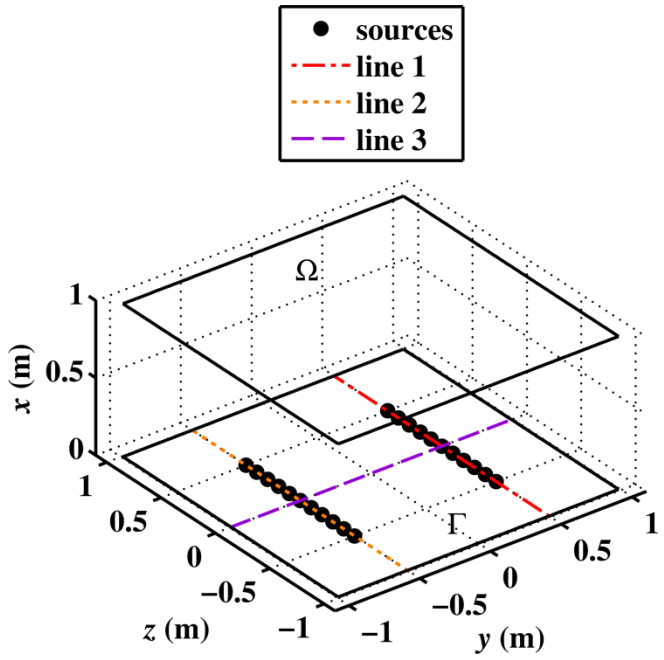

Figure 5.1 Diagram of the first numerical experiment. Two coherent line-arrays of monopole sources are placed a distance of 1 m apart. Measurement surface Ω is 1 m above the sources, and reconstruction surface Γ is 0.01 m above the sources.

The radiated field was represented, for the MSTR SONAH reconstruction, with two sets of cylindrical wave functions, each one centered on one of the source arrays. Cylindrical wave functions for outward-propagating waves can be expressed in terms of Hankel functions and complex exponentials as

$$\Phi_{k_z,n}(\mathbf{r}) = \Phi_{k_z,n}(r,\phi,z) \equiv \frac{H_n^{(1)}(k_r r)}{H_n^{(1)}(k_r r_s)} e^{in\phi} e^{ik_z z}, \quad r \geq r_s \,. \tag{5.24}$$

where $H_n^{(1)}$ is the nth-order Hankel function of the first kind, r_s is some small reference radius (traditionally the assumed source radius), and the radial wavenumber is

$$k_r = \begin{cases} \sqrt{k^2 - k_z^2}, & for\ |k| \geq |k_z|, \\ i\sqrt{k_z^2 - k^2}, & for\ |k| < |k_z|, \end{cases} \tag{5.25}$$

with $k = \omega/c$ being the angular frequency, and $c = 343$ m/s the ambient sound speed. This formulation implies an assumed time harmonicity of $e^{-i\omega t}$, where t is time. (Recall that Matlab, which is based on an assumed harmonicity of $e^{-i\omega t}$, requires the use of Hankel functions of the second kind, $H_n^{(2)}$.) In this experiment, Hankel functions of order $n = 0$ were used, since the source arrays are axisymmetric. Maximum axial wave numbers were specified by the axial grid spacing, Δz, by $k_{z,\max} = \pi/\Delta z$. Equation (5.24) was evaluated at all hologram locations, $\mathbf{r}_h$, with respect to two cylindrical "origins" to form $\mathbf{B}_1 = [\Phi_n^1(|\mathbf{r}_h - \mathbf{r}_0^1|)]$ and $\mathbf{B}_2 = [\Phi_n^2(|\mathbf{r}_h - \mathbf{r}_0^2|)]$, where $\mathbf{r}_0^1 = (x_0^1, y_0^1, z_0^1) = (0,0.5,0)$ m defines the point that is centered on the first source array, and where $\mathbf{r}_0^2 = (x_0^2, y_0^2, z_0^2) = (0,-0.5,0)$ m defines the point that is centered on the second source array. These were then concatenated to form the complete hologram wave function matrix, $\mathbf{A}$, as in Eq. (5.22). MSTR SONAH was then applied to reconstruct the source region.

In addition to the MSTR SONAH approach, traditional planar and cylindrical SONAH were applied to reconstruct the same field locations, for comparison. The processing for these methods was identical, but the equivalent-wave models (EWMs) used consisted of plane waves, as given by Hald,[54] and by one set of cylindrical waves centered on the first source array, as explained by Cho *et al*.[52] Reconstructions were calculated over a two-dimensional surface at a height of 0.01 m from the source plane, i.e. at Γ. Reconstructions are generated over the entire two-dimensional region of Γ shown in Figure 5.1, and are shown in the following section. In addition, the reconstructions at select one-dimensional regions of Γ, marked by lines 1, 2, and 3 of Figure 5.1. Lines 1 and 2 run parallel to the two respective source arrays, and are located exactly 0.01 m above them. Line 3 runs perpendicular to the two arrays, and is also 0.01 m above the source plane.

5.3.2 Results

All level results shown here are calculated relative to the maximum level on the hologram, $p_{\max}$. Hologram sound pressure levels (SPLs) at Ω are shown in Figure 5.2a. Note the presence of the interference pattern due to the coherence of the two source arrays. A benchmark at Γ is provided in Figure 5.2b, which exhibits a similar interference pattern. A reconstruction from the MSTR SONAH method is shown first. Figure 5.2c contains the SPLs of the reconstruction over Γ, and the errors (differences in decibels between the reconstructed and benchmark levels) are shown in Figure 5.2d. The error color range is restricted to ±10 dB. The reconstructed field is visually similar to the benchmark. The black line on Figure 5.2d corresponds to the locations on the benchmark where levels are 20 dB from the maximum level. This shows that errors are near 0 dB in the regions of highest amplitude. For another view, the reconstructed levels directly above each source, at $y = 0.5$ and at $y = -0.5$ m (see reconstruction line 1 and line 2 of Figure 5.1), are plotted as the red curves in Figure 5.3a and Figure 5.3b, respectively. The black circles show the benchmark levels. Finally, the reconstructed levels running perpendicular to the extent of the sources, at $z = 0$ m (see reconstruction line 3 of Figure 5.1) are shown by the red curve in Figure 5.3c, compared to the benchmark. The green dashed lines mark the level that is 20 dB below the maximum level. In Figure 5.3a-c, all the MSTR SONAH reconstructions above the dashed line follow the benchmark levels closely. Thus, in the maximum-amplitude region, the difference between the MSTR SONAH reconstruction and the benchmark is near 0 dB. All important features of the sound field, including source locations, levels, and interference patterns, are represented in the reconstructions.

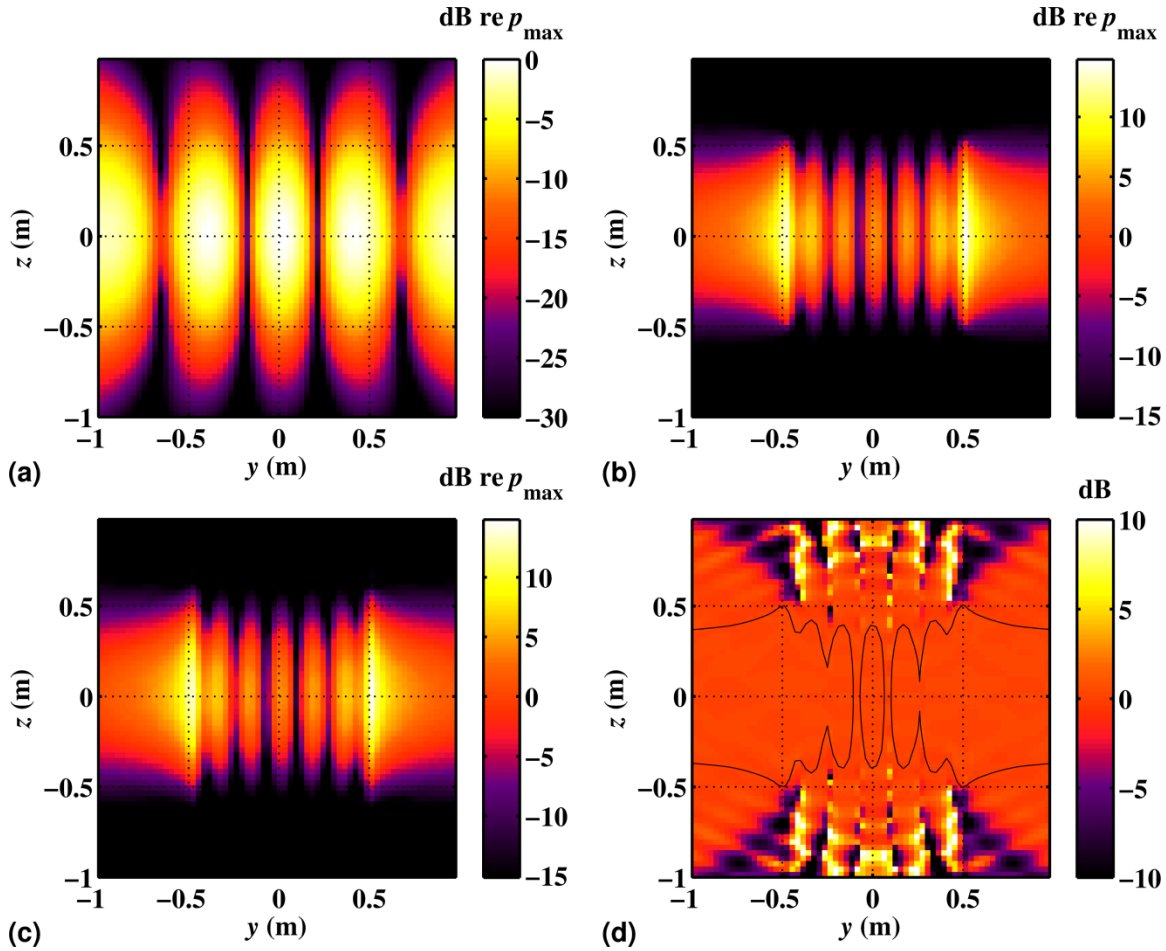

Figure 5.2 (a) Simulated SPLs (hologram) at Ω. (b) Simulated SPLs (benchmark) at Γ. (c) Reconstructed SPLs at Γ after implementation of MSTR SONAH. (d) Error (dB difference) between reconstruction and benchmark measurement. The black line marks the locations were benchmark levels are 20 dB below the maximum level.

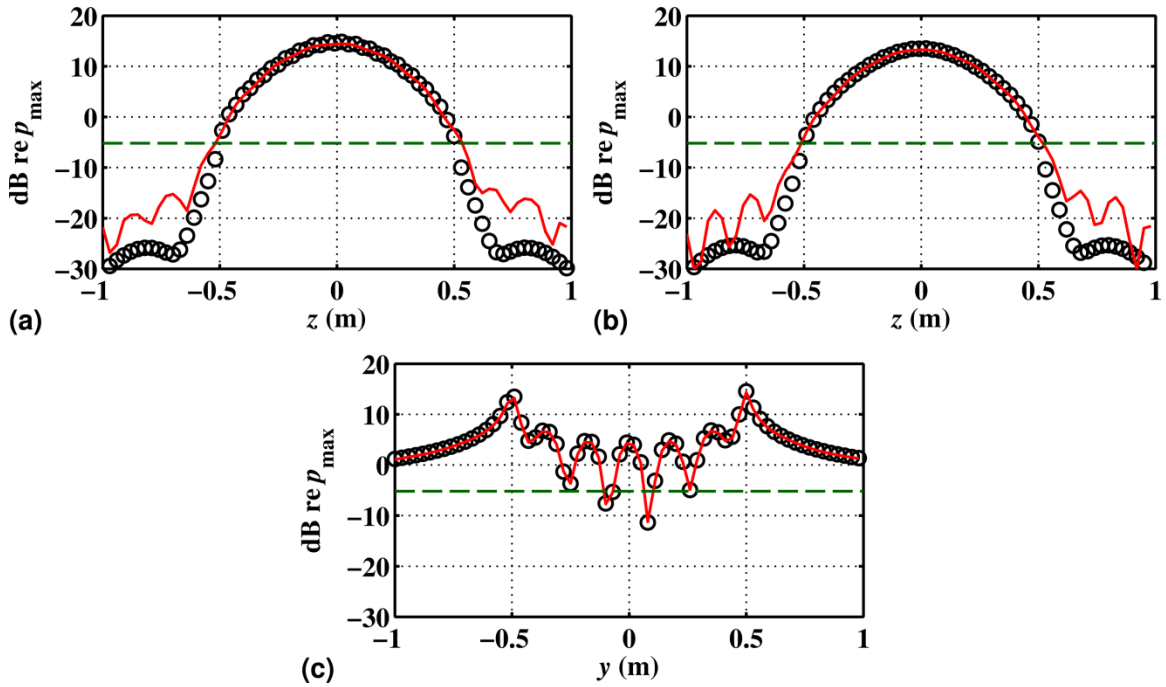

Figure 5.3 A comparison of MSTR SONAH reconstructed SPLs (red solid lines) and benchmark measurements (black circles), a distance of 0.01 m from the sources, (a) over reconstruction line 1 (at y = 0.5 m), (b) over reconstruction line 2 (at y = -0.5 m), and (c) over reconstruction line 3 (at z = 0 m). The green dashed line marks the level that is 20 dB below the maximum level.

Results for the planar SONAH reconstruction are provided in Figure 5.4 and Figure 5.5. Reconstructed SPLs at Γ are shown in Figure 5.4a, with the errors in Figure 5.4b. A comparison of Figure 5.4a to the benchmark of Figure 5.2b illustrates that the approximate source regions are localized within about a wavelength. In fact, careful inspection of Figure 5.5c, which displays the reconstructed levels at reconstruction line 3, shows that planar SONAH is able to accurately locate the sources and the main features of the interference pattern, as the locations of the reconstructed peaks and nulls correspond to those of the benchmark. However, the SPLs at these locations are underestimated, typically by about 10-15 dB. The levels along the extent of each source, shown in Figure 5.5a and b, demonstrate that the source distribution is accurately represented, but is underestimated consistently by about 10 dB. This is because it is difficult for

this particular plane-wave EWM of measurements, taken outside of the acoustic near field, to accurately represent the geometrical spreading that occurs in the vicinity of the sources.

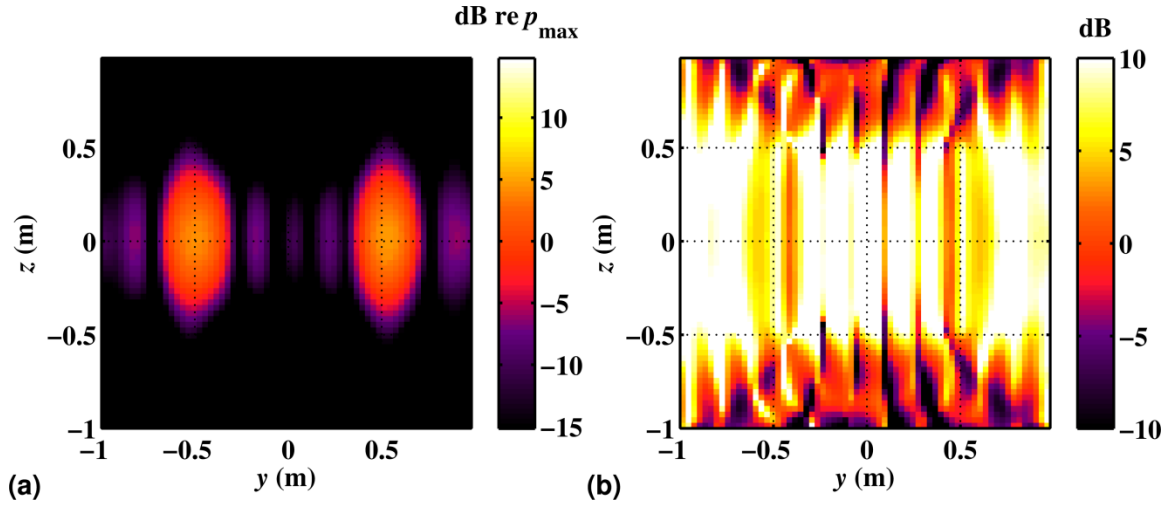

Figure 5.4 (a) Reconstructed SPLs at Γ after implementation of planar SONAH. (b) Error (dB difference) between reconstruction and benchmark measurement.

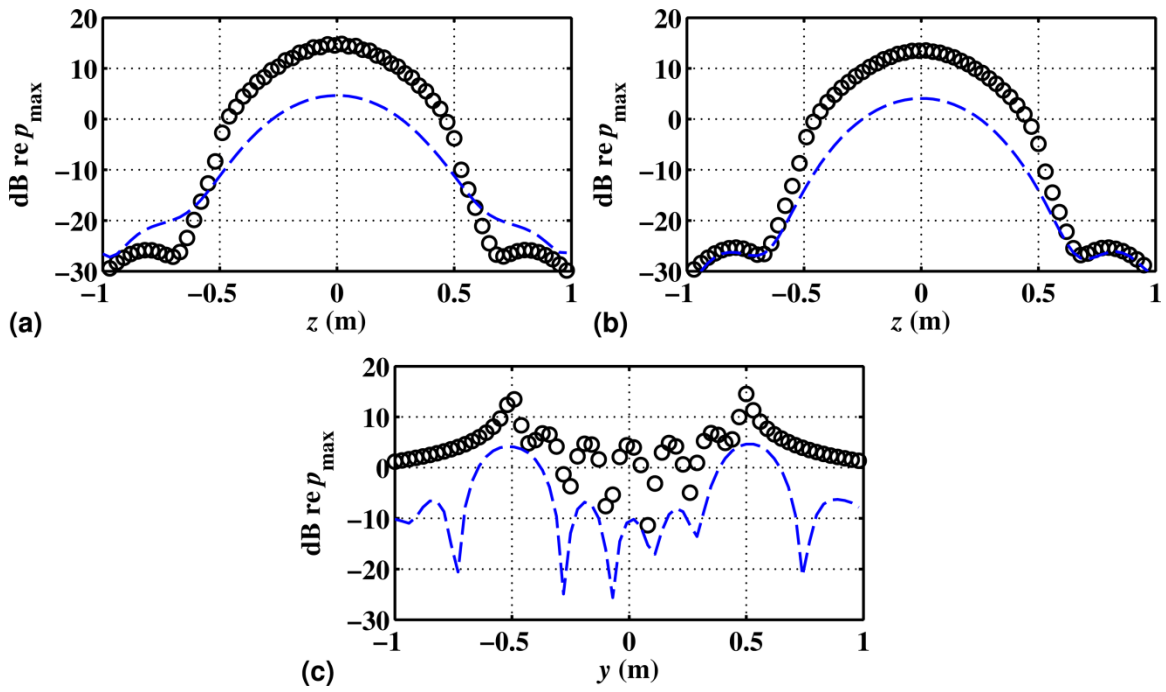

Figure 5.5 A comparison of planar SONAH reconstructed SPLs (blue dashed lines) and benchmark measurements (black circles), a distance of 0.01 m from the sources, (a) over reconstruction line 1 (at y = 0.5 m), (b) over reconstruction line 2 (at y = -0.5 m), and (c) over reconstruction line 3 (at z = 0 m).

Figure 5.6, and Figure 5.7 contain the reconstructions at Γ from the cylindrical SONAH method. Figure 5.6a and Figure 5.7c both show distinct maxima at $y = 0.5$ m, which demonstrates how cylindrical SONAH can provide an accurate location for the first source, which is collocated with the center of the cylindrical wave functions used in the expansion. However, the second source is missed completely, because the set of basis functions does not include cylindrical functions centered on the second source and thus does not represent it sufficiently. Theoretically, it should be possible to accomplish this, since the set of all cylindrical wave functions forms a complete basis in the field, but only with the inclusion of many high-order terms. A more dense measurement than the hologram used here would be required to capture these higher wavenumbers. The ripples visible in the reconstructions of Figure 5.6, and Figure 5.7 are due to the parsing of significant energy into the higher orders of the axial components of the wave functions that do not represent true source properties.

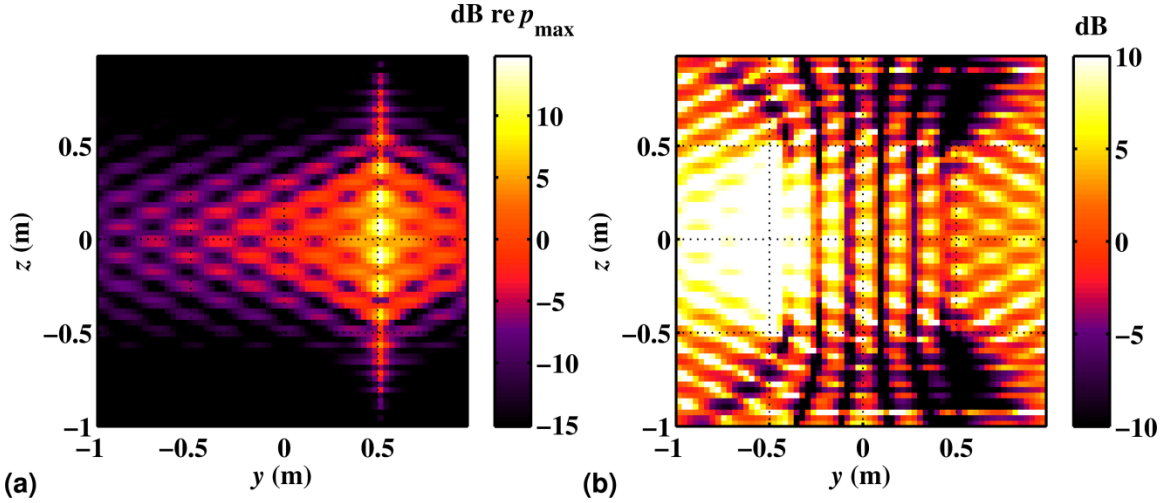

Figure 5.6 (a) Reconstructed SPLs a distance of 0.01 m from the sources after implementation of cylindrical SONAH. (b) Error (dB difference) between reconstruction and benchmark measurement.

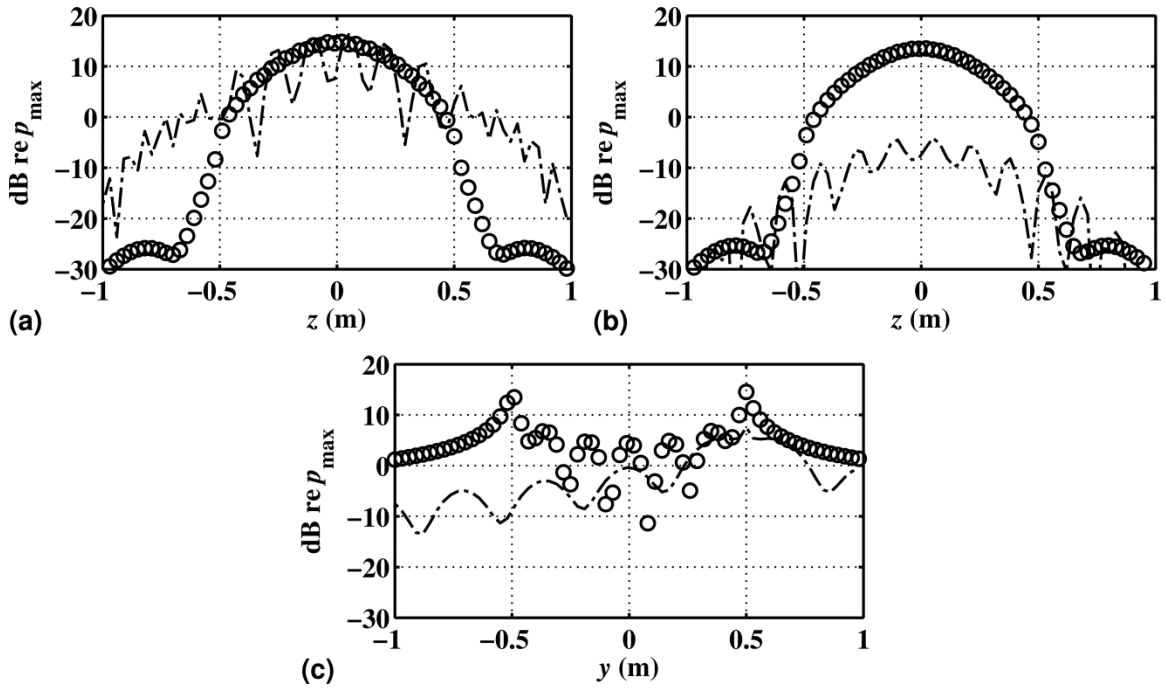

Figure 5.7 A comparison of cylindrical SONAH reconstructed SPLs (black dash-dot lines) and benchmark measurements (black circles), a distance of 0.01 m from the sources, (a) over reconstruction line 1 (at y = 0.5 m), (b) over reconstruction line 2 (at y = -0.5 m), and (c) over reconstruction line 3 (at z = 0 m).

5.3.3 Discussion

The reconstructions shown for the three SONAH methods depend both on the number of expansion terms in their respective EWM formulations, as well as the selection of measurement locations in the hologram. Due to the complicated interrelation of such parameters, there is no known ideal expansion or array deployment (in this or any inverse method) for a given source. Hence, the reconstructions shown here may not represent the most accurate reconstructions, although the trends shown hold for many practical realizations of the problem. In the actual implementation of an inverse method for a given source and a given array deployment, recall that benchmark measurements can be used to obtain the ideal number of expansion terms.[47]

In general, the selection of the EWM in NAH applications can affect the accuracy of a reconstruction. A basis of wave functions that conform to the source shape and location often requires fewer expansion terms than a basis that does not reflect the geometry of the source.

Stated equivalently, although any EWM exhibiting completeness in the sound field could theoretically be used, one that does not conform to the geometry of the source shape requires more terms for an accurate representation than one that does. MSTR SONAH is an algorithm that provides for such a convenient EWM, with a user-selected basis, derived from a rudimentary knowledge of the source shapes and locations. In the experiment shown here, it outperforms the straightforward applications of planar SONAH and cylindrical SONAH in capturing interference patterns and source levels on a global scale. It could be used in future NAH applications where the sound field is generated by multiple sources of interest, where an additional noise source of known location and shape interferes with the source of interest, or even where scattering off an object changes the sound field. For example, in a jet noise application, the scattering of sound off the rigid surfaces of the aircraft fuselage could be accounted for in the EWM by concatenating a set of spherical wave functions in the wave function array, that originate from point sources distributed over the aircraft.

5.4 Numerical Study in a Simulated Jet Environment

Unless the jet in a full-scale experiment can be raised up away from the ground or run in a large anechoic chamber, the interference effects from the rigid ground plane must be accounted for in the algorithms. In the current investigation, the properties of the full-scale jet experiment (on the F-22 A Raptor)[61] are simulated using a numerical line source to create a sound field on a large planar aperture near a rigid reflecting surface. Multisource-type representation statistically optimized near-field acoustical holography (MSTR SONAH), presented in Section 5.2, is used to reconstruct the sound field. This section was modified from a 2013 publication in *Proceedings of Meetings on Acoustics* under the name, "Modified statistically optimized near-field acoustical holography for multi-source fields."[125]

5.4.1 Numerical Experiment

In this numerical experiment, the simulated measurement and environment were designed to mimic that of NAH measurements made in the geometric near field of a full-scale jet, including the presence of a rigid reflecting surface.[61] No attempt was made to provide an equivalent source model of a jet. As illustrated in Figure 5.8, the source was a linear array of point monopoles that extended from $z = 0$ to $z = 15$ m, at $x = 0$, and a height of $y = 1.9$ m. An identical image source was simulated below the rigid ground-reflection plane (the *x*-*z* plane) at $y = -1.9$ m. For each frequency investigated, sources were placed one tenth of a wavelength apart to ensure a dense spacing. A Gaussian weighting was applied to the source array amplitudes, and a phase delay was applied to each source to give the array a directivity of 55° relative to the *z*-axis. Field values were calculated by applying the monopole Green's function to each source individually and summing. A numerical hologram was calculated over a planar surface at heights between $y = 0.4$ and 2.2 m and on the diagonal between $(z, x) = (1.6, 6.4)$ and $(24.5, 9.8)$ m. The hologram locations, $\mathbf{r}_h$, were spaced equally in both directions with a spacing of 0.15 m. For each frequency, prior to SONAH propagation, the hologram grid resolution was reduced by removing rows and columns, such that at least 2.5 measurements per acoustic wavelength were ensured. The reduction in measurement points led to an increase in computation speed.

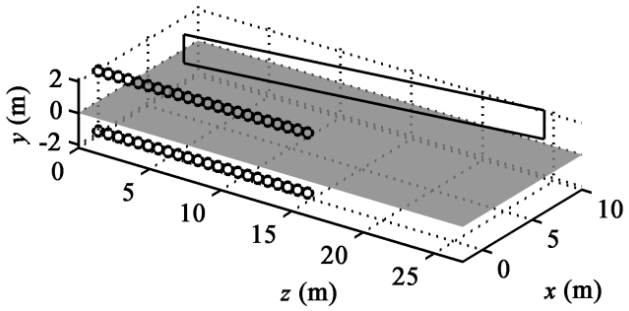

Figure 5.8 Simulation setup. The location of the source array and its image are marked by the circles. The rectangle outlines the hologram location. The gray rectangle represents the rigid reflecting surface.

The MSTR SONAH algorithm, explained in Section 5.2, was applied to reconstruct the sound field near the source. In this case, two sets of cylindrical wave functions were used. Elementary cylindrical wave functions at a given location $\mathbf{r}$ are defined by

$$\Phi_{k_z,n}(\mathbf{r}) = \Phi_{k_z,n}(r,\phi,z) \equiv \frac{H_n^{(1)}(k_r r)}{H_n^{(1)}(k_r r_s)} e^{in\phi} e^{ik_z z}, \quad r \geq r_0\,, \tag{5.26}$$

where $H_n^{(1)}$ is the nth-order Hankel function of the first kind, r_s is some small reference radius (traditionally the assumed source radius), and the radial wavenumber is

$$k_r = \begin{cases} \sqrt{k^2 - k_z^2}, & for\ |k| \geq |k_z|, \\ i\sqrt{k_z^2 - k^2}, & for\ |k| < |k_z|, \end{cases} \tag{5.27}$$

with $k = \omega/c$ being the angular frequency, and $c = 343$ m/s the ambient sound speed. In this experiment, Hankel functions of order $n = 0$ were used, since the sources were axisymmetric. Equation (5.26) was evaluated at all hologram locations with respect to two cylindrical "origins" to form $\mathbf{B}_1 = [\Phi_n^1(|\mathbf{r}_h - \mathbf{r}_0^1|)]$ and $\mathbf{B}_2 = [\Phi_n^2(|\mathbf{r}_h - \mathbf{r}_0^2|)]$, where $\mathbf{r}_0^1 = (x_0^1, y_0^1, z_0^1) = (0,1.9,0)$ m defines the point that is located at $z = 0$ and is collinear with the upper source array, and where $\mathbf{r}_0^2 = (x_0^2, y_0^2, z_0^2) = (0,-1.9,0)$ m defines the point that is located at $z = 0$ and is collinear with the lower source array. These were then concatenated to form the complete hologram wave function matrix, $\mathbf{A}$, as in Equation (5.22). A similar process was implemented to form the complete reconstruction wave function matrix, $\boldsymbol{\alpha}$. An illustration of the (real) values of two wave functions, each evaluated on a cylindrical surface in the respective shifted coordinate systems, is provided in Figure 5.9. (The wave functions shown correspond to a frequency of 100 Hz, the $n = -2$ mode for the top cylinder, the $n = 2$ mode for the bottom cylinder, a k_z value of 1 m^{-1}, and they are shown at cylindrical radii of 3 m. This is shown only as an example. Recall that the expansion was restricted to the $n = 0$ mode.) Finally, SONAH was implemented using Equation (5.17) to reconstruct the near-field pressures. Reconstructions were made over a

two-dimensional surface at a uniform height of $y = 1.9$ m (the same height as the top source array), which extended from $x = 0.1$ to 10 m and from $z = 0$ to 30 m.

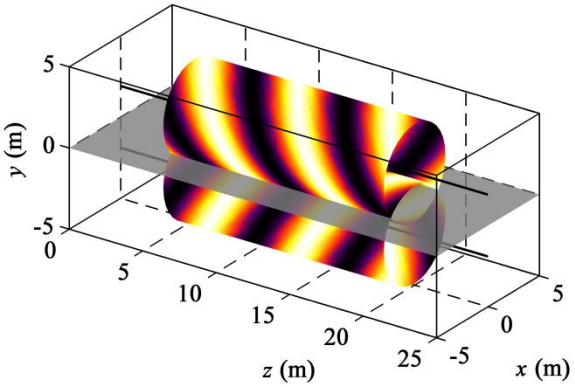

Figure 5.9 Two cylindrical wave functions evaluated over cylindrical surfaces with radii of 3 m. The wave function for the top cylinder is centered on a line collinear with the upper source array (at *y* = 1.9 m), and bottom cylinder is centered on a line collinear with the lower source array (at *y* = -1.9 m).

To evaluate the accuracy of the modified SONAH algorithm for the current experiment, benchmark values were calculated at the reconstruction locations. In addition, a traditional planar SONAH[54] algorithm, and a traditional cylindrical SONAH algorithm[52] with a single origin collinear with the top source array, were applied to the same data. As a final analysis of the accuracy of the modified SONAH algorithm, reconstructions were performed for several frequencies to determine the frequency range over which this algorithm is successful for the current numerical experiment.

The numerical source arrays here (as well as full-scale jets) represent sources of large extent. For the lower frequencies investigated, the width of the hologram aperture (in the *z* direction) was insufficient to prevent large errors resulting from edge effects. Hence, several aperture-extension techniques[122] were applied to the measured data, prior to holographic projection. A linear prediction algorithm[123] was used to numerically extend the effective aperture size by about 20 m in both the directions of increasing and decreasing *z* prior to MSTR SONAH. For the planar SONAH case, the aperture extension process described by Wall *et al*.[56]

was applied to the data, which includes a "mirror" of the data over the reflecting plane, then outward extrapolation using the analytic continuation method.[118] Prior to the cylindrical SONAH implementation, analytic continuation was applied to extrapolate the data 0.3 m in the positive and negative *y* directions, and about 20 m in the positive and negative *z* directions.

5.4.2 Results

The sound field from the numerical line array was calculated at a frequency of 125 Hz, which is the octave-band center frequency closest to the peak frequency in a typical full-scale jet spectrum.[61] SONAH reconstructions of the near field are given in Figure 5.10 and Figure 5.11. All levels shown are calculated relative to the maximum level on the hologram, $p_{\max}$. In addition, the levels that are more than 40 dB below the maximum level (of the benchmark) are excluded from the plot. These locations are indicated by the white space, which is sometimes found at interference nulls. For each plot, the *x*-axis is on the right side, with values increasing toward the left. A benchmark from the numerical model is provided in Figure 5.10a, against which reconstructions of the field can be compared. Note the directionality of the radiation and the presence of a null along $x \approx 4$ m, due to destructive interference from the image source array. The white dashed line marks the location of the vertical hologram, projected onto the *x*-*z* plane, for this and subsequent figures. Figure 5.10b shows the reconstructed field after the implementation of the modified SONAH algorithm, and Figure 5.10c is a map of the level difference (error) between the benchmark and reconstructed levels. The modified SONAH is able to capture the directivity, interference null, and near-source levels. For all high-amplitude regions (within 20 dB of the maximum) the error is less than 2 dB. For comparison, the alternate SONAH reconstructions are given in Figure 5.11. Figure 5.11a shows the near-field reconstruction from planar SONAH, and Figure 5.11b shows its respective error. Note that, near the source (at $x \approx 0.1$ m), the reconstruction levels underestimate the true levels by more than 10 dB. These demonstrate how planar SONAH does not predict the geometrical spreading

(increasing level toward the source) of the field, since the hologram was not close enough to sufficiently capture evanescent wave information in the acoustic near field. In contrast, both the MSTR SONAH and the cylindrical SONAH reconstructions represent the geometrical spreading. However, the cylindrical SONAH method does not account for interference from the secondary source, and therefore does not capture the interference null and distorts the shape of the source region (see Figure 5.11c and d).

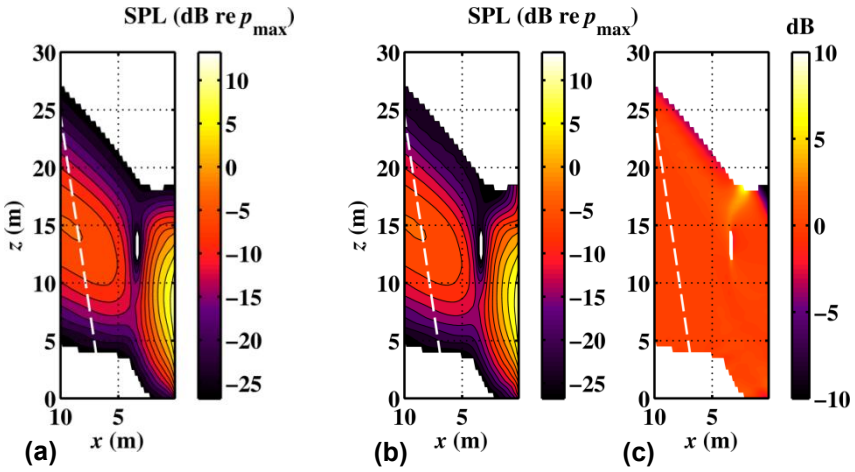

Figure 5.10 MSTR SONAH reconstruction of the numerically generated field at a height of y = 1.9 m, and at 125 Hz. The location of the hologram is marked by the white dashed lines. Levels within the top 40 dB are shown. (a) Benchmark. (b) Reconstruction. (c) Error (dB difference) between the reconstruction and benchmark.

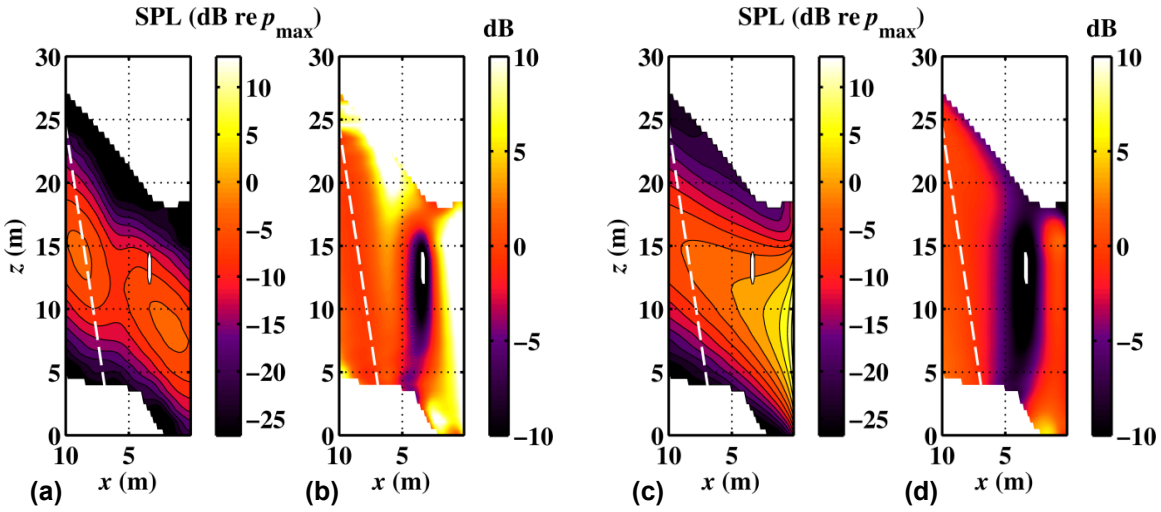

Figure 5.11 Alternate SONAH reconstructions of the numerically generated field at a height of y = 1.9 m, and at 125 Hz. The location of the hologram is marked by the white dashed lines. Levels within the top 40 dB are shown. (a) Planar SONAH reconstruction. (b) Error (dB difference) between the planar SONAH reconstruction and benchmark. (c) Cylindrical SONAH reconstruction. (d) Error (dB difference) between the cylindrical SONAH reconstruction and benchmark.

To provide a further comparison of the three methods, SONAH reconstructions were repeated for 32 Hz and 500 Hz, which are the octave band center frequencies two octaves below and above 125 Hz, respectively. Reconstructions are calculated at the same locations as the 125 Hz case. Consider first the 32 Hz case. A benchmark is provided in Figure 5.12a. Figure 5.12b displays the MSTR SONAH reconstruction, with the error shown in Figure 5.12c. Note that levels near the source array and beyond the edges of the hologram array ($z < 3$ m and $z >$ 23 m) are overestimated, shown by the dark regions in Figure 5.12c. This is likely due to a measurement aperture that does not extend far enough in the directions of increasing and decreasing z to capture the relevant energy in the field. Despite this overprediction, the main features of the sound field are captured accurately, with errors less than 1 dB at most locations.

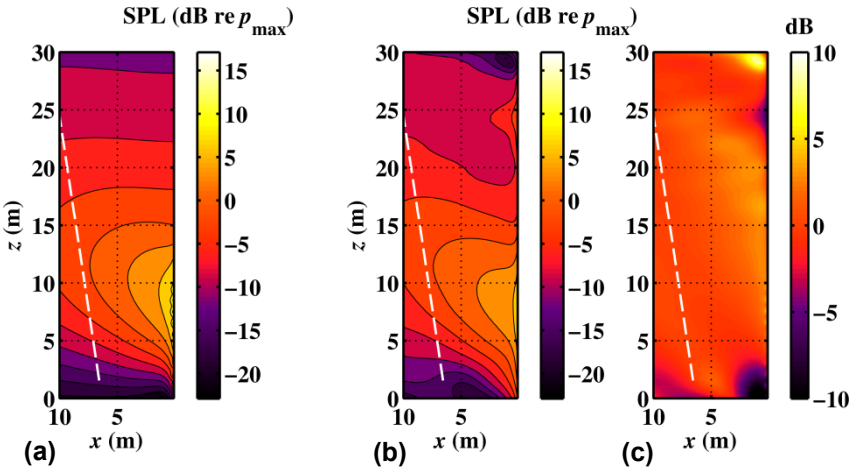

Figure 5.12 MSTR SONAH reconstruction of the numerically generated field at a height of y = 1.9 m, and at 32 Hz. The location of the hologram is marked by the white dashed lines. The color range spans the top 40 dB. (a) Benchmark. (b) Reconstruction. (c) Error (dB difference) between the reconstruction and benchmark.

Planar and cylindrical SONAH were also performed on the 32 Hz source. The planar SONAH reconstruction, with its error, is shown in Figure 5.13a and b, respectively. It is interesting to note that the geometrical spreading of the field (the increase in level toward the source) is captured at this frequency, in contrast to the planar SONAH reconstruction at 125 Hz (compare Figure 5.11a and b). This is because the measurement was performed in the acoustic near field (i.e. the hologram was close to the source, compared to a wavelength). Because of this, the errors are less than 2 dB at most locations. The levels and errors of the cylindrical SONAH reconstruction are shown in Figure 5.11c and d, respectively. Note that the overestimation which occurs near the cylinder origin, which was seen in the MSTR SONAH reconstruction, is more dramatic here, indicated by the larger black regions in Figure 5.11d. Despite this shortcoming, the cylindrical SONAH reconstruction provides a relatively large region where errors remain under 1 dB. In general, the hologram measurement for the 32 Hz case is in the acoustic near field, so accurate reconstructions are easier to obtain for any NAH technique.

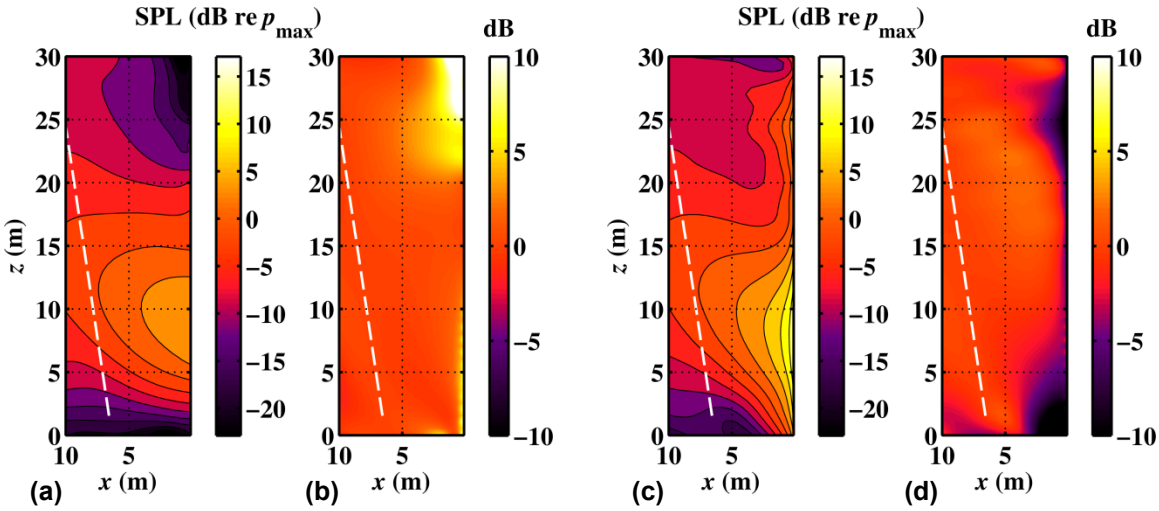

Figure 5.13 Alternate SONAH reconstructions of the numerically generated field at a height of y = 1.9 m, and at 32 Hz. The location of the hologram is marked by the white dashed lines. The color range spans the top 40 dB. (a) Planar SONAH reconstruction. (b) Error (dB difference) between the planar SONAH reconstruction and benchmark. (c) Cylindrical SONAH reconstruction. (d) Error (dB difference) between the cylindrical SONAH reconstruction and benchmark.

Reconstructions of the 500 Hz case are shown in Figure 5.14 and Figure 5.15. Again, the reconstructed field from MSTR SONAH, shown in Figure 5.14b is visually similar to the benchmark of Figure 5.14a. The error shown in Figure 5.14c is nearly 0 dB over most of the field shown, including at $x = 0.1$ m, which is near the source. In contrast, the planar SONAH reconstruction of Figure 5.15a is once again incapable of representing the geometrical spreading, such that the error increases as the source is approached. Cylindrical SONAH is able to represent the spreading, shown in Figure 5.15c, but it cannot account for the interference pattern. Even with the geometrical spreading, the levels at the source (near $x = 0.1$) are underestimated by about 5 dB.

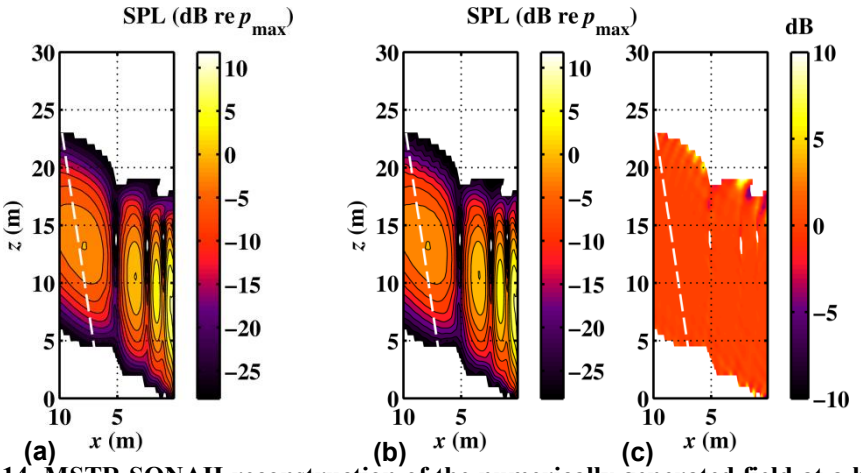

Figure 5.14 MSTR SONAH reconstruction of the numerically generated field at a height of y = 1.9 m, and at 500 Hz. The location of the hologram is marked by the white dashed lines. Levels within the top 40 dB are shown. (a) Benchmark. (b) Reconstruction. (c) Error (dB difference) between the reconstruction and benchmark.

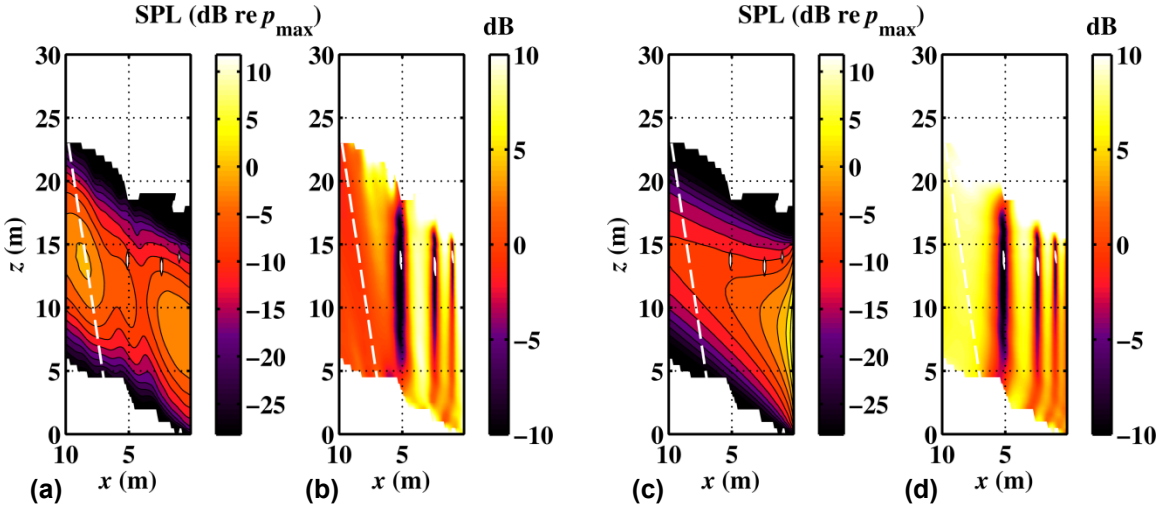

Figure 5.15 Alternate SONAH reconstructions of the numerically generated field at a height of y = 1.9 m, and at 500 Hz. The location of the hologram is marked by the white dashed lines. Levels within the top 40 dB are shown. (a) Planar SONAH reconstruction. (b) Error (dB difference) between the planar SONAH reconstruction and benchmark. (c) Cylindrical SONAH reconstruction. (d) Error (dB difference) between the cylindrical SONAH reconstruction and benchmark.

Source reconstructions and their respective calculated benchmarks are shown in Figure 5.16 for three frequencies. These are the values that were calculated at a height of $y = 1.9$ m, one quarter of a wavelength from the source array in x, and as a function of location in z. Note

that the error for 16 Hz is less than 1 dB at all locations, demonstrating that this method can be successfully employed down into the infrasonic range. Figure 5.16 also shows less than 1 dB error for the reconstruction at all locations at 1250 Hz, which is the highest one-third octave band center frequency for which good agreement holds. A reconstruction for the next one-third octave band, 1600 Hz, is also shown, and the error exceeds 10 dB in some locations. This is because the requirement for two sensors per acoustic wavelength on the hologram array is no longer met. In fact, the cutoff frequency for a grid with 0.15 m spacing is 1143 Hz, but because sound waves arrive at less than grazing incidence along the hologram array, reconstruction at 1250 Hz is still accurate. The trace acoustic wavelength is more critical than the acoustic wavelength, in this case.

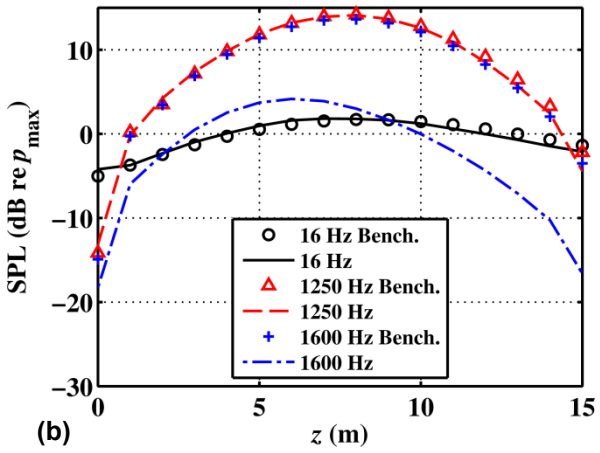

Figure 5.16 (a) MSTR SONAH reconstructions of the numerically generated field at a height of y = 1.9 m and one quarter of an acoustic wavelength from the source for 16, 1250, and 1600 Hz. Benchmark values are shown with markers.

5.4.3 Discussion

A modified SONAH method, MSTR SONAH, which allows for a representation of a sound field with a multiple-source equivalent wave model (EWM), has been presented in this section. This method allows for holographic reconstruction of sound fields from multiple sources with various shapes and complicated distributions. It has been applied here in a

numerical study that mimics the source and measurement configuration of a full-scale jet experiment, where the jet was located near a rigid reflecting surface.[61] For many of the frequencies of interest, hologram measurements were not taken sufficiently close to the numerical source to be considered in the acoustic near field; they did not capture significant evanescent wave information for a successful source reconstruction with traditional NAH methods. However, MSTR SONAH was able to reconstruct the directivity, levels, and interference patterns of the near field. For comparison, MSTR SONAH, traditional planar SONAH and cylindrical SONAH methods have all been employed to reconstruct the same region near the simulated sources. Neither planar nor cylindrical SONAH were able to represent both the geometric spreading and interference patterns of the field. However, MSTR SONAH, with its ability to mathematically account for the image source, was able to reproduce both of these effects.

It is clear that MSTR SONAH provides superior accuracy for an experimental setup like that of the current jet noise problem for a broad range of frequencies. For future application of acoustical holography to the full-scale jet noise experiment, it is desirable to understand the frequency range over which MSTR SONAH returns a reliable reconstruction. This has been explored for the current numerical line sources and hologram geometry. An investigation of the reliable frequency range has determined that MSTR SONAH can accurately reconstruct the field over seven octaves for this numerical experiment, ranging from the infrasonic regime up to the 1250 Hz one-third-octave band. This cutoff frequency is due to the fact that the hologram must contain two sensors per trace acoustic wavelength.

The MSTR SONAH method discussed has been presented here for the first time. Further investigation (not presented in this work) is required to quantify how much the aperture extension, described herein, influences the reconstruction accuracy. The effects of noise on reconstruction results also need to be addressed. In addition, the effects of varying the parameters in the SONAH algorithm, such as the Hankel function orders and the range of axial

wavenumbers included in the EWM, must be explored. An optimization of the expansion is performed in Section 5.5, prior to the implementation of MSTR SONAH on the full-scale jet data.

5.5 MSTR SONAH on Full-scale Jet Data

The implementation of MSTR SONAH on the full-scale jet is the focal point of this work. Holography techniques are useful for characterizing the three-dimensional sound fields and source properties of jet noise, particularly of the LST. The orderly structure of LST makes it approachable from a reduced-order EWM standpoint. Relatively few wave functions can be used to represent the radiation from these long, spatially coherent structures. Since radiation from LST structures tends to dominate the field, their characterization using holography methods holds a prominent place in the efforts to predict and reduce noise emissions from high-power military aircraft.

The full-scale jet studied in this work was measured in the presence of a rigid reflecting plane (the concrete run-up pad), which resulted in interference at the hologram measurement. This interference (image source) can be accounted for in MSTR SONAH, which is capable of representing the contributions of multiple, spatially distinct sources in an EWM with the inclusion of multiple sets of wave functions in a transfer-function calculation between hologram and reconstruction locations. Similar to the EWM discussed in Section 5.4, the field of the jet is modeled here as the superposition of two sets of cylindrical wave functions, one centered on the jet centerline and another on the centerline of the reflected jet image.

First, a brief review of the experiment (explained more fully in Section 2.2) is provided in Sections 5.5.1. In Section 5.5.2, an overview of the holography methodology used on these data is outlined, including the implementation of partial field decomposition (PFD), aperture extension, considerations for the hologram grid points, and the EWM used in conjunction with

MSTR SONAH to reconstruct the sound field. In addition, an optimization scheme for selecting the EWM expansion terms is presented. Sound-field reconstruction results, compared to benchmark measurements, are shown in Section 5.5.3 for 32, 125, and 500 Hz, at military engine conditions. Then, the error of reconstructions is shown over a larger range of one-third-octave center frequencies. For comparison, a brief example of a sound-field reconstruction at 125 Hz using planar SONAH is presented. Finally, a discussion about the utility of the MSTR SONAH method is given in Section 5.5.4.

5.5.1 The Experiment

Researchers at Blue Ridge Research and Consulting and Brigham Young University conducted static run-up tests on the Lockheed Martin/Boeing F-22A Raptor (see Section 2.2.1). The F-22A Raptor has two Pratt & Whitney F119-PW-100 turbofan engines that are each in the 160 kN (35,000 lbf) thrust class. The engines have two-dimensional convergent-divergent nozzles capable of ±20° thrust vectoring. The engine closest to the measurement arrays was cycled through four power conditions: idle, intermediate, military, and full afterburner, while the other engine was held at idle. During the static run-up measurements, the aircraft was tied down in the center of a 24.4 m (80 ft) wide concrete ground run-up pad. More than 6000 measurement points and the repetition of the measurement over four engine conditions make this the most extensive near-field measurement of a jet on a high-performance military aircraft to date.

The field array used in this experiment (see Figure 2.2) allowed for a series of dense, large-aperture, two-dimensional measurements. It was designed and built by Blue Ridge Research and Consulting and was composed of 90 6.35-mm (0.25-in) GRAS 40BE prepolarized microphones, each coupled with a 26CB preamplifier, arranged in 5 rows and 18 columns (when in the horizontal orientation) with 0.15-m (6.0-in) equal spacing. The array had an optional horizontal or vertical orientation, an adjustable height, and was mounted to an extruded aluminum guide rail.

Figure 5.17 describes the field measurement locations relative to the aircraft, and is repeated here for convenience. In addition to the *x* and *z* coordinates marked on the schematic, the vertical axis is represented by *y*, with a positive direction pointing up. The origin of the coordinate system is on the ground directly below the nozzle exit. Red triangles denote the locations of the field array center for each "scan" (see Section. 2.2.6). Planes 1 and 2 were measured by the field array, parallel to the estimated shear layer boundary in a series of scans each covering an area about 2 m by 24 m. The data at plane 2 are used as the hologram in this study. This choice was made because the reliability of some of the data on plane 1 is in question, since these measurements were performed first, and some of the transducers experienced saturation from the rapid rise times of the impinging acoustic shocks (see Section 2.2.5). Its total aperture spanned a planar surface at heights between $y = 0.4$ and 2.2 m, and on the diagonal between $(z, x) = (1.6, 6.4)$ and $(24.5, 9.8)$ m. The grid points were spaced equally in both directions with a spacing of 0.15 m. Plane 1 is used as a benchmark measurement for reconstruction accuracy, and plane 3 is not used in this part of the study. In addition, measurements were made along the arc shown in Figure 5.17 between heights of 1.6 and 2.2 m with the field array at seven locations. All measurement surfaces were located sufficiently far from the flow to render flow-induced noise negligible.

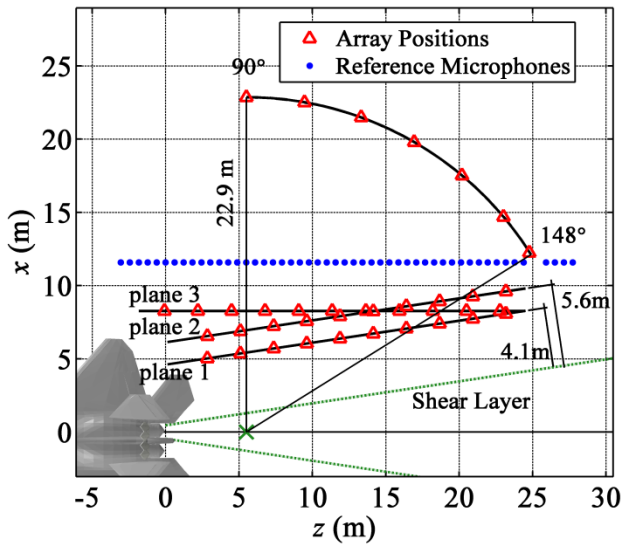

Figure 5.17 Schematic of the measurement locations, relative to the aircraft. The estimated shear layer boundary is marked by green dashed lines, and the green "x" delineates the estimated maximum-noise-source region and the center of the arc.

In addition to the three planar measurements, an arc-shaped surface was measured by the field array in the transition region from the near to the far field, which is also used for a benchmark. The arc was centered at a point 5.5 m (18.0 ft) downstream of the nozzle (marked by a green "*x*"), with a radius of 22.9 m (75 .0 ft). The location of the arc center and the radius of the arc are consistent with measurement locations used by Gee *et al.*[77] in a previous far-field study of the F-22A Raptor. Measurements were made along the arc at a height of 1.91 m and at six locations in 10° increments from 90° to 140°. A seventh location was measured at 148°, because the edge of the concrete pad made a measurement at 150° difficult. All angles reported in this work are measured relative to the front of the aircraft (inlet axis) and to the arc center at z = 5.5 m.

An additional 50 microphones (marked by yellow circles in Figure 2.2 and by blue dots in Figure 5.17) were placed in a fixed-location array to allow for the generation of coherent field measurements from temporally distinct scans. These reference microphones were placed on the ground 11.6 m (38.0 ft) from the centerline of the jet in the x-direction (11.7 m total distance in x

and *y*) and spaced 0.61 m (2.0 ft) apart in the *z*-direction. With references on the ground, multipath interference due to ground reflections was avoided.

5.5.2 Methodology

The method of implementing MSTR SONAH on the full-scale jet data is presented here. It is performed individually for the one-third-octave band center frequencies (narrowband) ranging from 20 Hz to 1600 Hz. In summary, the steps are as follows.

1. Extract complex pressures from recorded pressure waveforms.
2. Perform PFD on the complex pressures to generate partial fields.
3. Numerically extrapolate the pressures of each partial field beyond the measurement aperture.
4. Reduce the grid resolution of each partial field to increase computational speed.
5. Formulate the EWM from the two sets of cylindrical wave functions.
6. Project the pressures of each partial field to desired locations using the SONAH algorithm.
7. Sum the partial fields on an energy basis to produce the total reconstructed field.

MATLAB code for these processes is provided in Appendix C. The details of this process are discussed below. Then, a method for optimizing the expansion terms in the EWM is presented.

5.5.2.1 The Holography Process

First, complex pressures are calculated at the hologram-measurement locations. A time-harmonic sound field is assumed, and a Fourier transform is applied to the recorded waveforms from each microphone on the 90-channel field array. This is repeated for all scans over plane 2, and for all engine conditions. The complex pressures corresponding to the center frequencies of one-third-octave bands are selected from the arrays of pressures at all narrowband frequencies. Examples of these measured pressures are shown in Section 2.3.3.3.

For the second step, recall that a coherent hologram is required in an NAH projection. Hence, the incoherent scans are tied together with the implementation of PFD, based on a singular value decomposition of the 50-channel reference-array data (SVD-based PFD), as explained in Section 3.2. This results in a set of mutually incoherent partial fields, the sum of which make up the total sound field. To capture all the energy in the PFD, there must be as many or more reference microphones than independent sources, and each source must be sensed by at least one reference. The sufficiency of the reference array can typically be determined with the virtual coherence function.[110] Lee and Bolton[74] developed a PFD method, based on SVD and the virtual coherence method, which accounts for both source-level variation and which uses a regularization procedure to filter out noise in the reference pressures. This method is employed here. In general, a representation of all the energy in the field requires an increase in the number of references as the noise in the reference array increases. At 500 Hz and above, the reference array is not sufficient to simultaneously represent all source energy and filter out the noise, which spatial noise results in large propagation errors. This is due either to an insufficient number of references, a lack of azimuthal coverage of the source, or a combination of both (see Section 3.2.5). To mitigate this effect, all singular values after the tenth (out of 50) in the decomposition are removed, which process circumvents the use of the virtual coherence function. This results in a stable NAH propagation, but an underestimation of levels at the hologram and in the reconstructed field at high frequencies, where the decomposition may be considered "over-regularized."

The horizontal aperture of the measured hologram data is insufficient to reconstruct the field below about 100-200 Hz. Hence, in the third step, the data are extrapolated about 20 m in both the directions of decreasing and increasing z (upstream and downstream, respectively) numerically. This is performed with the linear prediction method discussed in Section 4.3. An extrapolation of data in the vertical direction does not improve reconstruction accuracy for any frequency investigated here.

The fourth step is to reduce the hologram grid resolution, for increased computational speed. The greatest factor in computational speed of the MSTR SONAH algorithm, as well as the memory requirements, is the number of points in the hologram. Because NAH represents the sound fields in an EWM manner. That is, the field is expanded into an approximately complete basis set of wave functions, all radiating at the acoustic frequency of the field. In a hologram, there must be at least two microphones per wavelength to capture all possible wave functions. The lower frequencies investigated here do not require a hologram with the dense spacing at which these measurements were taken (0.15 cm). Hence, rows and columns of the data are removed, after the aperture extension, such that there are at least 2.5 hologram points per acoustic wavelength. Note that in this case, requiring only 2 points per wavelength leads to anomalous errors at select frequencies, where the wavelength truly approaches two times the grid spacing. No improvement is found by increasing the requirement beyond 2.5 per wavelength.

Fifth, the EWM is formulated. For the MSTR SONAH implementation, an EWM of the sound field that models the effect of the reflecting ground plane is used. Similar to the field of the numerical source distribution in Section 5.4, two sets of cylindrical wave functions, defined by Eq. (5.26), are included in the expansion, one centered on a line collinear with the centerline of the jet distribution, at a height of $y = 1.9$ m, and a second at $y = -1.9$ m, representing the centerline of the image jet. A truncation of the infinite set of wave functions must occur for the computational implementation. The subset is described by the highest order of Hankel function (positive and negative), $n_{\max}$, that is used in the expansion, and by the maximum (positive and negative) axial wave number, $k_{z,\max}$. An optimization procedure for selecting the subset is described in Section 5.5.2.2.

Sixth, the sound field is reconstructed for all partial fields from the EWM expansion, using the SONAH algorithm provided in Section 5.2.1. The field is reconstructed at planes 1 and 2, and at the arc. The field is also reconstructed at the height of the jet centerline ($y = 1.9$ m), and covering the region from $z = 0$ to 30 m, and $x = 0.2$ to 25 m, and over a (half) conical

surface that is at the approximate location of the shear layer boundary. Seventh, the partial fields are summed on an energy basis to produce the total reconstructed field.

For the measurements and reconstructions shown hereafter, all pressures are scaled on the assumption that they represent the energy contained in the entire one-third-octave band and are transformed to a sound pressure level (SPL), according to the equation

$$\mathrm{SPL} = 10\log_{10}\left(\frac{p^2\frac{\Delta f_{1/3}}{\Delta f}}{(20\times 10^{-6}\ \mu\mathrm{Pa})^2}\right) \tag{5.28}$$

where $\Delta f_{1/3}$ is the bandwidth of the respective one-third octave band, Δf is the bandwidth that results from the Fourier transform processing, and $20\times 10^{-6}\ \mu$Pa is the root-mean-square reference pressure. This is feasible because the narrowband spectrum is broadband and smooth, with no strong tonal content.

5.5.2.2 EWM Expansion Optimization

There is no existing method for predicting the optimal set of wave functions to represent an arbitrary sound field, due to the complexity of an inverse problem. However, the benchmark measurements at planes 1 and 2 and at the arc provide for an optimization scheme for finding an optimal expansion in the current experiment, similar to the method employed by Wu.[47] Field reconstructions are performed, beginning with the plane 2 data, for a range of $n_{\max}$ and $k_{z,\max}$ values. The average reconstruction error is then calculated at each of the three reconstruction surfaces with the following equation,

$$E_{\mathrm{avg}} = \frac{1}{R}\sum_{r=1}^{R}\left|10\log_{10}(|\tilde{p}(\mathbf{r}_r)|^2) - 10\log_{10}(|p(\mathbf{r}_r)|^2)\right|, \tag{5.29}$$

where $\tilde{p}(\mathbf{r}_r)$ is the benchmark, measured pressure at each location, $\mathbf{r}_r$. In an attempt to generate a globally accurate result, the errors calculated for each frequency are summed over all three reconstruction surfaces, and the $n_{\max}$ / $k_{z,\max}$ pair that corresponds to the lowest total error is selected as representing the optimal expansion.

It is insightful to discuss the results of the optimization of the EWM, as a function of frequency. The wave functions of highest azimuthal order that can be represented depend on the azimuthal coverage of the hologram. In general, higher orders require more coverage.[71] For all frequencies investigated here, the lowest error in reconstruction is always returned by an EWM that restricted azimuthal modes to the axisymmetric ($n = 0$) mode. The limited azimuthal coverage of the hologram measurement (not the reference array) makes any expansion of the field into higher modes less accurate than a restriction to the axisymmetric mode. Aperture extension in the vertical direction prior to the inclusion of higher-order modes does not improve accuracy here. Thus, all reconstructions shown hereafter include only axisymmetric modes.

With a restriction to axisymmetric modes, the optimal axial wave numbers, $k_{z,\max}$, are also investigated. As a reminder, in a DFT-based NAH approach, the maximum wavenumber is determined strictly by the grid spacing, Δz, by $k_{z,\max} = \pi/\Delta z$. The values of $k_{z,\max}$ that returned the lowest errors are shown as a function of frequency in Figure 5.18, by the red circles. For comparison, the values of $\pi/\Delta z$ (after the reduction of the grid resolution in the current example) are also shown by the blue triangles. (Recall that Δz varies as a function of frequency, according to a 2.5-sensor-per-wavelegth criterion.) For all frequencies, the optimal $k_{z,\max}$ follows closely the values of $\pi/\Delta z$, which suggests that the requirements of a DFT provides an optimal maximum wavenumber, and an attempt to include more than the array can physically represent leads to higher errors. (The values that deviate from the smooth curve above 400 Hz are simply a result of the grid spacing) Thus, an expansion with a maximum axial wave number $\pi/\Delta z$ is enforced hereafter.

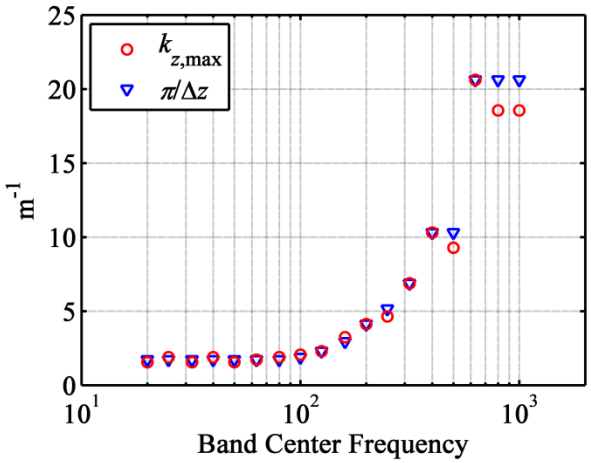

Figure 5.18 Maximum wavenumber in the expansion, $k_{z,max}$, which returns the lowest reconstruction error globally, against frequency. This is compared to values of $\pi/\Delta z$, which is the maximum wavenumber that results in a DFT of the hologram pressures, based on the grid spacing, Δz.

5.5.3 Results

In this section, reconstructions from MSTR SONAH applied to the plane 2 hologram data (5.6 m from the shear layer) are shown first for 125 Hz, which is where peak frequencies occur in the downstream region (see Figure 2.23), for military power. Then, to demonstrate the application of the MSTR SONAH method over a large range of frequencies results are also shown for 32 Hz and 500 Hz, which are two octaves above and below 125 Hz, respectively. Reconstruction error is shown as a function of frequency on both plane 1 (4.1 m from the shear layer) and on the arc (22.9 m from the arc center). For the purposes of comparison, an example of a reconstruction using planar SONAH is also provided for 125 Hz.

The results are shown first for the reconstruction of the 125 Hz-field at plane 1, in Figure 5.19a, compared to the measured benchmark in Figure 5.19b. The contour lines on each of these plots are separated by 5 dB increments. The color map for this and all subsequent level plots in this section span 30 dB, to facilitate comparison. In both the reconstruction and benchmark level maps, the line enclosing the region of maximum level (above 135 dB) extends from approximately $z = 10$ to 18 m. A comparison of the contour lines also demonstrates that the

level variation in the vertical direction is captured by the multi-source EWM, in spite of the fact that only the axisymmetric mode ($n = 0$) is used. Figure 5.19c shows the level difference between the benchmark and reconstructed levels over plane 1, and the black contour lines show the locations where ± 3 dB errors occur. Despite the limitation of this model to the $n = 0$ azimuthal mode, at 125 Hz the reconstruction error is less than 3 dB over almost all of plane 1, as shown by the outlined region of Figure 5.19c. Figure 5.20 is a similar reconstruction and benchmark comparison for 125 Hz, but at the arc location. The boundaries of the region that is within 5 dB of the maximum level, in the reconstruction, is between 130° and 150°+, and the benchmark shows a maximum-level region between 136° and 150°+. The error plot of Figure 5.20c shows that the error is less than 3 dB over most of the arc.

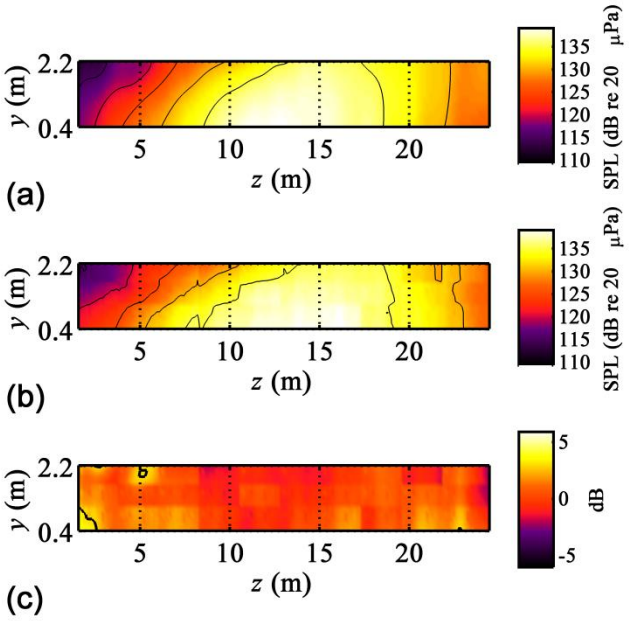

Figure 5.19 MSTR SONAH reconstruction at plane 1 for military power, 125 Hz. (a) Reconstructed SPL. (b) Benchmark measurement. (c) Difference between the reconstructed and benchmark levels in dB. The black line outlines the region where the difference is less than 3 dB. Average error is 1.0 dB.

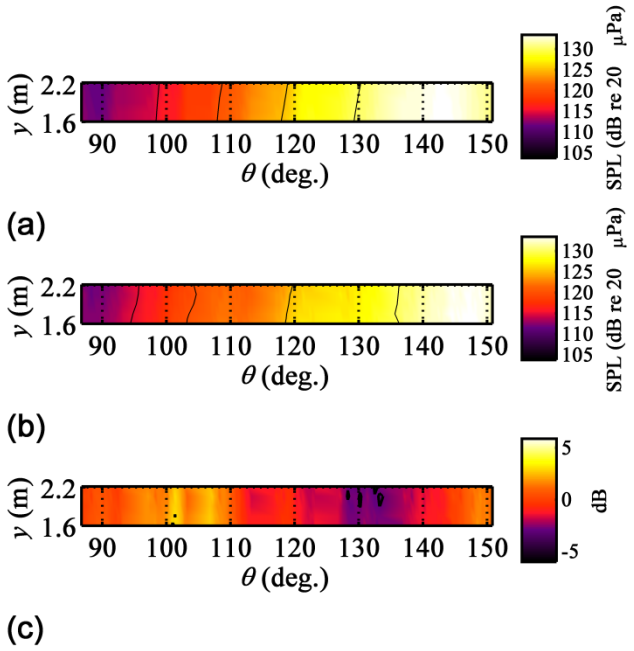

Figure 5.20 MSTR SONAH reconstruction at the arc for military power, 125 Hz. (a) Reconstructed SPL. (b) Benchmark measurement. (c) Difference between the reconstructed and benchmark levels in dB. The black line outlines the region where the difference is less than 3 dB. Average error is 1.4 dB.

One possible explanation for the under-prediction of levels at 125 Hz, on the arc, near 150° is worth mentioning here. Figure 2.23 and Figure 2.24, which are spatio/spectral maps along the reference array for military and afterburner conditions, respectively, contain multiple, localized maxima, separated by null regions. A plausible explanation for this is the presence of multiple, incoherent source mechanisms (more than are discussed in the two-source model), each with its own similarity spectrum, which peak in different locations. The idea of multiple, competing spectral peaks is shown more clearly for this (the F-22A) data set in the work of Neilsen *et al.*,[80] Figures 6 and 7, which show the one-third-octave spectra at military and afterburner conditions, respectively, at 10° increments along the reference array. A shift from 110° to 140° for both conditions shows that there is a clear transition from an initial peak near 300 Hz to the emergence and eventual dominance of a second peak at 125 Hz. Then, at 150°, the spectrum flattens out for military conditions. For afterburner, there seems to be the emergence

of a third peak, centered near 50 Hz. This suggests the presence of a third source mechanism at low frequencies, which is most clearly manifest far downstream. The current data set does not include measurements farther than 150°, so a verification of this is limited, but it is discussed further in context of the PFD results provided in Appendix A.

Figure 5.21 shows a reconstruction of the near-field region of the jet at 125 Hz, including over a half conical surface at the approximate location of the jet shear layer boundary and over a second surface with a uniform height of 1.9 m, which is the same height as the jet centerline. This demonstrates the overall directivity of the source, which, since the high-amplitude regions are accurately located at plane 1 and the arc, can be considered as a true representation. The fringe pattern in both the cone and planar surface is an artifact of the discrete sampling and discrete EWM representation.

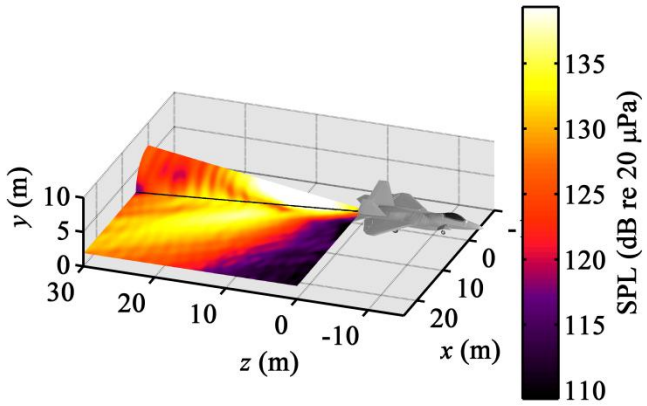

Figure 5.21 MSTR SONAH reconstruction in the vicinity of the jet for military power, 125 Hz. Levels are shown on a half conical surface (toward the side of the measurement) at the approximate location of the shear layer edge and over a plane at y = 1.9 m, the height of the centerline of the jet.

Figure 5.22 and Figure 5.23 show the reconstructions at 32 Hz at plane 1 and at the arc, respectively. The level distribution shown in Figure 5.22a is similar to that of the benchmark in Figure 5.22b, and the error of reconstruction is nearly zero over almost the entire surface. At 32

Hz, it is likely that some evanescent information was captured in the measurement, increasing the accuracy of a near-field reconstruction. The reconstruction at the arc for 32 Hz is, like the 125-Hz case, accurate in the high-amplitude region. However, the level is overestimated by more than 3 dB at angles between about 107° and 120°. This is due to the presence of a slight fringe pattern in the reconstruction, which is somewhat visible in the three-dimensional reconstruction provided in Figure 5.24. Note that the wavelength at 32 Hz is 10.7 m, and the fringes, most easily visible in the orange region running parallel to the beam direction, are equally spaced approximately every 5 m, near one half of the acoustic wavelength. The fringes also cause the null in the forward region (the dark purple in Figure 5.24) They are likely caused by the parsing of energy into wave functions of higher wavenumber, due to an overly sharp drop-off in level at the hologram edges. An improved aperture extension procedure could possibly mitigate this effect.

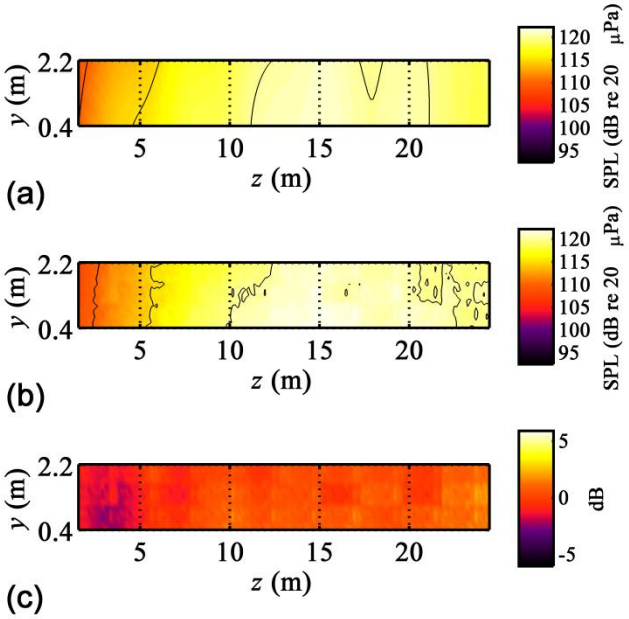

Figure 5.22 MSTR SONAH reconstruction at plane 1 for military power, 32 Hz. (a) Reconstructed SPL. (b) Benchmark measurement. (c) Difference between the reconstructed and benchmark levels in dB. The black line outlines the region where the difference is less than 3 dB. Average error is 0.7 dB.

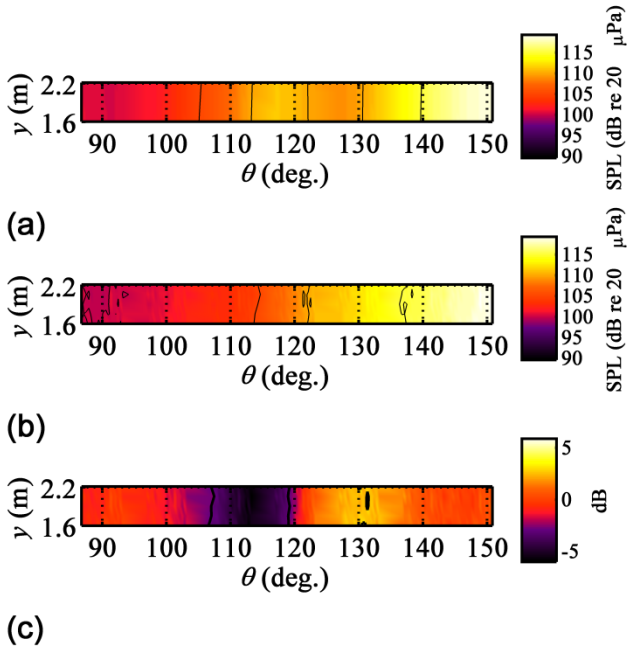

Figure 5.23 MSTR SONAH reconstruction at the arc for military power, 32 Hz. (a) Reconstructed SPL. (b) Benchmark measurement. (c) Difference between the reconstructed and benchmark levels in dB. The black line outlines the region where the difference is less than 3 dB. Average error is 1.7 dB.

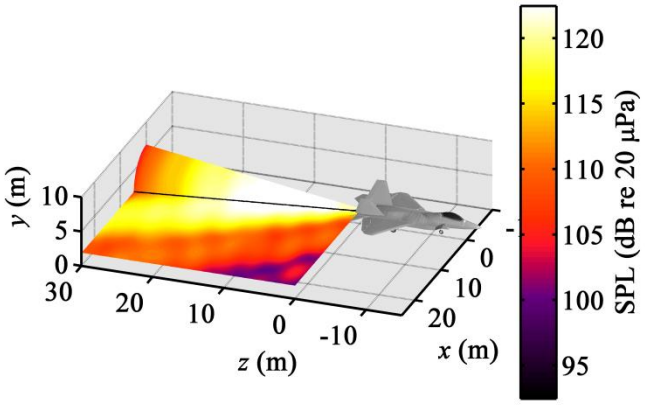

Figure 5.24 MSTR SONAH reconstruction in the vicinity of the jet for military power, 32 Hz. Levels are shown on a half conical surface at the approximate location of the shear layer edge, and over a plane at y = 1.9 m, the height of the centerline of the jet.

Figure 5.25 shows the reconstruction and benchmark at plane 1 for 500 Hz. The incorporation of the reflecting plane in the model allows an accurate placement of the interference pattern; both the reconstruction and benchmark show a high-amplitude region that spans about $z = 4$ to 12 m and an interference null running horizontally near $y = 0.5$ and another near the upper left corner of the array. However, the levels are underestimated over most of plane 1, except in the region of highest amplitude. This is because of the over-regularization of singular values in the PFD, discussed in the previous section. Allowing a less stringent regularization does bring the levels at the hologram (plane 2) closer to the benchmark measurement, but the resulting inclusion of noise causes the NAH projection to be unstable. This problem is likely aggravated by the fact that the reference array is one dimensional along the length of the jet; higher frequencies tend to require higher-order modes for an accurate representation. Despite this limitation, in the regions that are within 20 dB of the maximum level, the error is less than 3 dB. Figure 5.26 shows the 500-Hz arc reconstruction. Note how the benchmark Figure 5.26b shows a relatively wide distribution of levels, whereas the reconstruction is characterized by an over-focusing of energy—the levels are overestimated by more than 3 dB for much of the lower region between 100° and 140°, and are underestimated by more than 3 dB near the upper edges of the surface. Again, this is likely due to the over-regularized PFD, and the inclusion of excess energy into the first partial fields, which are spatially coherent and characterized by strong beaming effects.

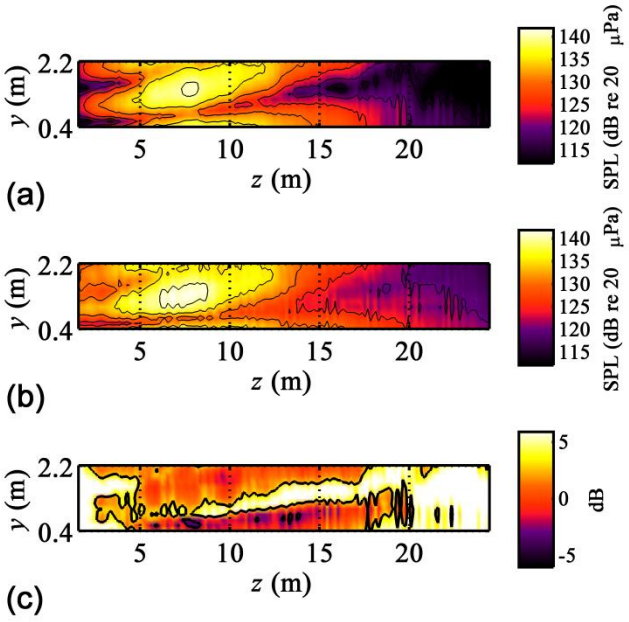

Figure 5.25 MSTR SONAH reconstruction at plane 1 for military power, 500 Hz. (a) Reconstructed SPL. (b) Benchmark measurement. (c) Difference between the reconstructed and benchmark levels in dB. The black line outlines the region where the difference is less than 3 dB. Average error is 3.9 dB.

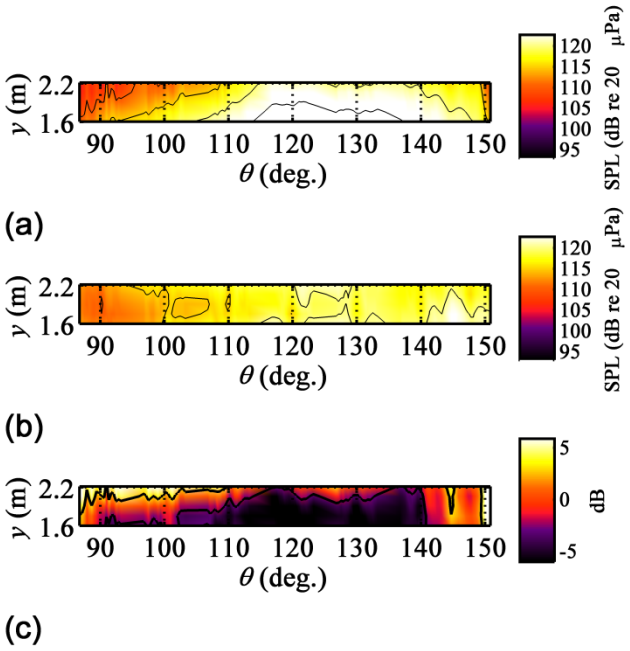

Figure 5.26 MSTR SONAH reconstruction at the arc for military power, 500 Hz. (a) Reconstructed SPL. (b) Benchmark measurement. (c) Difference between the reconstructed and benchmark levels in dB. The black line outlines the region where the difference is less than 3 dB. Average error is 3.5 dB.

Figure 5.27 provides the three-dimensional field reconstruction at 500 Hz. Note the locations of several interference nulls in the beam pattern, which, based on the previous results, are likely located accurately. An extrapolation of the comparisons to the benchmarks at plane 1 and the arc suggest that the field reconstruction shown here likely underestimates the levels globally, except in the region of highest amplitude in the beam far-field, where levels are overestimated.

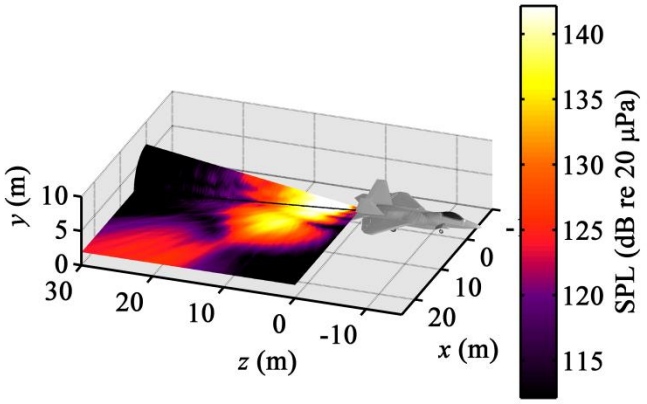

Figure 5.27 MSTR SONAH reconstruction in the vicinity of the jet for military power, 500 Hz. Levels are shown on a half conical surface at the approximate location of the shear layer edge, and over a plane at y = 1.9 m, the height of the centerline of the jet.

Reconstruction errors, obtained by comparison to benchmark levels, are shown in Figure 5.28. The average error, as defined by Eq. (5.29), is plotted as a function of frequency for the three reconstruction surfaces, plane 1, plane 2, and the arc. For most frequencies of 300 Hz and below, the average error at all locations is less than 3 dB, with a gradual increase in error with frequency. Above 300 Hz, the error increases more rapidly. It is at this point where the effect of the truncation of singular values begins to dominate the representation of the field. Hence, it is difficult to assess the accuracy of the MSTR SONAH above these frequencies, for the jet noise field. The errors on the arc for the 20-Hz through 50-Hz cases, which approach 2 dB, are likely due to the insufficient aperture in the horizontal direction.

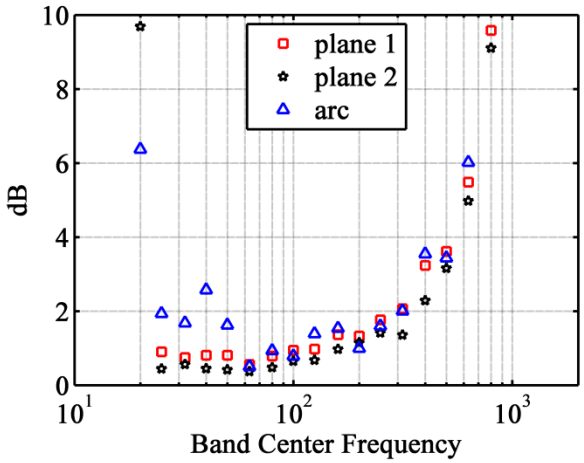

Figure 5.28 Average reconstruction error at plane 1, plane 2, and at the arc, against frequency, when a grid spacing of at least 2.5 microphones per wavelength is enforced.

To verify the utility of MSTR SONAH for this experiment, one example of a planar SONAH reconstruction is provided here. The results of Figure 5.29 and Figure 5.30 are planar SONAH reconstructions of the jet field at 125 Hz, again for the military case.[56] The plane-1 reconstruction of Figure 5.29a shows a high-amplitude region that matches the overall shape of the benchmark in Figure 5.29b, but the contour lines show how the vertical variation is not represented as well as the MSTR SONAH reconstruction in Figure 5.19a. As is shown in the numerical experiment of Section 5.4 (see Figure 5.11 in particular), the levels at plane 1 are generally underestimated, often by more than 3 dB, due to the inability of the planar SONAH to represent the geometrical spreading of the field. Similarly, the planar SONAH reconstruction at the arc, shown in Figure 5.30a, generally overestimates the levels. The planar SONAH method also places the maximum-amplitude region between about 130° and 140°, whereas the benchmark shows it between 135° and 150°+, which is a location error of about 5-10°, but this could also be a result of an additional source mechanism, not fully captured, as discussed previously. The average dB errors are 2.4 and 2.5 dB at plane 1 and 2, respectively, in contrast to the average errors of 1.0 and 1.4 dB in the MSTR SONAH case.

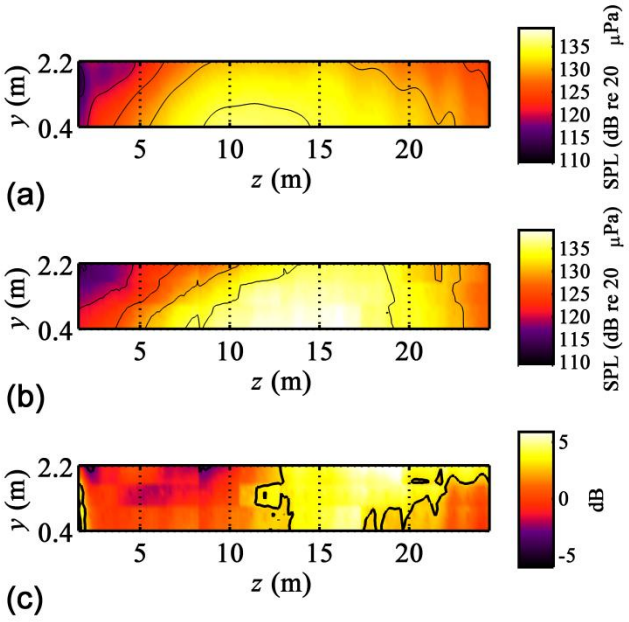

Figure 5.29 Planar SONAH reconstruction at plane 1 for military power, 125 Hz. (a) Reconstructed SPL. (b) Benchmark measurement. (c) Difference between the reconstructed and benchmark levels in dB. The black line outlines the region where the difference is less than 3 dB. Average error is 2.4 dB.

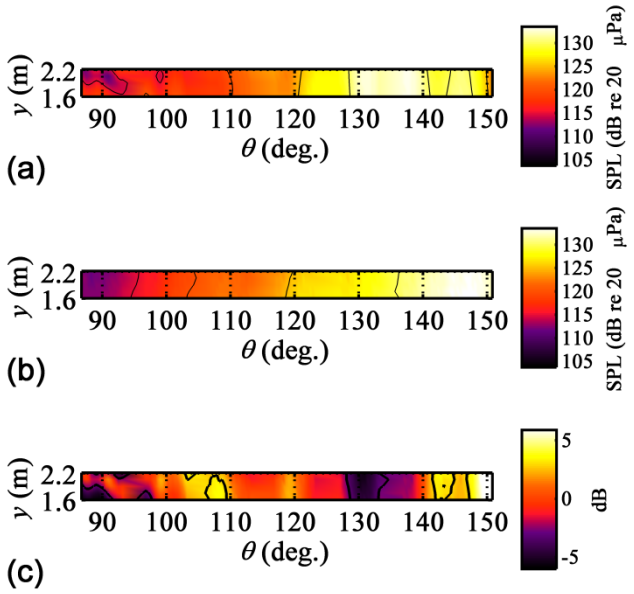

Figure 5.30 Planar SONAH reconstruction at the arc for military power, 125 Hz. (a) Reconstructed SPL. (b) Benchmark measurement. (c) Difference between the reconstructed and benchmark levels in dB. The black line outlines the region where the difference is less than 3 dB. Average error is 2.5 dB.

5.5.4 Discussion

It is important to understand that the measured data for the current experiment on a full-scale jet is not likely the ideal hologram for the source at hand. Rather, it represents a practical measurement setup and a first attempt to perform NAH on such a large scale. Despite these limitations, sound field reconstructions with typical errors less than 3 dB are possible through the MSTR SONAH method, and much insight can be gained about the full-scale jet noise sources and about improved measurement procedures for future NAH jet noise applications. One important insight from this study is that, although the spatial coverage of the source in the downstream direction proved to be sufficient at most frequencies, there is some evidence of a low-frequency source mechanism, not seen elsewhere, that is manifest farther downstream than the extent of the current measurement. This phenomenon is further investigated in Section 7.4 and in Appendix A, but future measurements with greater extent would serve to verify this. This

section has focused on the implementation of the MSTR SONAH method to the full-scale jet problem. More detailed analyses of the sound field and discussions of jet noise properties that are obtained from the present study are reserved for Chapter 7.

The two most critical limitations of this experiment are clearly the azimuthal coverage of the source and the reference array deployment, which might also be improved by a greater azimuthal distribution. The fact that restricting the EWM to axisymmetric modes provided the most accurate result, in spite of the previous studies that have demonstrated significant energy represented by the second and third azimuthal modes,[24-26] suggests that an increase in coverage could capture more critical information. In addition, missing energy at 500 Hz and above could likely be represented by an improved reference-array deployment, either by increasing its azimuthal coverage or by increasing the number of references. The type of errors introduced to the reconstructions of this study that are due to the assumption of a linear source at the jet centerline, as opposed to a volumetric source, is unclear. A future volumetric-source ESM would help to illuminate this issue. On a related note, it is difficult to quantify the accuracy of reconstruction in the region of the assumed hydrodynamic near field (i.e. on the conical reconstruction surface), without benchmark measurements, especially since the data were collected in the acoustic far field for many frequencies. Modified measurement techniques that allow for near-field measurements would result in improved verification, as well as more accurate near-field models.

5.6 Conclusion and Recommendations

This chapter presented a reduced-order EWM approach to near-field acoustical holography (NAH) for complex source configurations. This method, based on the algorithm of statistically optimized near-field acoustical holography (SONAH), is called multisource-type representation SONAH (MSTR SONAH). In general, it allows for the inclusion of wave

functions for multiple, spatially distributed sources. The theoretical development, verification through numerical experiments, and application of MSTR SONAH to a full-scale jet are performed here. In the jet experiment, the sound field is modeled as the superposition of two sets of cylindrical wave functions, one centered on the jet, and the second centered on the image source of the jet that represents the influence of a rigid ground reflection.

The numerical experiment that models the geometry and environment of the jet measurement results in an accurate reconstruction up to the 1250-Hz one-third-octave band (see Figure 5.16), but average reconstruction errors in the physical experiment exceed 3 dB at 400 Hz and higher. However, the inaccuracies in level do not prevent reasonable representations of the main features of the field at these higher frequencies. The most significant limitations of the physical experiment, which affect the frequency range over which holography is successful, are not related to the MSTR SONAH method, but rather to the deployment of the hologram and reference arrays. First, noise in the data and the restriction of the reference array to a linear distribution along the length of the jet prevent a full representation of the energy in the hologram, after implementation of a partial field decomposition (PFD). To prevent the resulting reconstruction from diverging, a truncation (over-regularization) of the singular values is necessary.

The second significant limitation is the azimuthal coverage of the jet by the hologram array. It was demonstrated by Vold *et al*.[71] that high-order azimuthal modes can often be measured with limited azimuthal coverage, but the accuracy of such a measurement degrades with an increase of noise. They show that, in the presence of noise, an increase of angular coverage of a jet causes a decrease in error of the estimate of the azimuthal modes. In general, larger coverage is required for higher modes. This has implications for the design of measurement arrays in future measurements. Since most modal-decomposition methods for LST sources require the inclusion of only up to the second or third modes,[24-26] it is likely that less than 180° coverage, which Vold *et al*. claim is always sufficient, is necessary for a full-scale jet

measurement. However, a quantitative estimate of the coverage required is difficult to obtain from the present data set.

The results of the MSTR SONAH implementation are instructive for future applications of NAH to jet sources. Based on the analyses presented here, the following recommendations are made for full-scale jet NAH experiments. Adherence to these guidelines will ensure an accurate characterization of the radiation from LST structures.

1. Properly crafted EWMs, such as MSTR SONAH, can be used to include the effects of a reflecting ground surface. Hence, it is not necessary to measure a full-scale jet in an anechoic environment or far from the ground, which would increase the cost and difficulty of a measurement. Although not performed here, it is feasible that accurate source reconstructions can allow for the isolation of the reflection effects in the future.[97]
2. Given a limited number of measurement points, the hologram-grid spacing should be sufficiently dense to ensure slightly more than 2 (2.5 was sufficient here) microphones per acoustic wavelength for the highest frequencies, which could exceed several kHz (see Section 2.3.3.3); the aperture should extend from as far upstream as the nozzle to several meters beyond that of the current hologram (say, 30+ m), to capture the lowest-frequency components; and the azimuthal coverage should extend as far as possible to represent second and perhaps third-order modes. One way to achieve greater azimuthal coverage with a fixed number of measurement points is to move the hologram array closer to the source, so long as the transducers are capable of recording the higher levels that result (see Section 2.3.5).
3. The azimuthal distribution of references should reflect at least as much angular coverage of the jet as does the hologram array to ensure it captures the energy present in the hologram. The number of references required in such an array is difficult to predict, but

may be estimated through an analysis of measured coherence lengths in the geometric near field of the jet, as presented in Section 3.3.

This chapter focused on the development and utility of MSTR SONAH. A partial field decomposition method that separates the reconstructed data into physically meaningful partial fields is presented in Chapter 6. Then, a discussion of jet noise properties obtained from holographic reconstruction and partial field decomposition is included in Chapter 7.

Chapter 6

Optimized-location Virtual Reference Partial Field Decomposition (OLVR)

6.1 Introduction

Jet noise emitted by military aircraft is a major source of hearing loss for military personnel, especially those who work on the deck of an aircraft carrier. The overall jet noise source region is comprised of an ambiguous number of extended, partially spatially coherent subsources. This chapter presents an attempt to isolate individual components of jet noise as a step toward the identification of independent source mechanisms. This has application to noise-reduction methods that are targeted towards specific, physical source mechanisms. Significant portions of this chapter are modified from a 2012 publication in *Proceedings of Meetings on Acoustics* under the name "Partial field decomposition of jet noise sources using optimally located virtual reference microphones,"[128] although the results presented here are new.

More than six decades of research have gone into understanding the acoustic source mechanisms of turbulent mixing noise in jets. One analysis tool that has been employed is the partial field decomposition (PFD) of sound fields, based on the theory of principal component analysis,[62,129] in conjunction with near-field acoustical holography (NAH).[55,56,60,72,106] Through

the use of a projection of the sound field onto a linearly independent basis set, PFD allows for the decomposition of a total sound field into a set of mutually incoherent partial fields, the sum of which returns the magnitude of total sound field. In a scan-based measurement, where the entire aperture of "field" pressures is comprised of a series of small, dense measurements, the scans are performed simultaneously with measurements at a fixed-location "reference" array. The pressures measured at these reference microphones serve as the basis for the PFD.

PFD has been often employed to simplify the representations of partially coherent jet sources (usually called proper orthogonal decomposition, or POD, in the literature dealing with turbulent flow measurements). Decompositions have historically been performed for various quantities in the jet field, including directly measured flow quantities, the pressure signatures of the hydrodynamic (or acoustic) near field, and acoustic quantities outside this regime. For example, a POD procedure was first proposed in 1962 by Lumley[65] to investigate structure in turbulent flow. Then, Glauser *et al*.[66,67] developed a method for performing a POD of directly measured flow structures in the 1980s. The application of POD methods to decompose the pressures at the outer edge of the jet shear layer (the hydrodynamic regime), which method will be distinguished here as a PFD, was first performed in 1981 by Long *et al*.[68] PFD was applied by Arndt *et al*.[69] to a hydrodynamic pressure measurement, which demonstrated that the decomposed eigenfunctions grow, saturate, and decay within about three wavelengths for any frequency. In a similar near-field measurement, Suzuki and Colonius[26] showed how the partial field that had the greatest eigenvalue matched their instability-wave model (in the high-amplitude region) when the field was dominated by one coherent source. Freund and Colonius[70] demonstrated a wave-packet structure from a PFD of near-field quantities in simulated jet data. For some examples of acoustic measurements made outside the hydrodynamic regime, Lee and Bolton[55] performed a PFD of measured pressures in the acoustic field around a laboratory-scale jet to allow for a SONAH reconstruction of the jet field. In addition, Shah *et al*.[60] demonstrated the general trend that more partial fields are required for decompositions of jet noise fields at

higher frequencies. Vold *et al.*[71] developed a model of a jet using random azimuthal distributions of "sound flares," or single, random, fluidic dynamic events in a turbulent flow. They then performed an eigendecomposition of the autospectral matrix of pressures outside the jet, and presented the weighted eigenvectors as partial fields.

Several types of PFD methods exist, each based on a different type of basis set for the decomposition. Theoretically, the sum total of partial fields, on an energy basis, will give the same result: a total field with the same levels as the original measured field. However, the partial fields generated are not unique. Hence, to understand the significance of individual partial fields, the basis set and decomposition method must be understood. In general, a PFD of an arbitrary sound field does not generate partial fields that are "physically meaningful," i.e., that represent independent source components, even if those sources are well-separated spatially. This is because each transducer in a measurement array receives information from multiple subsources. The PFD applications that most successfully generate physically relevant partial fields are performed with a set of reference transducers located close to individual subsources, which emphasizes the contribution of a single source to each reference measurement.

In consideration of a jet noise source, such a reference deployment is not feasible. The definition of what constitutes an independent source in a jet is ambiguous, since a turbulent flow field represents a "smearing" of extended sources with spatially decaying coherence. It cannot be described as a single coherent source, nor as a distribution of completely independent sources, but lies somewhere in between. Because of this fact, and the fact that references receive information from all source components, the resulting partial fields from the PFD methods described above are not typically physically meaningful, even though they are linearly independent.

In this chapter, a PFD method is discussed that attempts to isolate what might be considered "independent" sources. Kim *et al.*[64] developed a method that is called here the optimized-location virtual reference method (OLVR), which is a post-NAH PFD procedure that

makes it possible to identify optimal reference sensor locations and then to place "virtual references" at those locations. Other PFD methods that utilize virtual references exist,[63,109,110] but this one was developed specifically to find the optimal virtual reference locations. The optimal locations are defined as those at which the multiple signal classification (MUSIC) power[130] is maximized in the three-dimensional region near the source. The MUSIC power quantifies the likelihood of finding an actual source in a set of candidate source locations. Since the pressures at these candidate locations cannot be measured directly, the necessary sound pressures for the MUSIC algorithm are obtained from a projection of the measured sound field toward the source with NAH. The projected pressures at these optimal locations then serve as the virtual references. Insofar as the optimized virtual references are located near actual sources, when the sound field is decomposed using the virtual references as a basis set, the result is a set of physically meaningful partial fields.

Holographic projection of the jet noise field for a full-scale military aircraft was done previously, using a planar statistically optimized near-field acoustical holography (SONAH) method,[56] as well as with the multisource-type SONAH (MSTR SONAH) method (see Section 5.5). The full-scale jet used in this experiment was measured over a rigid reflecting plane (a concrete run-up pad). Planar SONAH represented a first attempt to reconstruct the field by assuming an image source from the reflection, "mirroring" the measured data over the ground plane, and projecting data into the field with a plane-wave expansion. OLVR was then applied to decompose the jet field from this reconstruction, which results are published in Reference 128. MSTR SONAH improved upon the planar SONAH reconstruction by modeling the field as the superposition of two sets of cylindrical wave functions, one centered on the jet centerline and the other on the image centerline. For the present full-scale jet measurement, the MSTR SONAH results are generally more accurate than the planar SONAH results (see Sections 5.3, 5.4, and 5.5.3). In this chapter, OLVR is implemented on these latter reconstructions.

Section 6.2 provides a brief overview of the OLVR implementation procedure that is employed in this work. Because the theory is described in detail by Kim *et al*.,[64] a summary of the methodology is provided here for completeness and to provide context for the modification to their method. In the selection of candidate references, multiple locations very near a source can be "good" virtual reference locations, and thus will return high MUSIC powers. Kim *et al.* recommend that the redundant virtual references, characterized by large coherence, be removed, leaving only the one with highest MUSIC power for each source. In the case of spatially distinct sources, this process is straightforward. However, in a jet noise field, the spatial coherence is characterized by gradual changes and no clear source distinctions. Hence, in the present work, an algorithm for the removal of redundant references that accounts for partial spatial coherence is developed. The full-scale jet noise experiment on which the OLVR analysis was performed is summarized in Section 6.3. (Detailed descriptions of the experiment were provided previously in Section 2.2.) OLVR is applied to the full-scale jet data at 125 Hz and 400 Hz for military engine conditions in Section 6.4. The application of OLVR to additional frequencies and engine conditions is reserved for a comprehensive jet noise analysis in Chapter 7. In Section 6.4, the NAH reconstruction, virtual reference selection, and decomposition of the field are shown. Partial fields are shown for the three-dimensional sound field and are also used to model independent source distributions. Evidence for the presence of multiple independent source mechanisms is provided, which cannot be distinguished in an NAH reconstruction alone. In addition, the partial fields that result from the SVD-based PFD are shown to demonstrate the ability of OLVR to produce physically meaningful partial fields. A summary of key findings is provided in Section 6.5.

6.2 Methodology

The OLVR procedure relies on the sub-processes of back propagation toward the source through the use of NAH, a PFD method based on a singular value decomposition (SVD-based PFD),[63,110] the MUSIC algorithm,[130] and the Gauss elimination technique (Cholesky decomposition) that is integral to a second PFD algorithm, called partial coherence decomposition (PCD).[131] In the following discussion of each step, it may be helpful for the reader to refer to the process outlined in Figure 6.1. Note that, like NAH, the OLVR process is performed independently for each frequency. A sample code for OLVR processing is provided in Appendix C.6.

A. NAH sound field reconstruction
   1. *Perform SVD-based PFD of measured hologram data.*
   2. *Propagate each partial field using NAH.*

B. Selection of virtual reference locations
   1. *Select "candidate" virtual reference locations.*
   2. *Calculate the noise subspace of the candidate virtual references.*
   3. *Calculate the MUSIC power for each candidate virtual reference location.*
   4. *Select virtual reference locations with high MUSIC power and low total coherence.*

C. Generation of partial fields
   1. *Perform a Cholesky decomposition of the virtual references.*
   2. *Project sound field signals onto decomposed reference basis.*

Figure 6.1 Outline of the virtual reference methodology for generating physically meaningful partial fields.

6.2.1 NAH Sound Field Reconstruction

The first step in the OLVR process is to perform an NAH reconstruction of the three-dimensional sound field in the proximity of the source. For sound fields generated by multiple, independent sources, a multi-reference PFD procedure must be used to obtain mutually incoherent partial fields before NAH is implemented. Although detailed descriptions of these methods are not provided here, the reader is directed to References 74 and 63, and to Section 3.2 for the theoretical development of SVD-based PFD, and to Section 5.5 for the NAH method applied in this experiment.

In summary, SVD-based PFD provides mutually incoherent partial fields from a measured hologram. An SVD of the cross spectrum of measured complex pressures at the references is performed, resulting in a linearly independent basis. The virtual coherence method[63] is then used to obtain an estimate of the number of source-related partial fields, K, which is an important number in the noise estimation procedure of the following subsection. The singular vectors represent new references, and the measured field is projected onto these new references, which generates a linearly independent set of partial fields contained in the rows of the matrix $\mathbf{P}$. The relative strengths of these partial fields are ordered and monotonically decreasing. Recall that these partial fields do not necessarily correspond to independent sources, even though the partial fields are themselves linearly independent. It should be noted that, in this experiment, the virtual coherence method was bypassed, and the number of singular values in the PFD were restricted to 10. This was due to the insufficiency of the reference array to filter spatial noise from the hologram, as discussed in Sections 5.5.2.1 and 5.5.3.

For clarity in the following discussion, the dimensions of matrices are specified as superscripts in the equations, e.g. $\mathbf{P}^{L\times I}$ where L is the number of partial fields and I is the number of hologram grid points. Each partial field is propagated to a new location using NAH. The acoustic field on a reconstruction surface can be represented by

$$\mathbf{Y}' = \mathbf{H_{yp}P} \ , \tag{6.1}$$

where $\mathbf{Y}'^{R\times L}$ is the matrix containing the entire set of L partial fields reconstructed on the surface at all R reconstruction locations, and $\mathbf{H}_{\mathbf{yp}}^{R\times I}$ is the transfer matrix that relates field pressures on the hologram and reconstruction surfaces. This transfer matrix represents the entire NAH back-propagation procedure,[56] including spatial windowing and aperture extension,[122] regularization,[115] etc. MSTR SONAH is used here, as explained in Section 5.5. MSTR SONAH is an NAH method that incorporates multiple, spatially distinct sources into the wave-function expansion of the field. In this experiment, since the jet was measured over a concrete run-up pad, which introduced a rigid reflection, the sound field is modeled as two sets of cylindrical wave functions, one that is centered on the centerline of the jet, and a second set centered on the reflected image of the jet below the reflecting plane. Such a model accounts for the interference pattern in the hologram measurement, and was shown to provide an accurate reconstruction of the field in Section 5.5.3.

6.2.2 Selection of Virtual References

The virtual references are selected by the experimenter from the reconstructed partial field matrices, evaluated at the reconstruction locations. Virtual references can be placed anywhere in the sound field reconstructed by the NAH projection. If they are selected such that they correspond to independent source regions, then they provide a means whereby the field can be decomposed into the contributions from individual radiators. This is not generally feasible for the SVD-based PFD procedure described above. NAH serves to localize sources in the field, allowing for their separation. The PFD method of Kim *et al*.[64] is an automated optimization method for selecting the locations of the virtual references, which is particularly useful if the exact source locations are unknown. It was successful in identifying the locations of numerical point sources and physical loudspeakers in an experiment, and in isolating the fields radiated by

each of these sources. A variation of this method is implemented here to determine the optimal locations of virtual references in the jet noise field.

From all possible reconstruction locations accessible through an NAH prediction of sound pressures in the field a subset of "candidate" virtual reference locations must be selected. Let the matrix $\mathbf{Y}^{N\times L}$ be the matrix $\mathbf{Y}'^{R\times L}$ limited to a subset of N such points. The intuitive approach is to select all points within a plausible source region. A volumetric region of candidate locations is desirable,[64] because small variations in the location of a reference near a source can impact results. In a jet, sources are extended and don't have a clearly defined location within the shear layer. In this context, the utility of the MUSIC algorithm, described below, is its ability to optimize those reference locations. The implementation given in this paper uses a planar region of candidate locations that extends from near the jet centerline to the region outside the shear layer. Note that the region within the shear layer is characterized by nonlinear turbulent flow, temperature variations, and other phenomena that affect acoustic propagation. Hence, the placement of virtual references in this region may not represent actual source locations, but rather provides an optimal equivalent source distribution for the reconstructed field.

Next, in preparation for the calculation of the MUSIC power, the noise subspace must be estimated at all N locations. To do this, the cross-spectral matrix of the candidate references, using all L partial fields for each reference,

$$\mathbf{S}_{\mathbf{yy}}^{N\times N} = \mathbf{Y}\mathbf{Y}^{\mathrm{H}} \ , \tag{6.2}$$

is decomposed using an SVD to obtain

$$\mathbf{S}_{\mathbf{yy}}^{N\times N} = \mathbf{W}\mathbf{\Sigma}\mathbf{W}^{\mathrm{H}} \ , \tag{6.3}$$

where the superscript H is the Hermitian transpose, and the diagonal elements of $\Sigma^{N\times N}$ are the singular values. The unitary matrix, $\mathbf{W}^{N\times N}$, can be expressed in terms of singular vectors, i.e.,

$\mathbf{W} = [\mathbf{w}_1\ \mathbf{w}_2\ \cdots \mathbf{w}_N]$, where $\mathbf{w}_n^{N\times 1}$ is the *n*th singular vector associated with the *n*th singular value. If there are K independent sources that generate the field, then there are K source-related singular vectors and the noise subspace can be defined in terms of the noise-related vectors, $\mathbf{w}_n$, $(n = K+1 \text{ to } N)$, as

$$\mathbf{R}_{\text{noise}}^{N\times N} = \sum_{n=K+1}^{N} \mathbf{w}_n \mathbf{w}_n^{\text{H}} \quad . \tag{6.4}$$

In terms of a jet, the number of sources is ambiguous, characterized by a gradual tapering of singular values (see Section 3.2.5). The value of K can generally be determined to return a total field that approaches the measured energy within a desired precision using the virtual coherence method.[55,74] However, in this work, limitations in the reference array made such an approach difficult. Hence, as explained in Section 5.5.2.1, K was restricted to a value of 10.

With the noise subspace estimated, the MUSIC powers can be calculated at all locations. All of the eigenvectors are orthogonal, so the subspace spanned by the source-related eigenvectors, $\mathbf{w}_n$ $(n = 1 \text{ to } K)$, is orthogonal to the noise subspace. The calculation of the MUSIC powers, which is the next step in the OLVR process, relies on this fact. To obtain the MUSIC powers, it is first assumed that a source is located at the *n*th point on a reconstruction surface, which is represented by a "trial vector,"

$$\mathbf{u}_n^{N\times 1} = [0\ \cdots 0\ 1\ 0\ \cdots 0]^{\text{T}} \ , \tag{6.5}$$

where T is the matrix transpose. The *n*th element of $\mathbf{u}_n$ is unity, and all other N-1 elements are zero. The MUSIC power corresponding to the *n*th location is then calculated in terms of the trial vectors and the noise subspace as

$$P_{\text{MUSIC}} = \frac{1}{\mathbf{u}^{\text{H}}\mathbf{R}_{\text{noise}}\mathbf{u}} \quad . \tag{6.6}$$

Theoretically, the MUSIC power is infinite when $\mathbf{u}^{N\times 1} = \mathbf{w}_n^{N\times 1}$, $n = 1$ to K, or in other words, when the trial vector represents an actual source distribution exactly. In the case of trial vectors that approximate the singular vectors, the MUSIC power is higher for trial vectors that most closely reflect actual source locations. The calculation of the MUSIC power is therefore repeated for all N candidate reference locations. The optimal virtual reference locations are those at which the MUSIC power is the highest.

Differences between the application of the MUSIC power calculation for traditional, localized sources[64] and for jet noise sources should be considered. The trial vector of Eq. (6.5) represents a point source located at the *n*th position. The application of such trial vectors for a sound field generated by discrete localized sources results in a map of MUSIC powers with discrete localized maxima. However, distributed, partially spatially coherent sources, such as jets, result in spatially extended regions of high MUSIC powers. Sound pressures in these regions can be highly coherent, resulting in redundant virtual references. Therefore, a way is provided to remove redundant virtual reference locations, described below. Alternative trial vectors that represent distributed sources could be developed—a study which merits further investigation.

The removal of redundant virtual references begins by placing virtual references at *all N* candidate reconstruction locations. Then, from the candidate-virtual-reference cross-spectral matrix, $\mathbf{S}_{\mathbf{x}'\mathbf{x}'}^{N\times N} = \mathbf{X}'\mathbf{X}'^{\mathrm{H}}$, where $\mathbf{X}'$is $N \times L$, the coherence between locations i and j can be calculated as

$$\gamma_{ij}^2 = \frac{|S_{ij}|^2}{S_{ii}S_{jj}}, \tag{6.7}$$

where S_{ii} and S_{jj} are the autospectra of references i and j, respectively, and S_{ij} is the cross spectrum between the two. If the coherence between two candidate source locations is nearly unity, then the sources are coherent and the reference at the location of smaller MUSIC power

should be removed. This is repeated until the remaining virtual references are incoherent and equal in number to the number of incoherent subsources. For sound fields of high coherence that gradually tapers away from a maximum over large spatial regions, a coherence threshold is selected, and all but the one virtual reference with the maximum MUSIC power from within the region of high coherence is discarded. The coherence threshold can be selected such that exactly K virtual reference locations remain after the redundancy removal process. The lowest possible threshold that meets this criterion is desirable, so as to most effectively separate independent processes. The result is a set of K references, sorted in order of highest to lowest MUSIC powers, and low mutual coherence.

The next step is to obtain the virtual reference matrix. It is simply made of the partial fields (SVD-based) at the selected virtual reference locations,

$$\mathbf{X}^{K\times L} = \begin{bmatrix} \mathbf{Y}_{R_1} \\ \mathbf{Y}_{R_2} \\ \vdots \\ \mathbf{Y}_{R_k} \\ \vdots \\ \mathbf{Y}_{R_K} \end{bmatrix}. \tag{6.8}$$

where $\mathbf{Y}_{R_k}$ represents the R_kth row of $\mathbf{Y}^{N\times L}$, and R_k is the corresponding index of the kth candidate virtual reference. This formulation is simple to implement in a computational program with matrix operations. Written more rigorously,

$$\mathbf{X}^{K\times L} = \begin{bmatrix} \mathbf{c}_1^{\mathrm{T}}\mathbf{Y}_1 \\ \mathbf{c}_2^{\mathrm{T}}\mathbf{Y}_2 \\ \vdots \\ \mathbf{c}_k^{\mathrm{T}}\mathbf{Y}_k \end{bmatrix}. \tag{6.9}$$

where, from Kim *et al.*,[10] in Eq. (6.9), $\mathbf{c}_m$ "represents the N by 1 reference selection vector: when the mth virtual reference is positioned at the ith field position on the reconstruction surface, all elements of $\mathbf{c}_m$ are zeros, except for the element at the ith row, which is itself unity. Note that

the matrix $\mathbf{Y}_m^{1\times L}$ represents the partial field matrix on the reconstruction surface at which the *m*th virtual reference is placed, and that the vector, $\mathbf{c}_m$, denotes the *m*th virtual reference location on the *m*th reconstruction surface. Thus, the location of the *m*th reconstruction surface in combination with the vector, $\mathbf{c}_m$, determines the location of the *m*th virtual reference in a three-dimensional space." In essence, $\mathbf{X}^{K\times L}$ is comprised of the selected pressures from $\mathbf{Y}^{M\times L}$, corresponding to the respective virtual reference locations.

6.2.3 Generation of Partial Fields

With virtual references selected, they can then be decomposed to form a linearly independent basis set. This is performed with the PCD method, which iteratively allocates and removes energy from the reference cross-spectral matrix. A rigorous mathematical derivation of the PCD technique is provided by Bendat.[131] Hallman and Bolton[132] and Kwon and Bolton[108] provide comparisons of SVD-based PFD (sometimes called the "virtual coherence" method) and PCD. Here, a Cholesky decomposition of the complex pressures of the virtual references is used to perform the PCD, represented by

$$\mathbf{S}_{\mathbf{xx}}^{K\times K} = \mathbf{X}\mathbf{X}^{\mathrm{H}} = \mathbf{L}\mathbf{L}^{\mathrm{H}}, \tag{6.10}$$

where $\mathbf{L}^{K\times K}$ is a lower triangular matrix containing the now linearly independent basis vectors. In essence, all information in the virtual reference set that is coherent with the first reference is taken as the first basis vector. This is then subtracted from the remaining virtual references. A second reference is then chosen, and all remaining information that is coherent with this vector is removed from the set, and so on. Hence, Cholesky decomposition represents an iterative allocation and removal of virtual reference energy.

Finally, the OLVR partial fields are generated from the basis set of the new, decomposed virtual references. The cross spectral matrix between all *M* field points and *K* virtual references is calculated as

$$\mathbf{S}_{\mathbf{xy}}^{K\times M} = \mathbf{X}\mathbf{Y}^{\mathrm{H}} \ . \tag{6.11}$$

The OLVR partial fields are obtained with

$$\mathbf{P}_{\mathbf{x}}^{M\times K} = \mathbf{S}_{\mathbf{xy}}^{\mathrm{H}}(\mathbf{L}^{\mathrm{H}})^{-\mathbf{1}} \ . \tag{6.12}$$

These partial fields, $\mathbf{P}_{\mathbf{x}}^{M\times K}$, are the K physical partial fields radiated by independent subsources insomuch as each virtual reference senses one and only one independent subsource, and insomuch as the NAH reconstruction is accurate.

6.3 Experiment

To demonstrate its utility, OLVR was applied to the NAH measurements of a full-scale jet. A brief summary of the experiment is provided here. See Section 2.2 for a comprehensive description. Sound pressures in the near field of a jet on a Lockheed Martin/Boeing F-22A Raptor were recorded with a 5 x 18 array of microphones, which had 0.15 cm (6 in.) spacing. An approximately 2 x 24 m vertical planar region 5.6 m from the shear layer was scanned, which measurement was used as the hologram for NAH (see plane 2 in Figure 6.2). In addition, 50 fixed reference microphones (blue dots in Figure 6.2) were placed on the ground with 0.6 m (2 ft.) spacing, spanning more than 30 m. Measurements were repeated for four engine conditions ranging from idle to full afterburner. The results of this chapter focus on the components of the sound field radiated at 125 Hz and 400 Hz for military engine power. Figure 6.2 specifies the coordinate system used in this experiment, with the origin on the ground directly below the jet nozzle. In addition to the x and z coordinates shown, the y-axis points up away from the ground. A single jet was operated at military conditions, while the second engine was held at idle.

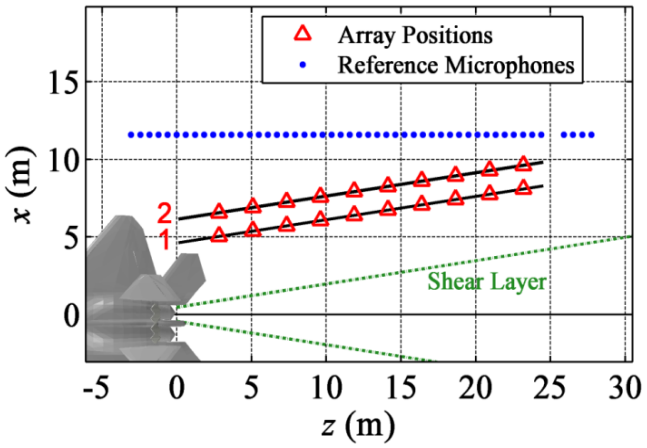

Figure 6.2 Schematic of the hologram measurements relative to the aircraft. Locations of the field array are marked by red triangles. Blue dots show the location of the reference array. Plane 2, which is the measurement used for NAH in this work, has a perpendicular distance of 5.6 m from the approximate shear layer location.

6.4 Results and Discussion

Figure 6.3 shows the total measured SPLs at plane 2 for the 125 Hz one-third-octave band. For all levels shown here, the squared pressures are calculated for narrowband, one-third-octave band center frequency of 125 Hz, scaled by the corresponding one-third-octave bandwidth, and converted to a level. Since the narrowband spectrum of the jet is broadband and void of strong tones, or rapid level changes as a function of frequency, such a scaling can be considered to approximate the energy in the one-third-octave band. The first six corresponding partial fields at plane 2 from SVD-based PFD are shown in Figure 6.4, and in the three dimensional field in Figure 6.5. Note how energy is allocated into the first partial field, due to the SVD. In general, the number of independent source mechanisms, according to an SVD-based PFD, increases as frequency increases.

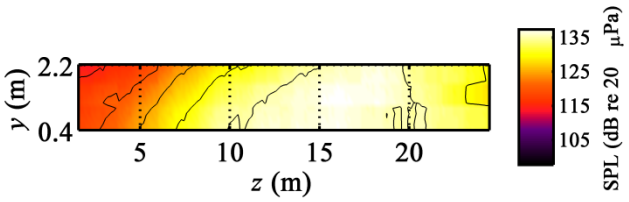

Figure 6.3 Total measured SPLs at plane 2 for 125 Hz, military engine conditions.

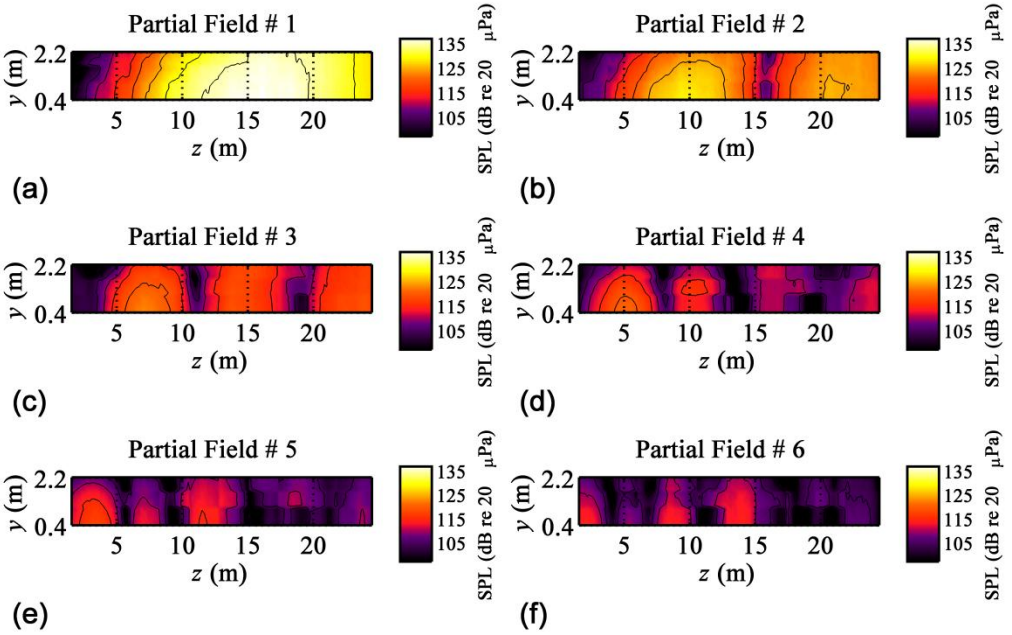

Figure 6.4 First six partial fields from SVD-based PFD at plane 2 for 125 Hz, military engine conditions.

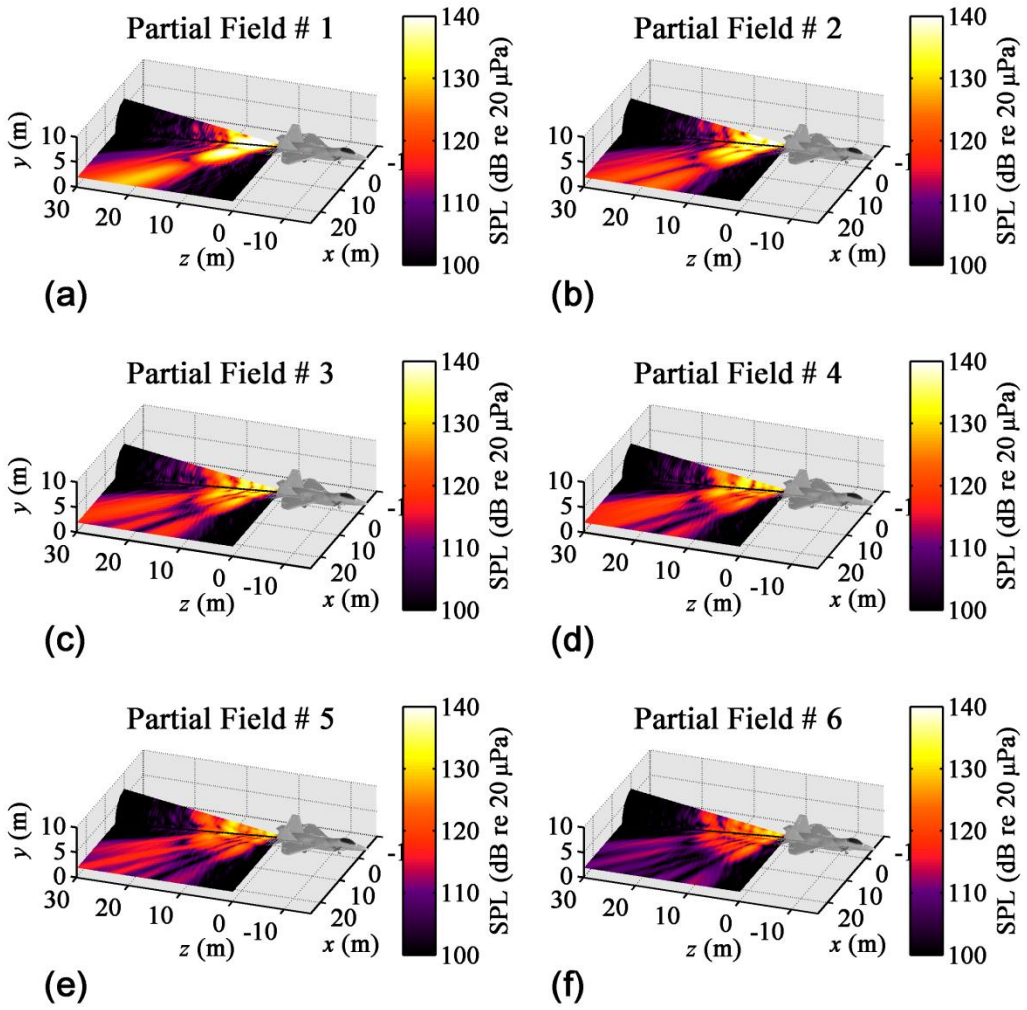

Figure 6.5 First six partial fields from SVD-based PFD over the planar surface defined by *y* = 1.9 m and on a conical surface at the approximate shear layer boundary for 125 Hz, military engine conditions.

In addition, note how the overall shapes of each partial field in Figure 6.4 are highly structured—the first partial field has one maximum region, the second has two regions of local maxima, and so on. In Figure 6.5, these same respective partial fields contain one radiation lobe, then two radiation lobes, then three, and so on. Recall that the reference array used in this PFD is restricted to a linear region along the ground. When an SVD is taken of the cross-spectral

matrix of a linear array, the overall shapes of the singular vectors take on modal characteristics, similar to the shapes of standing waves on a string.[107] These modal-like shapes are reflected in the partial fields as well. Although the partial fields from an SVD-based PFD are completely valid mutually incoherent components that, in total, represent the sound field, the physical interpretation of the individual fields is tenuous, which motivates the OLVR approach.

MSTR SONAH is implemented on each of these mutually incoherent partial fields, using the methods explained in Section 5.5. The reconstructed sound pressure levels (SPLs) in the jet vicinity, at a height of 1.9 m and over the region from $x = 0.2$ to 25 m are shown in Figure 6.6. Black contour lines represent increments of 3 dB. The reconstruction of the field demonstrates a large main lobe radiating in a preferred aft direction. The local minimum near $x = 3$ m and $z = 11$ m, which runs nearly perpendicular to the direction of the main lobe, is a result of the incorporation of the reflecting plane into the field model. The reconstructed partial fields are used in the OLVR method to select virtual reference locations, based on the MUSIC power, and are then decomposed into the new partial fields as described in Section 6.2.

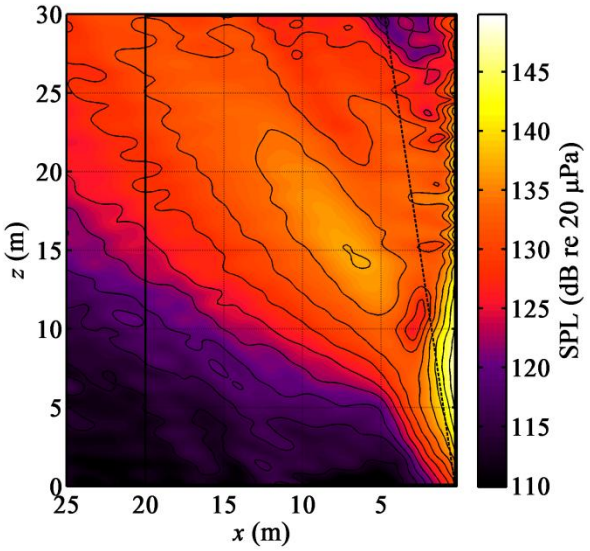

Figure 6.6 Reconstructed SPLs at a height of y = 1.9 m, after the application of MSTR SONAH to the measured data, for 125 Hz and at military engine conditions. Black contour lines are separated by 3 dB increments. The black dashed line shows the approximate location of the jet shear-layer boundary. The black rectangle surrounding x = 0.2 to 20.0 m and z = 0.0 to 30.0 m marks the locations of the candidate locations for virtual references.

Since the hologram aperture for this experiment was limited in its azimuthal coverage of the jet (see Section 5.5.2.2), the candidate locations for the virtual references are restricted to the reconstruction surface shown in Figure 6.6. In particular, the candidate locations are limited to the region between $x = 0.2$ and 20.0 m, and between $z = 0.0$ and 30.0 m, as outlined by the black rectangle. The calculated MUSIC powers at these respective locations are shown in Figure 6.7. Note the broad regions of high MUSIC power, demonstrating the high spatial coherence of the source and the need for a redundancy-removal process.

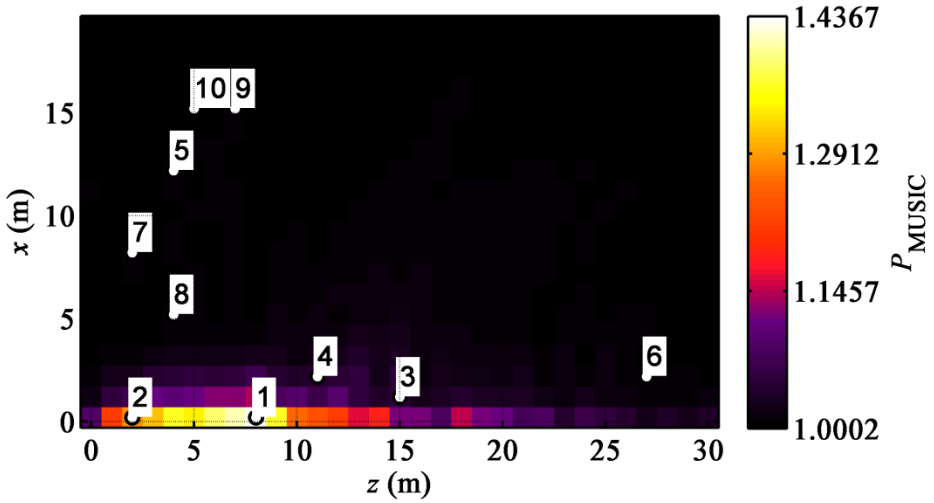

Figure 6.7 MUSIC powers calculated over the y = 1.9 m reconstruction surface for 125 Hz. Markers show the locations of the K = 10 virtual references after the redundancy-removal process.

The numbered markers on Figure 6.7 show the end-result locations of the 10 virtual references, after redundancy removal was implemented. Note that virtual reference 1 corresponds to the location of highest MUSIC power. Without the removal of redundant (coherent) references, reference 2 would have been at the location of the next highest MUSIC power, directly adjacent to reference 1. Here, all virtual references that have a larger coherence with reference 1 than a certain threshold are eliminated from the set. Hence, reference 2 is the location of highest MUSIC power that has a coherence with reference 1 that is below the threshold. Similarly, reference 3 is the location of highest MUSIC power that has coherence with references 1 and 2 below the threshold, and so on. For this frequency, a coherence threshold of 0.30 ± 0.1 is the lowest threshold that results in the necessary $K = 10$ virtual references, which K was chosen as an estimate for the number of partial fields with significant source-related energy. They are appropriately spread out and located near localized maxima of MUSIC powers. Figure 6.8 shows how the coherence between all the resulting virtual references is below the 0.30 threshold. The color range is limited to coherence values between 0 and 0.5, but the diagonal elements are all unity.

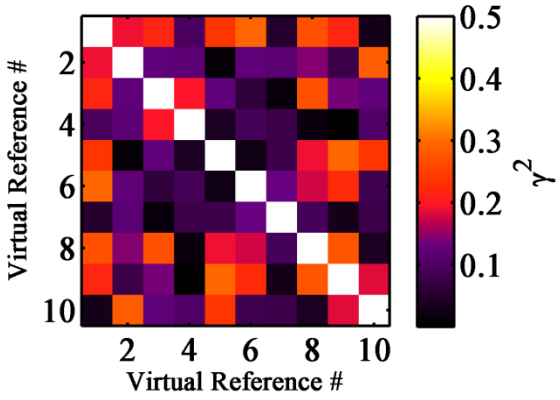

Figure 6.8 Ordinary coherence between the 10 virtual references for the jet field at 125 Hz at military engine conditions. A coherence threshold of 0. 30 ± 0.1 is selected for the redundancy-removal process. Color scale is limited from 0 to 0.5.

The Cholesky decomposition of the virtual references is demonstrated in Figure 6.9 and Figure 6.10. The level magnitudes of the virtual reference vectors in **X** are shown in Figure 6.9. The decomposed vectors, **L**, are shown in Figure 6.10. Their linear independence is demonstrated by the triangular nature of the matrix.

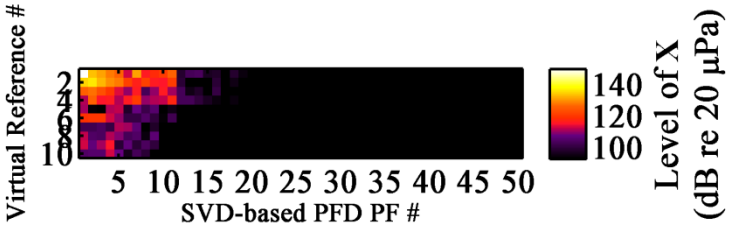

Figure 6.9 Ten virtual reference vectors, X, (magnitude in decibels) for the 125 Hz, military engine condition case.

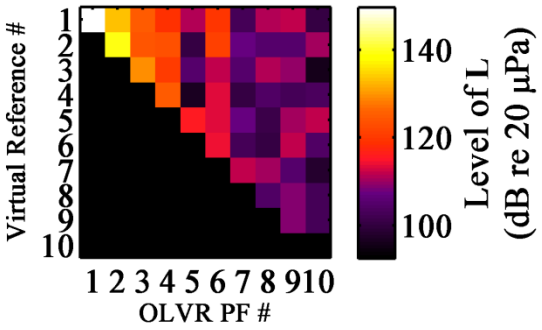

Figure 6.10 Cholesky-decomposed virtual reference vectors, L, (magnitude in decibels) for the 125 Hz, military engine condition case.

Figure 6.11 shows the total reconstructed field from NAH in three dimensions for the case of 125 Hz and military engine conditions, including the reconstruction on a conical surface surrounding the approximate shear-layer boundary. Figure 6.12 shows the first six partial fields (PFs) that are generated with the above virtual references, from this reconstruction. A comparison of the strengths of these PFs reveals that the radiation at 125 Hz and military engine conditions is dominated by about four independent sources, represented by PF 1 through 4. The radiation lobe of PF 1 points farther downstream than does the lobe of, say, PF 2, by about 10-20°. It is important to note that these four main independent components are not resolvable in the overall field of Figure 6.11, where they combine to make one wide lobe (dominated by PF 1), nor is this distinction clear from an SVD-based PFD, as demonstrated by Figure 6.4 and Figure 6.5. Only in the PFD based on virtual references located near the jet sources is this apparent. In addition, some low-magnitude information is contained in the remaining PFs, demonstrating that these main sources are not perfectly spatially coherent themselves.

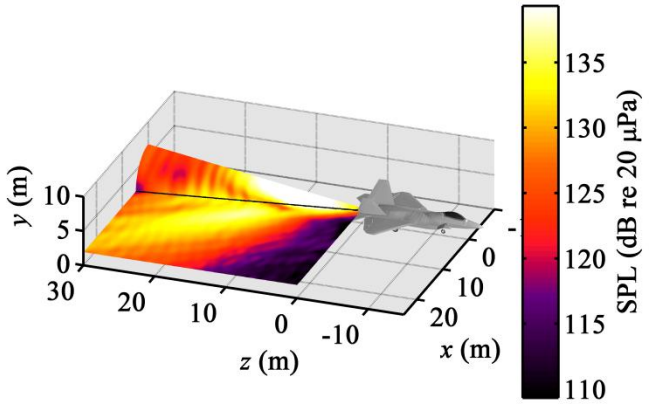

Figure 6.11 Reconstructed SPLs in the jet vicinity, after the application of MSTR SONAH to the measured data, for 125 Hz and at military engine conditions.

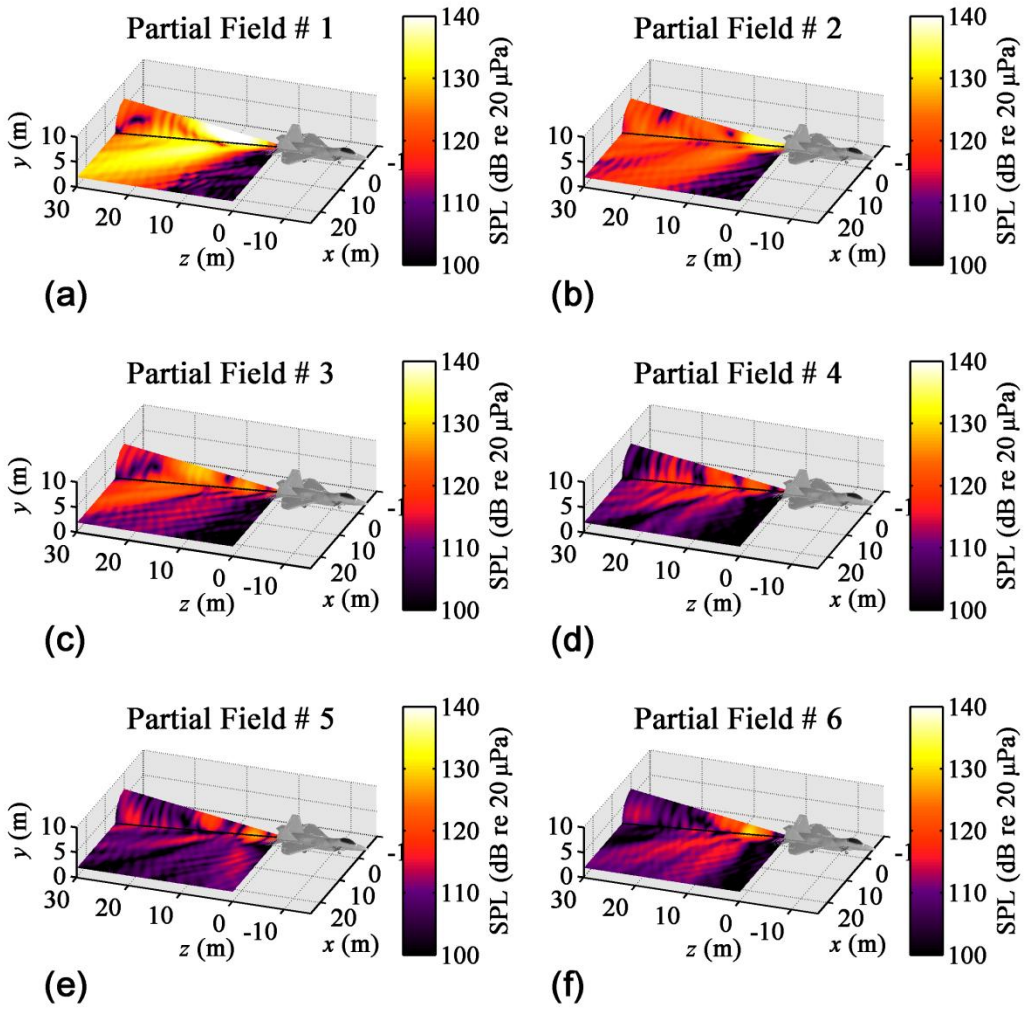

Figure 6.12 The first six partial fields generated from OLVR on jet noise data at 125 Hz and at military engine conditions.

A similar two-lobe decomposition can be seen in the implementation of OLVR on the planar SONAH reconstruction of the jet field at 105 Hz, for military engine conditions, found in Figure 11 of Reference 128. In that publication, difficulties in the holography implementation introduced errors into the reconstruction region between the measurement and source regions. This made the results of the decomposition unclear. It was explained that the first and second

partial fields contained energy from the same dominant source, which was so decomposed because it was partially spatially coherent. However, a careful inspection of those partial fields shows that the two partial fields are likely two different radiation mechanisms. They too are characterized by a difference in directivity of about 10-20°, and the locations and relative strengths of each lobe is similar to the respective lobe shown here at 125 Hz.

Care must be taken in the interpretation of the independent PFs generated by OLVR. It is possible that the double-lobe scenario described above could be attributed to one partially spatially coherent source mechanism. In such an interpretation, two well-separated virtual references (see reference locations 1 and 4 of Figure 6.7) that are both in the region of a source with spatially decaying coherence (which has been demonstrated in jet field measurements and jet models[71,133]) could result in two seemingly "independent" lobes emitted by the same source. For example, the 10-20° difference in directivity could be explained in the context of Mach wave radiation. An extended object with an irregular surface that convects at supersonic speed will emit highly directional sound waves. This is often called the "wavy wall" interpretation of large-scale jet noise sources.[13,18] The directivity angle of such radiation is dictated by the convection velocity—faster objects emit radiation closer to perpendicular to the direction of travel. Hence, it is logical to guess that the lobe of PF 1 comes from turbulent structures that have slowed down as they have moved farther downstream compared to the faster-moving structures of PF 2, which originate closer to the nozzle.

However, there is further evidence to support the idea that these lobes are caused by truly independent source mechanisms. There is a clear separation in the spatial/frequency levels measured by the ground-based reference array at military engine conditions, as shown by the null region of Figure 6.13, which suggests the existence of multiple source mechanisms contributing to the overall field. The spatial locations of the local maxima on the reference array (measured along $x = 11.6$ m) correspond well to the respective maximum regions in the two lobes shown here, as marked by the stars. The spatial distinction is more pronounced at higher frequencies,

particularly 200 Hz where the double-lobe is evident in the total field as well as the decomposed PFs, which results are presented in Appendix A.

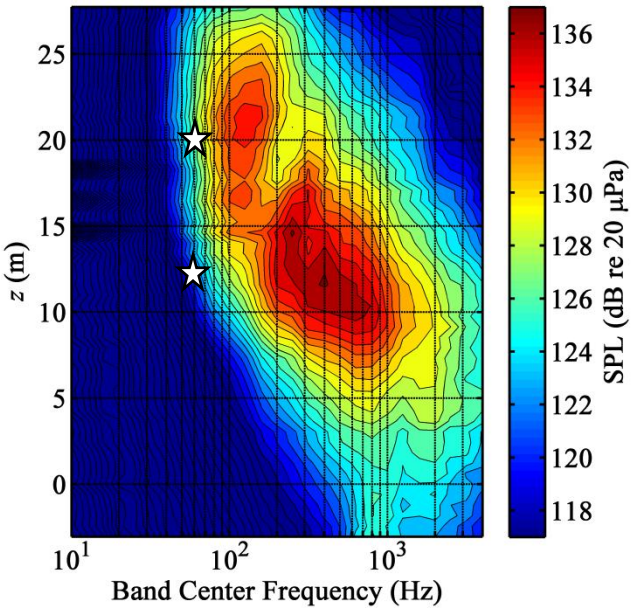

Figure 6.13 One-third octave spectral variation over location along reference array at military engine conditions. Each contour line represents a step size of 1dB. The stars mark the locations of the peaks of the partial fields along the reference array location for the 125 Hz case, with PF 1 peaking at z = 20.0 m and PF 4 at 12.3 m.

One potential application of the OLVR method is to generate physically meaningful source models from the decomposed pressures in the approximate region of the hydrodynamic near field. Since the jet itself is characterized by a nonlinear, turbulent flow field, a source model is defined for the boundary of this region (the hydrodynamic near field), and not within it. Careful inspection of the source regions on the conical surfaces of PFs 1 and 2 in Figure 6.12 reveals that the peak locations of the two sources are different, though their respective distributions overlap. The lobe of PF 2 originates closer to the nozzle than that of PF 1. Figure 6.14 shows the OLVR PFD of the reconstructed field along the shear layer boundary (on the conical surface) at a height of $y = 1.9$ m, or in other words, restricted to the azimuthal locations that intersect the planar surface reconstruction. The first six PFs are separated into two plots for

convenience, and the total reconstruction is also shown. Note the relative distributions of PFs 1 and 2. PF 1 peaks at $z = 7.5$ m, and PF 2 at $z = 3.6$ m. It is a joint contribution from these two components that represents most of the energy in the maximum region spanning $z = 0$ to 12 m. In addition, note that the secondary maximum region, which spans $z = 12$ m to 30 m is represented almost completely by the energy in PF 1. Hence, the strongest source spans from about $z = 5$ to 30 m, and is highly spatially coherent. The null in the total reconstruction, near $z = 12$ m, is a result of the incorporation of the ground reflection in the model of the field, and not of a distinction between multiple sources. The secondary source mechanism of PF 2, compared to the primary source, dominates a relatively small region the first 4 m after the nozzle exit.

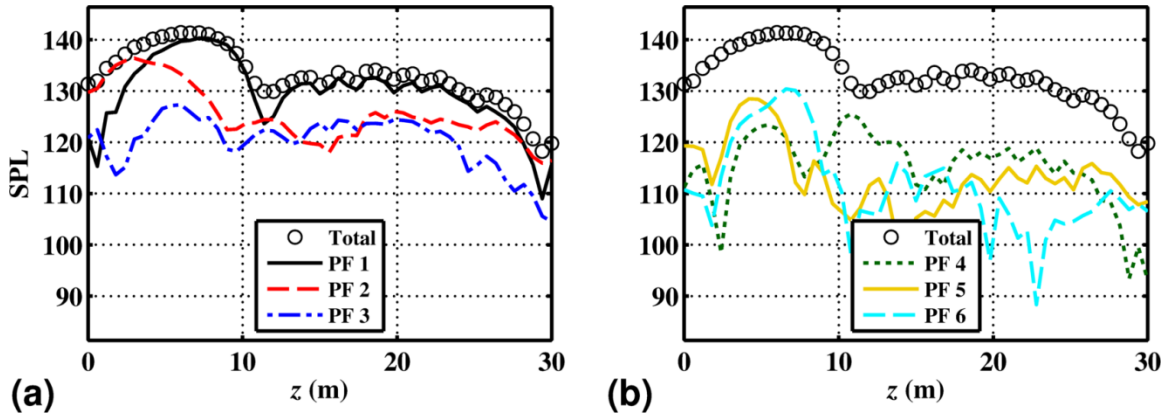

Figure 6.14 The first six partial fields, compared to the reconstruction total, at the approximate shear-layer boundary that intersects the plane defined by y = 1.9 m, generated from OLVR on jet data at 125 Hz and at military engine conditions. (a) Partial fields 1-3. (b) Partial fields 4-6.

To gain insight about the physical interpretation of an OLVR PFD, PFs generated by both SVD-based PFD and OLVR are compared at 400 Hz, over the planar reconstruction surface defined by $y = 1.9$ m, and for military power in Figure 6.15 and Figure 6.16, respectively. First, note that PF 1 of the SVD-based PFD in Figure 6.15 is characterized by a single radiation lobe in the direction of maximum radiation. Then, PF 2 supplements PF 1 by adding energy on either side of the main lobe of PF 1. This is repeated in PF 3 with three main radiation lobes, and so

on, until PF 6, where energy is spread out spatially into 6 radiation lobes. This modal-like decomposition of the total field is a result of the implementation of SVD on the reference array data. Contrast this with the OLVR PFs in Figure 6.16. The radiation of all the PFs, at least those of PF 1 through 4, are characterized by a single, localized main lobe. The lobes of each PF still overlap to produce the total field, but their spatial separation indicates the spatial distinction between independent source mechanisms, which are each self-coherent and produce highly directional radiation. The physical insights gained from such PFs are explored further in Section 7.4.

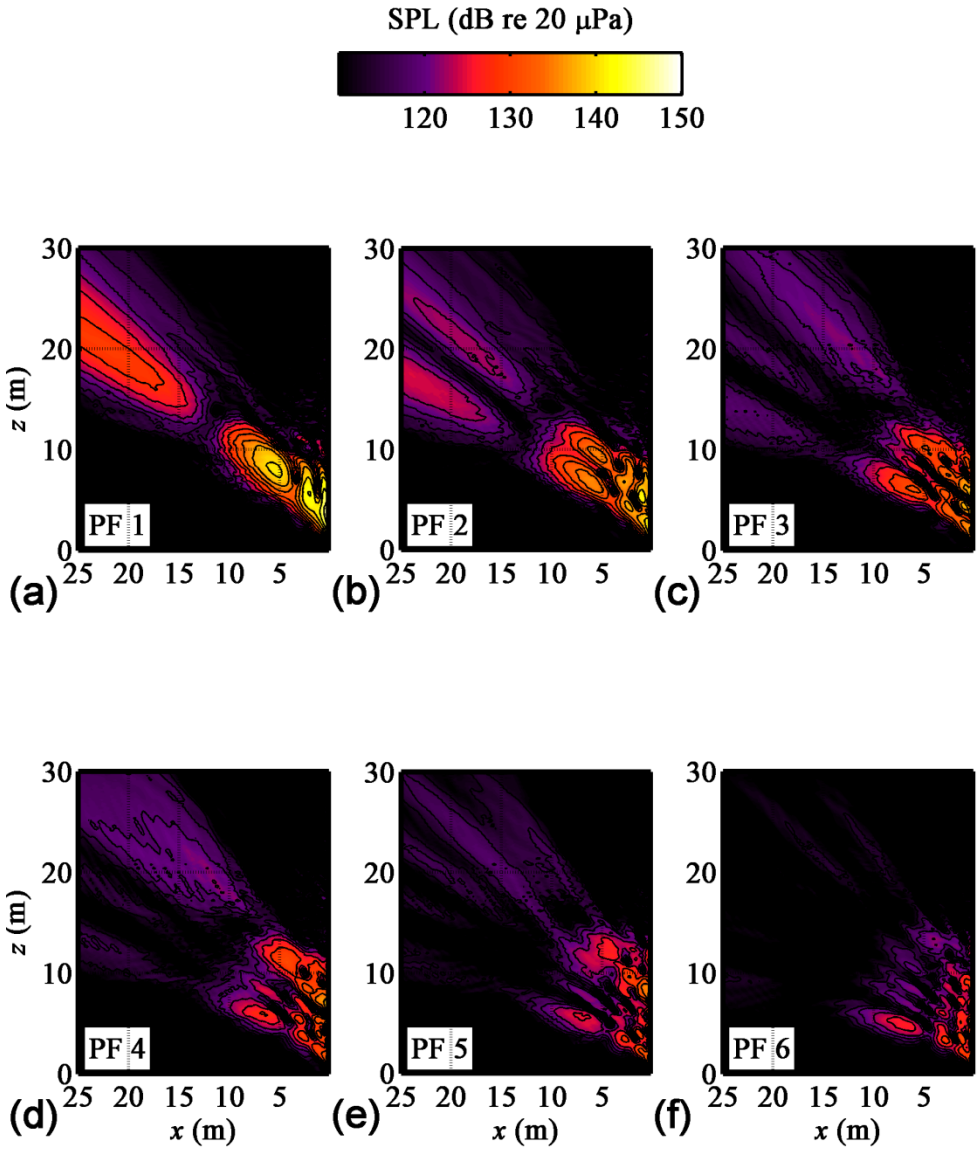

Figure 6.15 The first six partial fields at the plane defined by y = 1.9 m, generated from SVD-based PFD on jet data at 400 Hz and at military engine conditions.

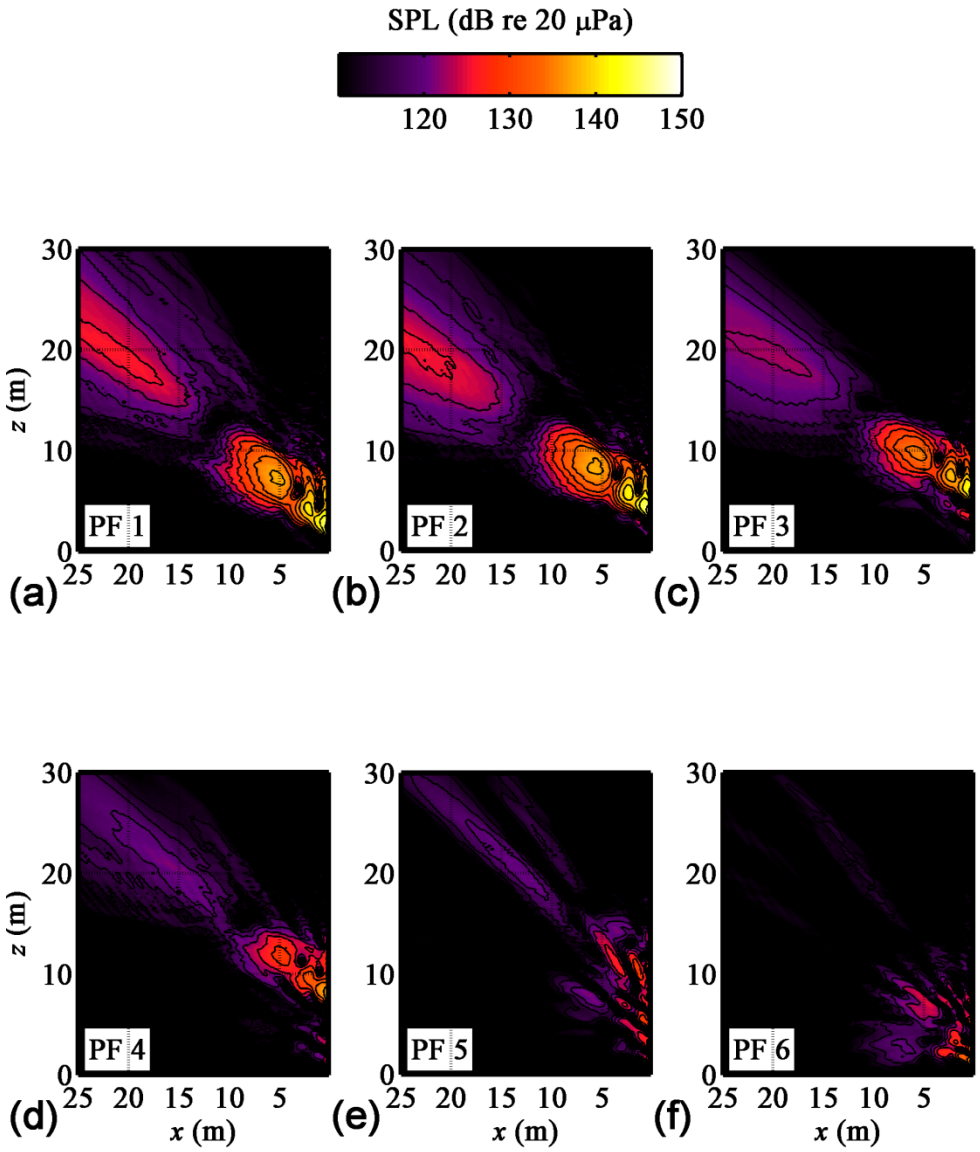

Figure 6.16 The first six partial fields at the plane defined by y = 1.9 m, generated from OLVR on jet data at 400 Hz and at military engine conditions.

6.5 Conclusion

The optimized-location virtual reference method (OLVR) for partial field decomposition (PFD) of jet noise sources has been explained in this chapter. OLVR generates an optimal

virtual reference set for the decomposition from complex pressures obtained through holographic reconstruction of the three-dimensional field. The quality of the OLVR field decomposition therefore relies on the quality of the MSTR SONAH field reconstruction. In the application of OLVR to a jet source, it is important to remember that turbulent flow fields are generally characterized by extended sources of decaying spatial coherence. Hence, the separation of independent source mechanisms is complicated. Nevertheless, OLVR is shown here to generate a set of partial fields for a full-scale jet noise source that are intuitive and provide physical insight about source coherence and distributions. For the sources at 125 Hz at 400 Hz, with the engine operating at military conditions, it was shown that multiple, localized radiation lobes were generated by independent source mechanisms. In Section 7.4 of the following chapter, application of OLVR to the jet noise field at multiple frequencies and engine conditions provides extensive information about source distributions and coherence properties, and further substantiates the evidence for multiple, independent source mechanisms in the full-scale jet.

Chapter 7

Full-scale Jet Noise Characteristics

7.1 Introduction

Jet noise reduction methods are currently being targeted toward the identification and control of large-scale turbulence (LST) structures in the jet flow. This is because radiation from LST has been shown to dominate the sound field. Its coherent, ordered structure makes it possible to represent LST with relatively few terms in a wave function expansion. Such an expansion can be used in an equivalent wave model (or equivalent source model), in conjunction with an acoustical inverse method, to generate images of jet sources and fields. Acoustical imaging techniques can also incorporate partial field decomposition (PFD), to separate imaged fields into the contributions of mutually independent partial fields. In this work, PFD leads to a greater understanding of source distributions and the spatial coherence of independent processes within a jet.

A review of inverse methods used in conjunction with equivalent source and equivalent wave models of jets is found in Section 1.2, which is summarized here. Equivalence models use some prior knowledge of source location, distribution, shape, or spatial coherence to generate an expansion of wave functions, which satisfy the Helmholtz equation (in terms of single-frequency

analysis) in a homogeneous, free-field region. An inverse method uses measured acoustic quantities at an array of transducers in the field to find the expansion coefficients of such a model in some optimized sense. These weighted functions can then be used to predict acoustic quantities at other desired locations, such as on the surface of the source. Equivalence models and inverse methods have been applied to jets in numerous past investigations. Studies that have applied inverse methods to predict source and field properties from array-based jet noise measurements include those of Lee and Bolton,[55,106] Tam *et al*.,[41] Shah *et al*.[60] Wall *et al*.[56] Krueger,[124] Morgan *et al*.,[42,43] and Hart *et al*.[44] In particular, Suzuki and Colonius[26] employed an eigenfunction representation of acoustic waves in the jet near field, which eigenfunctions were derived from linear instability analysis (a model of the spatial development of magnitudes and phases of instability waves, or LST structures). They then applied beamforming to specify the near field in terms of these eigenfunctions (as opposed to monopoles typically used in beamforming algorithms). Reba *et al*.[134] used a Gaussian wave-packet model to represent LST structures, and fitted their model to measurements made in the hydrodynamic regime over a conical array surrounding the jet. This model was then projected to the acoustic far field. Schlinker *et al*.[9] also represented the LST structures as a convecting wave packet, based on pressure measurements in the near-field, without attempting to equate instability waves to measured flow quantities. The wave-packet approach was then used by Reba *et al*.[39] to include the effects of spatially varying amplitude, phase, and coherence.

In this work, near-field acoustical holography (NAH) methods are applied to visualize source and field properties of the full-scale jet from an installed engine on an F-22A Raptor. In particular, multisource-type representation statistically optimized near-field acoustical holography (MSTR SONAH), developed in Chapter 5, is used to model the full-scale jet environment. The jet was, of necessity, measured over a concrete run-up pad, which introduced an interference pattern into the measurements. MSTR SONAH is based on the theory of SONAH,[51-54] which uses an equivalent wave model of a field to calculate transfer functions

between measurement and reconstruction positions. MSTR SONAH has the additional ability to account for multiple, spatially distinct sources of various shapes. It was initially applied to the full-scale jet problem at select frequencies in Section 5.5, and is used to investigate jet noise properties in this chapter.

Partial field decomposition (PFD) methods, based on the theory of principal component analysis,[62,129] have also proven to be useful tools in imaging analyses. Specifically, many inverse techniques require coherent fields to generate parameter-fitted equivalence models. PFD of a field that is generated by multiple, incoherent processes results in mutually incoherent partial fields (PFs), each of which can be imaged individually. Decompositions have historically been performed for various quantities in the jet field, including directly measured flow quantities,[65-67] the pressure signatures of the hydrodynamic near field,[26,68-70] and acoustic quantities outside this regime.[55,60,83,128] These studies represent several kinds of PFD methods, and the PFs that result from them are not unique. The energy-based summation of PFs will give the same result (theoretically) for any PFD method: a total field with the same levels as the original measured field. In general, a PFD of an arbitrary sound field does not generate PFs that are "physically meaningful," i.e., that represent independent source components, even if those sources are well separated spatially. This is because each transducer in a measurement array receives information from multiple subsources. The PFD applications that most successfully generate physically relevant partial fields are performed with a set of reference transducers that are located close to individual subsources, which emphasizes the contribution of a single source to each reference.

The PFD method used in this study, called optimized-location virtual reference PFD (OLVR), is based on the one developed by Kim *et al*.[64] OLVR uses an optimal selection of virtual references placed in a source field to separate independent (incoherent) source mechanisms (or processes) based on their relative contributions at specific locations in the field. The PFs that result from OLVR in this work are linked more directly to independent sources than

has been possible in previous PFDs of jet sources. The development of OLVR and its initial implementation to the jet at one frequency and engine condition have been carried out in Chapter 6. This chapter incorporates a more comprehensive analysis of jet source properties using OLVR.

Key findings from past studies about jet noise properties are summarized here. First, Venkatesh[31] and Lee and Bridges[33] used beamforming techniques to obtain source distributions, wherein they showed that sources become more compact and move upstream as frequency increases. A similar effect was shown in phased-array reconstructions of both model-scale and full-scale jets by Schlinker.[32] Some past investigations have used a "small-eddy approximation," where the source models are limited to distributions of compact, independent radiators. For the second key finding, Michalke[135] discussed how the small-eddy approximation is only applicable when the variation in the power spectrum is negligible within a "coherence volume," or when the volume over which the source at a given frequency is coherent is much smaller than the overall size of the source. He shows that increasing source coherence makes radiation directivity more pronounced, which directivity is apparent in the majority of jet-noise analyses. Michalke[135] and Tam[117] both provide a calculation for the directivity of an extended source. They demonstrate that the direction of radiation is based on the convective velocity of the LST structures. As velocity increases, the radiation tends to point farther away from the direction of convection and toward the perpendicular.

Additional studies on the data set for the current full-scale jet experiment are worth mentioning here. In the first study, Morgan *et al.*[42,43] applied a Rayleigh distribution-weighting to the amplitudes of a linear monopole array, and included both coherent and incoherent source components, to model the full-scale jet data of this experiment. The parameters of the model have been optimized by Hart *et al.*,[44] using Bayesian methods, to match measured pressures. Although this model generates accurate sound-field reconstructions for most cases, it was found that the broad extent of the high-amplitude region at 315 Hz and at military engine conditions

(military power) could not be matched in the model. The present investigation with OLVR on the jet data provides an explanation for the discrepancy, based on the influence of multiple source mechanisms. In the second study, Krueger[124] applied an alternative NAH method to reconstruct the full-scale jet field. Instead of an attempt to account for the interference pattern in the hologram measurements, a linear array of microphones placed on the ground, and running parallel to the jet centerline (the reference array discussed in Section 2.2.4), was the hologram measurement, similar to the approach of Long *et al*.[106] A PFD of the measured data using Spatial Transformation of Sound Fields[63] was performed. The data were extrapolated numerically beyond the measurement array using analytic continuation.[118] Then, an axisymmetric source distribution was assumed, and the data were propagated throughout the sound field with a cylindrical NAH method based on a discrete Fourier transform.[22] A subtraction of 6 dB was applied to the reconstruction to account for the pressure doubling at the boundary, and the field and source reconstructions provided were treated as equivalent to that obtained in a free-field environment. In the context of the current work, this process is called the cylindrical axisymmetric near-field acoustical holography method (CA-NAH).

This chapter presents a comprehensive application of MSTR SONAH and OLVR methods to the jet at military and afterburner engine powers and over a range of frequencies to investigate the spatial extent, coherence, directionality and distribution of sources. First, to verify consistency in holography methods, a brief comparison of source distributions reconstructed on the shear layer using the MSTR SONAH method and the CA-NAH method is made in Section 7.2. Section 7.3 provides results of the total MSTR SONAH reconstructions of the jet field as a function of frequency. Source models obtained with MSTR SONAH are presented, and preliminary evidence of multiple source mechanisms is shown. The PFD of the field and sources, using OLVR, is given in Section 7.4. Here, each total reconstructed field is compared to the PFs that comprise it, and their individual contributions to the field are discussed. Specifically, the source models are separated into independent, spatially overlapping source

mechanisms. The behaviors of multiple source mechanisms are explored as a function of frequency. Section 7.5 is a concluding discussion of important jet noise properties that are found from the current investigation. It should be noted that the focus of this chapter is on military and afterburner conditions. This is because there is some evidence that the data at idle are dominated by noise components other than jet noise.[80] The relative non-stationarity of the field at intermediate power, due to the fact that there is no set throttle position, make the interpretation of results for this engine power unclear (see Section 2.3.3.2). Averaging and data-smoothing techniques could make future analysis of intermediate-power data feasible.

7.2 Comparisons to Axisymmetric, Cylindrical NAH

To verify consistency in NAH methods applied to the current data set, prior to the discussion of field and source properties, some of the shear-layer distributions obtained from MSTR SONAH are compared here to the shear-layer reconstructions using CA-NAH.[124] Data for the shear layer are taken from MSTR SONAH reconstructions along the location of the black solid line shown in Figure 7.1, which runs along the approximate shear-layer boundary at a height of $y = 1.9$ m. CA-NAH is applied to the measurements on the reference array, as described in Section 7.1, with one exception. Instead of the use of analytic continuation to numerically extend the aperture, a linear prediction[123] scheme is used. It has been shown that, at some frequencies, linear prediction offers a more accurate representation of the true pressures beyond the measurement aperture, and restores more of the "missing" energy to the field (see Section 4.3). It is the extrapolation method employed in the MSTR SONAH processing, so for the sake of comparison, it is also used in the CA-NAH reconstruction.

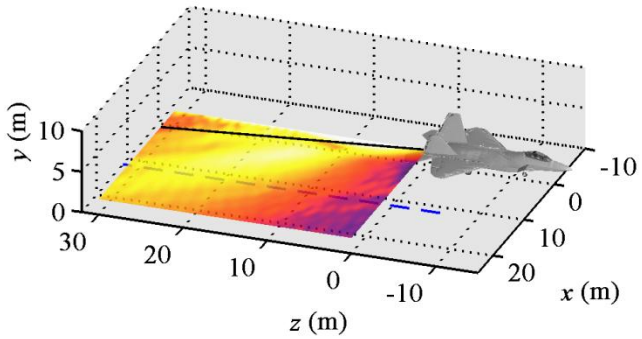

Figure 7.1 Schematic showing the various reconstruction locations used in the results of this chapter. The planar colored region is at a height of y = 1.9 m, which is equal to the height of the jet centerline. (The data shown over this surface serve only as an illustrative example.) The black solid line on this planar surface marks the location of the approximate shear-layer boundary at the same height. The blue dashed line is on the ground at x = 11.6 m, and is collinear with the ground-based reference array.

For all levels shown in this chapter, the squared pressures are calculated for narrowband, one-third-octave band center frequencies, and converted to a sound pressure level (SPL) by the equation

$$\mathrm{SPL} = 10 \times \log_{10}\left(\frac{p^2 \frac{\Delta f_{1/3}}{\Delta f}}{(20 \times 10^{-6}\ \mu\mathrm{Pa})^2}\right), \tag{7.1}$$

where $\Delta f_{1/3}$ is the bandwidth of the respective one-third-octave band, Δf is the bandwidth that results from the Fourier transform processing, and 20×10^{-6} μPa is the root-mean-square reference pressure. Since the narrowband spectrum of the jet is broadband and void of strong tones or rapid level changes as a function of frequency, at these higher engine powers, such a scaling can be used to approximate the energy in each one-third-octave band.

Source reconstructions using the two NAH methods are compared at three frequencies in Figure 7.2. Line plots are used for the MSTR SONAH results, and markers are used for CA-NAH. All reconstructions in the high-amplitude regions between $z = 0$ and 10 m agree to within 2 dB. Downstream of this region, the reconstructions deviate by as much as 15 dB in

select locations. Deviations are likely caused by a combination of multisource interference patterns in the MSTR SONAH field model, and the ability of the linear prediction to account for differences in the axial coverage of the two different holography arrays. However since both the planar hologram measurement and the reference-array hologram measurement capture similar portions of the main radiation lobes, further investigation is required to clarify the causes. This might include an analysis of the relative magnitudes of the cylindrical wave functions used in each expansion.

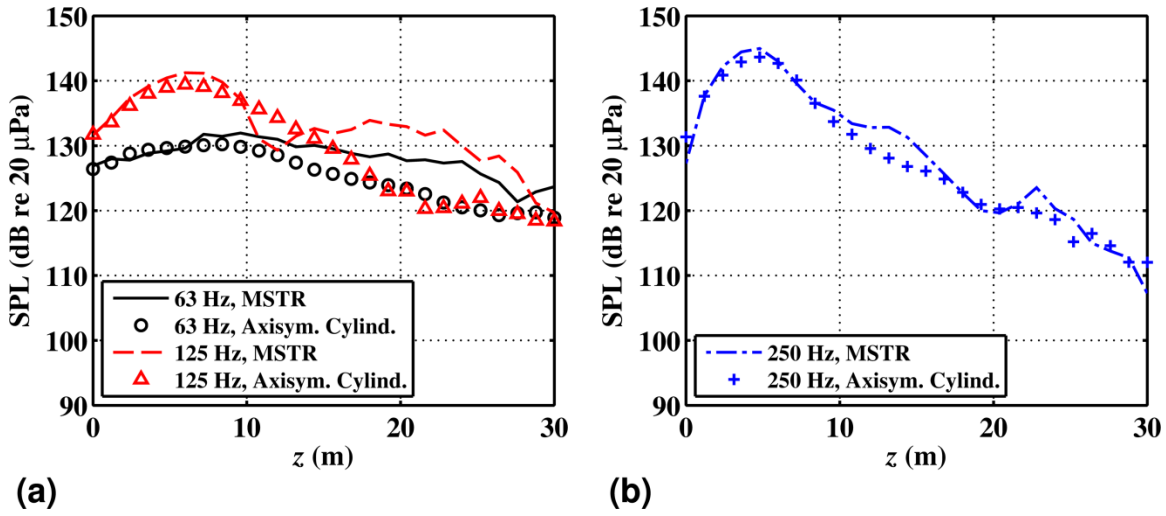

Figure 7.2 Reconstructed source distributions along the shear layer using both MSTR SONAH and the axisymmetric cylindrical DFT-based NAH methods for the jet at military engine conditions.

At 63 Hz, both reconstructions in Figure 7.2a (solid black line and circles) show broad shear-layer distributions. At 125 Hz, CA-NAH (red triangles) shows a gradual tapering of levels downstream of the maximum. In contrast, the nulls and peaks of the interference cause the MSTR SONAH reconstruction (red dashed line) to dip below and rise above the CA-NAH result. It is likely that the true levels in the field lie somewhere between these two curves, since interference does play a part in level distributions, but it is probably not as pronounced an effect as the MSTR SONAH curve shows. This is likely because the equivalent wave model used in the MSTR SONAH algorithm is based on cylindrical sources localized at the jet centerline,

instead of a volumetric source model. The two curves at 250 Hz in Figure 7.2a (blue dash-dot line and "+" symbols) agree better than any other frequency, with deviations consistently less than 5 dB, and often smaller. This may be due to the fact that the main lobe is captured more fully within the two respective measurement apertures for 250 Hz than for 32 or 125 Hz.

7.3 MSTR SONAH Field and Source Reconstructions

MSTR SONAH reconstructions of the jet field were performed for all one-third-octave band frequencies between 20 Hz and 500 Hz. First, it is instructive to view the reconstructions compared to benchmark measurements made at the location of the ground-based reference array (see the blue dashed line in Figure 7.1). Levels from the integrated one-third-octave bands measured along the array are shown in Figure 7.3a as a function of band center frequency and downstream location in z. Black contour lines are separated by 3 dB increments. Note that there exist two local maxima in the map, one centered near 125 Hz and $z = 21$ m, and a second around 300 Hz and $z = 12$ m. Recall that these measurements were made along the ground, so the local maxima are not a result of reflected interference. To show that this double-maximum phenomenon is captured in the reconstruction, the spatial/band level map at the same location and frequencies that is predicted with MSTR SONAH is shown in Figure 7.3b. Local maxima occur at the same respective locations and frequencies. All main features of the map are represented in the reconstruction, except for what may be some missing energy upstream of $z = 0$ m for all frequencies. Recall that the hologram array (measurement plane 2) was limited in its axial coverage of the source—the hologram measurements farthest upstream occurred at $z = 1.6$ m and $x = 6.4$ m. The missing energy is likely due to an insufficient measurement of upstream data.

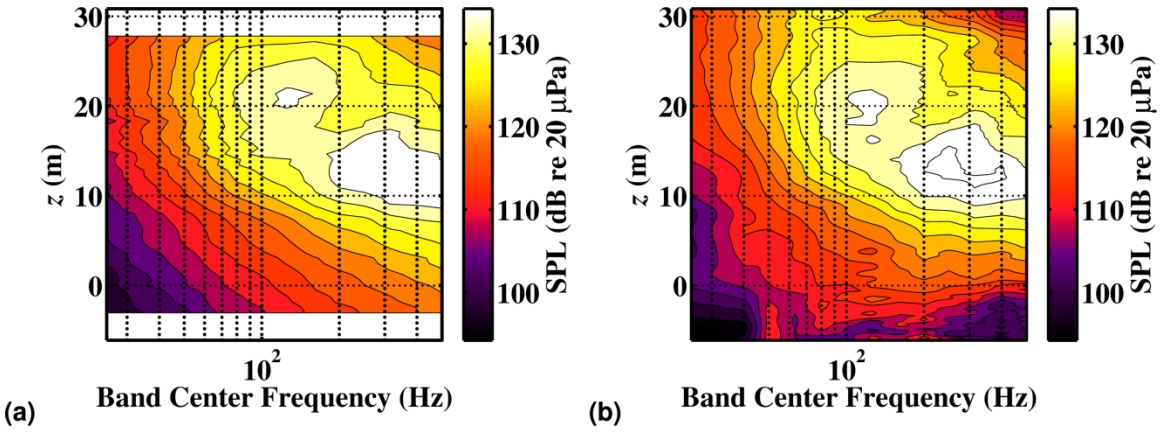

Figure 7.3 (a) One-third octave spectral variation over location along reference array at military engine conditions. (b) Total MSTR SONAH reconstructions at the same locations and frequencies. Black contour lines occur at 3 dB increments.

Reconstructions were also made at a uniform height of $y = 1.9$ m above the ground, which is the height of the jet centerline. The location of this reconstruction surface relative to the aircraft is shown by the colored surface in Figure 7.1. Reconstructions are shown for all one-third-octave bands, and for military power, as a function of location in Figure 7.4, where x is the distance from the jet centerline, and z is the distance downstream of the nozzle. Note that the direction of increasing x-values is from right to left. All reconstructed fields are characterized by directional radiation, demonstrating that at these frequencies the dominant sources are the spatially coherent LST structures. As frequency increases there is a shift in directionality of the radiation toward the forward direction. However, this is not a smooth shift that tracks with increasing frequency. Rather, the main lobes from 25 Hz to 125 Hz all point farther downstream, toward the approximate location of $(x, z) = (20\text{ m}, 30\text{ m})$. At 315 Hz and above the main lobe is broader and points toward about $(25\text{ m}, 25\text{ m})$. In the intermediate frequency region 160-250 Hz the presence of both lobes can be seen, suggesting that there is a gradual decrease in energy of one lobe, and an increase of a second. Note that high errors occur in the 20 Hz field, possibly due to the insufficient axial coverage of the extended source region by the hologram array.

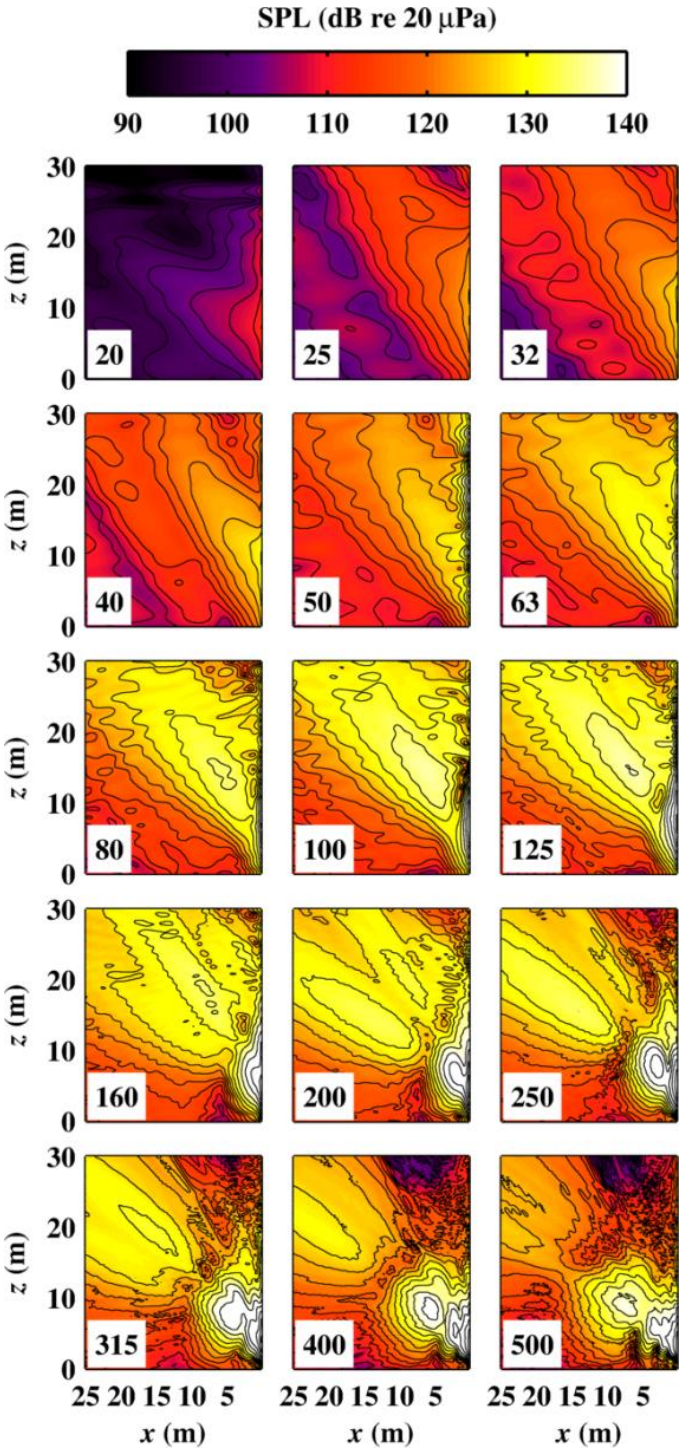

Figure 7.4 Field reconstructions of the full-scale jet at military engine conditions at a height of y = 1.9 m. Levels are scaled to represent all energy in the one-third-octave band. Band center frequencies are shown in the bottom left of each map. Black contour lines are separated by 3 dB.

The effects of the reflecting plane are accounted for in the model used in the MSTR SONAH algorithm, which are seen in the interference patterns of the reconstructed field in Figure 7.4. Beginning around 100 Hz, an interference null becomes visible in the reconstruction. It is seen in the local minimum between the main lobe and source regions, near $(3\text{ m}, 8\text{ m})$. As frequency increases, this null moves farther from the source region and increases in depth, and additional nulls appear in the source region, consistent with the interference pattern of a source of increasing frequency and decreasing size in the presence of a reflecting plane. It was shown for the simulated data in Section 5.4.2, and for the full-scale jet data in Section 5.5.3, that the locations of null and maximum regions are predicted to within 0.1 m of benchmark features with the MSTR SONAH method. Hence, it is likely that the interference patterns shown here are characterized by a similar accuracy.

The reconstruction data at the shear layer boundary, marked by the solid black line in Figure 7.1, are shown here. Such a reconstruction provides a model of the source, as would be found in the hydrodynamic regime. (However, recall that these models may not include acoustic near-field information, since hologram measurements were made too far from the jet to include the evanescently decaying waves.) Levels are shown as a function of downstream location (in z) and of frequency (25 to 500 Hz) in Figure 7.5, for military power. Similar to the jet noise reconstructions of Venkatesh,[31] Lee and Bridges,[33] and others, the shear-layer distributions become more compact and move upstream with an increase in frequency. For example, the top 6 dB of the distributions at frequencies below about 100 Hz extend 20-30 m downstream. At 500 Hz, the top-6-dB region extends only about 6 m. Note that these shear-layer distributions are somewhat obscured by the presence of the null running from the bottom left to the top right of the figure, which is due to destructive interference between the real and image sources.

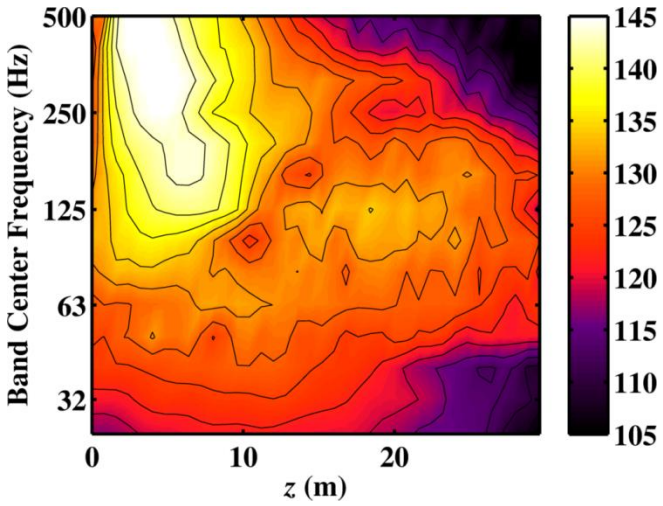

Figure 7.5 Reconstructed source distributions along the shear layer as a function of one-third-octave band for military engine conditions.

To make the shear-layer distributions clearer, the source levels for octave-band center frequencies at military power are repeated, shown as the curves in Figure 7.6. The sources at 250 Hz and 500 Hz have an asymmetric distribution, which supports the idea that jet sources are characterized by rapid growth past the nozzle due to energy transfer from the high-speed potential core to the LST structures, and gradual decay beyond the end of the potential core.[43,44,85,136,137] At 125 Hz, the interference null at $z = 12$ m makes it difficult to discern the shear-layer distribution shape, and the relationship between the two local maxima at $z = 7$ and 18 m is difficult to assess. The coherence between these two local maxima is explored in Section 7.4. The sources at 32 Hz and 63 Hz are characterized by a relatively broad distribution.

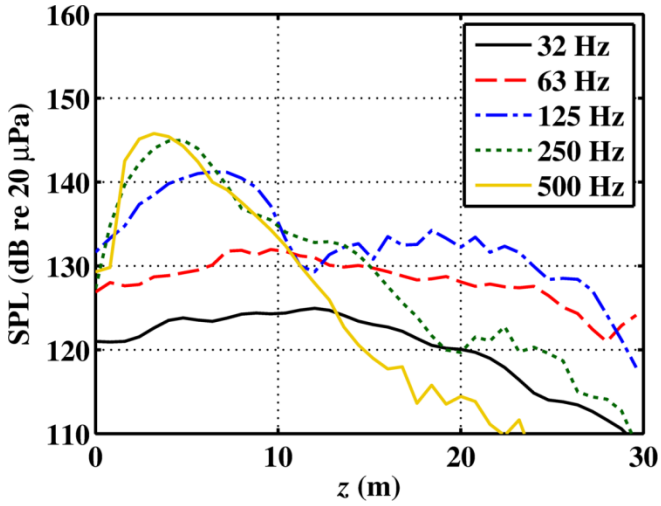

Figure 7.6 One-third-octave band reconstructed source distributions along the shear layer for select frequencies, for military engine conditions.

Figure 7.7 shows the reconstructions on the horizontal plane at the height of the nozzle at afterburner power for frequencies between 20 and 500 Hz. The same trends in field and source properties from the military results are apparent here. Specifically, the field reconstructions of Figure 7.7 show a shift in energy from one radiation lobe to another. However, the presence of a third lobe can also be seen. Between about 32 and 63 Hz, this lobe radiates toward the approximate location $(13\text{ m}, 30\text{ m})$. The presence of the next lobe is visible from about 50 Hz to 200 Hz, which points toward $(25\text{ m}, 27\text{ m})$. The third lobe is visible between 200 Hz and 500 Hz, pointing toward $(25\text{ m}, 15\text{ m})$. In fact, the downstream lobe seen in the military reconstructions in Figure 7.4 could also be interpreted as two closely-spaced lobes, with a gradual transition from one to the other between 25 Hz and 160 Hz, but the third lobe is much more pronounced here in the afterburner case. Recall that directivity angle moves toward the perpendicular with an increase in convection speed. Hence, the higher jet velocity of the jet at afterburner power may cause a forward-shift of radiation lobes, accompanied by a more dramatic separation between them.[117,135] An analysis of the overlapping radiation lobes is difficult with total sound field maps shown here. It will be demonstrated in Section 7.4 that the overall radiation lobes shown in Figure 7.4 and Figure 7.7 for both military and afterburner engine

powers, respectively, can in fact be separated into multiple, independent source mechanisms—numbering more than the two or three lobes visible in these figures.

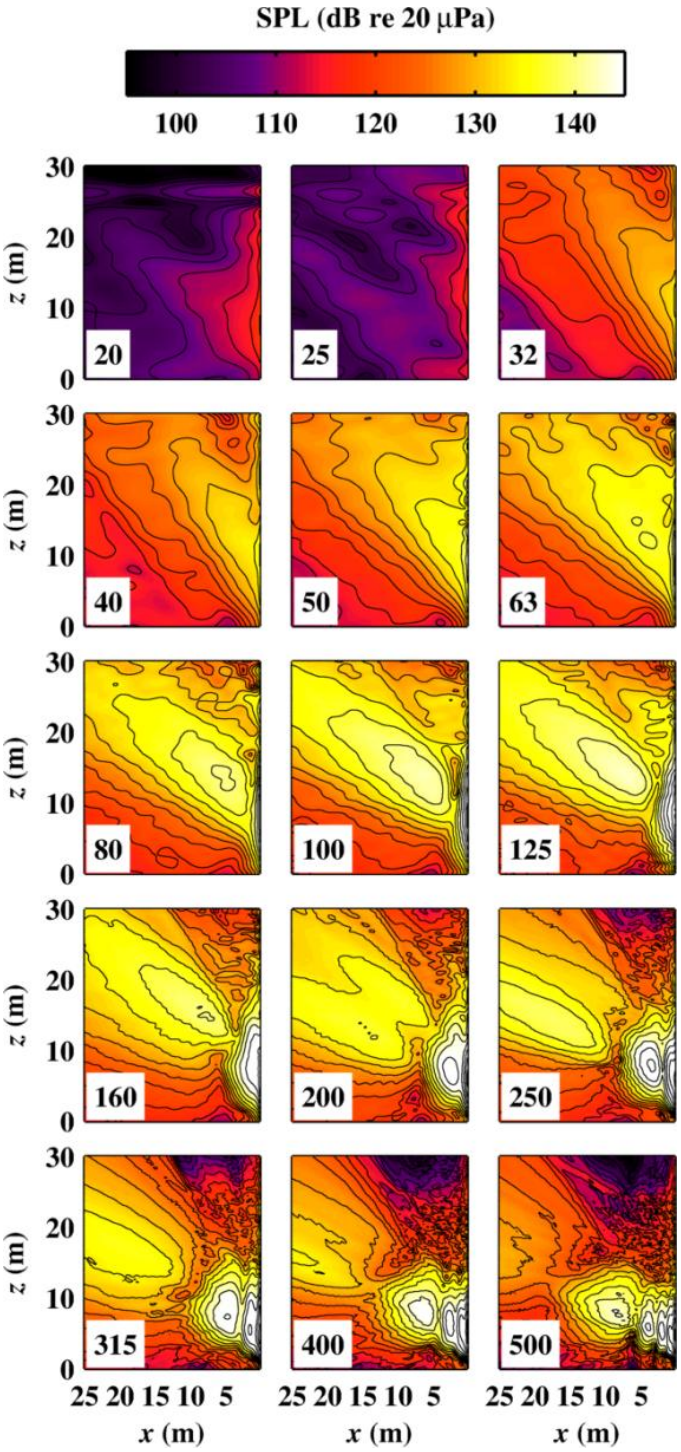

Figure 7.7 Field reconstructions of the full-scale jet at afterburner engine conditions at a height of y = 1.9 m. Levels are scaled to represent all energy in the one-third-octave band. Band center frequencies are shown in the bottom left of each map. Black contour lines are separated by 3 dB.

The shear-layer distributions at afterburner power, shown in Figure 7.8, further corroborate the presence of multiple source mechanisms. There are local maxima at $z = 11$ m and 50 Hz, a second at $z = 8$ m and 160 Hz, a third at $z = 6$ m and 250 Hz, and a fourth at $z = 6$ m and 400 Hz. These first three frequencies correspond to the frequencies that are dominated by a single radiation lobe in the planar reconstructions of Figure 7.7. However, care should be taken in the interpretation of these results. Some of the local null regions of Figure 7.8 can be ascribed to interference effects. This supports the need for the source-separation analysis of Section 7.4. The shear-layer distributions at select frequencies in Figure 7.9 show similar characteristics to those of the military results, namely an asymmetric distribution at the higher frequencies, a broad distribution at low frequencies, and a distribution at 125 Hz that is obscured by an interference null.

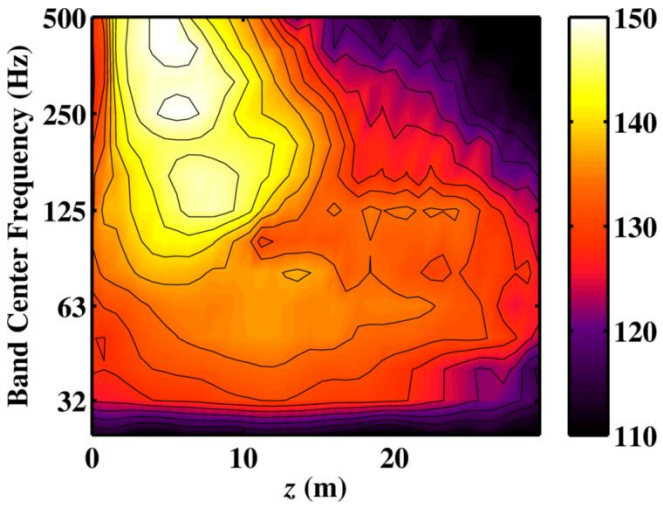

Figure 7.8 Reconstructed source distributions along the shear layer as a function of one-third-octave band for afterburner engine conditions.

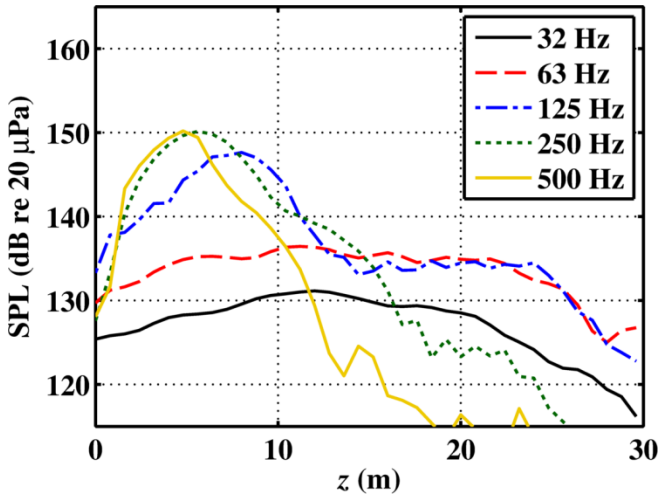

Figure 7.9 One-third-octave band reconstructed source distributions along the shear layer for select frequencies, for afterburner engine conditions.

7.4 Source and Field Models from OLVR Partial Field Decomposition

The separation of multiple source mechanisms is performed in this section with the OLVR method. Preliminary evidence has been presented for the existence of multiple, independent sources within the jet field in Section 7.3. Recall that a turbulent jet field is characterized by spatially decaying coherence, and the overlap of information from these source mechanisms makes it difficult to distinguish them in the reconstructions of the total field. Hence, the PFs that are based on virtual references placed throughout the field, with locations optimized in the OLVR process, are provided. These PFs represent independent processes in the field, which in turn represent independent source mechanisms insofar as each virtual reference captures information exclusively from each source. This representation clarifies the spatial separation of independent source mechanisms. Because many figures are required to view multiple PFs at various frequencies and engine conditions, results are divided into two parts for clarity and flow. First, PFs are shown for two frequencies at military engine power in this section, which demonstrate key insights into the source and field properties. Then, for further

evidence of these findings, and to serve as a reference for future investigations, Appendix A shows partial fields for additional frequencies at both military and afterburner powers with limited discussion.

Figure 7.10 shows the total MSTR SONAH reconstruction of the planar jet field region at $y = 1.9$ m, discussed in Section 7.3, for 160 Hz and at military power. Black contour lines for this and subsequent figures are separated by 3 dB increments. The main radiation lobe is supplemented by what appear to be two secondary, side lobes. However, the coherence between these features, and the spatial origins of the respective lobes, are unclear. Thus, in Figure 7.11, the first six PFs of this reconstruction, obtained with OLVR, are shown, and the separation is more apparent. The first PF, shown in Figure 7.11a, contributes most of the energy to the main lobe of the overall field. The energy of the side lobe that is upstream of the first (in the direction of decreasing z) is largely found in PF 2 of Figure 7.11b. The third lobe (or at least the local region of high amplitude) downstream of the jet is made mostly of energy from PFs 2 and 3 of Figure 7.11b-c, respectively. Note that PF 2 contains information for both of the secondary lobes. This energy representation over a relatively large spatial extent could represent a coherent mechanism, or could be due to "leakage," where one virtual reference senses the dominant contributions of multiple processes. If the latter is the case, then an improved virtual reference selection would serve only to further distinguish the multiple sources.

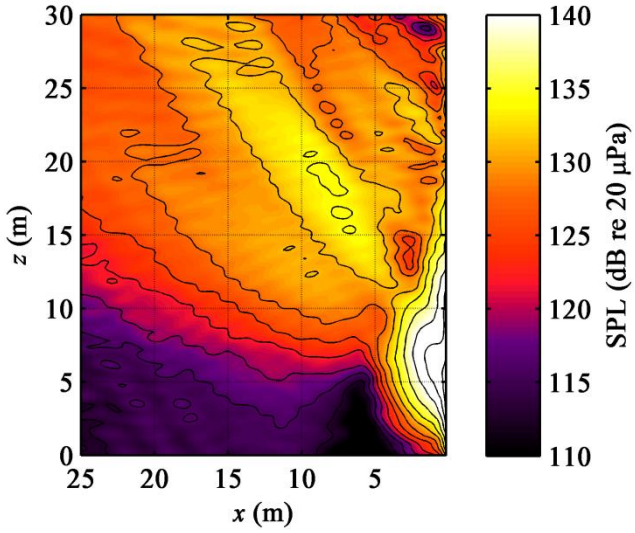

Figure 7.10 Total field reconstruction from MSTR SONAH of the full-scale jet noise at military power and at 160 Hz at a height of y = 1.9 m. Black contour lines occur at 3 dB increments.

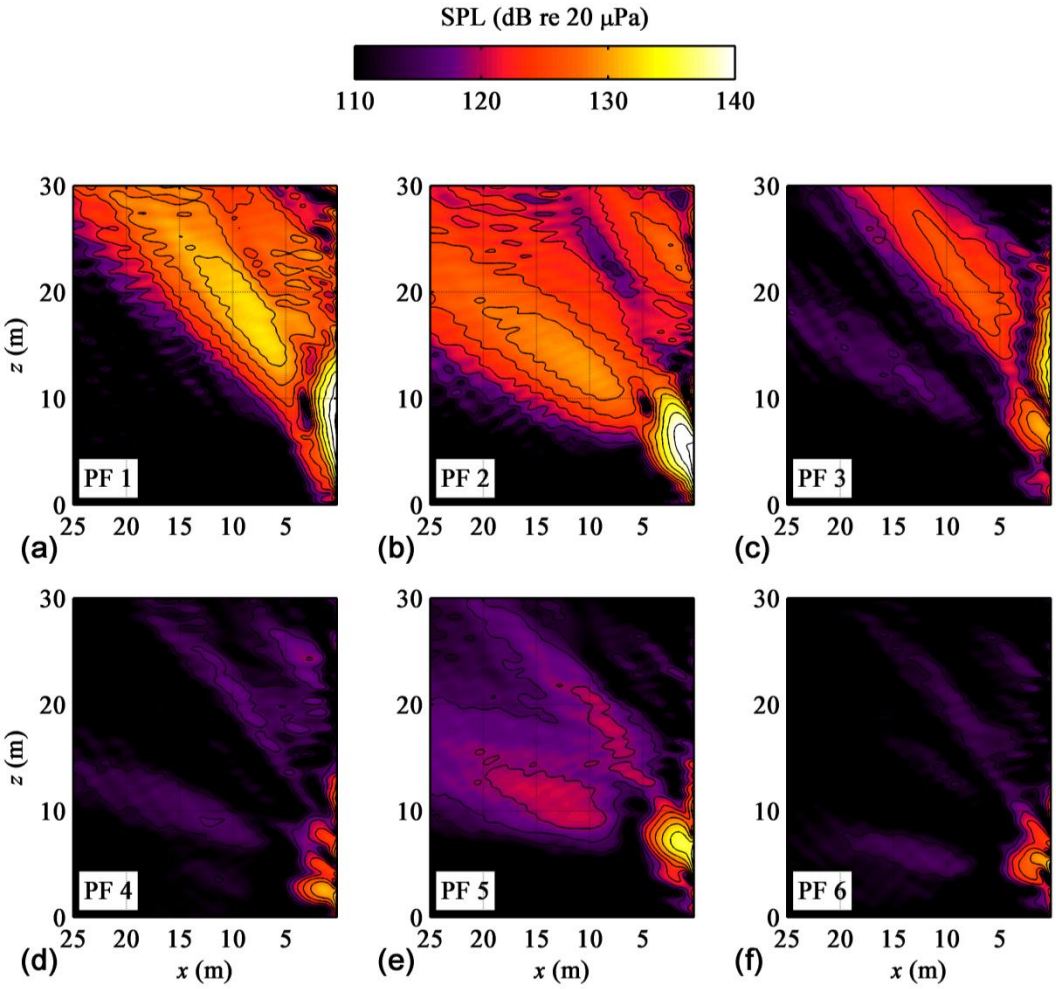

Figure 7.11 First six PFs, (a-f) respectively, from the OLVR decomposition of the full-scale jet noise at military power and at 160 Hz at y = 1.9 m. Black contour lines occur at 3 dB increments.

To facilitate the comparison of the distributions and relative levels of these PFs, and to allow for a more comprehensive discussion of PF behavior, the first six partial fields generated by OLVR are shown at two key locations. In the following analyses, PFs are shown along a line that is collinear with the ground-based reference array (blue dashed line in Figure 7.1). This is done to mitigate the effect of an interference pattern along the extent of the data, and all frequencies (theoretically) experience a uniform pressure-doubling at a reflective surface. The second location explored is along the shear layer boundary (black solid line in Figure 7.1).

Shear-layer decompositions from the OLVR method can be used to make connections between PFs and source phenomena more directly than has been possible in past PFD investigations of jet sources.

It is common that independent mechanisms, which cannot be easily distinguished in total field reconstructions, are clearly separated in the OLVR PFD. Figure 7.12a shows the 160 Hz case, where the two local maxima in the total field reconstruction (inverted black triangles) around $z = 14$ and 20 m—each of nearly equal magnitude at the location of the reference array—receive energy selectively from PFs 2 and 1, respectively (shown by the red dashed and black solid lines). These two distinct maxima in the field are generated by overlapping source mechanisms that cannot be distinguished in the maximum region between $z = 0$ and 14 m of the total reconstruction at the shear layer, shown in Figure 7.12c (black circles). However, the spatial separation of the sources of PFs 2 and 1 is evident in the local maximum of each shear-layer PF at $z = 6$ and 9 m,respectively. In addition, PFs 4 (green dotted line) and 6 (light blue dashed line) dominate the field energy below $z = 6$ m in Figure 7.12b, although their energy at the shear layer is relatively low, as shown in Figure 7.12d. Note that the line styles and colors of Figure 7.12 are adhered to throughout the remainder of this chapter.

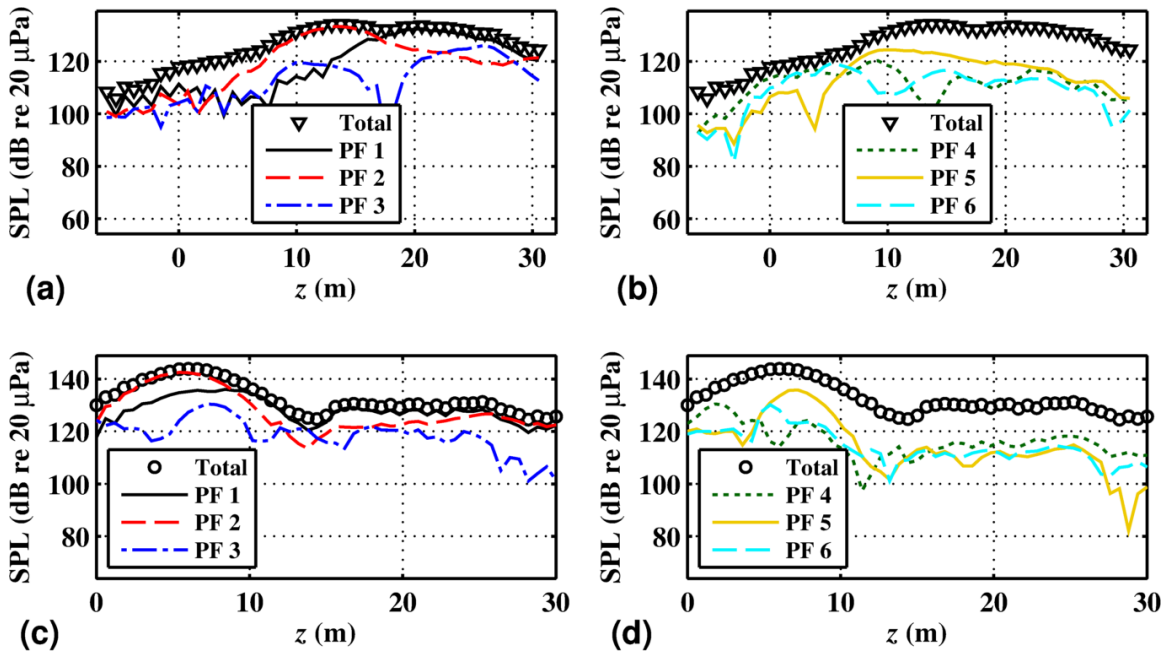

Figure 7.12 OLVR decompositions of the field at 160 Hz, military engine conditions. (a) Along reference array location, PFs 1-3. (b) Along reference array location, PFs 4-6. (c) Along shear layer boundary, PFs 1-3. (d) Along shear layer boundary, PFs 4-6.

Below 400 Hz, most of the energy in the total field is dominated by one or two PFS. At about 400 Hz and above, this is replaced by a more uniform spreading of energy across multiple PFs. In general, as frequency increases the number of significant sources (i.e. the number of independent PFs containing energy close to that of the dominant PF) increases. This is consistent with the trends found with SVD-based PFD (see section 3.2). For example, Figure 7.13 shows the overall MSTR SONAH reconstruction at 400 Hz. The total field at 400 Hz has a relatively broad beam pattern, as seen in the separation of contour lines by more than 5 m in the high-amplitude, downstream region. However, the beam widths in the downstream regions of each PF in Figure 7.14 are narrower; few contour lines, characterized by 3-dB increments, are separated by more than 2 m. The local maximum levels in the downstream regions of each beam for PFs 1, 2, and 3 are all within about 2 dB. It is the sum total of these narrow beams with nearly uniform magnitude that generates the wide beam in the total field. Note also that each source mechanism must be spatially self-coherent to generate narrow beam patterns. These

phenomena occur at many frequencies investigated here, between 25 Hz and 500 Hz, but they are especially apparent in the 400 Hz case.

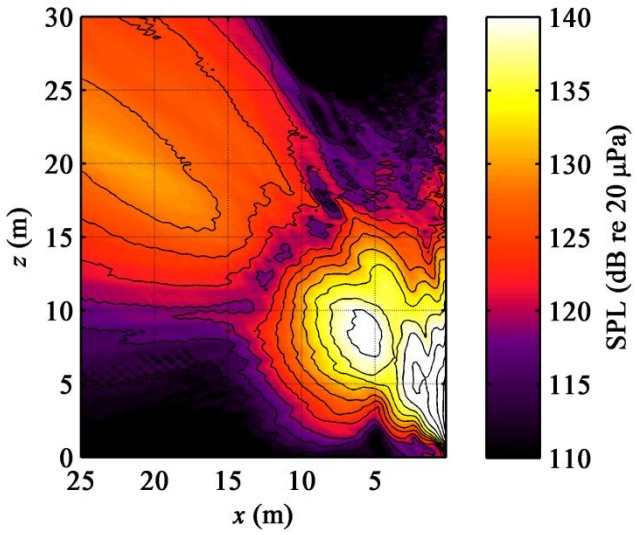

Figure 7.13 Total field reconstruction at y = 1.9 m from MSTR SONAH of the full-scale jet noise at military power and at 400 Hz, at y = 1.9 m. Black contour lines occur at 3 dB increments.

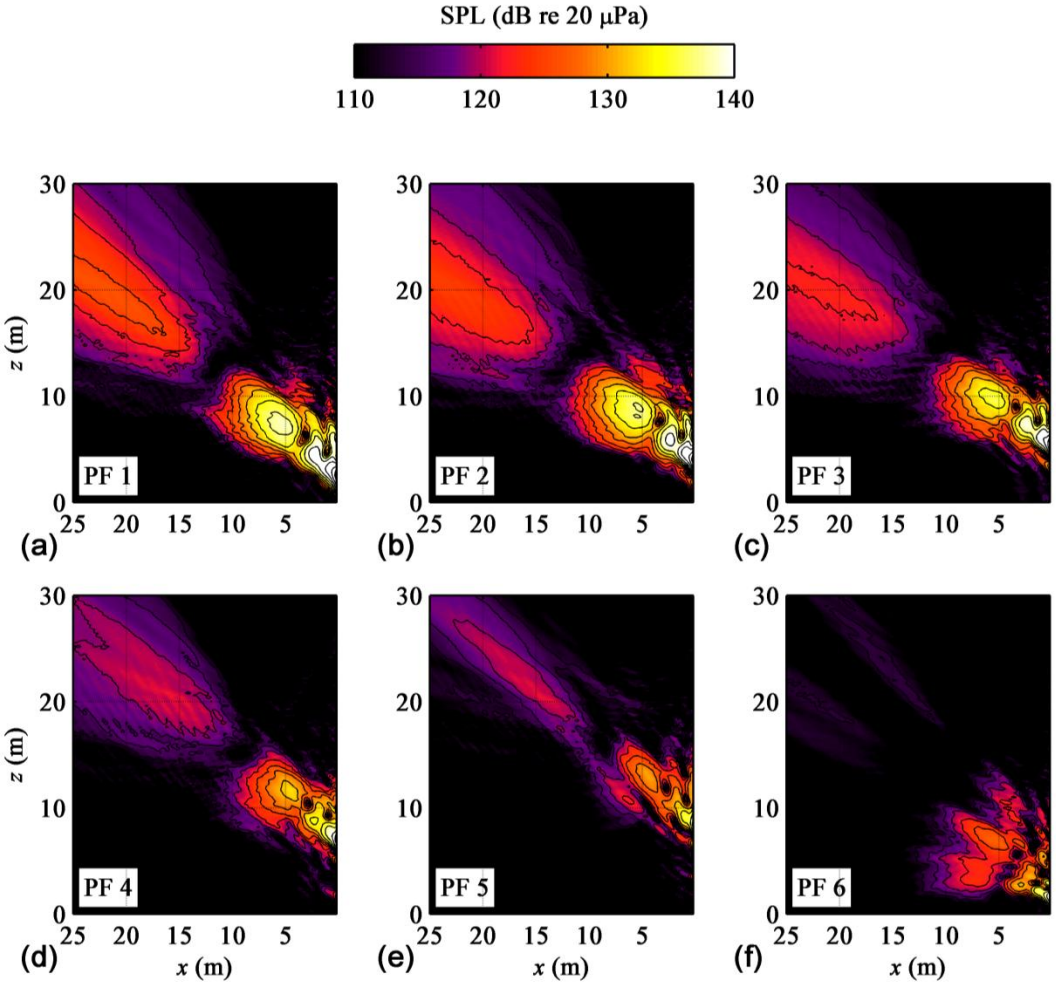

Figure 7.14 First six PFs, (a-f) respectively, from the OLVR decomposition of the full-scale jet noise at y = 1.9 m and at military power and at 400 Hz. Black contour lines occur at 3 dB increments.

Another important trend is visible in the 400 Hz, military power OLVR PFs. In general, at and above 200 Hz there exists a clear spatial ordering of the individual PFs. For example, Figure 7.15 shows the OLVR PFs at the reference location and shear layer for 400 Hz, military power. The source-related PFs of Figure 7.15c-d can be ordered spatially by the locations of their respective local maxima with increasing z as PF 6, 1, 2, 3, 4, and 5.

It is important to recognize that the spatial ordering of PF local maxima at the shear layer track the relative directionality of each PF in the radiated field. For example, each PF for the 400

Hz case Figure 7.14 contributes mainly in one localized direction of the overall field, and can be ordered spatially as PF 6, 1, 2, 3, 4, and 5—the same as the ordering of the PFs at the shear layer in Figure 7.15. The directionality varies about 10-20° from the upstream to the downstream lobes. (This directionality is difficult to see at the reference array in Figure 7.15a-b, due to the fact that the interference null occurs in the same location at this frequency.) An explanation of the relationship between source location and directionality is found in the fact that directivity depends on convection velocity. As velocity increases, the radiation tends to point farther away from the direction of convection and more toward the perpendicular. This combined with the fact that the convection velocity of turbulence structures decreases with distance downstream, indicates that directionality of radiation should point farther downstream as sources move farther downstream and slow down. A range of about 10-20° in the variation of directionality can be seen for all PF results shown in Appendix A.

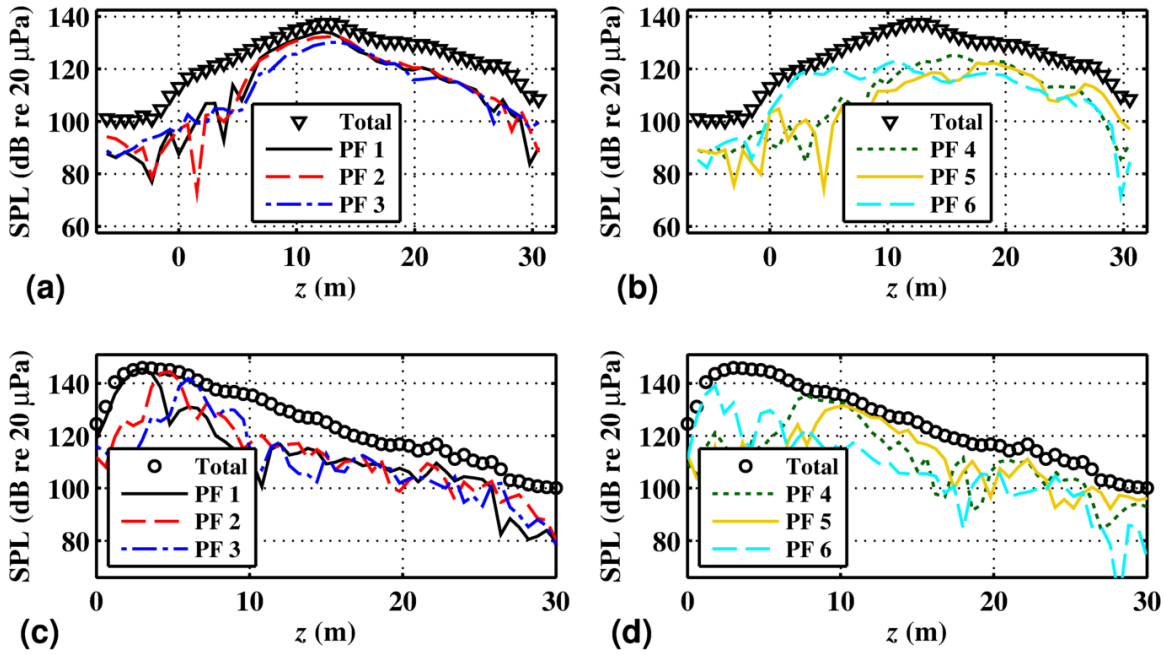

Figure 7.15 OLVR decompositions of the field at 400 Hz, military engine conditions. (a) Along reference array location, PFs 1-3. (b) Along reference array location, PFs 4-6. (c) Along shear layer boundary, PFs 1-3. (d) Along shear layer boundary, PFs 4-6.

7.5 Conclusions

Near-field acoustical holography (NAH) and partial field decomposition (PFD) methods have been implemented on a full-scale jet from the installed engine on a military aircraft. In particular, multisource-type representation statistically optimized near-field acoustical holography (MSTR SONAH) has been used to account for the presence of a rigid reflection plane in the jet environment and reconstruct the total sound field. Then, optimized-location virtual reference PFD (OLVR) has been implemented to decompose the reconstructed field into partial fields that represent independent source mechanisms. In summary, the following properties of the full-scale jet field and sources have been demonstrated.

1. As frequency increases, the total source region (represented by a one-dimensional reconstruction at the shear layer boundary) grows more compact and shifts upstream.
2. The directivity of the beam patterns tend to move farther forward with an increase in frequency. This can be explained in the context of a decrease in convection velocity downstream and the relative axial locations of sources at different frequencies.
3. Total shear-layer reconstructions reveal that, above 125 Hz, for both military and afterburner power, sources are characterized by an asymmetric distribution. Below 125 Hz the sources tend to be spatially extended, on the order of 20 m in length.
4. In the OLVR PFD, multiple, spatially distinct source mechanisms with overlapping distributions are shown to comprise the total source region. These independent sources radiate directionally according to their downstream location, with variations as high as 10-20°, which also fits the prediction of directivity based on convection velocity. The independent sources discussed here all result from large-scale turbulence (LST) radiation, which is spatially coherent, and are

not to be confused with the two-source model of jet noise, which separates sources into fine-scale turbulence (FST) and LST.[10,17]

5. In general, the distinction between multiple source mechanisms is not visible in the total field, since these sources overlap. However, at select frequencies (such as 160-315 Hz for military power), the beam patterns of the multiple sources are distinct enough to be seen in the field away from the sources. This accounts for the regions of local maxima seen in spatial/frequency maps measured along the reference array. The combination of multiple, narrow beam patterns with varying directivity serve to generate broad, total beams.
6. At low frequencies (below about 125 Hz for military power and about 100 Hz for afterburner), the total field is dominated by a single source mechanism, although the presence of additional sources are visible. As frequency increases, there is a transition to fields that are comprised of a greater number of sources with more evenly distributed contributions. In addition, as frequency increases the directivities of the dominant partial fields shift forward, in accordance with the upstream shift in dominant source locations.

It is yet to be determined whether the independent sources represented by the partial fields generated with OLVR correspond to truly distinct, localized source mechanisms, or are spatially separated simply as a result of a continuous source with decaying spatial coherence. A possible investigation to answer this question includes an analysis of the variation of the distribution of the individual partial fields as the set of virtual references is altered.

Several limitations of this study should be noted. The accuracy of the decomposition of the field is limited by the accuracy in the reconstruction of the field. This, in turn, is limited by the axial and azimuthal coverage of the jet by the hologram and reference arrays (see Section 5.5). It has been shown that relatively large errors occur at 20 and 25 Hz in the current study. These are due to the insufficient axial coverage of the hologram aperture for the long sources at

these frequencies, combined with the inability of the linear prediction scheme to predict data beyond the aperture. Extending the aperture axially (perhaps by as much as 5-10 m) in future measurements could assist in accurate reconstructions at these frequencies. Similarly, the limited azimuthal coverage of the hologram precluded a representation of the field by more than the axisymmetric wave functions, centered on the real and image jet locations. Although MSTR SONAH has been shown to provide accurate reconstructions of numerical sources of frequencies as high as 1250 Hz, the limited reference array restricts accurate field reconstructions to 400 or 500 Hz. Hence, the data above 500 Hz are not given in the present study. In future measurements, increased coverage of the source by distributing references in the azimuthal direction could allow for the current techniques to be applied at frequencies below 25 Hz and above 500 Hz. In addition, a more accurate representation of the azimuthal variation in the source model would allow the current, one-dimensional source models to be extended to the entire conical region surrounding the jet shear layer.

Chapter 8

Conclusion

Noise emissions from military jet aircraft pose several problems. The greatest concern is the risk of hearing loss experienced by aircraft maintainers and other flight deck personnel on aircraft carriers. In addition, jet noise causes community disturbances that affect the health and well-being of people who live near air force bases and airports. The jet noise community is addressing these problems on two fronts. First, noise reduction methods are being investigated to reduce emissions from jets at the source. Second, knowledge of the radiation properties of jets are used to guide regulations and operational procedures for jet-propelled aircraft activity, such as flight paths, takeoff and landing patterns, and the frequency of aircraft use. The current work presents an attempt to characterize and quantify jet noise source and radiation properties using near-field acoustical holography (NAH) and partial field decomposition (PFD) method. The imaging of jet noise sources can be used to investigate reduction methods, and resulting source models can be used to predict and regulate jet noise exposure.

8.1 Summary of Methods

NAH measurements were made of the jet from the engine of an F-22A Raptor. It was shown that hologram measurements must be made over tens of meters in the axial direction to fully cover the source region. The spatial/spectral measurements that were presented gave the first evidence of multiple source mechanisms.

Since the hologram measurements were made of a set of scans, or multiple measurements at different locations and times, the resulting scans were incoherent. Reconstruction of a field from a scan-based measurement requires the use of a PFD, which relies on information recorded at a fixed array of reference sensors, measuring simultaneously with each scan. It has been shown how PFD methods generate coherent holograms. The partial fields that are generated are mutually incoherent and can be propagated into the field individually with NAH.

The virtual coherence function provides an estimate for the number of independent sources in the field and quantifies the sufficiency of a reference array to represent all the energy in the hologram. This method of determining the sufficiency of a reference array was used to develop a figure of merit, first introduced by Gardner,[75] to guide array design based on measured coherence lengths in the geometric near field of a source, called references per coherence length. It was established that the deployment of one reference per coherence length leads to a sufficient array. This has been shown to be a robust guideline regardless of frequency, spatial source coherence, reference aperture, and standoff distance, over a broad range of these parameters.

The NAH method of multisource-type representation SONAH (MSTR SONAH) was presented as a method to represent spatially separated sources with an equivalent wave model, and to reconstruct the three-dimensional sound field. It allows for the inclusion of multiple sets of wave functions, one for each source shape and location. MSTR SONAH was validated through its application to several numerical and physical experiments. It was then applied to the full-scale jet data to account for the presence of the rigid reflecting ground below the jet. It was

used to estimate jet source distributions, based on reconstructions at the jet shear layer, and radiation properties as a function of frequency.

Although the reconstructed partial fields from the PFD method discussed above are valid, mutually incoherent components that, in total, represent the sound field, the physical interpretation of these individual fields is tenuous. The sound fields of sources that are characterized by decaying spatial coherence are represented by partial fields with normal mode-like distributions rather than partial fields that contain exclusive information about spatially distinct source mechanisms. This motivates the use of a secondary PFD method, which re-decomposes the partial fields into new partial fields that are physically meaningful. The optimized location virtual reference method (OLVR) generates an optimal set of virtual references from the partial fields at specific locations in the reconstructed field. In the application of OLVR to the jet, it is important to remember that turbulent flow fields are generally characterized by extended sources of decaying spatial coherence. Hence, the separation of independent source mechanisms is complicated. Nevertheless, OLVR is shown here to generate a set of partial fields for a full-scale jet noise source that are intuitive and provide physical insight about source coherence and distributions.

8.2 Summary of Findings

The reference microphone array was placed in a straight line along the ground, running parallel to the jet. Since it did not cover more of the jet azimuthally, it was insufficient to represent all the information in the field measurements above about 500 Hz. NAH cannot be used to reconstruct field energy that is missing from the hologram, no matter how accurate the propagation. Hence, NAH results were performed at frequencies of 500 Hz and below.

Coherence length values for the jet provided evidence that most of the energy in the high-amplitude regions for all frequencies (10 Hz to 1600 Hz shown here) is dominated by

contributions from the spatially coherent large-scale turbulence structures. In general, coherence length values diminished with increasing frequency. This is consistent with the idea that the number of effective sources increases with frequency, and the spatial extent of those sources decreases with frequency. The analyses presented demonstrated the utility of the coherence length as it is defined here in summarizing near-field spatial coherence and in making inferences about spatial source coherence.

After the development and validation of MSTR SONAH and OLVR, Chapter 7 presented the reconstructed and decomposed fields for the full scale jet, at multiple engine conditions, and over a range of frequencies from 20 Hz to 500 Hz. Source models were provided, both for the overall field and for the decomposed contributions of multiple source mechanisms. It was shown that the jet source is comprised of independent sources that are distinct, but overlap, in the axial direction. As frequency increases, the energy content in the partial fields gradually shifts from one dominant partial field to a more equal contribution from multiple sources. The directivity of the beam patterns radiated by these multiple sources is mainly dictated by their respective axial location, suggesting a relationship between downstream location and convection velocity.

8.3 Contributions

In the present study, the SONAH algorithm was reformulated to include multiple sets of wave functions, for multisource configurations in the method called MSTR SONAH. It was used to reconstruct full-scale jet sources and fields in the presence of the ground reflection, demonstrating that jet fields can be measured without placing the jet in an anechoic chamber or high above the ground. The OLVR algorithm was modified to automate the selection and rejection of virtual references when source locations are not easily distinguishable. OLVR was used to connect partial fields to independent, physical jet source mechanisms. This was the first

time that a clear connection was made between decomposed partial fields and specific source properties in a jet.

8.4 Implications and Recommendations

The fact that the reference array was insufficient to represent all the information in the field measurement above about 500 Hz limits the accuracy of NAH methods. It is likely that a distribution of reference microphones around the jet azimuthally, instead of a linear array, would improve the results in future measurements. References should cover at least the same azimuthal aperture as does the hologram array. The number of references required in such an array is difficult to predict from the present data set, but may be estimated through an analysis of measured coherence lengths in the geometric near field of a jet

The results of the MSTR SONAH implementation are also instructive for future applications of NAH to jet sources. Based on the analyses present here, it is not necessary to measure a full-scale jet in an anechoic environment or far from the ground, which would increase the cost and difficulty of a measurement. Although not performed here, it is feasible that accurate source reconstructions can allow for the isolation and removal of the reflection effects in the future.[97]

The partial fields generated with OLVR represent spatially distinct source mechanisms. However, it is yet to be determined whether the independent sources represented by the partial fields correspond to truly distinct, localized source mechanisms, or are spatially separated simply as a result of a continuous source with decaying spatial coherence. To answer this question, an analysis of the variation of the distribution of the individual partial fields as the set of virtual references is altered would show their stability or instability, which could be linked to a fixed or arbitrary distribution of sources, respectively.

References

[1]S. A. McInerny, G. Lu and S. Olcmen, "Rocket and jet mixing noise, background and prediction procedures", National Center for Physical Acoustics, University of Mississippi, 2004.

[2]V. Mestre, "Effects of aircraft noise: Research update on selected topics", Airport Cooperative Research Program, **Synthesis 9**, Project 11-03, Topic S02-01, 2008.

[3]M. J. Lighthill, "On sound generated aerodynamically. I. General theory," Royal Society of London. Series A, Mathematical and Physical Sciences **211**, 564-587 (1952).

[4]M. J. Lighthill, "On sound generated aerodynamically. II. Turbulence as a source of sound," Royal Society of London. Series A, Mathematical and Physical Sciences **222**, 1-32 (1954).

[5]G. M. Lilley, "On the noise from air jets", Aeronautical Research Council Reports and Memoranda, **20**, 1958.

[6]G. M. Lilley, "Jet noise classical theory and experiments," in *Aeroacoustics of flight vehicles: Theory and practice*, Vol. 1. Noise Sources, edited by H. H. Hubbard (Acoustical Society of America, Woodbury, NY, 1995), pp. 211-289.

[7]C. K. W. Tam, "Jet noise: Since 1952," Theoretical and Computational Fluid Dynamics **10**, 393-405 (1998).

[8]C. K. W. Tam, "Recent advances in computational aeroacoustics," Fluid Dynamics Research **38**, 591-615 (2006).

[9]R. H. Schlinker, R. A. Reba, J. C. Simonich, T. Colonius, K. Gudmundsson and F. Ladeinde, "Towards prediction and control of large scale turbulent structure supersonic jet noise," Proceedings of 2009 ASME Turbo Expo, pp. 217-229, 2009.

[10]C. K. W. Tam, K. Viswanathan, K. K. Ahuja and J. Panda, "The sources of jet noise: Experimental evidence," J. Fluid Mech. **615**, 253-292 (2008).

[11]Mollo-Christensen, "Jet noise and shear flow instability seen from an experimenter's viewpoint," American Society of Mechanical Engineers Journal of Applied Mechanics **89**, 1-7 (1967).

[12]S. C. Crow and F. H. Champagne, "Orderly structure in jet turbulence," J. Fluid Mech. **48**, 547-591 (1971).

[13]G. L. Brown and A. Roshko, "On density effects and large structure in turbulent mixing layers," J. Fluid Mech. **64**, 775-816 (1974).

[14]R. H. Schlinker, *Supersonic jet noise experiments* (Ph.D. Dissertation, University of Southern California, Los Angeles, CA, 1975).

[15]J. Laufer, R. Schlinker and R. E. Kaplan, "Experiments on supersonic jet noise," AIAA J. **14**, 489-497 (1976).

[16]C. K. W. Tam, M. Golebiowsky and J. M. Seiner, "On the two components of turbulent mixing noise from supersonic jets," AIAA Paper 96-1716, May 1996.

[17]K. Viswanathan, "Mechanisms of jet noise generation: Classical theories and recent developments," International Journal of Aeroacoustics **8**, 355-408 (2009).

[18]H. V. Fuchs, "Space correlations of the fluctuation presure in subsonic turbulent jets," J. Sound Vib. **23**, 77-99 (1972).

[19]R. R. Mankbadi, "On the interaction between fundamental and subharmonic instability waves in a turbulent round jet," J. Fluid Mech **160**, 385-419 (1985).

[20]P. J. Morris, M. G. Giridharan and G. M. Lilley, "On the turbulent mixing of compressible free shear layers," Proceedings of the Royal Society of London. Series A: Mathematical and Physical Sciences **431**, 219-243 (1990).

[21]K. Viswanathan, "Investigation of the sources of jet noise," AIAA Paper 2007-3601, May 2007.

[22]E. G. Williams, *Fourier acoustics: Sound radiation and nearfield acoustical holography* (Academic Press, San Diego, 1999).

[23]B. D. Van Veen and K. M. Buckley, "Beamforming: A versatile approach to spatial filtering," IEEE ASSP Magazine, 4-24 (1988).

[24]V. F. Kopiev, S. A. Chernyshev, M. Y. Zaitsev and V. M. Kuznetsav, "Experimental validation of instability wave theory for round supersonic jet," AIAA

[25]U. Michel, "The role of source interference in jet noise," AIAA Paper 2009-3377, May 11-13, 2009.

[26]T. Suzuki and T. Colonius, "Instability waves in a subsonic round jet detected using a near-field phased microphone array," J. Fluid Mech. **565**, 197-226 (2006).

[27]J. Billingsley and R. Kinns, "The acoustic telescope," J. Sound Vib. **48**, 485-510 (1976).

[28]M. J. Fisher, M. Harper-Bourne and S. A. L. Glegg, "Jet engine noise source location: The polar correlation technique," J. Sound Vib. **51**, 23-54 (1977).

[29]M. Schaffar, "A localized study of the density of a jet-noise source in its mixing zone using an elliptical acoustic mirror associated with a laser velocimeter," Acustica **50**, 180-188 (1982).

[30]H. V. Fuchs, "On the application of acoustic 'mirror', 'telescope', and 'polar correlation' techniques to jet noise source location," J. Sound Vib. **58**, 117-126 (1978).

[31]S. R. Venkatesh, D. R. Polak and S. Narayanan, "Beamforming algorithm for distributed noise source localization and its application to jet noise," AIAA J. **41**, 1238-1246 (2003).

[32]R. H. Schlinker, S. A. Liljenberg, D. R. Polak, K. A. Post, C. T. Chipman and A. M. Stern, "Supersonic jet noise source characteristics & propagation: Engine and model scale," AIAA Paper 2007-3623, May 21-23, 2007.

[33]S. S. Lee and J. Bridges, "Phased-array measurements of single flow hot jets," AIAA Paper 2005-2842, May 2005.

[34]T. F. Brooks and W. M. Humphreys, Jr., "Extension of DAMAS phased array processing for spatial coherence determination (DAMAS-C)," AIAA Paper 2006-2654,

[35]J. D. Maynard, E. G. Williams and Y. Lee, "Nearfield acoustic holography: 1. Theory of generalized holography and the development of NAH," J. Acoust. Soc. Am. **78**, 1395-1413 (1985).

[36]Z. Wang and S. F. Wu, "Helmholtz equation--least-squares method for reconstructing the acoustic pressure field," J. Acoust. Soc. Am. **102**, 2020-2032 (1997).

[37]J. Hald, "Patch near-field acoustical holography using a new statistically optimal method," Proceedings of INTER-NOISE, pp. 2203-2210, 2003.

[38]M. Lee, J. S. Bolton and L. Mongeau, "Application of cylindrical near-field acoustical holography to the visualization of aeroacoustic sources," J. Acoust. Soc. Am. **114**, 842-858 (2003).

[39]R. Reba, S. Narayanan and T. Colonius, "Wave-packet models for large-scale mixing noise," International Journal of Aeroacoustics **9**, 533-558 (2010).

[40]R. Reba, J. C. Simonich and R. H. Schlinker, "Sound radiated by large-scale wave-packets in subsonic and supersonic jets," AIAA Paper 2009-3256, May 2009.

[41]C. K. W. Tam, K. Viswanathan, N. N. Pastouchenko and B. Tam, "Continuation of the near acoustic field of a jet to the far field. Part II: Experimental validation and noise source characteristics," AIAA Paper 2010-3729, June 7-9, 2010.

[42]J. Morgan, T. B. Neilsen, K. L. Gee, A. T. Wall and M. M. James, "Simple-source model of military jet aircraft noise," Proceedings of Inter-Noise 2012, 2012.

[43]J. Morgan, K. L. Gee, T. B. Neilsen and A. T. Wall, "Simple-source model of military jet aircraft noise," Noise Control Eng. J. **60**, 435-449 (2012).

[44]D. M. Hart, T. B. Neilsen, K. L. Gee and M. M. James, "A Bayesian based equivalent sound source model for a military jet aircraft," Proceedings of 21st International Congress on Acoustics, 2012.

[45]M. Ochmann, "Comments on ‘‘transient sound radiation from impulsively accelerated bodies’’," J. Acoust. Soc. Am. **97**, 542–553 (1995).

[46]I. Y. Jeon and J. G. Ih, "On the holographic reconstruction of vibroacoustic fields using equivalent sources and inverse boundary element method," J. Acoust. Soc. Am. **118**, 3473 (2005).

[47]S. F. Wu, "On reconstruction of acoustic pressure fields using the helmholtz equation least squares method," J. Acoust. Soc. Am. **107**, 2511-2522 (2000).

[48]S. F. Wu, "Techniques for implementing near-field acoustical holography," Sound Vib. **44**, 12-16 (2010).

[49]T. Semenova and S. F. Wu, "On the choice of expansion functions in the helmholtz equation least-squares method," J. Acoust. Soc. Am. **117**, 701 (2005).

[50]S. F. Wu, "Methods for reconstructing acoustic quantities based on acoustic pressure measurements," J. Acoust. Soc. Am. **124**, 2680-2697 (2008).

[51]R. Steiner and J. Hald, "Near-field acoustical holography without the errors and limitations caused by the use of spatial DFT," Int. J. Sound Vib. **6**, 83-89 (2001).

[52]Y. T. Cho, J. S. Bolton and J. Hald, "Source visualization by using statistically optimized near-field acoustical holography in cylindrical coordinates," J. Acoust. Soc. Am. **118**, 2355 (2005).

[53]F. Jacobsen and V. Jaud, "Statistically optimized near field acoustic holography using an array of pressure-velocity probes," J. Acoust. Soc. Am. **121**, 1550 (2007).

[54]J. Hald, "Basic theory and properties of statistically optimized near-field acoustical holography," J. Acoust. Soc. Am. **125**, 2105-2120 (2009).

[55]M. Lee and J. S. Bolton, "Source characterization of a subsonic jet by using near-field acoustical holography," J. Acoust. Soc. Am. **121**, 967-977 (2007).

[56]A. T. Wall, K. L. Gee, T. B. Neilsen, D. W. Krueger, M. M. James, S. D. Sommerfeldt and J. D. Blotter, "Full-scale jet noise characterization using scan-based acoustical holography," AIAA Paper 2012-2081, June 4-6, 2012.

[57]J. Hald, "Patch holography in cabin environments using a two-layer hand-held array and an extended sonah algorithm," Proceedings of Euronoise 2006, 2006.

[58]V. D. Kupradze, "On the approximate solution of problems in mathematical physics," Russian Mathematical Surveys **22**, 58-108 (1967).

[59]Y. A. Eremin, "Complete systems of functions for the study of boundary value problems in mathematical physics," Proceedings of Soviet Physics Doklady, pp. 635, 1987.

[60]P. N. Shah, H. Vold and M. Yang, "Reconstruction of far-field noise using multireference acosutical holography measurements of high-speed jets," AIAA Paper 2011-2772, June 5-8, 2011.

[61]A. T. Wall, K. L. Gee, M. M. James, K. A. Bradley, S. A. McInerny and T. B. Neilsen, "Near-field noise measurements of a high-performance military jet aircraft," Noise Control Eng. J. **60**, 421-434 (2012).

[62]D. Otte, P. Sas, R. Snoeys, P. V. Ponseele and J. Leuridan, "Use of pricnicapl component analysis and virtual coherences for dominant noise source identification," Proceedings of Second International Seminar on Noise Source Identification and Numerical Methods in Acoustics, 1987.

[63]J. Hald, "STSF—A unique technique for scan-based nearfield acoustical holography without restriction on coherence," Technical Report No. 1, from Bruel & Kjaer, Naerum, Denmark, 1989.

[64]Y. J. Kim, J. S. Bolton and H. S. Kwon, "Partial sound field decomposition in multireference near-field acoustical holography by using optimally located virtual references," J. Acoust. Soc. Am. **115**, 1641-1652 (2004).

[65]J. Lumley, "The structure of inhomogeneous turbulent flows," Atmospheric turbulence and radio wave propagation, 166-178 (1967).

[66]M. Glauser and W. George, "Orthogonal decomposition of the axisymmetric jet mixing layer including azimuthal dependence," Advances in turbulence, 357-366 (1987).

[67]M. N. Glauser and W. K. George, "An orthogonal decomposition of the axisymmetric jet mixing layer utilizing cross-wire velocity measurements," Proceedings of 6th Symposium on Turbulent Shear Flows, pp. 10-11, 1987.

[68]D. Long, T. van Lent and R. Arndt, "Jet noise at low reynolds number," Proceedings of AIAA, Astrodynamics Specialist Conference, 1981.

[69]R. E. A. Arndt, D. Long and M. Glauser, "The proper orthogonal decomposition of pressure fluctuations surrounding a turbulent jet," J. Fluid Mech. **340**, 1-33 (1997).

[70]J. Freund and T. Colonius, "Turbulence and sound-field pod analysis of a turbulent jet," International Journal of Aeroacoustics **8**, 337-354 (2009).

[71]H. Vold, P. Shah, P. Morris, Y. Du and D. Papamoschou, "Axisymmetry and azimuthal modes in jet noise," AIAA Jue 4-6, 2012.

[72]H. Vold, P. N. Shah, J. Davis, P. G. Bremner, D. McLaughlin, P. Morris, J. Veltin and R. McKinley, "High-resolution continuous scan acoustical holography applied to high-speed jet noise," AIAA Paper 2010-3754, June 7-9, 2010.

[73]H. Vold, P. Shah and M. Yang, "On the computation of farfield cross-spectra and coherences from reduced parameter models of high speed jet noise," J. Acoust. Soc. Am. **130**, 2512 (2011).

[74]M. Lee and J. S. Bolton, "Scan-based near-field acoustical holography and partial field decomposition in the presence of noise and source level variation," J. Acoust. Soc. Am. **119**, 382-393 (2006).

[75]M. Gardner, *Scan-based near-field acoustical holography on partially correlated sources* (M.S. Thesis, Brigham Young Univ., Provo, UT, 2009).

[76]M. F. Hamilton and D. T. Blackstock, *Nonlinear acoustics* (Acoustical Society of America, Melville, NY, 2008).

[77]K. L. Gee, V. W. Sparrow, M. M. James, J. M. Downing, C. M. Hobbs, T. B. Gabrielson and A. A. Atchley, "The role of nonlinear effects in the propagation of noise from high-power jet aircraft," J. Acoust. Soc. Am. **123**, 4082-4093 (2008).

[78]M. Muhlestein and K. Gee, "Experimental investigation of a characteristic shock formation distance in finite-amplitude noise propagation," Proc. Mtgs. Acoust. **12**, 045002 (2011).

[79]K. L. Gee, J. M. Downing, M. M. James, R. C. McKinley, R. L. McKinley, T. B. Neilsen and A. T. Wall, "Nonlinear evolution of noise from a military jet aircraft during ground run-up," AIAA Paper 2012-2258, 04 - 06 June 2012.

[80]T. B. Neilsen, K. L. Gee, A. T. Wall and M. M. James, "Similarity spectra analysis of high-performance jet aircraft noise," JASA Express Letters, (accepted 2013).

[81]M. M. James, K. L. Gee, A. T. Wall, J. M. Downing, K. A. Bradley and S. A. McInerny, "Aircraft jet source noise measurements of a lockheed martin F-22 fighter jet using a prototype near-field acoustical holography measurement system," J. Acoust. Soc. Am. **127**, 1878 (2010).

[82]M. M. James and K. L. Gee, "Aircraft jet plume source noise mesurement system," Sound Vib. **44**, 14-17 (2010).

[83]A. T. Wall, K. L. Gee, M. D. Gardner, T. B. Neilsen and M. M. James, "Near-field acoustical holography applied to high-performance jet aircraft noise," Proc. Mtgs. Acoust. **9**, 040009 (2011).

[84]C. K. W. Tam, "Supersonic jet noise," Annu. Rev. Fluid Mech. **27**, 17-43 (1995).

[85]C. K. W. Tam, N. N. Pastouchenko and R. H. Schlinker, "Noise source distribution in supersonic jets," J. Sound Vib. **291**, 192-201 (2006).

[86]J. C. Yu and D. S. Dosanjh, "Noise field of a supersonic mach 1.5 cold model jet," J. Acoust. Soc. Am. **51**, 1400-1410 (1972).

[87]R. Reba, J. Simonich and R. Schlinker, "Measurement of source wave-packets in high-speed jets and connection to far-field sound," AIAA Paper 2008-2891, May 5-7, 2008.

[88]K. Viswanathan, "Does a model-scale nozzle emit the same jet noise as a jet engine?," AIAA J. **46**, 1715-1737 (2008).

[89]B. Greska and A. Krothapalli, "On the far-field propagation of high-speed jet noise," Proceedings of NCAD / NoiseCon 2008, 2008.

[90]A. T. Wall, K. L. Gee, M. M. James and M. D. Gardner, "Application of near-field acoustical holography to high-performance jet aircraft noise," J. Acoust. Soc. Am. **127**, 1879 (2010).

[91]A. T. Wall, K. L. Gee, T. B. Neilsen and M. M. James, "Considerations for near-field acoustical inverse measurements on partially correlated sources," J. Acoust. Soc. Am. **128**, 2285 (2010).

[92]C. K. W. Tam, "Influence of nozzle geometry on the noise of high-speed jets," AIAA J. **36**, 1396-1400 (1998).

[93]T. J. S. Jothi and K. Srinivasan, "Acoustic characteristics of non-circular slot jets," Acta Acustica united with Acustica **94**, 229-242 (2008).

[94]R. T. Taylor, K. L. Gee, J. H. Giraud, S. D. Sommerfeldt, J. D. Blotter and C. P. Wiederhold, "On the use of prepolarized microphones in rocket noise measurements," J. Acoust. Soc. Am. **130**, 2512 (2011).

[95]T. B. Neilsen, K. L. Gee, A. T. Wall and M. M. James, "Comparison of near-field military jet aircraft noise with similarity spectra," J. Acoust. Soc. Am. **129**, 2442 (2011).

[96]K. L. Gee, T. B. Gabrielson, A. A. Atchley and V. W. Sparrow, "Preliminary analysis of nonlinearity in military jet aircraft noise propagation," AIAA J. **43**, 1398-1401 (2005).

[97]D. K. McLaughlin, C.-W. Kuo and D. Papamoschou, "Experiments on the effect of ground reflections on supersonic jet noise," AIAA Paper 2008-22, January 2008.

[98]T. D. Norum, D. P. Garber, R. A. Golub, O. L. Santa Maria and J. S. Orme, "Supersonic jet exhaust noise at high subsonic flight speed," (2004).

[99]S. A. McInerny, K. L. Gee, J. M. Downing and M. M. James, "Acoustical nonlinearities in aircraft flyover data," AIAA Paper 2007-3654, May 2007.

[100]J. Morgan, K. L. Gee, T. B. Neilsen and A. T. Wall, "A simple-source model of military jet aircraft noise," J. Acoust. Soc. Am. **129**, 2442 (2011).

[101]T. B. Gabrielson, T. M. Marston and A. A. Atchley, "Nonlinear propagation modeling: Guidelines for supporting measurements," Proceedings of Noise-Con, pp. 275-282, 2005.

[102]S. A. McInerny, "Launch vehicle acosutics part 2: Statistics of the time domain data," Journal of Aircraft **33**, (1996).

[103]J. S. Bendat and A. G. Piersol, *Random data: Analysis and measurement procedures*, Fourth ed. (John Wiley & Sons, Inc., Hoboken, New Jersey, 2010).

[104]A. Michalke, "Some remarks on source coherence affecting jet noise," J. Sound Vib. **87**, 1-17 (1983).

[105]H. S. Kwon, Y. J. Kim and J. S. Bolton, "Compensation for source nonstationarity in multireference, scan-based near-field acoustical holography," J. Acoust. Soc. Am. **113**, 360-368 (2003).

[106]D. Long, J. Peters and M. Anderson, "Evaluating turbofan exhaust noise and source characteristics from near field measurements," AIAA Paper 2009-3214, May 11-13, 2009.

[107]D. M. Photiadis, "The relationship of singular value decomposition to wave-vector filtering in sound radiation problems," J. Acoust. Soc. Am. **88**, 1152-1159 (1990).

[108]H. S. Kwon and J. S. Bolton, "Partial field decomposition in nearfield acoustical holography by the use of singular value decomposition and partial coherence procedures," Proceedings of NOISE-CON, pp. 649-654, 1998.

[109]K.-U. Nam and Y.-H. Kim, "Visualization of multiple incoherent sources by the backward prediction of near-field acoustic holography," J. Acoust. Soc. Am. **109**, 1808-1816 (2001).

[110]S. M. Price and R. J. Bernhard, "Virtual coherence: A digital signal processing technique for incoherent source idientification," Proceedings of 4th International Modal Analysis Conference, pp. 1256-1262, 1986.

[111]A. T. Wall, K. L. Gee and T. B. Neilsen, "On near-field acoustical inverse measurements of partially coherent sources," Proc. Mtgs. Acoust. **11**, 040007 (2012).

[112]A. T. Wall, M. D. Gardner, K. L. Gee and T. B. Neilsen, "Coherence length as a figure of merit in multireference near-field acoustical holography," J. Acoust. Soc. Am. **132**, EL215-EL221 (2012).

[113]G. K. Ackermann and J. Eichler, *Holography: A practical approach* (Wiley-VCH Verlag GmbH & Co. KGaA, Weinheim, 2007), pp. 75-78.

[114]J. M. Collis, T. F. Duda, J. F. Lynch and H. A. DeFerrari, "Observed limiting cases of horizontal field coherence and array performance in a time-varying internal wavefield," J. Acoust. Soc. Am. **124**, EL97-EL103 (2008).

[115]E. G. Williams, "Regularization methods for near-field acoustical holography," J. Acoust. Soc. Am. **110**, 1976-1988 (2001).

[116]In a previous conference proceedings (see Reference 12) the average value was used.

[117]C. K. W. Tam, "Mach wave radiation from high-speed jets," AIAA J. **47**, 2440-2448 (2009).

[118]E. G. Williams, "Continuation of acoustic near-fields," J. Acoust. Soc. Am. **113**, 1273-1281 (2003).

[119]L. B. Jackson, *Digital filters and signal processing*, Second ed. (Kluwer Academic Publishers, 1989), pp. 255-257.

[120]I. Kauppinen and J. Kauppinen, "Reconstruction method for missing or damaged long portions in audio signal," J. Audio Engin. Soc. **50**, 594-602 (2002).

[121]S. Vaseghi and R. Frayling-Cork, "Restoration of old gramophone recordings," J. Audio Engin. Soc. **40**, 791-801 (1992).

[122]A. T. Wall, K. L. Gee, D. W. Krueger, T. B. Neilsen and S. D. Sommerfeldt, "Aperture extension for near-field acoustical holography of jet noise," Proc. Mtgs. Acoust. **14**, (pending submission).

[123]R. Scholte, I. Lopez, N. B. Roozen and H. Nijmeijer, "Truncated aperture extrapolation for Fourier-based near-field acoustic holography by means of border-padding," J. Acoust. Soc. Am. **125**, 3844-3854 (2009).

[124]D. W. Krueger, *Array-based characterization of military jet aircraft noise* (M.S. Thesis, Brigham Young University, Provo, 2012).

[125]A. T. Wall, K. L. Gee and T. B. Neilsen, "Modified statistically optimized near-field acoustical holography for multi-source fields," Proc. Mtgs. Acoust., (accepted 2013).

[126]T. K. Moon and W. C. Stirling, *Mathematical methods and algorithms for signal processing* (Prentice Hall New York, 2000), pp. 139 and 183.

[127]N. Rayess and S. F. Wu, "Experimental validations of the hels method for reconstructing acoustic radiation from a complex vibrating structure," J. Acoust. Soc. Am. **107**, 2955 (2000).

[128]A. T. Wall, K. L. Gee, T. B. Neilsen and M. M. James, "Partial field decomposition of jet noise sources using optimally located virtual reference microphones," Proc. Mtgs. Acoust. **18**, 045001 (2012).

[129]D. Otte, P. Sas and P. V. Ponseele, "Noise source identification by use of principal component analysis," Proceedings of Inter-Noise 88, pp. 199, 1988.

[130]D. H. Johnson and D. E. Dudgeon, *Array signal processing: Concepts and techniques* (Prentice-Hall, 1993).

[131]J. S. Bendat, "Modern analysis procedures for multiple input/output problems," J. Acoust. Soc. Am. **68**, 498-503 (1980).

[132]D. L. Hallman and J. S. Bolton, "A comparision of multi-reference nearfield acoustical holography procedures," NOISE-CON 94, Ft. Lauderdale, Florida, 1994, pp. 929-933.

[133]K. Viswanathan, J. Underbrink and L. Brusniak, "Space-time correlation measurements in near fields of jets," AIAA J. **49**, 1577-1599 (2011).

[134]R. Reba, J. Simonich and R. Schlinker, "Sound radiated by large-scale wave-packets in subsonic and supersonic jets," AIAA Paper 2009-3256, May 11-13, 2009.

[135]A. Michalke, "On the effect of spatial source coherence on the radiation of jet noise," J. Sound Vib. **55**, 377-394 (1977).

[136]C. K. W. Tam, "Supersonic jet noise generated by large scale disturbances," J. Sound Vib. **38**, 51-79 (1975).

[137]R. H. Schlinker, J. C. Simonich, D. W. Shannon, R. A. Reba, T. Colonius, K. Gudmundsson and F. Ladeinde, "Supersonic jet noise from round and chevron nozzles: Experimental studies," AIAA Paper 2009-3257, May 2009.

[138]A. D. Pierce, *Acoustics: An introduction to its physical principles and applications*, 1994 ed. (Acoustical Society of America, Melville, NY, 1989), pp. 58.

Appendix

A OLVR PFD Results for All Frequencies

This section shows partial fields for all frequencies investigated and at both military and afterburner powers with limited, focused discussion. Insights about jet noise phenomena shown here can be understood in context of the results discussed in Chapter 6. Results shown here also serve as a repository of OLVR decomposed PFs for comparison with future analyses. All color maps shown have a color region spanning 40 dB. PFs for military power at 160 and 400 Hz are repeated here for ease of comparison. Since large reconstruction errors occur in the 20 Hz case for military power (see Figure 7.4), and in the 20 and 25 Hz cases for afterburner (see Figure 7.7), PFs for these reconstructions are excluded from the current section.

The jet source and field, when decomposed with the OLVR method, is dominated at low frequencies (about 20 Hz to 125 Hz for military power, shown in Figure A.1 through Figure A.16) by one partial field. As an example, Figure A.2a-b shows the first six PFs along the reference location for military power, 25 Hz. Note that most of the energy in the total field curve, marked by black inverted triangles, is within 1-2 dB of PF 1, the black solid line. Notable exceptions occur far upstream near $z = -3$ m, where PF 4 (the golden dotted line) is the dominant field, and near $z = 10$ m, where the localized "bump" in the total field receives nearly equal contributions (within 1 dB) from PF 1, PF 2 (the red dashed curve), and PF 5 (the green

solid curve). These suggest the presence of multiple source mechanisms, or multiple processes in the field generation, even at these low frequencies.

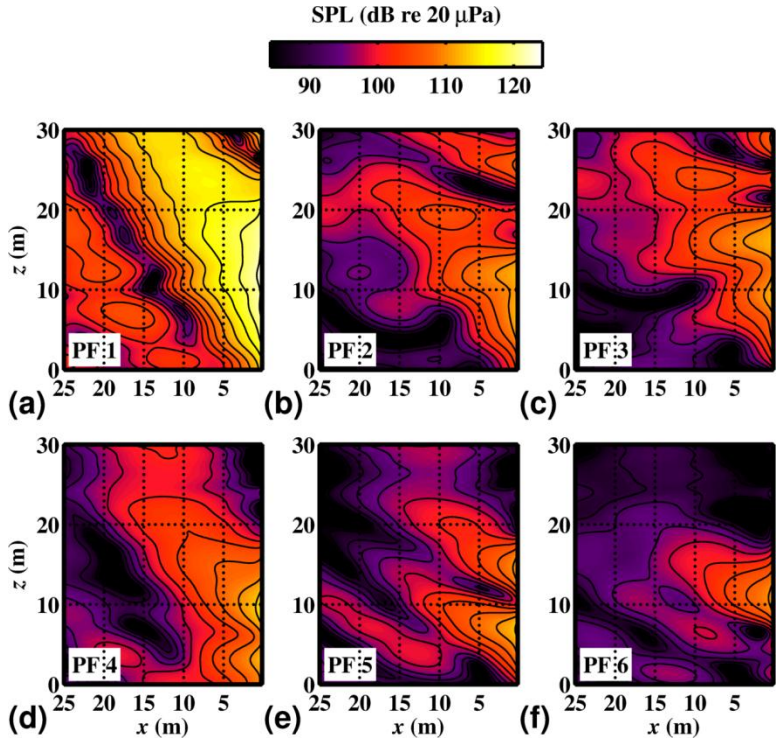

Figure A.1 First six PFs, (a-f) respectively, from the OLVR decomposition of the full-scale jet noise at military power and at 25 Hz. Black contour lines occur at 3 dB increments.

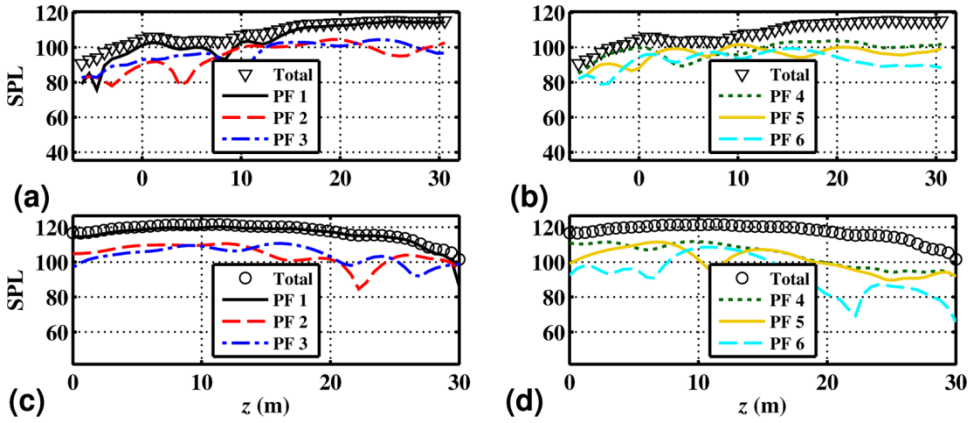

Figure A.2 OLVR decompositions of the field at 25 Hz, military engine conditions. (a) Along reference array location, PFs 1-3. (b) Along reference array location, PFs 4-6. (c) Along shear layer boundary, PFs 1-3. (d) Along shear layer boundary, PFs 4-6. SPLs are calculated relative to 20 μPa.

Figure A.2c-d shows the OLVR PFs along the location of the shear-layer boundary at 25 Hz. PF 1 is the primary PF for the entire source, with a nearly exclusive difference between PF 1 and the total field of <1 dB. In Figure A.2a-b, PFs 2, 4, and 5 each contribute significant energy to localized regions of the field at the reference array location, even though they do not do so at the source. This suggests that they are low-amplitude, extended, self-coherent sources characterized by a beaming of energy in localized directions, which localization is more easily discernible farther from the source.

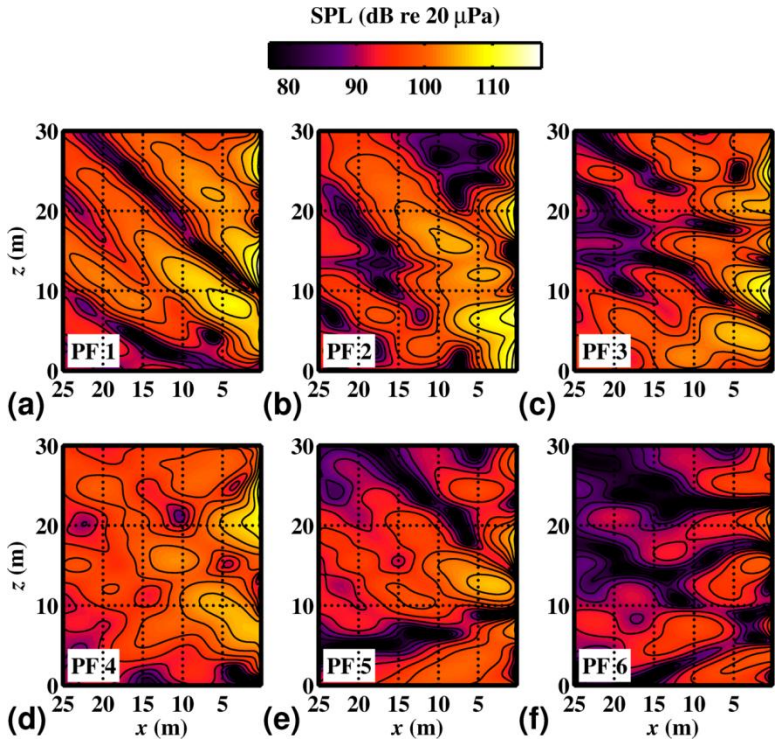

Figure A.3 First six PFs, (a-f) respectively, from the OLVR decomposition of the full-scale jet noise at military power and at 32 Hz. Black contour lines occur at 3 dB increments.

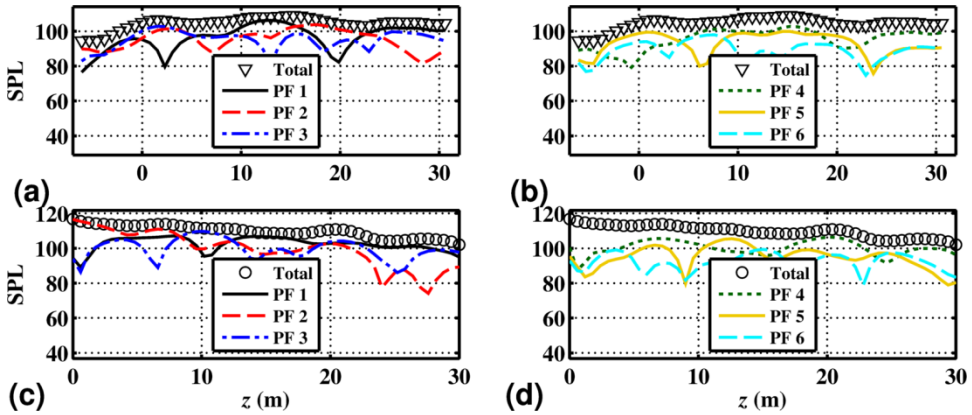

Figure A.4 OLVR decompositions of the field at 32 Hz, military engine conditions. (a) Along reference array location, PFs 1-3. (b) Along reference array location, PFs 4-6. (c) Along shear layer boundary, PFs 1-3. (d) Along shear layer boundary, PFs 4-6. SPLs are calculated relative to 20 μPa.

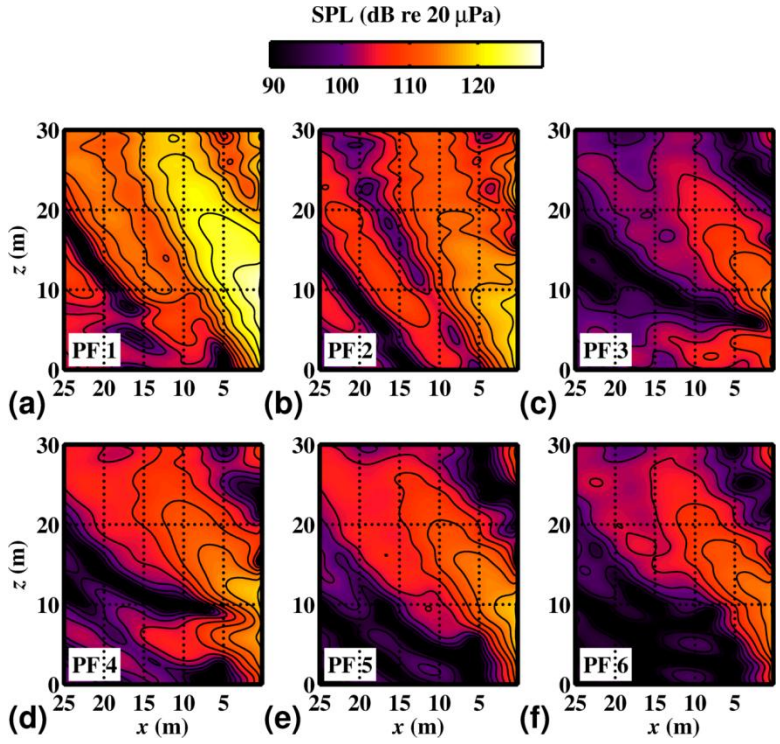

Figure A.5 First six PFs, (a-f) respectively, from the OLVR decomposition of the full-scale jet noise at military power and at 40 Hz. Black contour lines occur at 3 dB increments.

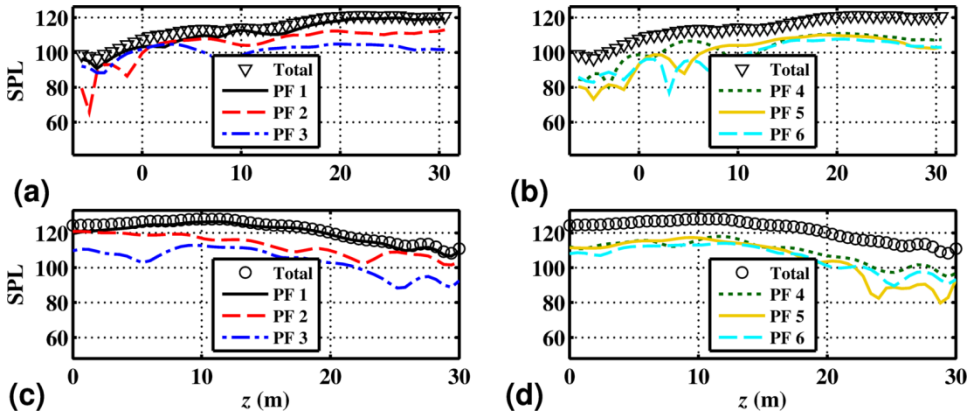

Figure A.6 OLVR decompositions of the field at 40 Hz, military engine conditions. (a) Along reference array location, PFs 1-3. (b) Along reference array location, PFs 4-6. (c) Along shear layer boundary, PFs 1-3. (d) Along shear layer boundary, PFs 4-6. SPLs are calculated relative to 20 µPa.

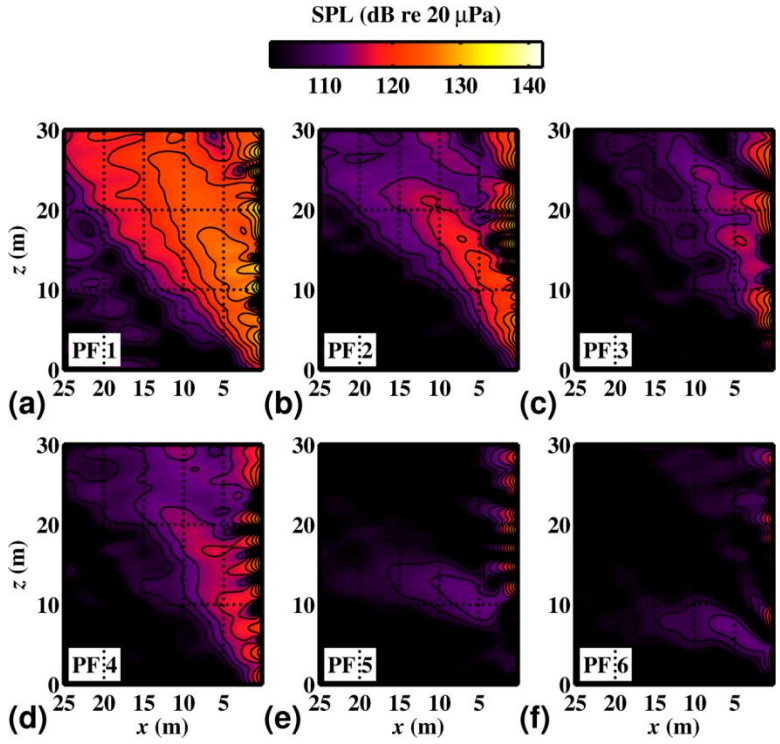

Figure A.7 First six PFs, (a-f) respectively, from the OLVR decomposition of the full-scale jet noise at military power and at 50 Hz. Black contour lines occur at 3 dB increments.

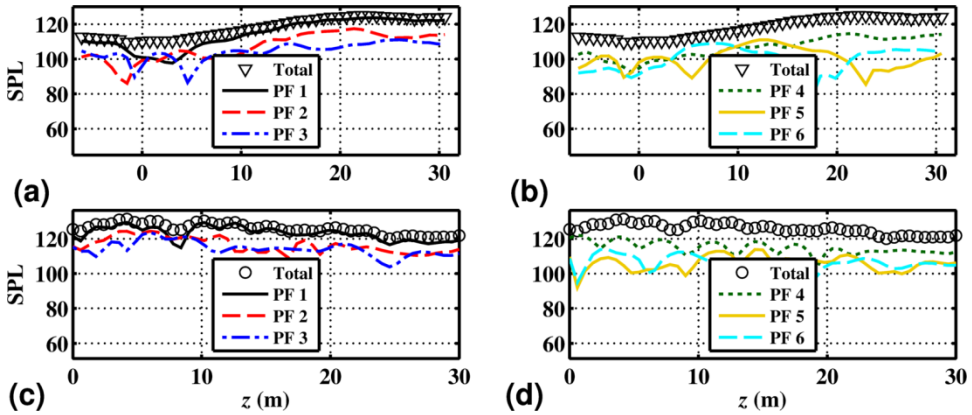

Figure A.8 OLVR decompositions of the field at 50 Hz, military engine conditions. (a) Along reference array location, PFs 1-3. (b) Along reference array location, PFs 4-6. (c) Along shear layer boundary, PFs 1-3. (d) Along shear layer boundary, PFs 4-6. SPLs are calculated relative to 20 µPa.

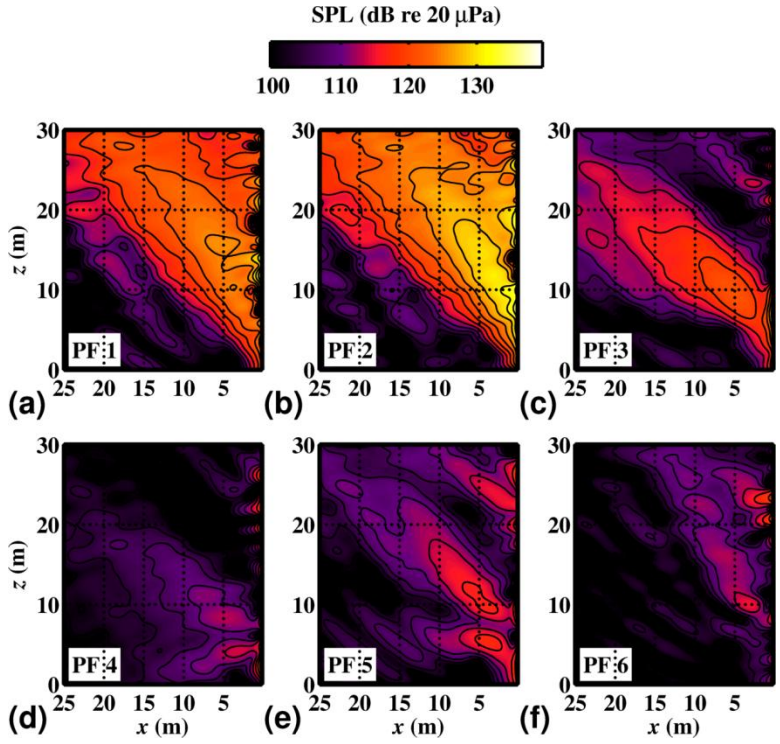

Figure A.9 First six PFs, (a-f) respectively, from the OLVR decomposition of the full-scale jet noise at military power and at 63 Hz. Black contour lines occur at 3 dB increments.

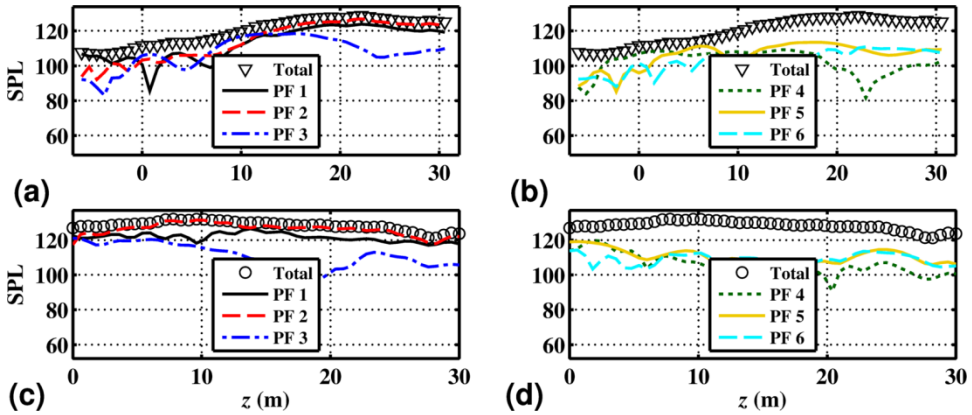

Figure A.10 OLVR decompositions of the field at 63 Hz, military engine conditions. (a) Along reference array location, PFs 1-3. (b) Along reference array location, PFs 4-6. (c) Along shear layer boundary, PFs 1-3. (d) Along shear layer boundary, PFs 4-6. SPLs are calculated relative to 20 µPa.

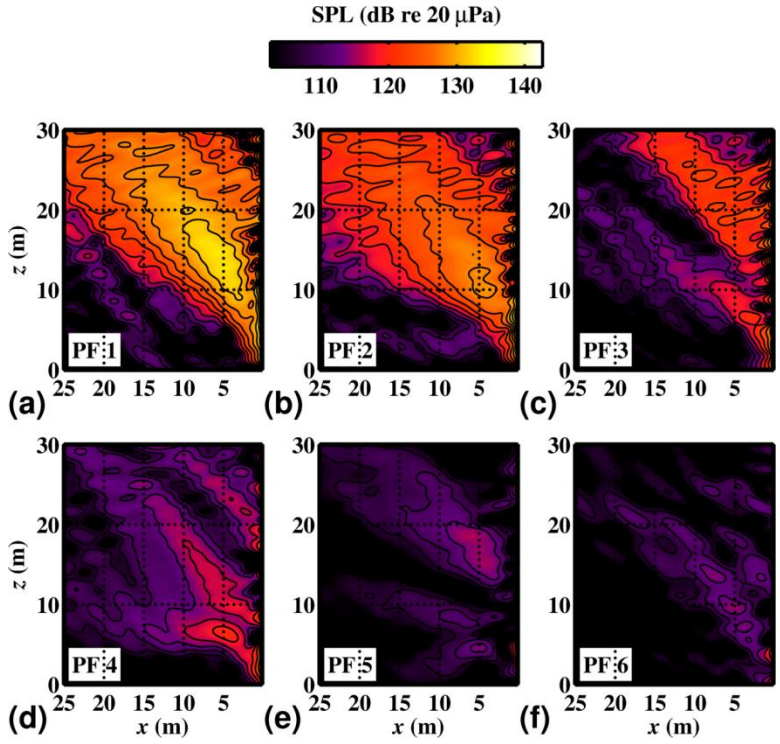

Figure A.11 First six PFs, (a-f) respectively, from the OLVR decomposition of the full-scale jet noise at military power and at 80 Hz. Black contour lines occur at 3 dB increments.

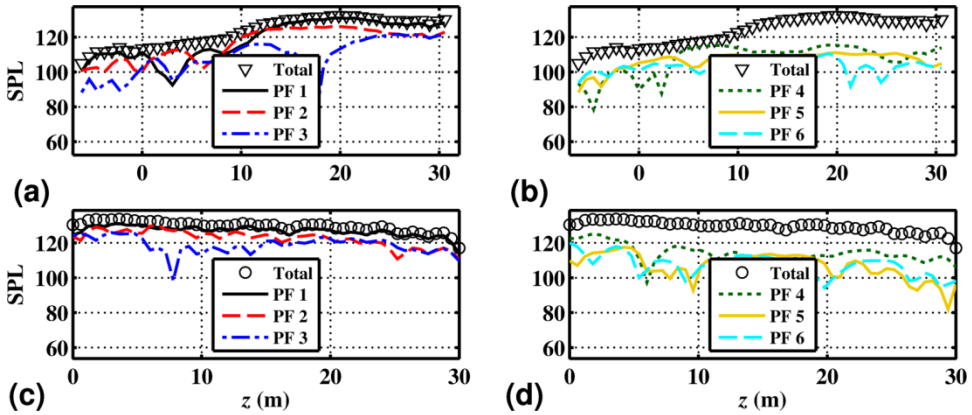

Figure A.12 OLVR decompositions of the field at 80 Hz, military engine conditions. (a) Along reference array location, PFs 1-3. (b) Along reference array location, PFs 4-6. (c) Along shear layer boundary, PFs 1-3. (d) Along shear layer boundary, PFs 4-6. SPLs are calculated relative to 20 µPa.

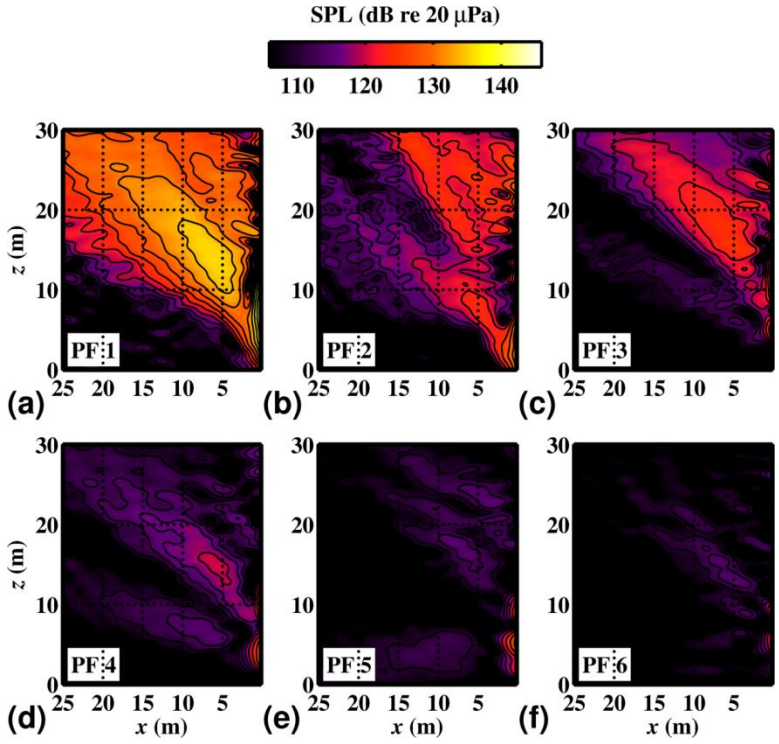

Figure A.13 First six PFs, (a-f) respectively, from the OLVR decomposition of the full-scale jet noise at military power and at 100 Hz. Black contour lines occur at 3 dB increments.

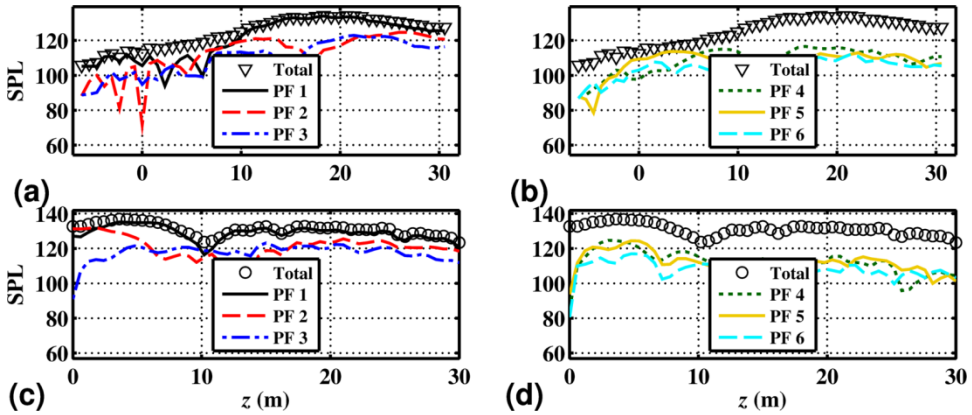

Figure A.14 OLVR decompositions of the field at 100 Hz, military engine conditions. (a) Along reference array location, PFs 1-3. (b) Along reference array location, PFs 4-6. (c) Along shear layer boundary, PFs 1-3. (d) Along shear layer boundary, PFs 4-6. SPLs are calculated relative to 20 μPa.

Between about 125 Hz and 315 Hz, the presence of the two independent processes, characterized by well-separated beam patterns, is apparent in the overall level maps of Figure 7.4. However, additional independent fields that are not visible in the total reconstruction at these frequencies are separated with OLVR (see Figure A.15 through Figure A.24). The PFs can be considered independent source mechanisms, even when their contributions do not result in multiple local maxima in the field.

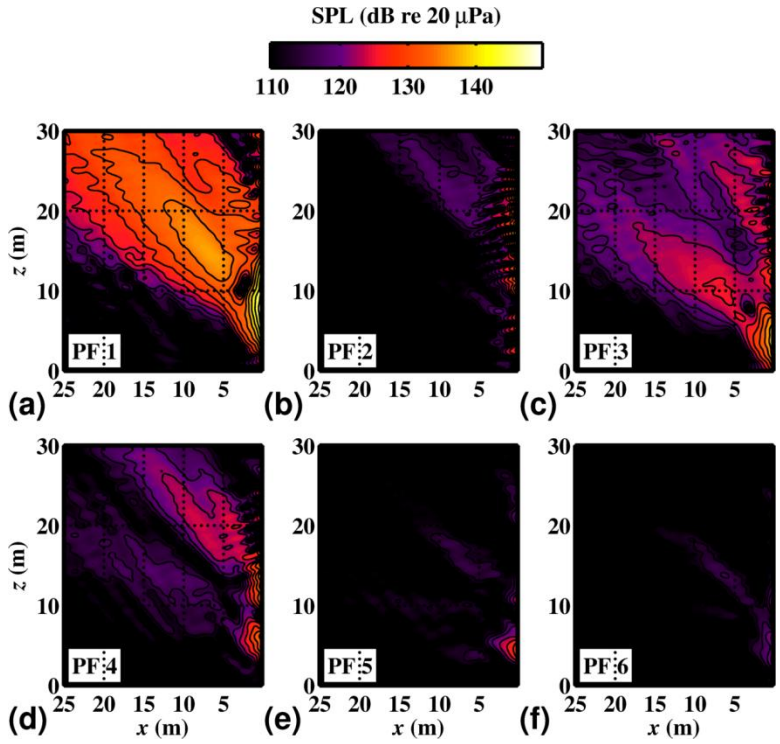

Figure A.15 First six PFs, (a-f) respectively, from the OLVR decomposition of the full-scale jet noise at military power and at 125 Hz. Black contour lines occur at 3 dB increments.

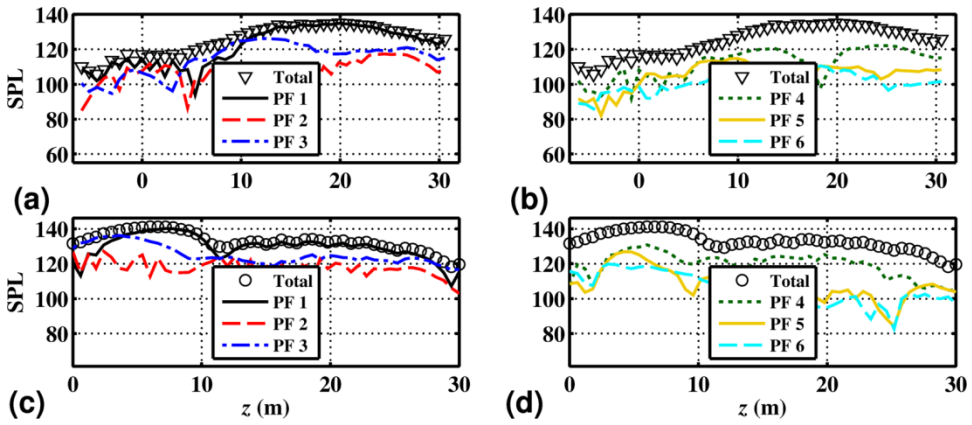

Figure A.16 OLVR decompositions of the field at 125 Hz, military engine conditions. (a) Along reference array location, PFs 1-3. (b) Along reference array location, PFs 4-6. (c) Along shear layer boundary, PFs 1-3. (d) Along shear layer boundary, PFs 4-6. SPLs are calculated relative to 20 µPa.

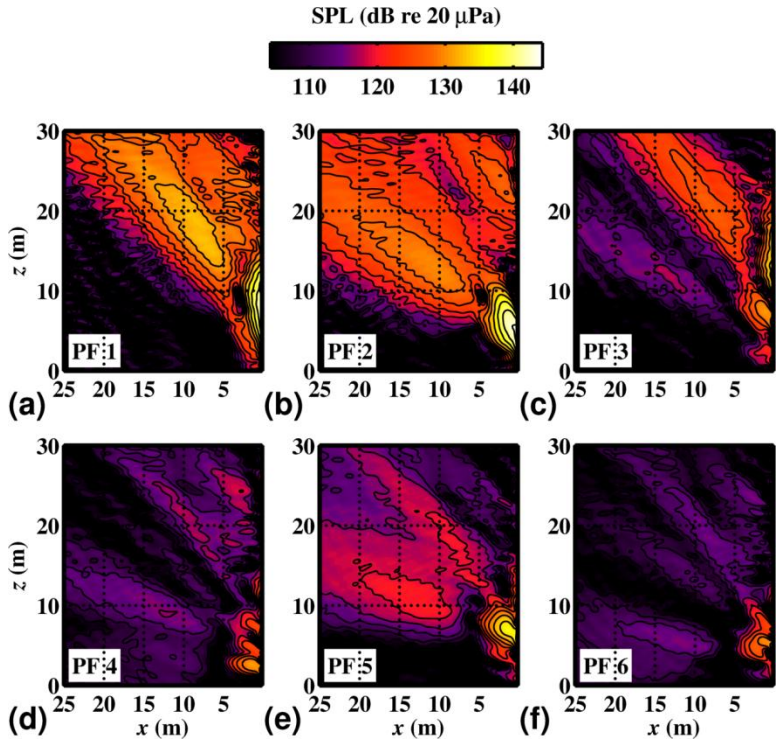

Figure A.17 First six PFs, (a-f) respectively, from the OLVR decomposition of the full-scale jet noise at military power and at 160 Hz. Black contour lines occur at 3 dB increments.

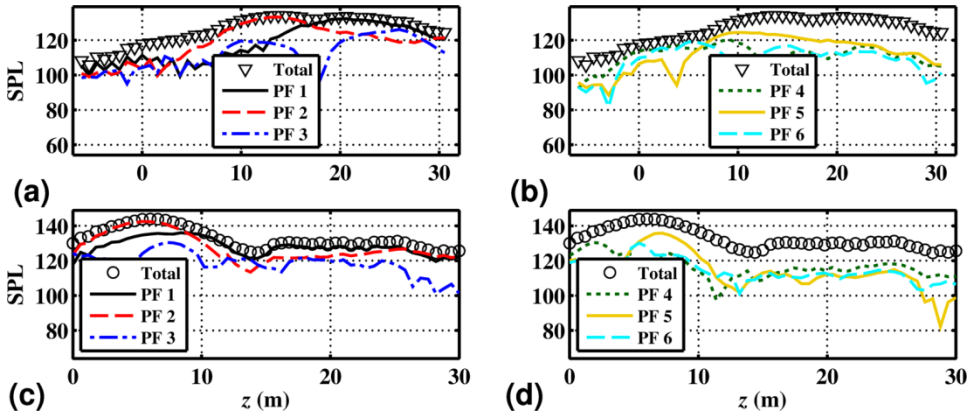

Figure A.18 OLVR decompositions of the field at 160 Hz, military engine conditions. (a) Along reference array location, PFs 1-3. (b) Along reference array location, PFs 4-6. (c) Along shear layer boundary, PFs 1-3. (d) Along shear layer boundary, PFs 4-6. SPLs are calculated relative to 20 µPa.

Between 200 and 500 Hz for military power (Figure A.19 through Figure A.28) the spatial ordering of the decomposed sources and the corresponding directionality of the individual PFs is more pronounced that at lower frequencies.

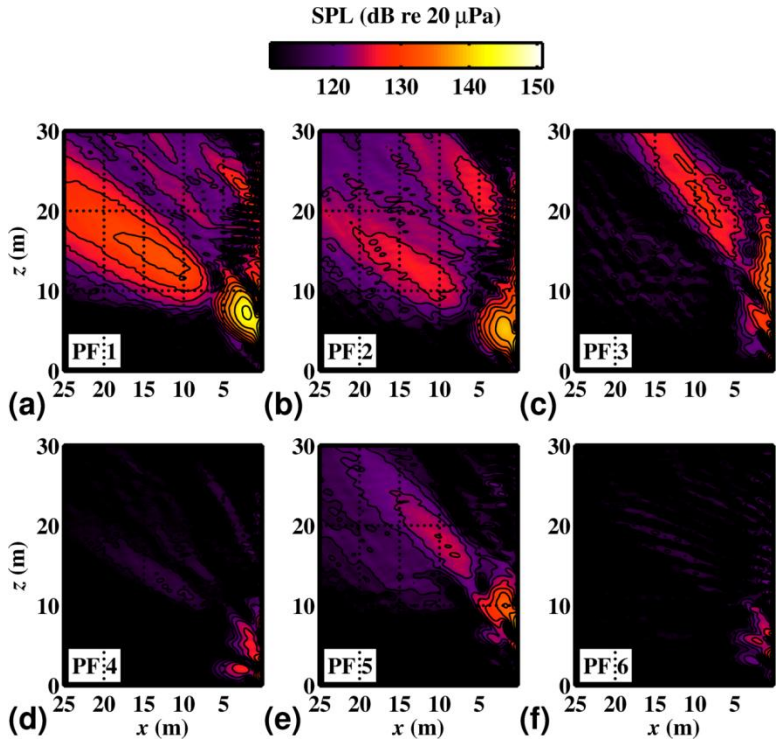

Figure A.19 First six PFs, (a-f) respectively, from the OLVR decomposition of the full-scale jet noise at military power and at 200 Hz. Black contour lines occur at 3 dB increments.

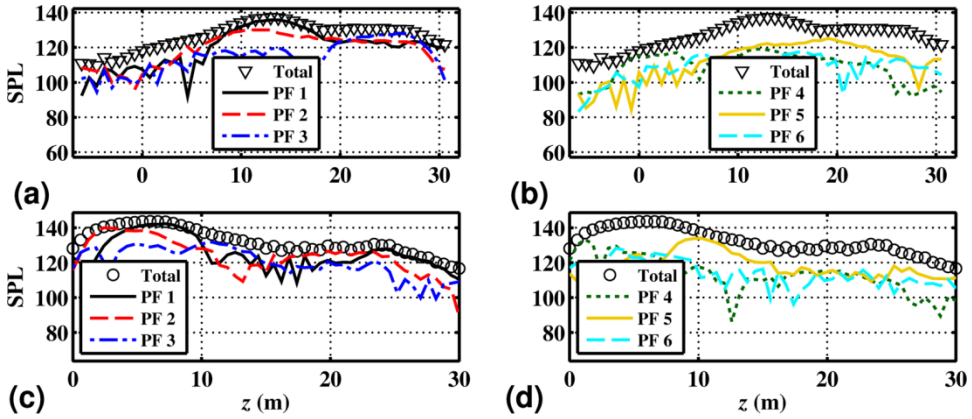

Figure A.20 OLVR decompositions of the field at 200 Hz, military engine conditions. (a) Along reference array location, PFs 1-3. (b) Along reference array location, PFs 4-6. (c) Along shear layer boundary, PFs 1-3. (d) Along shear layer boundary, PFs 4-6. SPLs are calculated relative to 20 μPa.

At 250 Hz, military power, in Figure A.22a-b, PFs 6, 2, 1, 3, 5, and 4, have respective maxima at the reference array locations $z = 1, 10, 14, 22,$ and 26 m. These local maxima produce localized "bumps," features that are less obvious than actual local maxima, in the total field curve.

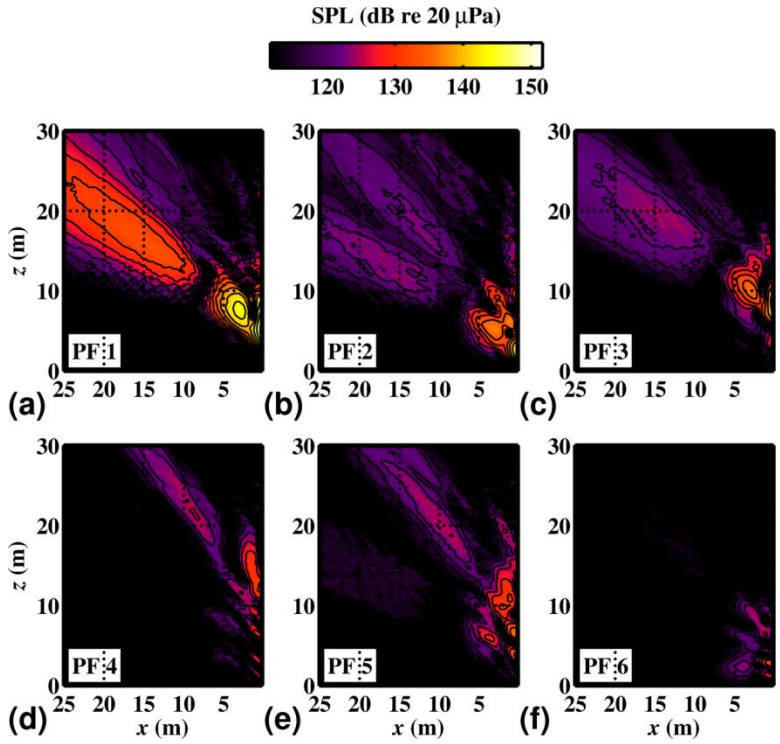

Figure A.21 First six PFs, (a-f) respectively, from the OLVR decomposition of the full-scale jet noise at military power and at 250 Hz. Black contour lines occur at 3 dB increments.

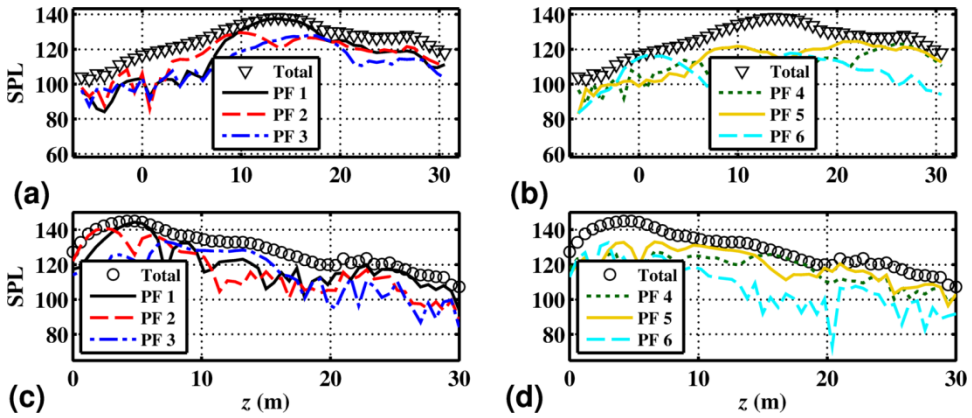

Figure A.22 OLVR decompositions of the field at 250 Hz, military engine conditions. (a) Along reference array location, PFs 1-3. (b) Along reference array location, PFs 4-6. (c) Along shear layer boundary, PFs 1-3. (d) Along shear layer boundary, PFs 4-6. SPLs are calculated relative to 20 µPa.

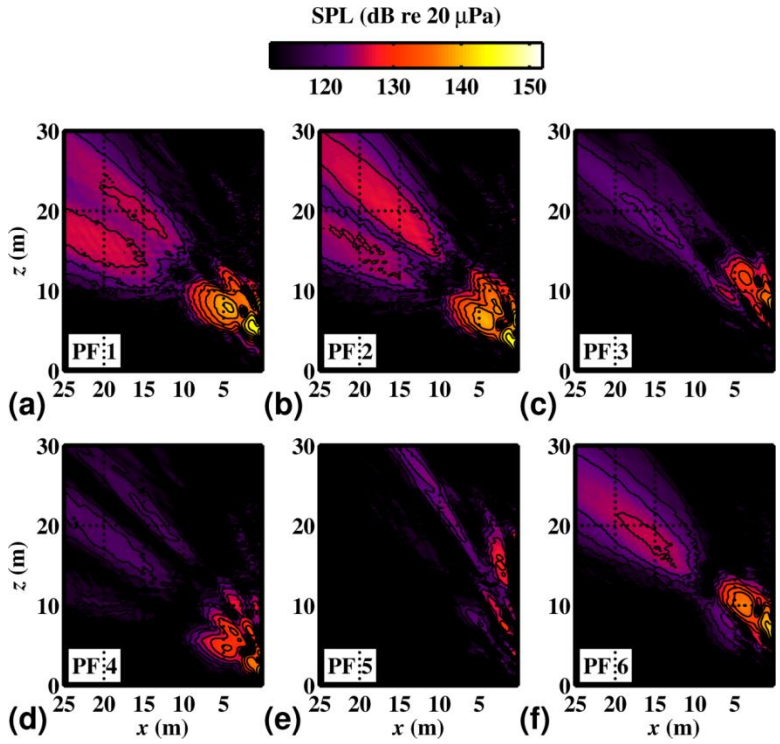

Figure A.23 First six PFs, (a-f) respectively, from the OLVR decomposition of the full-scale jet noise at military power and at 315 Hz. Black contour lines occur at 3 dB increments.

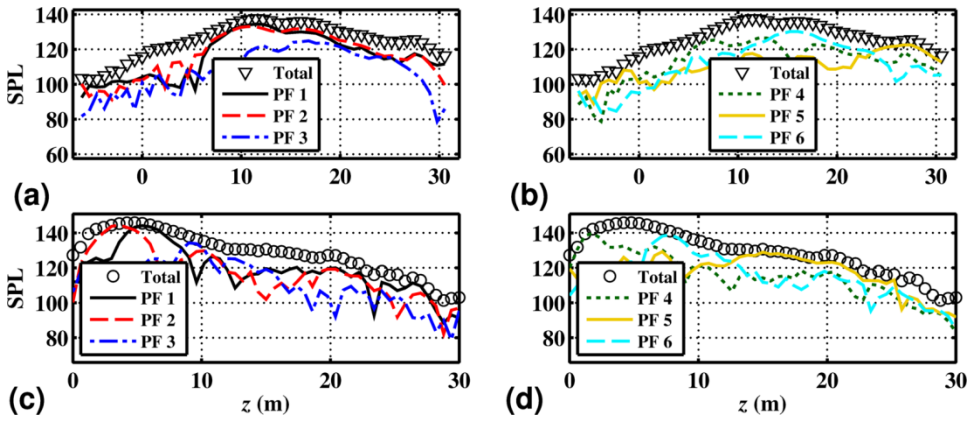

Figure A.24 OLVR decompositions of the field at 315 Hz, military engine conditions. (a) Along reference array location, PFs 1-3. (b) Along reference array location, PFs 4-6. (c) Along shear layer boundary, PFs 1-3. (d) Along shear layer boundary, PFs 4-6. SPLs are calculated relative to 20 µPa.

At 400 and 500 Hz, military power (Figure A.25 through Figure A.28), the spatial ordering of the partial fields at the source becomes the dominant effect, and the distinction between multiple source mechanisms in the total distribution is obscured.

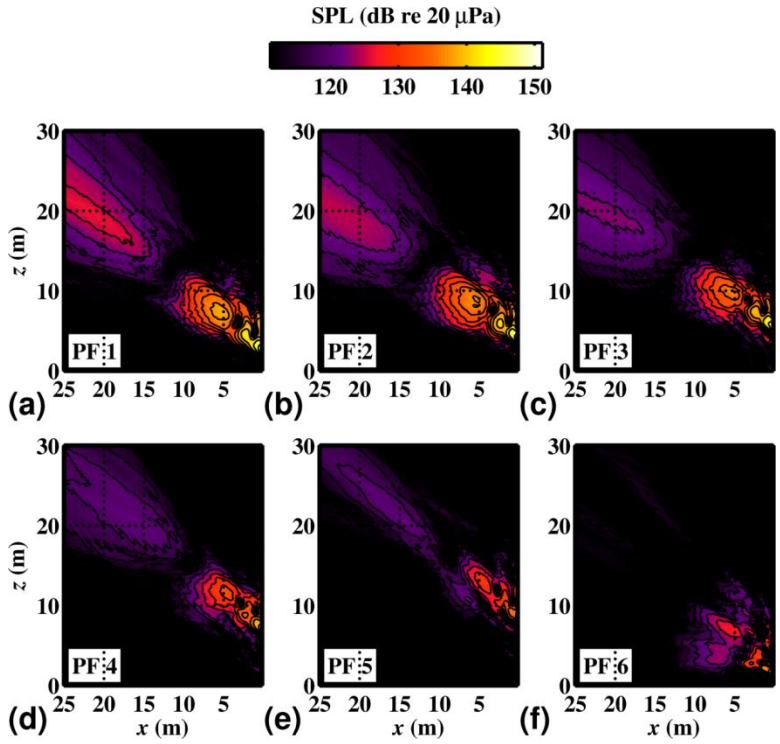

Figure A.25 First six PFs, (a-f) respectively, from the OLVR decomposition of the full-scale jet noise at military power and at 400 Hz. Black contour lines occur at 3 dB increments.

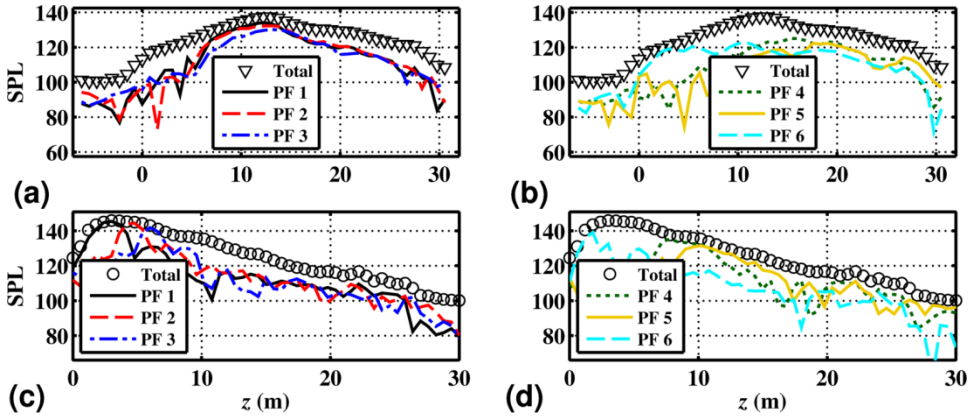

Figure A.26 OLVR decompositions of the field at 400 Hz, military engine conditions. (a) Along reference array location, PFs 1-3. (b) Along reference array location, PFs 4-6. (c) Along shear layer boundary, PFs 1-3. (d) Along shear layer boundary, PFs 4-6. SPLs are calculated relative to 20 µPa.

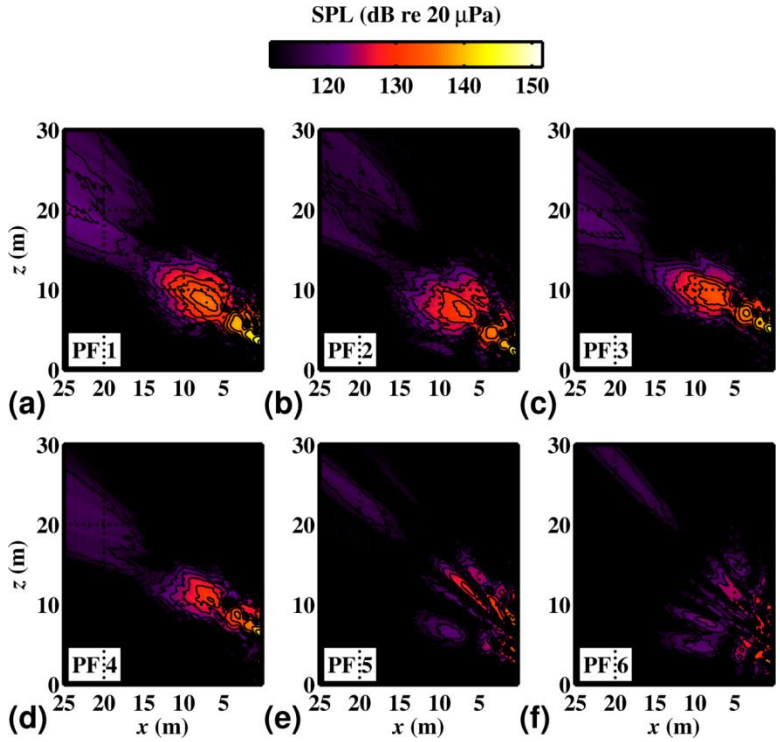

Figure A.27 First six PFs, (a-f) respectively, from the OLVR decomposition of the full-scale jet noise at military power and at 500 Hz. Black contour lines occur at 3 dB increments.

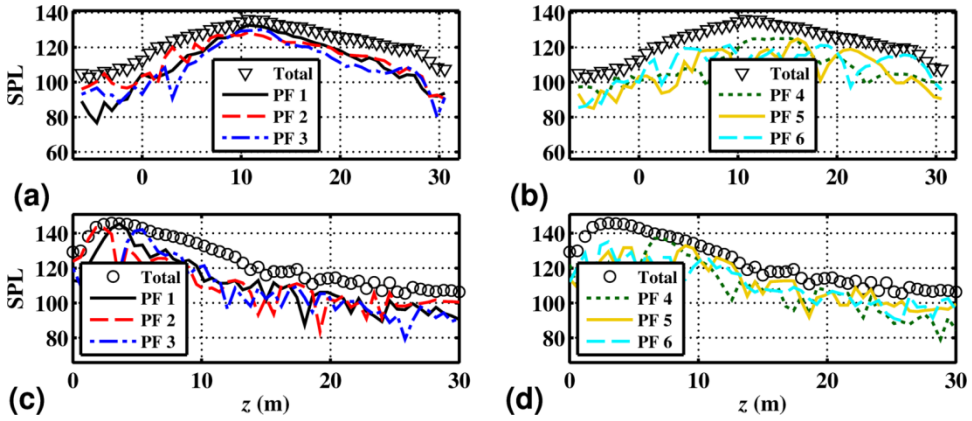

Figure A.28 OLVR decompositions of the field at 500 Hz, military engine conditions. (a) Along reference array location, PFs 1-3. (b) Along reference array location, PFs 4-6. (c) Along shear layer boundary, PFs 1-3. (d) Along shear layer boundary, PFs 4-6. SPLs are calculated relative to 20 µPa.

Results are now shown for afterburner conditions in Figure A.29 through Figure A.54. Similar phenomena are seen here as are found in the OLVR PFs for military power.

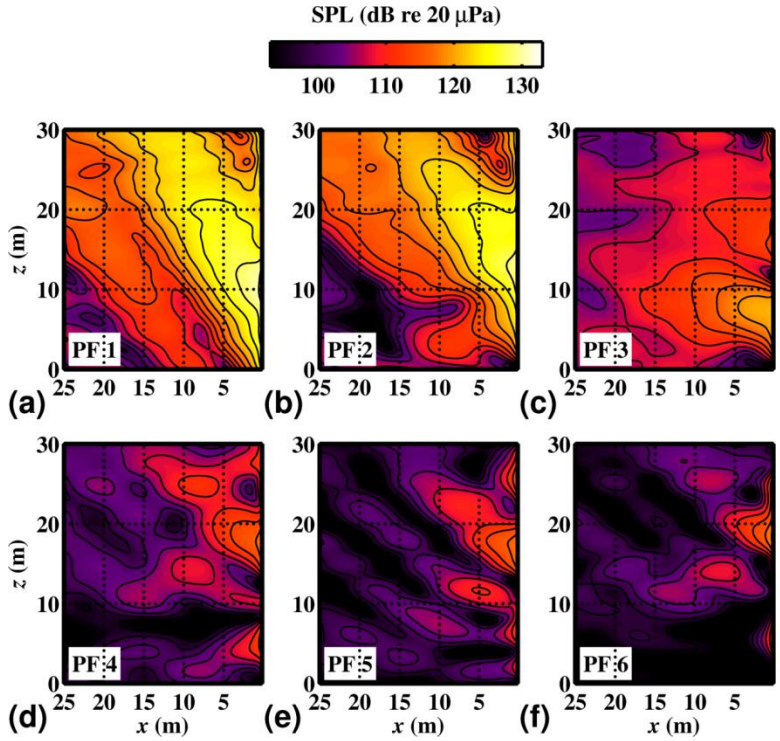

Figure A.29 First six PFs, (a-f) respectively, from the OLVR decomposition of the full-scale jet noise at afterburner power and at 32 Hz. Black contour lines occur at 3 dB increments.

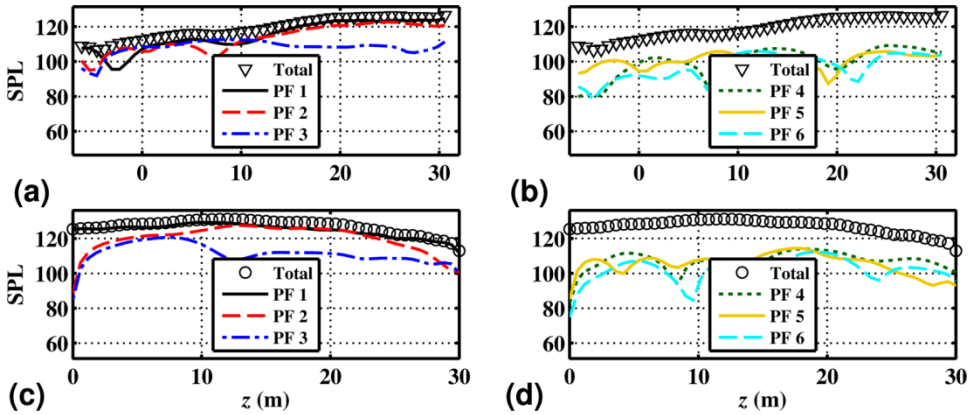

Figure A.30 OLVR decompositions of the field at 32 Hz, afterburner engine conditions. (a) Along reference array location, PFs 1-3. (b) Along reference array location, PFs 4-6. (c) Along shear layer boundary, PFs 1-3. (d) Along shear layer boundary, PFs 4-6. SPLs are calculated relative to 20 μPa.

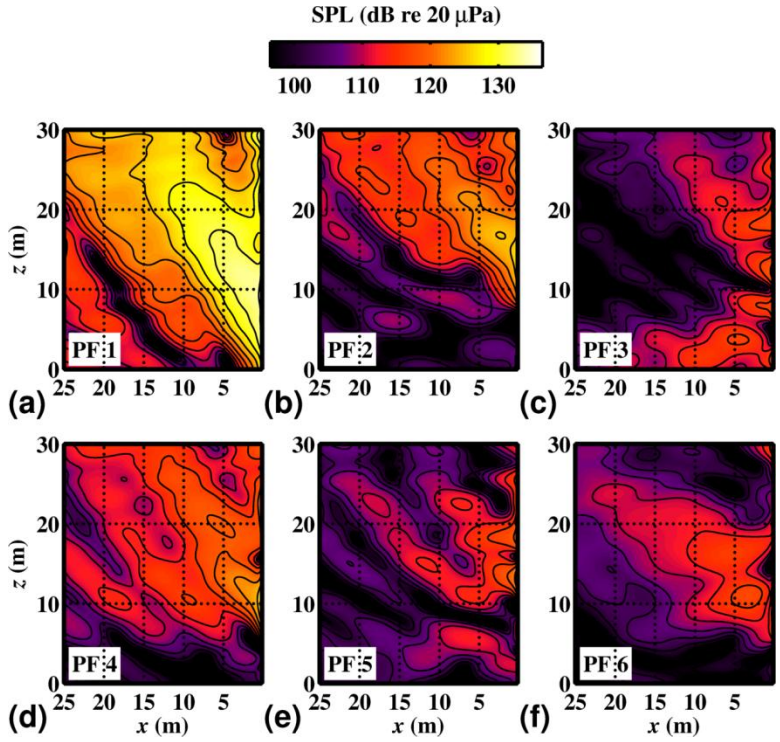

Figure A.31 First six PFs, (a-f) respectively, from the OLVR decomposition of the full-scale jet noise at afterburner power and at 40 Hz. Black contour lines occur at 3 dB increments.

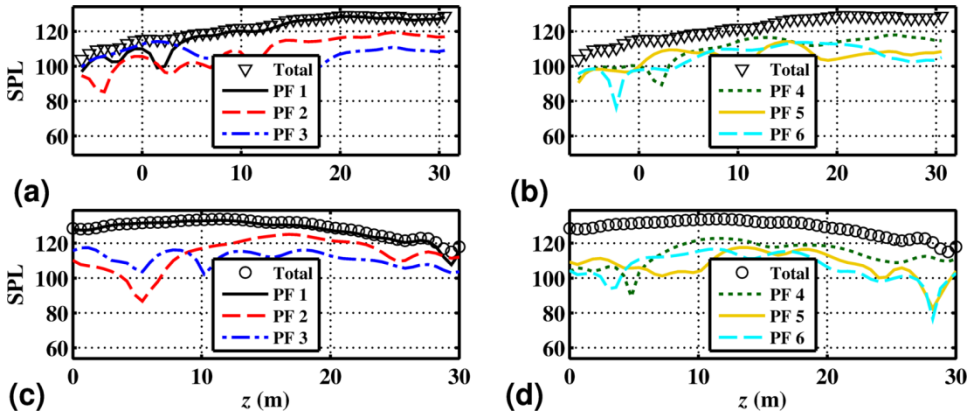

Figure A.32 OLVR decompositions of the field at 40 Hz, afterburner engine conditions. (a) Along reference array location, PFs 1-3. (b) Along reference array location, PFs 4-6. (c) Along shear layer boundary, PFs 1-3. (d) Along shear layer boundary, PFs 4-6. SPLs are calculated relative to 20 μPa.

Recall from Section 5.5.3 that low-frequency levels are slightly under-predicted in the extreme downstream region. There is some indication that important source information exists far downstream at low frequencies, below about 100 Hz, particularly at afterburner conditions, that is not entirely captured by the hologram measurement aperture. Figure A.34a shows that the total field along the reference array for 50 Hz, afterburner power, is dominated in most locations by PF 2. However, past $z = 24$ m PF 1 begins to overtake PF 2. The fact that the SPL of PF 1 near $z = 30$ is only about 3 or 4 dB less than the maximum SPL for PF 1 suggests that important information radiated by its corresponding source is likely found beyond the measurement aperture.

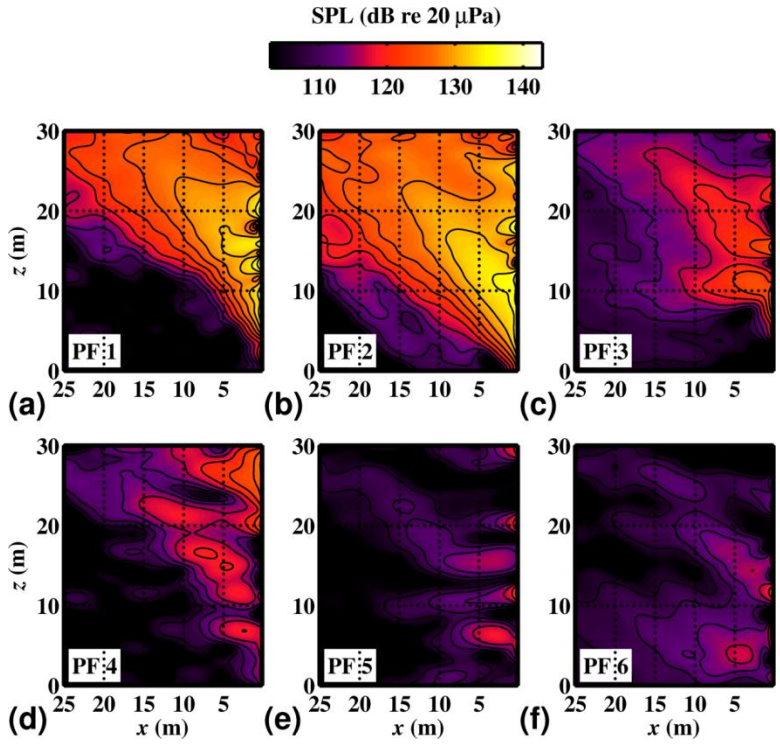

Figure A.33 First six PFs, (a-f) respectively, from the OLVR decomposition of the full-scale jet noise at afterburner power and at 50 Hz. Black contour lines occur at 3 dB increments.

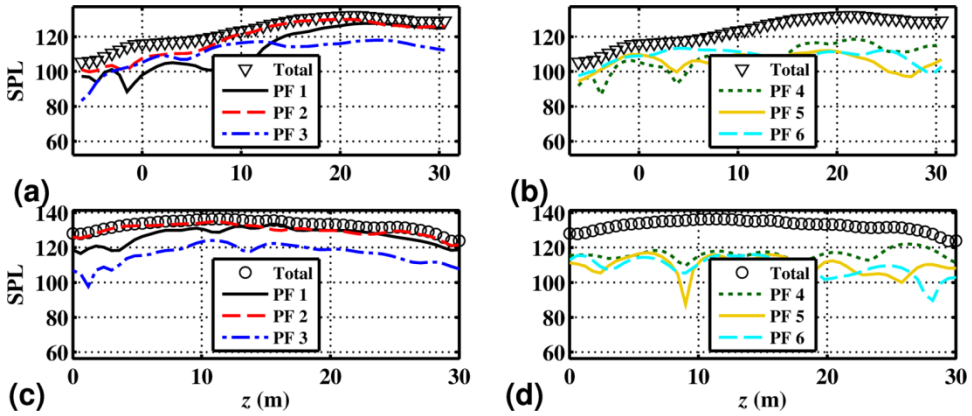

Figure A.34 OLVR decompositions of the field at 50 Hz, afterburner engine conditions. (a) Along reference array location, PFs 1-3. (b) Along reference array location, PFs 4-6. (c) Along shear layer boundary, PFs 1-3. (d) Along shear layer boundary, PFs 4-6. SPLs are calculated relative to 20 µPa.

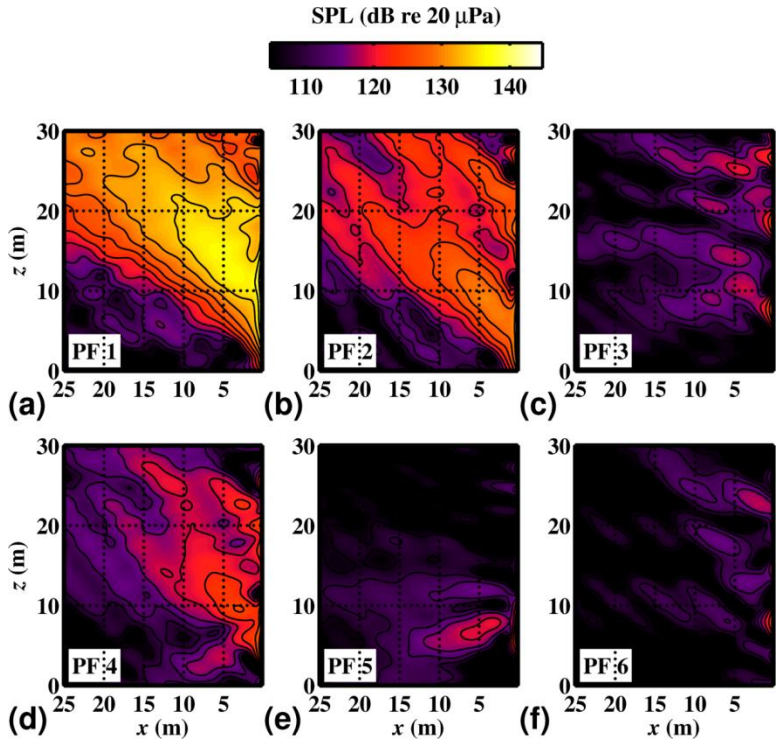

Figure A.35 First six PFs, (a-f) respectively, from the OLVR decomposition of the full-scale jet noise at afterburner power and at 63 Hz. Black contour lines occur at 3 dB increments.

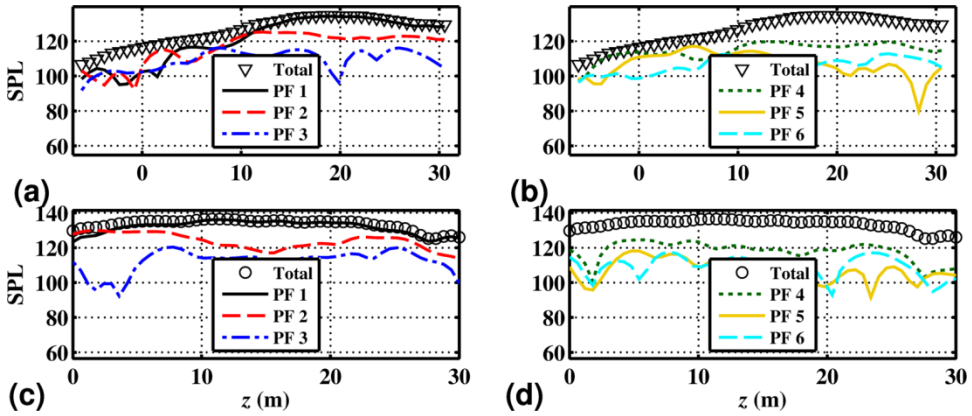

Figure A.36 OLVR decompositions of the field at 63 Hz, afterburner engine conditions. (a) Along reference array location, PFs 1-3. (b) Along reference array location, PFs 4-6. (c) Along shear layer boundary, PFs 1-3. (d) Along shear layer boundary, PFs 4-6. SPLs are calculated relative to 20 µPa.

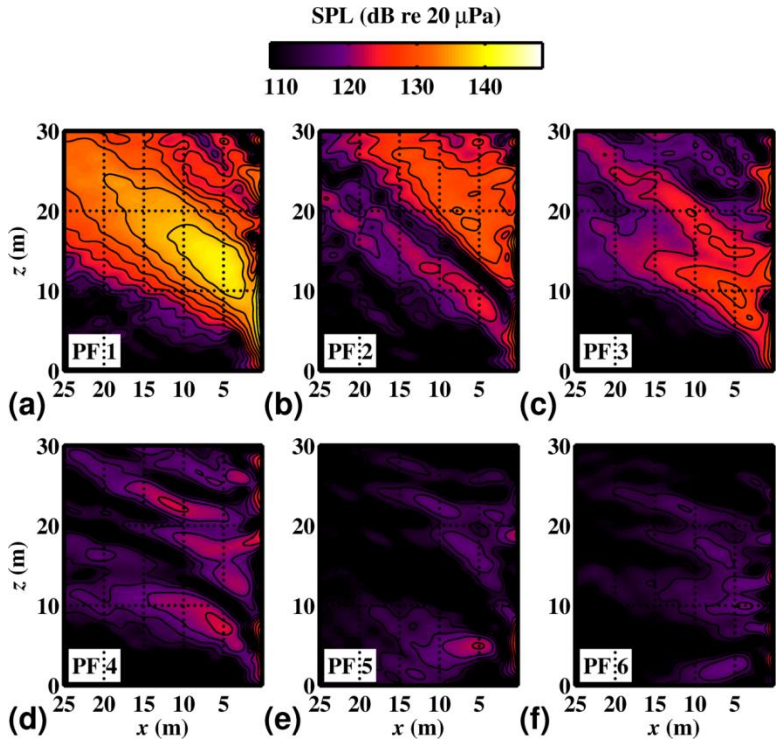

Figure A.37 First six PFs, (a-f) respectively, from the OLVR decomposition of the full-scale jet noise at afterburner power and at 80 Hz. Black contour lines occur at 3 dB increments.

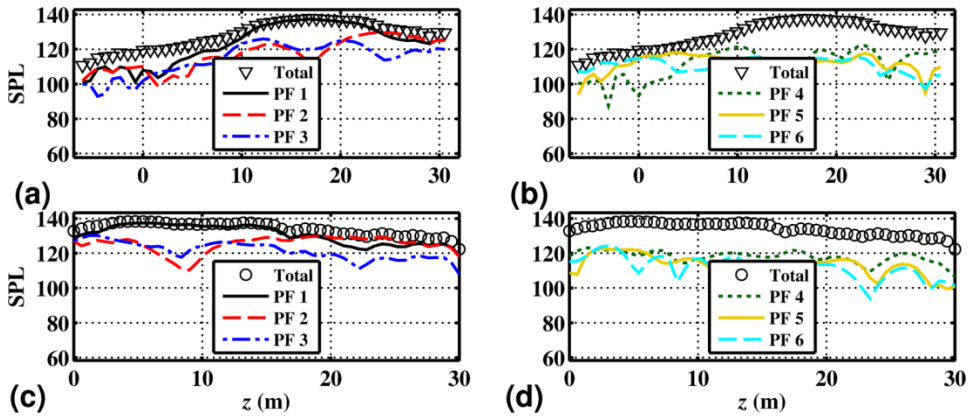

Figure A.38 OLVR decompositions of the field at 80 Hz, afterburner engine conditions. (a) Along reference array location, PFs 1-3. (b) Along reference array location, PFs 4-6. (c) Along shear layer boundary, PFs 1-3. (d) Along shear layer boundary, PFs 4-6. SPLs are calculated relative to 20 µPa.

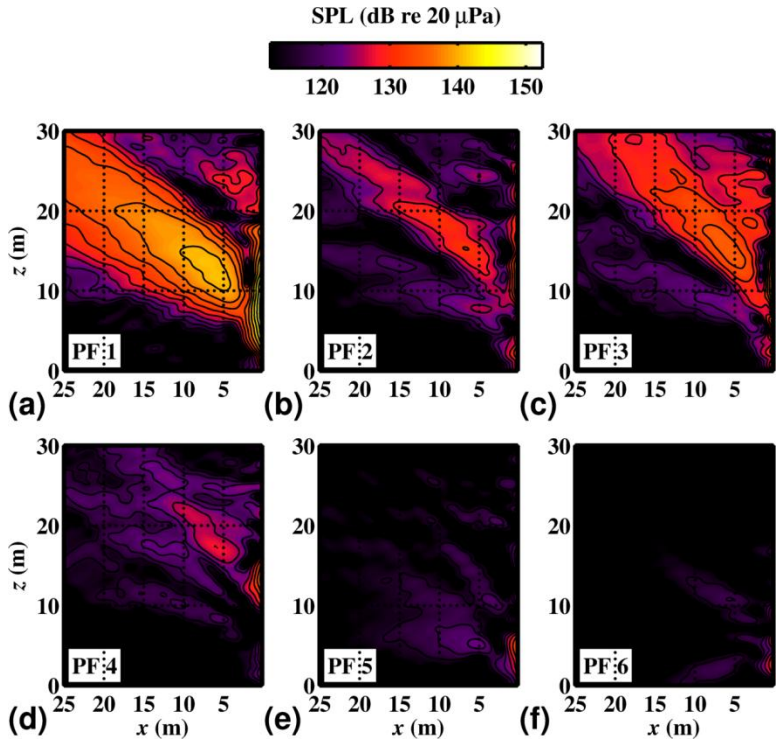

Figure A.39 First six PFs, (a-f) respectively, from the OLVR decomposition of the full-scale jet noise at afterburner power and at 100 Hz. Black contour lines occur at 3 dB increments.

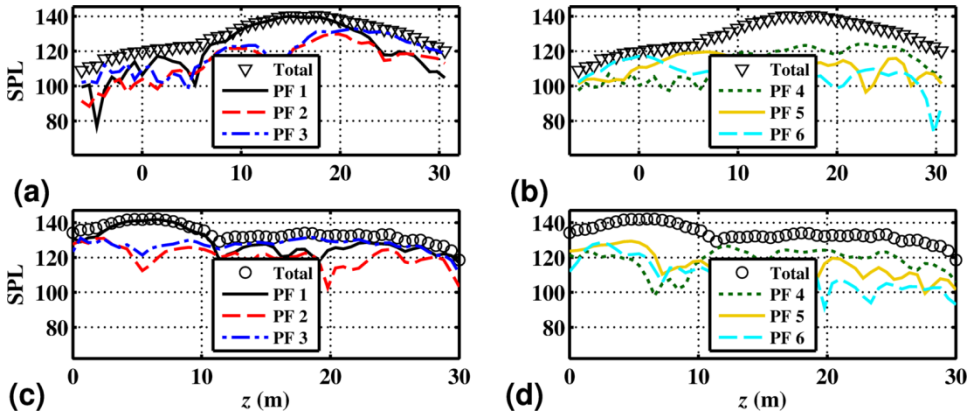

Figure A.40 OLVR decompositions of the field at 100 Hz, afterburner engine conditions. (a) Along reference array location, PFs 1-3. (b) Along reference array location, PFs 4-6. (c) Along shear layer boundary, PFs 1-3. (d) Along shear layer boundary, PFs 4-6. SPLs are calculated relative to 20 µPa.

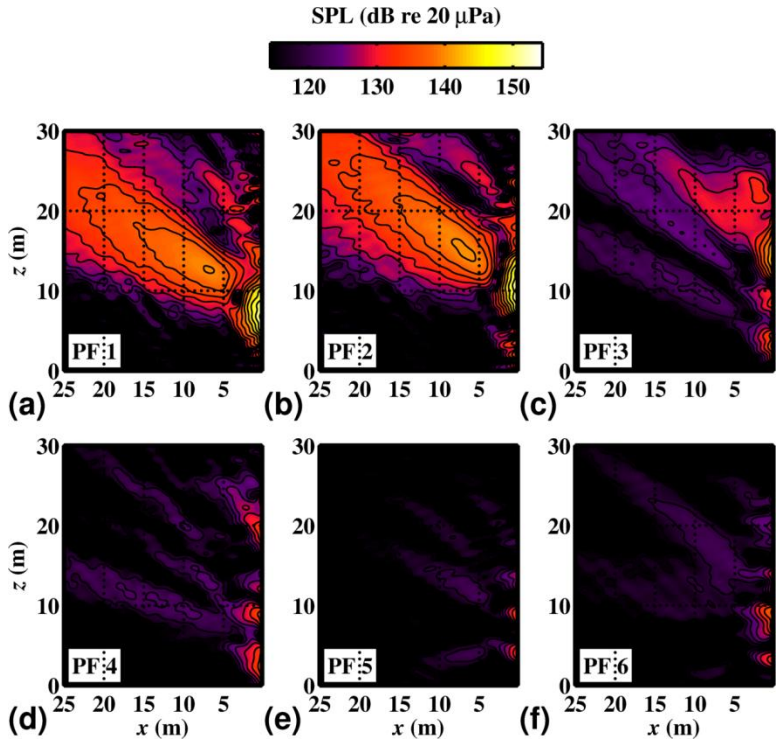

Figure A.41 First six PFs, (a-f) respectively, from the OLVR decomposition of the full-scale jet noise at afterburner power and at 125 Hz. Black contour lines occur at 3 dB increments.

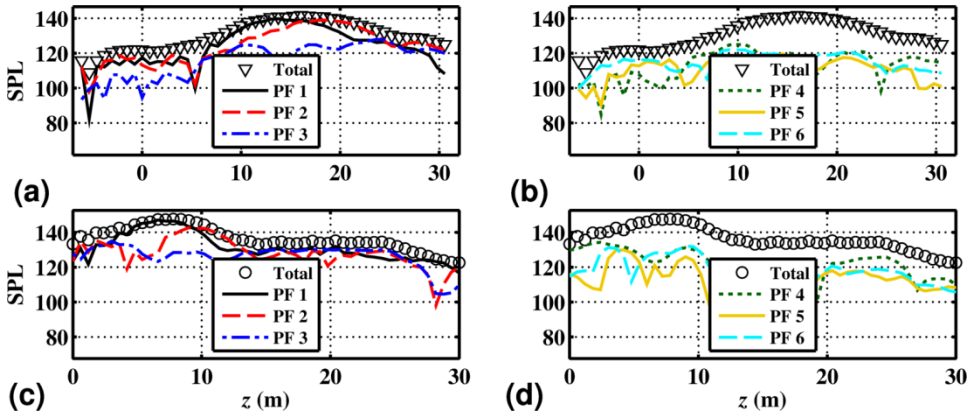

Figure A.42 OLVR decompositions of the field at 125 Hz, afterburner engine conditions. (a) Along reference array location, PFs 1-3. (b) Along reference array location, PFs 4-6. (c) Along shear layer boundary, PFs 1-3. (d) Along shear layer boundary, PFs 4-6. SPLs are calculated relative to 20 µPa.

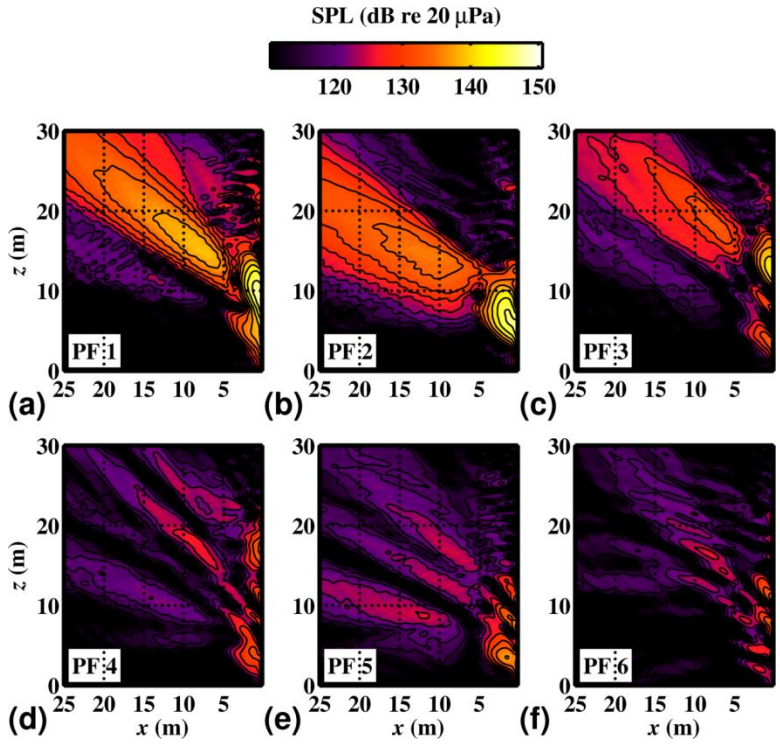

Figure A.43 First six PFs, (a-f) respectively, from the OLVR decomposition of the full-scale jet noise at afterburner power and at 160 Hz. Black contour lines occur at 3 dB increments.

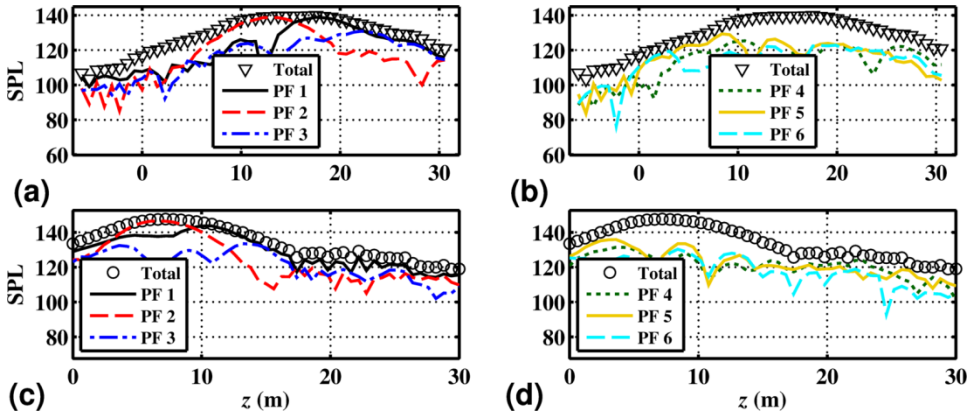

Figure A.44 OLVR decompositions of the field at 160 Hz, afterburner engine conditions. (a) Along reference array location, PFs 1-3. (b) Along reference array location, PFs 4-6. (c) Along shear layer boundary, PFs 1-3. (d) Along shear layer boundary, PFs 4-6. SPLs are calculated relative to 20 µPa.

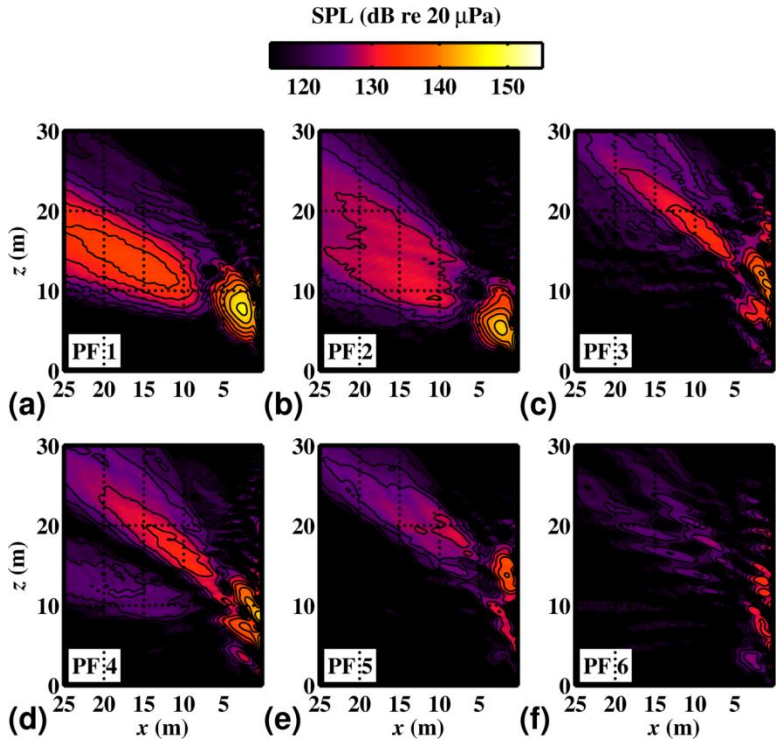

Figure A.45 First six PFs, (a-f) respectively, from the OLVR decomposition of the full-scale jet noise at afterburner power and at 200 Hz. Black contour lines occur at 3 dB increments.

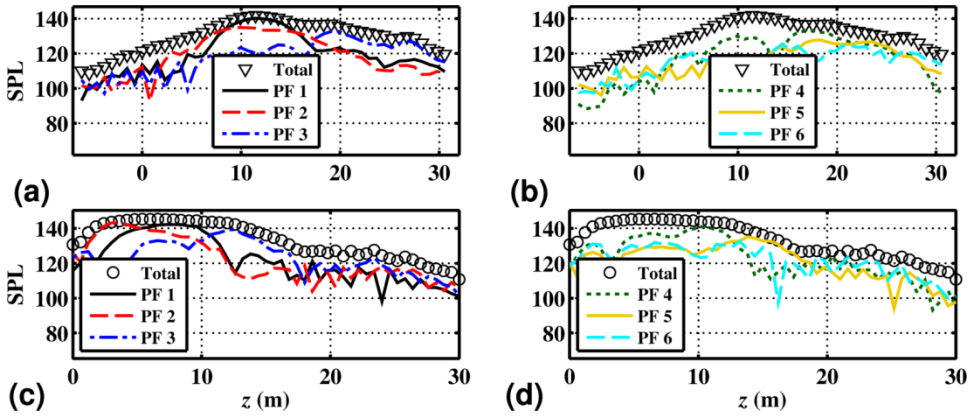

Figure A.46 OLVR decompositions of the field at 200 Hz, afterburner engine conditions. (a) Along reference array location, PFs 1-3. (b) Along reference array location, PFs 4-6. (c) Along shear layer boundary, PFs 1-3. (d) Along shear layer boundary, PFs 4-6. SPLs are calculated relative to 20 µPa.

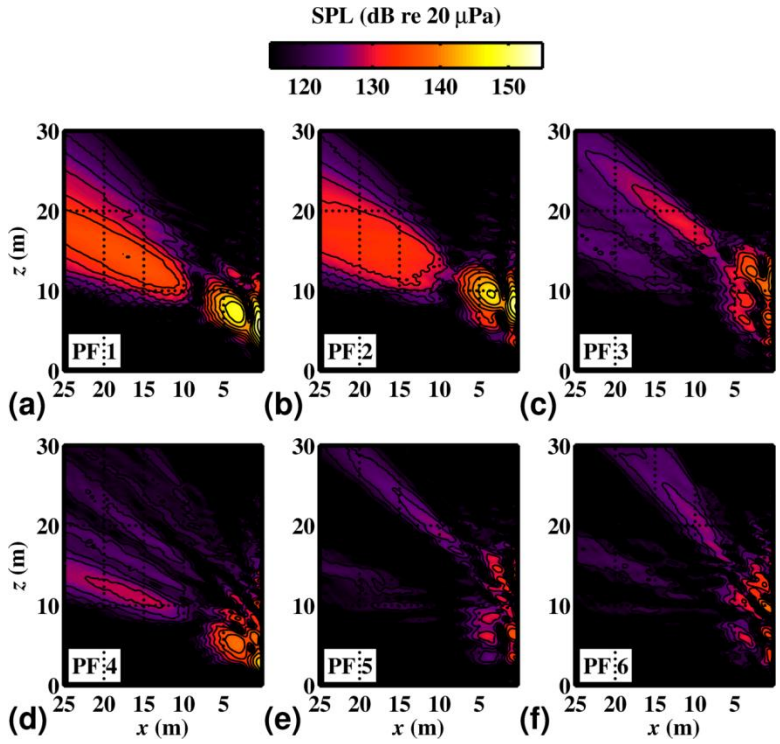

Figure A.47 First six PFs, (a-f) respectively, from the OLVR decomposition of the full-scale jet noise at afterburner power and at 250 Hz. Black contour lines occur at 3 dB increments.

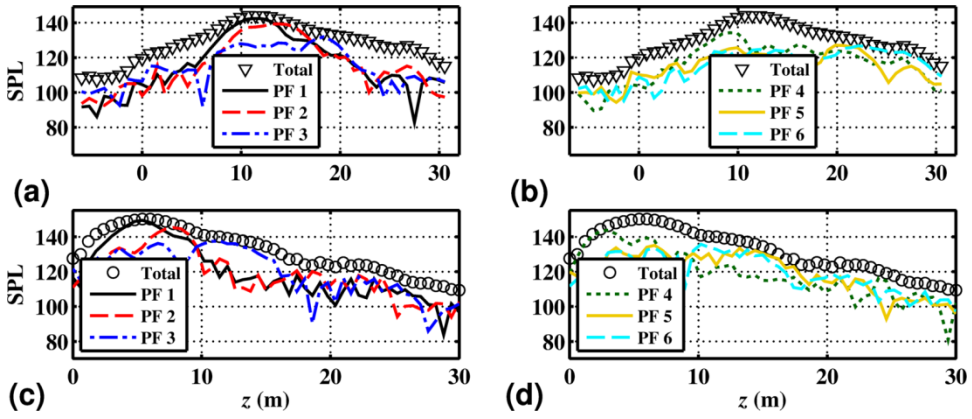

Figure A.48 OLVR decompositions of the field at 250 Hz, afterburner engine conditions. (a) Along reference array location, PFs 1-3. (b) Along reference array location, PFs 4-6. (c) Along shear layer boundary, PFs 1-3. (d) Along shear layer boundary, PFs 4-6. SPLs are calculated relative to 20 µPa.

The equivalent source model of Hart *et al.*[44] for the current data set could not capture the relatively broad maximum region in the far field at 315 Hz (at afterburner, which exhibits a

similar decomposition as the military power results shown here). This model consisted of a single coherent and an additional incoherent distribution of monopoles. Note that PFs 1 and 2 from the OLVR decomposition of the source shown at 315 Hz in Figure A.49c have maximum levels within about 1 dB, and both contribute to the broad source maximum. (In fact, at afterburner power, at 200 Hz and above, the overall shear-layer distributions in the maximum region are flatter than those for military power, with nearly equal contributions from two or three partial fields.) In addition, note that their contributions to the field at the reference array in Figure A.49a are also comparable in shape and level. This suggests that multiple, mutually incoherent source distributions with varying maximum location and directivity angle can account for broader level distributions.

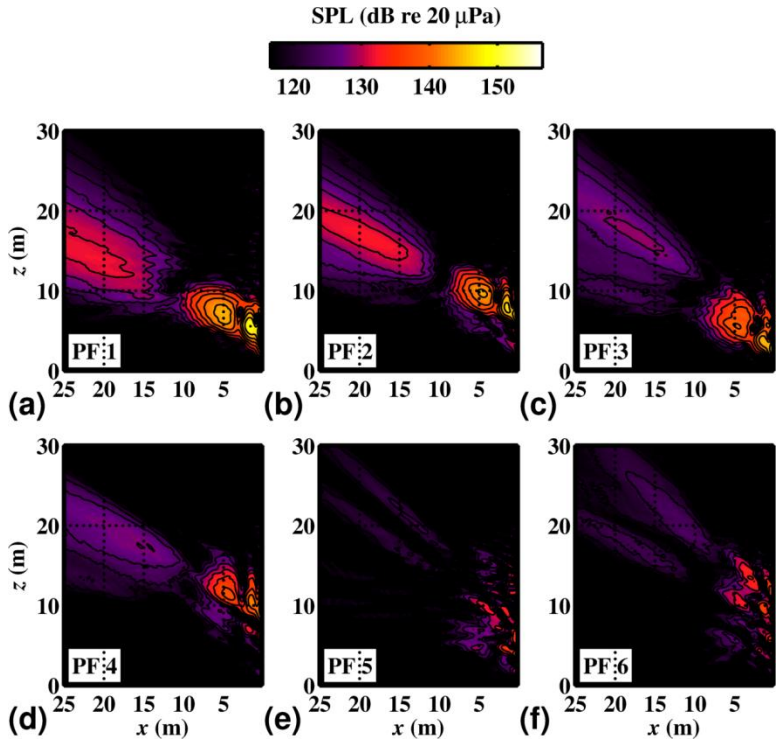

Figure A.49 First six PFs, (a-f) respectively, from the OLVR decomposition of the full-scale jet noise at afterburner power and at 315 Hz. Black contour lines occur at 3 dB increments.

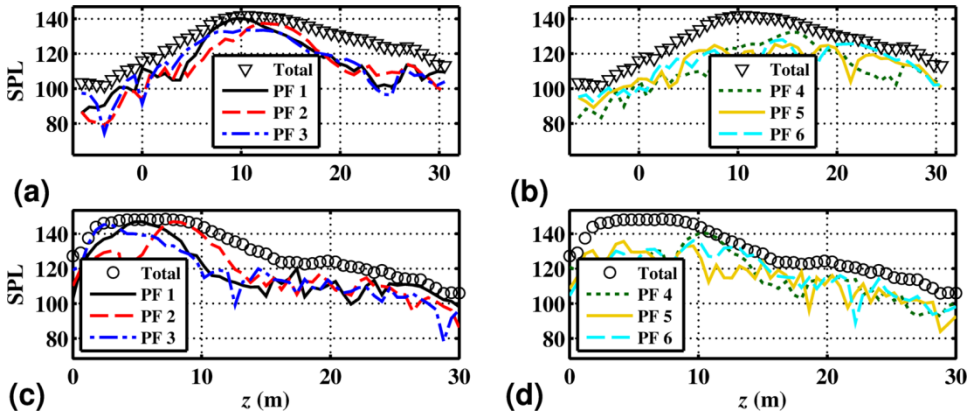

Figure A.50 OLVR decompositions of the field at 315 Hz, afterburner engine conditions. (a) Along reference array location, PFs 1-3. (b) Along reference array location, PFs 4-6. (c) Along shear layer boundary, PFs 1-3. (d) Along shear layer boundary, PFs 4-6. SPLs are calculated relative to 20 µPa.

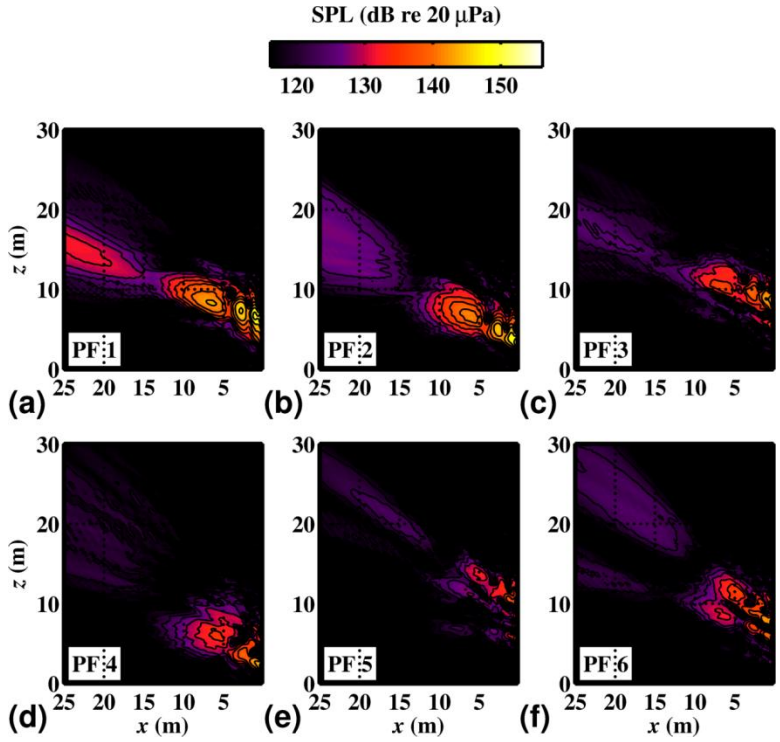

Figure A.51 First six PFs, (a-f) respectively, from the OLVR decomposition of the full-scale jet noise at afterburner power and at 400 Hz. Black contour lines occur at 3 dB increments.

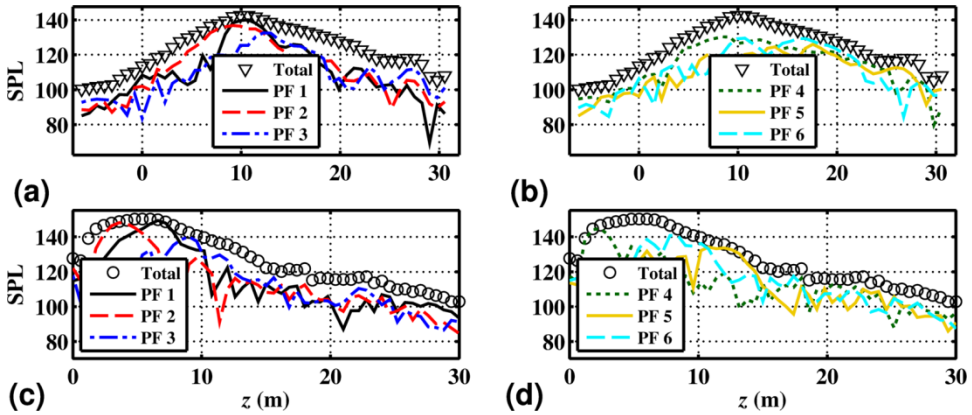

Figure A.52 OLVR decompositions of the field at 400 Hz, afterburner engine conditions. (a) Along reference array location, PFs 1-3. (b) Along reference array location, PFs 4-6. (c) Along shear layer boundary, PFs 1-3. (d) Along shear layer boundary, PFs 4-6. SPLs are calculated relative to 20 µPa.

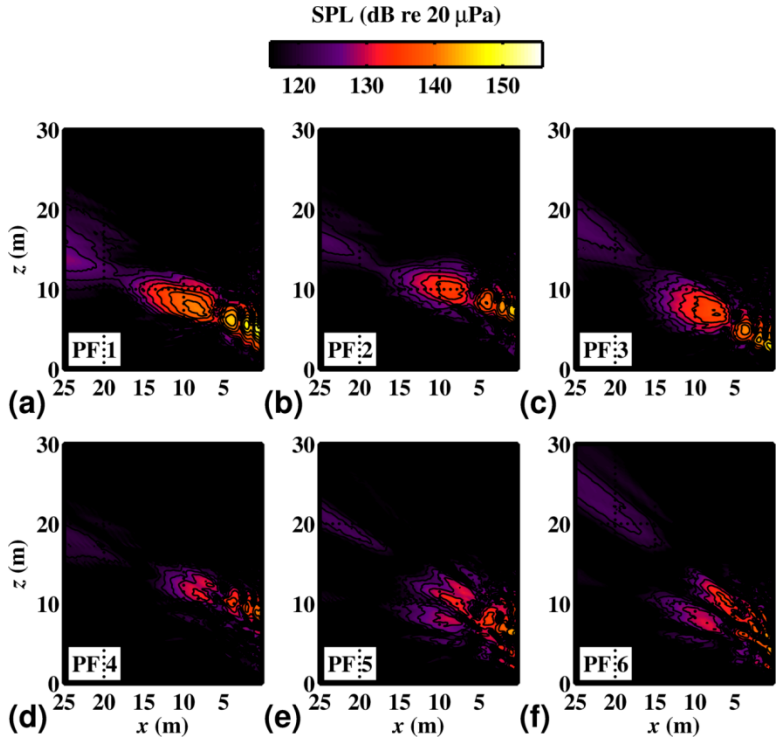

Figure A.53 First six PFs, (a-f) respectively, from the OLVR decomposition of the full-scale jet noise at afterburner power and at 500 Hz. Black contour lines occur at 3 dB increments.

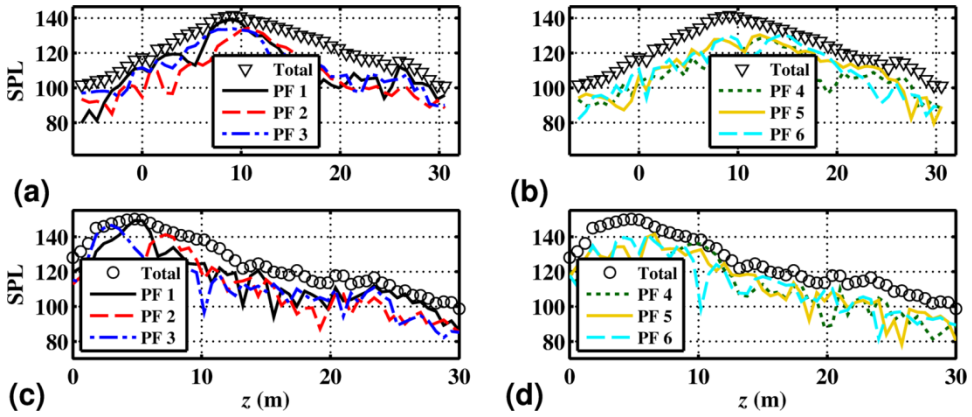

Figure A.54 OLVR decompositions of the field at 500 Hz, afterburner engine conditions. (a) Along reference array location, PFs 1-3. (b) Along reference array location, PFs 4-6. (c) Along shear layer boundary, PFs 1-3. (d) Along shear layer boundary, PFs 4-6. SPLs are calculated relative to 20 µPa.

B Pertinent Parameters for Jet-noise Processing

Parameters that were used in the processing methods of partial field decomposition, aperture extension, MSTR SONAH and OLVR for the full-scale data are provided here as a reference for future calculations. These parameters apply to results shown in Chapter 5, Chapter 6, and Chapter 7.

Complex pressures were calculated with a discrete Fourier transform procedure, with a narrowband frequency bandwidth of 3 Hz. Then the data nearest the preferred one-third-octave band center frequencies[138] were written to file and the remainder discarded. Sound pressure levels reported were scaled by the one-third-octave bandwidth according to Eq. (5.28) to approximate the total (integrated) energy contained in each one-third octave band.

In the virtual coherence function used in conjunction with SVD-based PFD [see Section 3.2.3, Eq. (3.4)], a coherence criterion of 0.9999 was enforced, which would lead to the retention of all 50 singular values. However, to remove noise, the number of singular values retained was always limited to 10, regardless of the virtual coherence result.

In the linear prediction algorithm that numerically extends the measurement aperture, the hologram data were extrapolated 50 points with $\Delta x = 0.15$ m (6 in) spacing, equal to the grid spacing of the array, in both the upstream and downstream directions. The filter order in the linear prediction algorithm was $\nu = 4$.

After aperture extension, rows and columns of data were removed for increased computational efficiency. Every *j*th row and column was kept, according to the formula

$$j = \left\lfloor \frac{c}{2.5 f \Delta x} \right\rfloor ., \tag{B.1}$$

where $c = 343$ m/s is the ambient speed of sound, and *f* is the frequency in Hz. The brackets $\lfloor \cdot \rfloor$ indicate the floor function (or rounding down). A lower limit of $j = 1$ and an upper limit of $j = 12$ was enforced. This formula ensures that there are at least 2.5 microphones per acoustic wavelength.

In the SONAH calculations involving cylindrical wave functions, as described in Section 5.3.1, the highest axial wave number (positive and negative) was determined strictly by the axial grid spacing, Δz, by

$$k_{z,\max} = \frac{\pi}{\Delta z}. \tag{B.1}$$

The spacing between axial wave numbers was determined by

$$\Delta k_z = \frac{\pi}{L} ., \tag{B.2}$$

where *L* was the length of the hologram array in the axial direction. The azimuthal modes used were always limited to the axisymmetric ($n = 0$) mode.

C.1 MSTR SONAH Algorithm for Two Cylindrical Sources

```
function pr = sonahmstr2cyl(ms,p,rc,f,gv,d,m,ks)
%SONAHMSTR2CYL Multisource-type representation statistically
```

```
%   optimized near-field acoustical holography: Two
%   cylinder-type sources.
%
%   PR = SONAHMSTR2CYL(MS,P,RC,F) performs an
%   NAH sound field reconstruction at locations RC,
%   using measured hologram data P at
%   locations MS.  The frequency (in Hz) is
%   specified by F.
%
%   MS is a structured array of three elements:
%
%       ms.X, ms.Y, and ms.Z.
%
%   Each element of MS is a three-dimensional array
%   of the locations of measurement points in their
%   respective Cartesian coordinates, (x,y,z).
%
%   RC is a structured array, RC, or a cell array
%   of structured arrays, RC.{Q}, in the case of
%   multiple sets of reconstruction locations.  It
%   has three elements:
%
%       rc.X, rc.Y, and rc.Z.
%
%   Each element of RC is a three-dimensional array
%   of the locations of reconstruction points in
%   their respective Cartesian coordinates, (x,y,z).
%
%   P is the matrix of hologram pressures.  Each
%   column of P is a partial field, and each row
%   is the complex pressure at a hologram
%   location, with
%
%       length(p(:,1)) = numel(ms.X).
%
%   PR = SONAHMSTR2CY(MS,P,RC,F,1) is the same as
%   SONAHMSTR2CYL(MS,P,RC,F), and does not employ
%   global variables.
%   PR = SONAHMSTR2CY(MS,P,RC,F,2) defines variables
%   A, U, G, V, and RALPHA as global variables, so
%   that they are not recreated with each call of
%   SONAHMSTR2CYL.
%
%   PR = SONAHMSTR2CY(MS,P,RC,F,GV,D) locates the
%   origin of each set of cylindrical wave functions
%   a distance D from the y axis.  The nozzle center
%   of an F-22A is 75 inches from the ground.
%   PR = SONAHMSTR2CY(MS,P,RC,F,GV) uses
%   D = 75 * 0.0254;
%
%   PR = SONAHMSTR2CY(MS,P,RC,F,GV,D) uses M = 0.
%   PR = SONAHMSTR2CY(MS,P,RC,F,GV,D,M) includes
%   Hankel functions of orders -M through M in the
%   expansion.
%
```

```
%   PR = SONAHMSTR2CY(MS,P,RC,F,GV,D,M) uses KS = 1.
%   PR = SONAHMSTR2CY(MS,P,RC,F,GV,D,M,KS) scales
%   the maximum wave number in the axial direction
%   by KS.  With KS = 1, the maximum wave number is
%   PI divided by the axial grid spacing of the
%   hologram grid,
%
%   The regularization is capable of running in
%   parallel, for speed.  If desired, use the command
%   MATLABPOOL OPEN N, where N is the number of
%   processors to be used, prior to calling
%   SONAHMSTR2CYL.
%
%   Example:
%       This example generates the measurement and
%       reconstruction variables.
%
%       [ms.X,ms.Y,ms.Z] = ndgrid(0.2, -1:0.1:1, -1:0.1:1);
%       [rc.X,rc.Y,rc.Z] = ndgrid(0.01, -1:0.1:1, -1:0.1:1);
%
%       The next example simulates a measurement of
%       two line arrays of monopoles, and reconstructs
%       pressures near the sources.
%
%       p = sourcex(ms,1000);
%       pr = sonahmstr2cyl(ms,reshape(p,[numel(p) 1]),...
%           rc,1000,1,0.5);
%       pr = reshape(pr,size(rc.X));
%       figure
%       subplot(1,2,1)
%       pcolor(squeeze(ms.Z),squeeze(ms.Y),...
%           squeeze(10*log10(abs(p).^2)))
%       shading flat; axis image;
%       xlabel('{\itz} (m)'); ylabel('{\ity} (m)')
%       title('Measurement, {\itx}=0.2 m')
%       h = colorbar; ylabel(h,'SPL')
%       subplot(1,2,2)
%       pcolor(squeeze(rc.Z),squeeze(rc.Y),...
%           squeeze(10*log10(abs(pr).^2)))
%       shading flat; axis image;
%       xlabel('{\itz} (m)'); ylabel('{\ity} (m)')
%       title('Reconstruction, {\itx}=0.01 m')
%       h = colorbar; ylabel(h,'SPL')
%
%   See also SONAHPL, SONAHCYL.
%
%   Subroutines:
%   CSVD, MODGCVFUN
%
%   References:
%   Y. T. Cho and J. S. Bolton, "Source visualization by using
%   statistically optimized near-field acoustical holography in
%   cylindrical coordinates", J. Acoust. Soc. Am. 118, 2355-
%   2364 (2005).
%
```

```
%   E. G. Williams, "Regularization methods for near-field
%   acoustical holography," J. Acoust. Soc. Am. 110, 1976-1988
%   (2001).
%
%   J. Hald, "Basic theory and properties of statistically
%   optimized near-field acoustical holography", J. Acoust.
%   Soc. Am. 125, 2105-2120 (2009).
%
%   A. T. Wall, K. L. Gee, T. B. Neilsen and M. M. James,
%   The characterization of military aircraft jet noise
%   using near-field acoustical holography methods, Chapter 5,
%   (Dissertation, Brigham Young University, Provo, UT, 2013).
%
%   Date: 2013/02/23

if gv == 2
    %create global variables
    disp('Global variables created.')
    global A Ralpha %#ok<TLEV>
elseif nargin < 5 || gv == 1
    disp('No global variables.')
    A = [];
else
    disp('Error: Incorrect choice for global variable creation.')
    return
end
if nargin < 6, d = 75 * 0.0254; end
if nargin < 7
    m = 0;
elseif ~mod(m,1)
    disp('Hankel orders must be of integer value.')
    return
end
if nargin < 8, ks = 1; end

%define constants
c=343;              %Speed of sound
k=2*pi*f/c;         %Wave number

%generate wavenumber space parameters
%maximum kz (See Cho (2005), Eq. 11)
% Note: if you are getting poor results, this is the
% first parameter I would adjust.
kzmax = abs(pi / diff(ms.Z (1, 1, 1 : 2))) * ks;
%delta kz (See Cho (2005), Eq. 25; Hald (2009), Eq. 18
%and respective paragraph)
dkz = abs(2 * pi / (abs(ms.Z(1, 1, end) - ms.Z(1, 1, 1))) / 2);
%array of kz values
kz = -kzmax : dkz : kzmax;

%array of kr values (See Cho (2005), Eq. 3)
kr = sqrt(k ^2 - kz .^2);

%transform to first cylindrical coordinate system`
```

```
ms.PHIup = atan((ms.Y - d) ./ ms.X);
ms.Rup = sqrt(ms.X .^2 + (ms.Y - d) .^2);
rc.PHIup = atan((rc.Y - d) ./ rc.X);
rc.Rup = sqrt(rc.X .^2 + (rc.Y - d) .^2);
%transform to second cylindrical coordinate system
ms.PHIdn = atan((ms.Y + d) ./ ms.X);
ms.Rdn = sqrt(ms.X .^2 + (ms.Y +d ) .^2);
rc.PHIdn = atan((rc.Y + d) ./ rc.X);
rc.Rdn = sqrt(rc.X .^2 + (rc.Y + d) .^2);

%reference radius
% In some cases, I have found the stability of my final
% result to be highly sensitive to this parameter.
rs = 1/.000005; %See Cho (2005)

%define cylindrical wave functions (See Cho (2005), Eq. 5)
% Note: The last value in the BESSELJ function, 1, gives
% the function a scaling factor to prevent instabilities.
% If your answer is blowing up, please use this
% instead of searching for the problem for two
% weeks straight.
% Note: The formula given here (besselj - 1i*bessely) is
% for a Hankel function of the SECOND kind. In the
% literature, Hankel functions of the first kind
% represent outward propagation, and Hankel functions of the
% second kind are for inward.  However, due to the way
% Matlab defines the imaginary unit, the present
% formulation is required.
Phi = @(r, phi, z, b) (besselj(b, kr * r, 1) - ...
    1i * bessely(b, kr * r, 1)) ./ (besselj(b, kr * rs, 1) - ...
    1i * bessely(b, kr * rs, 1)) .* exp(1i * (b * phi + kz * z));

if isempty(A)

    %form A, a matrix of wave functions.
    % The size of A is (number of wavefunctions, number of
    % measurement points).  (See Cho (2005), Eq. 12a)
    A = zeros(2*numel(kr)*numel(-m:m), numel(ms.X));
    for zz = 1 : length(ms.Z(1,1,:))
        for yy = 1 : length(ms.Y(1,:,1))
            for xx = 1 : length(ms.X(:,1,1))
                i = numel(ms.X(:,:,1))*(zz-1)+ ...
                    length(ms.X(:,1,1))*(yy-1)+xx;
                for mm = -m : m
                    %first set of cylindrical wave functions
                    A(1+length(kr)*(mm+m) : length(kr)* ...
                        (mm+1+m), i) = Phi(ms.Rup(xx,yy,zz), ...
                        ms.PHIup(xx,yy,zz), ms.Z(xx,yy,zz), mm);
                    %second set of cylindrical wave functions
                    A(length(kr)*length(-m:m) + ...
                        (1+length(kr)*(mm+m) : length(kr)* ...
                        (mm+1+m)), i) = Phi(ms.Rdn(xx,yy,zz), ...
                        ms.PHIdn(xx,yy,zz), ms.Z(xx,yy,zz), mm);
                end
            end
```

```
        end
        disp(['Form A: ',...
            num2str(round(1000*zz/length(ms.Z(1, 1, :)))/10),...
            '%']);
    end

    %regularized inverse
    % (See Cho (2005), Eq. 32)
    Ralpha = mtreg(A, p, kr);
end

%form alpha, a matrix of wave functions.
% The size of alpha is (number of wavefunctions,
% number of measurement points).  (See Cho (2005), Eq. 12b)
alpha = zeros(numel(kz) * numel(-m : m), numel(rc.X));
for zz = 1 : length(rc.Z(1, 1, :))
    for yy = 1 : length(rc.Y(1, :, 1))
        for xx = 1 : length(rc.X(:, 1, 1))
            i = numel(rc.X(:,:,1))*(zz-1) + ...
                length(rc.X(:,1,1))*(yy-1) + xx;
            for mm = -m : m
                %first set of cylindrical wave functions
                alpha(1+length(kr)*(mm+m) : length(kr) * ...
                    (mm+1+m), i) = Phi(rc.Rup(xx, yy, zz), ...
                    rc.PHIup(xx, yy, zz), rc.Z(xx, yy, zz), mm);
                %second set of cylindrical wave functions
                alpha(length(kr)*length(-m:m)+...
                    (1+length(kr)*(mm+m) : length(kr)* ...
                    (mm+1+m)), i) = Phi(rc.Rdn(xx,yy,zz), ...
                    rc.PHIdn(xx,yy,zz), rc.Z(xx,yy,zz), mm);
            end
        end
    end
    disp(['Form alpha: ',...
        num2str(round(1000*zz/length(rc.Z(1,1,:)))/10),...
        '%']);
end

%reconstruct pressures
% (See Cho (2005), Eqs. 27-30)
disp('Reconstruction: Working...')
pr = zeros(numel(rc.Z), length(p(1, :)));
for pfn = 1 : length(p(1, :))
    pr(:, pfn) = p(:, pfn).' * Ralpha(:, :, pfn) * A' * alpha;
end

clear alpha
```

C.2 Compact Singular Value Decomposition

```
function [U,s,V] = csvd(A,tst)  %#ok<INUSD>
```

```
%CSVD Compact singular value decomposition.
%
%   U = CSVD(A) Computes the compact form of the SVD
%   of A:
%
%       A = U*diag(s)*V'.
%
%   where
%       U  is  m-by-min(m,n),
%       s  is  min(m,n)-by-1,
%       V  is  n-by-min(m,n).
%
%   [U,S,V] = csvd(A)
%   [U,S,V] = csvd(A,'full')
%
%   If a second argument is present, the full U, S, and
%   V are returned.
%
% Per Christian Hansen, IMM, 06/22/93.

if (nargin==1)
  if (nargout > 1)
    [m,n] = size(A);
    if (m >= n)
      [U,s,V] = svd(full(A),0); s = diag(s);
    else
      [V,s,U] = svd(full(A)',0); s = diag(s);
    end
  else
    U = svd(full(A));
  end
else
  if (nargout > 1)
    [U,s,V] = svd(full(A)); s = diag(s);
  else
    U = svd(full(A));
  end
end
```

C.3 Modified Tikhonov Regularization

```
function ralpha = mtreg(A,ph,kr)
%MTREG Modified Tikhonov regularization.
% RALPHA = MTREG(A,PH) generates a modified
%   Tikhonov regularization filter, using
%   generalized cross-validation (GCV) to
%   optimize the filter parameter.  A is the
%   cross spectral matrix of wave functions.
%   PH is the vector of hologram pressures.
%
%   RALPHA is the regularized inverse of the
```

```
%   cross spectral matrix.
%
%   References:
%   E. G. Williams, "Regularization methods for
%   near-field acoustical holography," J. Acoust.
%   Soc. Am. 110, 1976-1988 (2001).
%
%   Y. T. Cho and J. S. Bolton, "Source
%   visualization by using statistically optimized
%   near-field acoustical holography in cylindrical
%   coordinates", J. Acoust. Soc. Am. 118, 2355-
%   2364 (2005).
%
%   Date: 2013/02/23

%take SVD
% (See Cho (2005), Eq. 31)
disp('SVD: Working...');
pause(0.1)
[V, s, U] = csvd(A' * A);
%rough filter
% A cutoff of noise-related singular values is necessary
% here to prevent instabilities.
NUM = sum(kr > 0);
s(round(NUM * 2 + 1) : end) = 0;

alphara = logspace(-45, 45, 45);    %alpha array
ralpha = zeros([size(A'*A) length(ph(1,1,:))]);
for pfn = 1 : length(ph(1, :))
    disp(['Regularization, PF ',num2str(pfn),...
        ': Working...']);
    J = zeros(1, length(alphara));
    parfor n = 1 : length(alphara)
        %generate filter funtion
        % (See Williams (2001), Eq. 57)
        F1alpha1 = diag(alphara(n) ./ ...
            (alphara(n) + s.^2 .* ...
            ((alphara(n) + s.^2) / alphara(n)).^2));
        %cost function
        % (See Williams (2001), Eq. 58)
        J(n) = norm(F1alpha1*U'*ph)^2 / trace(F1alpha1)^2;
    end
    %minimization of J
    [~, ind] = min(J);
    alphalow = alphara(ind);
    ra = fminbnd('modgcvfun', .01*alphalow, 100*alphalow, ...
        optimset('Display', 'off'), s, U, ph);

    %modified Tikhonov filter
    % (See Cho (2005), Eq. 33 and respective paragraph,
    % and Williams (2001), Eq. 57)
    g=diag(s);
    F1a = diag(ra ./ (ra + s .^2 .* ...
        ((ra + s .^2) / ra) .^2));
    % (See Cho (2005), Eq. 32)
```

```
    ralpha(:,:,pfn) = V * ...
        (ra * F1a .^2 + g' * g)^(-1) * g' * V';
end
```

C.4 SVD-based PFD with Virtual Coherence

```
function [C,n] = pfdsvd(A,B,eta)
%PFDSVD SVD-based partial field decomposition
%   with virtual coherence.
%
%   [C,N] = PFDSVD(A,B,ETA) calculates the N
%   mutually incoherent partial fields C from scan-
%   based hologram data, A, and with reference
%   pressures B.  ETA is the coherence criterion
%   that dictates N.
%
%   A contains measured hologram complex pressures
%   from a scan-based measurement, allowing for both
%   horizontal and vertical scans.  Its first
%   dimension corresponds to array channels, the
%   second to time blocks, the third to runs (vertical
%   scans), and the fourth to horizontal scans.
%
%   The reference array B, and the output pressure
%   array C, are arranged similarly,
%   with the four dimensions corresponding to
%   channels, time blocks, runs, and scans.
%
%   Subroutines:
%   CSVD
%
%   References:
%   M. Lee and J. S. Bolton, "Scan-based near-field
%   acoustical holography and partial field
%   decomposition in the presence of noise and source
%   level variation", J. Acoust. Soc. Am. 119, 382-393
%   (2006).
%
%   A. T. Wall, K. L. Gee, T. B. Neilsen and M. M. James,
%   The characterization of military aircraft jet noise
%   using near-field acoustical holography methods, Chapter 3,
%   (Dissertation, Brigham Young University, Provo, UT, 2013).
%
%   Date: 2013/02/23

%initialize
blocks = length(A(1,:,1,1));
runs = length(A(1,1,:,1));
scans = length(A(1,1,1,:));
Crp = zeros(length(B(:,1,1,1)), length(A(:,1,1,1)), runs, ...
scans);
Cpp = zeros(length(A(:,1,1,1)), length(A(:,1,1,1)), runs, ...
```

```
    scans);
Cvp = Crp;
Crr_sc = zeros(length(B(:,1,1,1)), length(B(:,1,1,1)), ...
    runs, scans);
U_sc = Crr_sc;
sigma_sc = Crr_sc;
V_sc = Crr_sc;
Sigma_sc = Crr_sc;

for j = 1:scans
    for i = 1:runs
        %cross spectra
        % (See Lee (2006), Eq. 4-6)
        Crr_sc(:,:,i,j) = ...
            conj(B(:,:,i,j)) * B(:,:,i,j).' / blocks;
        Crp(:,:,i,j) = ...
            conj(B(:,:,i,j)) * A(:,:,i,j).' / blocks;
        Cpp(:,:,i,j) = ...
            conj(A(:,:,i,j)) * A(:,:,i,j).' / blocks;
        %svd on each cross spectral matrix
        % (See Lee (2006), Eq. 7)
        [U_sc(:,:,i,j) sigma_sc(:,i,j) V_sc(:,:,i,j)] = ...
            csvd(Crr_sc(:,:,i,j));
        Sigma_sc(:,:,i,j) = diag(sigma_sc(:,i,j));
        Cvp(:,:,i,j) = U_sc(:,:,i,j)' * Crp(:,:,i,j);
    end
end

%svd on mean cross spectral matrix
% (See Lee (2006), Eq. 7)
Crr_a = mean(mean(Crr_sc, 3), 4);
[U_a, sigma_a, ~] = csvd(Crr_a);  %SVD
Sigma_a = diag(sigma_a);

%virtual reference cross spectral matrix
% (See Lee (2006), Eq. 8)
Cvv = Sigma_sc;
gamma_2 = zeros([length(A(:,1,1,1)) length(B(:,1,1,1)) ...
    runs scans]);
for j = 1:scans
    for i = 1:runs
        %virtual coherence function
        % (See Lee (2006), Eq. 28)
        gamma_2(:,:,i,j) = (abs(Cvp(:,:,i,j)).^2 ./ ...
            (diag(Cvv(:,:,i,j)) * diag(Cpp(:,:,i,j)).')).';
    end
end

%select cutoff singular value
% (See Lee (2006), Eq. 29)
J = zeros(runs,scans);
CCobtain = 0;
for i = 1:runs
    for j = 1:scans
        for l = 1:length(B(:,1,1,1))
```

```
            bool = sum(gamma_2(:,1:l,i,j), 2) >= eta;
            if bool == 1
                J(i,j) = l;
                CCobtain = CCobtain + 1;
                break
            end
            J(i,j) = l;
        end
    end
end
%Note: Due to the presence of noise in the signals,
% if all 50 singular values are included the partial
% fields are contaminated.  For higher frequencies,
% where the number of sources approaches or
% exceeds 50, this method cannot remove noise.
% Here, the maximum number of singular values
% is limited to 10.  (See Wall (2013), Section
% 6.5.2.1).
n = min( [ceil(median(reshape(J, [1 numel(J)]))) 10] );

%regularize singular values
% (See Lee (2006), Eq. 26)
Sigma_sc_inv = ...
    zeros(length(B(:,1,1,1)), length(B(:,1,1,1)), runs, scans);
for i = 1:runs
    for j = 1:scans
        Sigma_sc_inv(1:n, 1:n, i, j) = ...
            diag(1 ./ sigma_sc(1:n, i, j));
    end
end

%partial fields
% (See Lee (2006), Eq. 25)
C = zeros([length(A(:,1,1,1)) length(B(:,1,1,1)) runs scans]);
for i = 1:runs
    for j = 1:scans
        C(:,:,i,j) = (U_sc(:,:,i,j) * (Sigma_sc_inv(:,:,i,j))...
            * U_sc(:,:,i,j)' * Crp(:,:,i,j)).'...
            * conj(U_a) * sqrt(Sigma_a);
    end
end
```

C.5 Linear Prediction for Aperture Extension

```
function [B,H] = lp(A,C,nu,G)
%LP Linear prediction for two-dimensional arrays.
%   B = LP(A,C) extends the aperture of a
%   two-dimensional array, A, in all directions,
%   as specified by the number of extension points in
%   the vector C, using MATLAB's LPC function,
%   row-by-row then column-by-column.
```

```
%
%   C is a four-element array of the number of
%   point to predict in each direction:
%       C(1)    points to left
%       C(2)    points to right
%       C(3)    points up
%       C(4)    points down
%
%   B = LP(A,C) uses the filter order NU = 4.
%
%   [B,Y] = LP(A,C,NU,G) also returns the extended
%   geometry variables H.X, H.Y, and H.Z, based on
%   the input geometry variables G.X, G.Y, and G.Z.
%
%   Reference:
%   R. Scholte, I. Lopez, N. B. Roozen and H. Nijmeijer,
%   "Truncated aperture extrapolation for Fourier-based
%   near-field acoustic holography by means of border-padding,"
%   J. Acoust. Soc. Am. 125, 3844-3854 (2009).
%
%   A. T. Wall, K. L. Gee, D. W. Krueger, T. B. Neilsen, S. D.
%   Sommerfeldt and M. M. James, "Aperture extension for
%   near-field acoustical holography of jet noise," Proc.
%   Mtgs. Acoust. 14, 065001 (2013).
%
%   Date: 2012/11/19

if nargin < 3, nu = 4; end
if nargin == 4
    dx = diff(G.X(1, 1:2));
    dz = diff(G.Z(1, 1:2));
    dy = diff(G.Y(1:2, 1));
    x = linspace(G.X(1, 1) - C(1) * dx, G.X(1, end) + ...
        C(2) * dx, length(G.X(1, :)) + C(1) +C(2));
    y = linspace(G.Y(1, 1) - C(3) * dy, G.Y(end, 1) + ...
        C(4) * dy, length(G.Y(:, 1)) + C(3) +C(4));
    z = linspace(G.Z(1, 1) - C(1) * dz, G.Z(1, end) + ...
        C(2) * dz, length(G.Z(1, :)) + C(1) +C(2));
    [H.Y, H.Z] = ndgrid(y,z);
    [~,H.X] = ndgrid(y,x);
end

%zero pad
B = zeros(C(3) + length(A(:,1)) + C(4), C(1) + ...
    length(A(1,:)) + C(2));
B(C(3) + (1:length(A(:,1))), C(1) + (1:length(A(1,:)))) = A;

%loop through rows
for m = 1:length(A(:,1))
    %predict right
    for n = 1:C(2)
        a = lpc(B(C(3) + m, C(1) + ...
            (1 : length(A(1,:)) - 1 + n)), nu);
        B(C(3) + m, C(1) + length(A(1,:)) + n) = ...
            sum(-a(2:end) .* ...
```

```
            B(C(3) + m, C(1) + (length(A(1,:)) - 1 + n : -1 :...
            length(A(1,:)) + n - nu)));
    end
    %predict left
    for n = 1:C(1)
        b = lpc(B(C(3) + m, C(1) + ...
            (length(A(1,:)) : -1 : 2 - n)), nu);
        B(C(3) + m, C(1) + 1 - n) = ...
            sum(-b(2:end) .* B(C(3) + m, C(1) + ...
            (2 - n : 1 + nu - n)));
    end
end

%loop through columns
for n = 1:length(B(1,:))
    %predict bottom
    for m = 1:C(4)
        a = lpc(B(C(3) + (1 : length(A(:,1)) - 1 + m), n), nu);
        B(C(3) + length(A(:,1)) + m, n) = ...
            sum(-a(2:end) .*B (C(3) + (length(A(:,1)) - 1 + m :-1: ...
            length(A(:,1)) + m - nu), n).');
    end
    %predict top
    for m = 1:C(3)
        b = lpc(B(C(3) + (length(A(:,1)) : -1 : 2 - m), n), nu);
        B(C(3) + 1 - m, n) = ...
            sum(-b(2:end) .* B(C(3) + (2 - m : 1 + nu - m), n).');
    end
end
```

C.6 OLVR Algorithm

```
function pf = olvr(g,pr)
%OLVR Optimized-location virtual reference PFD.
%
%   PF = OLVR(G,PR,CS) performs an optimized
%   partial field decomposition of the reconstructed
%   pressures PR over geometry G.
%
%   G is a structured cell array of three elements:
%
%       g{q}.X, g{q}.Y, and g{q}.Z.
%
%   Each cell of G corresponds to a reconstruction
%   surface, and each element of G{Q} is a three-
%   dimensional array of the locations of measurement
%   points in their respective Cartesian coordinates,
%   (x,y,z).
%
%   Each cell of PR corresponds to a reconstruction
%   surface.  PR{Q} has three dimensions that
%   correspond to locations in (x,y,z), respectively,
%   and a fourth dimension that corresponds to the
```

```
%   partial field.
%
%   References:
%   Y. J. Kim, J. S. Bolton and H. S. Kwon, "Partial
%   sound field decomposition in multireference near-
%   field acoustical holography by using optimally
%   located virtual references," J. Acoust. Soc. Am.
%   115, 1641-1652 (2004).
%
%   A. T. Wall, K. L. Gee, T. B. Neilsen and M. M. James,
%   The characterization of military aircraft jet noise
%   using near-field acoustical holography methods, Chapter 6,
%   (Dissertation, Brigham Young University, Provo, UT, 2013).
%
%   Date: 2013/02/26

%limit candidate locations
cs = 2; %candidate reconstruction surface
xmaxi = find(g{cs}.X(:,1,1) >= 20, 1);
jj = 5;
pc = pr{cs}(1:jj:xmaxi, 1:jj:end, 1:jj:end, :);
g{cs}.X = g{cs}.X(1:jj:xmaxi, 1:jj:end, 1:jj:end);
g{cs}.Y = g{cs}.Y(1:jj:xmaxi, 1:jj:end, 1:jj:end);
g{cs}.Z = g{cs}.Z(1:jj:xmaxi, 1:jj:end, 1:jj:end);
N = numel(pc(:,:,:,1));
J = length(pr{cs}(1, 1, 1, :));
K = 10;

%svd of reconstructed field
% (See Wall (2013), Eq. 6.2-7.3)
Yv = reshape(pc, [N J]);
Syy = conj(Yv) * Yv.';
[W, ~, ~] = svd(Syy);

%noise subspace
% (See Wall (2013), Eq. 6.4)
R_noise = zeros(length(W(:, 1)));
for n = K + 1 : N
    disp(['R_noise, ', num2str(n/N*100), '%'])
    R_noise = R_noise + W(:, n) * W(:, n)';
end

%music powers
% (See Wall (2013), Eq. 6.5-6.6)
pmusic = zeros(N, 1);
for n = 1:N
    u = zeros(N, 1);
    u(n) = 1;
    pmusic(n) = 1 / (u' * R_noise * u);
end

%sort by decreasing music power
P_sort(:, 1) = pmusic;
P_sort(:, 2) = 1:length(pmusic);
```

```
P_sort(:, 3) = reshape(g{cs}.X, [N 1]);
P_sort(:, 4) = reshape(g{cs}.Y, [N 1]);
P_sort(:, 5) = reshape(g{cs}.Z, [N 1]);
P_M_all = sortrows(P_sort, -1);

%all possible virtual reference pressures
i = P_M_all(:, 2);
c = zeros(length(P_M_all(:, 1)));
X = zeros([length(P_M_all(:, 1)) J]);
for k = 1:length(i)
    c(i(k), k) = 1;
    X(k, :) = c(:, k).' * Yv;
end
Sxx = X * X';

%find non-redundant virtual references
Sii = repmat(diag(Sxx), [1 N]);
Sjj = Sii.';
% (See Wall (2013), Eq. 6.7)
gamma_sq = abs(Sxx).^2 ./ Sii ./ Sjj;
i_new = zeros([K 1]);
for m = 0.01:0.01:0.99
    coh_thresh = m;
    gamma_new = gamma_sq;
    i_temp = i;
    i_new(1) = i(1);

    for k = 2:K
        ind_rem = find(gamma_new(:, 1) < coh_thresh).';
        gamma_new = gamma_new(ind_rem, ind_rem);
        i_temp = i_temp(ind_rem);
        if ~isempty(i_temp)
            i_new(k) = i_temp(1);
        else
            break
        end
    end

    if sum(i_new > 0) >= K
        disp(num2str(coh_thresh))
        break
    end
end

%calculate virtual references
% (See Wall (2013), Eq. 6.9)
c_new = zeros(N, K);
X_new = zeros(K,J);
for k = 1:length(i_new)
    c_new(i_new(k), k) = 1;
    X_new(k, :) = c_new(:, k).' * Yv;
end

%decompose virtual references
```

```
% (See Wall (2013), Eq. 6.10)
Sxx_new = X_new * X_new';
L = chol(Sxx_new,'lower');

%generate olvr partial fields
% (See Wall (2013), Eq. 6.11-6.12)
pf = cell(size(pr));
for dd = 1:length(pr)
    Y = reshape(pr{dd}, [numel(pr{dd} (:, :, :, 1)) J]);
    Sxy = X_new * Y';
    pf{dd} = Sxy' * (L')^-1;
end
```